Advancing Electron Microscopy Cryogenic Workflows: Reducing Damage and Integrating STEM and SEM for *in-Situ* Structural Biology



William H. D. Bowles

Linacre College

University of Oxford

A thesis submitted for the degree of

Interdisciplinary Biosciences

10th October, 2025

Supervised by Maud Dumoux, C. Alistair Siebert, and James H. Naismith

This thesis is dedicated to
my Grandfather, John,
who instilled in me a love and curiosity
for science from a young age.

Abstract

The advancement of *in situ* structural biology by cryo-electron tomography (cryo-ET) is fundamentally limited by the challenge of locating specific macromolecules within the crowded cellular environment. While tag-based workflows offer a solution, their success is constrained by a trade-off between a tag's size and its detectability.

This thesis first establishes a theoretical framework which demonstrates that the confident detection of small, minimally perturbing tags in scanning transmission electron microscopy (STEM) requires a substantial electron fluence, and identifies the electron 'dose budget' as the primary limiting factor. However, a comprehensive, quantitative understanding of the mechanisms of beam-induced damage in vitrified biological specimens, particularly from scanning probes, remains incomplete.

Consequently, this thesis presents a systematic, quantitative investigation into the mitigation of damage caused by scanning electron beams in vitrified biological samples. Using mass loss in vitreous ice as a metric, the spatio-temporal distribution of the dose is shown to be an important parameter; an interleaved scan pattern is demonstrated to significantly reduce mass loss compared to a conventional raster scan at long pixel dwell times.

This analysis is then extended to high-resolution structural damage. The impact of preparatory low-voltage SEM imaging, as used in advanced correlative workflows, is quantified using single-particle analysis of apoferritin as a sensitive damage reporter. A non-linear, depth-dependent damage mechanism is revealed, whereby the shallow penetration of very low-energy electrons can paradoxically preserve deeper structures.

The findings presented in this thesis provide systematic quantification of the structural consequences of scan-based irradiation under cryogenic conditions. By establishing a link between spatio-temporal dose distribution and sample damage, this work informs the ongoing development of more dose-efficient imaging strategies, contributes to a deeper understanding of damage processes in biological cryo-EM, and establishes a path towards more robust, high-resolution, tag-based discovery workflows.

Acknowledgements

Thanks must go to many people who have been involved in both small and large ways over these last years, from their technical expertise, to their collaboration, and their emotional support.

Firstly, my three main supervisors: To **Dr. Maud Dumoux**, I am especially grateful. Her boundless enthusiasm and guidance formed the foundation of this project, while challenging me to push my work to a deeper level.

My sincere thanks go to **Dr. Alistair Siebert**, for his patient mentorship and for always asking the incisive questions that pushed me to think more critically about my data and its interpretation.

And to **Prof. Jim Naismith**, for fostering an environment of intellectual freedom, and for his unwavering support and advice not only within this DPhil, but also for my future career.

My thanks also go to all of the **Rosalind Franklin Institute** and **Diamond Light Source** staff. Most importantly, to Dr. Abner Velazco-Torrejon for his collaboration in acquiring and interpreting the STEM data, and for accompanying me on many late-night manual collection sessions on the microscope. Also, to Dr. Jon Barnard for help in the technical aspects of STEM, and Drs. Dan Clare and Casper Berger for advice on processing, and Dr. Siva Ramadurai for guidance in the wet-lab aspects. I am grateful to my **external collaborators** for their insightful discussions regarding SEM damage, including Dr. David Klebl (MPI Martinsreid) and Prof. Peter Dahlberg (SLAC). At **Oxford University**, I would like to thank my Course Directors, Profs. Gail Preston and Esther Becker, for their guidance, and the Biotechnology and Biological Sciences Research Council (**BBSRC**) and **Diamond Light Source** for their generous financial support.

I am thankful for the other **students in the Rosalind Franklin Institute** – Particularly, Helena Watson, Jake Smith, Emily Barot, Niamh Morris and Nadisha Gamage – who have been a constant source of inspiration, support, and camaraderie.

As a requirement of completion of this DPhil, I have had the pleasure of an internship

hosted by **ThermoFisher Scientific's Electron Microscopy Division**. Several people made this a reality, most importantly, Rebecca Thompson and John Mitchels who organised and supervised this period, to whom I am extremely grateful.

I would like to thank the **microscopes** 'Ruska', 'Dorothy', 'Rosalind', and 'Franklin' for producing all of the data for this thesis. I would also like to thank the engineers who designed these complex instruments, though my resolve was certainly tested by the placement of JEOL's uncapped 'Low-Mag' button directly next to the astigmatism controls – a lesson I learned more than once.

Finally, on a more personal note, I owe so much to my **family and friends**: to my partner Freya and her brother Luke for their support and invaluable help proof-reading this thesis, to my Parents, Vicki and Rod, for always giving me so much support and encouragement especially during these last few months, to Paul and Barbara for their kind support and care, to my closest friends (Tom, Helena, Matthew, Adi, Emma, Pierce and Spencer), and to the **greyhounds**: Norman and Blossom for their wordless sup-paw-t.

Contents

Abbreviations **xiv**

1 Introduction and Review of Literature **1**

1.1 The Challenge: Locating Proteins in the Cell 2

1.1.1 Why *in-Situ* Structural Biology? 2

1.1.2 Cryo-ET: a Tool for *in-Situ* Structural Biology 4

1.1.3 Limitations for *in-Situ* Structural Biology with Cryo-ET and Current Solutions 6

1.2 The Toolbox: What Can Electron Microscopy Offer? 19

1.2.1 Energy-Filtered Transmission Electron Microscopy 21

1.2.2 Scanning Transmission Electron Microscopy 23

1.2.3 The Advantages and Limitations of Cryo-STEM for Biological Samples 25

1.2.4 Phase-Contrast STEM Techniques Applied to Biological Samples 30

1.2.5 SEM and Volume Imaging 34

1.3 A Proposed Workflow 36

1.4 The Overarching Barrier: Radiation Damage in Cryo-EM 39

1.4.1 Damage Processes in Electron Microscopy 40

1.4.2 Damage Mitigation Strategies in Electron Microscopy 44

1.5 Thesis Aims and Outline 50

2 Background Information **52**

2.1 Wave Properties of Electrons 53

2.1.1 Imaging with Electrons 53

2.1.2 Electron Wavelength 53

2.2 Electron-Specimen Interactions 56

2.3 Principles of Image Formation and Contrast 59

2.4 Electron Optics and Microscope Components 65

2.4.1 The Electron Source 65

2.4.2 The Electron Lenses and Apertures 66

2.4.3 Beam Deflection and Correction Systems 69

2.5 Image Formation and Detection System 72

2.5.1 Magnification 74

2.5.2 Energy Filter 75

2.5.3 Detectors 75

2.6 Resolvability 77

2.6.1 The Third Dimension 82

3 Theoretical Considerations for STEM Nanoparticle Localisation 86

3.1 Introduction 87

3.2 Considerations for the Theoretical Model 89

3.2.1 3-Dimensional Localisation Approaches 89

3.2.2 Geometry of STEM on Lamellae 97

3.2.3 Beam Broadening 99

3.3 Theoretical Model for Nanoparticle Detection 102

3.3.1 Detectability - Scattering Cross Section 102

3.3.2 Application to Thicker Samples 106

3.3.3 Model Results 111

3.4 Experimental Application of the Model 117

3.4.1 Experimental Methods 118

3.4.2 Experimental Results 121

3.5 Discussion 123

3.5.1 Approach for 3D-localisation and Geometry of the STEM . . 123

3.5.2 Beam Broadening Limits the Achievable STEM Resolution in Lamellae . . . 124

3.5.3 Theoretical Model and the Detectability of Nanoparticles in Vitreous Ice . . . 125

3.5.4 Conclusion . . . 128

4 Cryo-STEM Radiation Damage Mitigation Using An Interleaved Scanning Pattern 129

4.1 Introduction . . . 130

4.2 Materials and Methods . . . 131

4.2.1 Sample Preparation . . . 131

4.2.2 Raster and Interleaved Pattern Creation . . . 132

4.2.3 Trench Patterns . . . 134

4.2.4 STEM Microscopy Hardware and Alignment . . . 136

4.2.5 Scan Generator . . . 138

4.2.6 Sample Screening . . . 138

4.2.7 Experimental Data Collection . . . 139

4.2.8 Thickness Measurements . . . 141

4.2.9 Data Analysis . . . 142

4.3 Results . . . 146

4.3.1 Scanning Methods Affect Mass Loss in Vitreous Ice 147

4.3.2 Statistical Analysis Across All Datasets 150

4.3.3 Trench Experiments and Directional Mass Loss of Vitreous Ice 158

4.4 Discussion 164

4.4.1 Findings 164

4.4.2 Future Directions and Conclusion 170

5 SEM Damage for High-Resolution Cryo-Electron Tomography Workflows 172

5.1 Introduction 173

5.2 Materials and Methods 174

5.2.1 Simulations of SEM Conditions in Vitreous Ice 174

5.2.2 Protein Purification 175

5.2.3 Sample Preparation 176

5.2.4 Scanning Electron Microscopy 176

5.2.5 Transmission Electron Microscopy of Single Particle Analysis Data Collection 178

5.2.6 Single Particle Analysis Data Processing 179

5.3 Results 182

5.3.1 Simulation of low-energy SEM electrons in Vitreous Ice . . . 182

5.3.2 Dose Applied to the Sample 185

5.3.3 SEM Exposure Causes Loss of High-Resolution Information 186

5.3.4 Exploratory Damage Mitigation Using Interleaved SEM Scanning 200

5.4 Discussion 205

5.4.1 Practical Considerations for Biologists: Workflow and Instrumentation 208

5.4.2 Limitations of the Methods Used 210

6 Conclusions and Future Perspectives **212**

6.1 Recapitulation and Summary of Findings 213

6.1.1 The Vision: An Integrated Workflow for *in-Situ* Structural Biology 213

6.1.2 Summary of the Investigation 214

6.2 A Revised Perspective: The Cumulative Damage Budget 214

6.3 Future Directions 216

6.3.1 Systematic Optimisation of Spatio-Temporal Dose Delivery . 216

6.3.2 Standardisation of 'Low-Damage' Correlative SEM Protocols 217

6.4 Conclusion 217

References **218**

Appendices

A Appendix **247**

A.1 Appendix for Chapter 1: Introduction 247

A.1.1 STEM-TEM Correlation Attempts 247

A.2 Appendix for Chapter 2: Background 251

A.2.1 Calibration of Titan Krios G4 Collection angles 251

A.3 Appendix for Chapter 3: Theoretical Considerations for STEM Nanoparticle Localisation 256

A.4 Appendix for Chapter 4: STEM Damage 260

A.4.1 Further Examples of Trench Scanning Experiments 266

A.4.2 Further Explanations of the Raster and Interleaved Scanning 268

A.5 Appendix for Chapter 5: SEM Damage 271

A.5.1 Preliminary Tomography Dataset 277

Abbreviations

ADF Annular Dark Field

AI Artificial Intelligence

AuNP Gold Nanoparticle

BF Bright Field

BSE Backscattered Electron

CFEG Cold Field Emission Gun

CL Condenser Lens

CLEM Correlative Light and Electron Microscopy

CTF Contrast Transfer Function

DED Direct Electron Detector

DNA Deoxyribonucleic Acid

DPC Differential Phase Contrast

DQE Detective Quantum Efficiency

Abbreviations

EDX Electron Dispersive X-Ray Spectroscopy

EELS Electron Energy Loss Spectroscopy

EFTEM Energy-Filtered Transmission Electron Microscopy

EM Electron Microscopy/Microscope

ET Electron Tomography

ETD Everhart–Thornley Detector

FEG Field Emission Gun

FIB Focused Ion Beam

FLM Fluorescence Light Microscopy

FWHM Full-Width at Half Maximum

GFP Green Fluorescent Protein

HAADF High-Angle Annular Dark Field

PMT Photo Multiplier Tube

RNA Ribonucleic Acid

SEM Scanning Electron Microscopy/Microscope

SFEG Schottkey Field Emission Gun

SNR Signal to Noise Ratio

SRFLM Super Resolution Fluoresence Light Microscopy

STA Subtomogram Averaging

STEM Scanning Transmission Electron Microscopy/Microscope

TEM Transmission Electron Microscopy/Microscope

TLD Through–Lens Detector

vEM Volume Electron Microsocpy

WD Working Distance

WPOA Weak Phase Object Approximation

1

Introduction and Review of Literature

Contents

1.1 The Challenge: Locating Proteins in the Cell 2
1.1.1 Why *in-Situ* Structural Biology? 2
1.1.2 Cryo-ET: a Tool for *in-Situ* Structural Biology 4
1.1.3 Limitations for *in-Situ* Structural Biology with Cryo-ET and Current Solutions 6
1.2 The Toolbox: What Can Electron Microscopy Offer? . 19
1.2.1 Energy-Filtered Transmission Electron Microscopy . . . 21
1.2.2 Scanning Transmission Electron Microscopy 23
1.2.3 The Advantages and Limitations of Cryo-STEM for Biological Samples 25
1.2.4 Phase-Contrast STEM Techniques Applied to Biological Samples 30
1.2.5 SEM and Volume Imaging 34
1.3 A Proposed Workflow 36
1.4 The Overarching Barrier: Radiation Damage in Cryo-EM 39
1.4.1 Damage Processes in Electron Microscopy 40
1.4.2 Damage Mitigation Strategies in Electron Microscopy . 44
1.5 Thesis Aims and Outline 50

This Chapter establishes the scientific context and motivation for the work presented in this thesis. It begins by reviewing the current landscape of *in-situ* structural

biology, its key technological challenges and the methods used to overcome these challenges. Subsequently, it details the overarching aims of this thesis by introducing the proposed workflow to address these limitations. Finally, the value and future potential of this workflow will be considered in light of ongoing developments in electron microscopy, highlighting the central challenge of beam-induced radiation damage. Key concepts and techniques introduced in this Chapter will be defined in greater detail in Chapter 2, which provides the necessary technical background for this thesis.

1.1 The Challenge: Locating Proteins in the Cell

1.1.1 Why *in-Situ* Structural Biology?

Determination of the three-dimensional architecture of biological macromolecules is a critical prerequisite to a mechanistic understanding of their roles, from mediating biological processes to driving disease pathology and informing drug design. Structural biology has historically relied on the characterisation of these purified macromolecules in isolation. Techniques such as X-ray crystallography, nuclear magnetic resonance (NMR) spectroscopy, and cryogenic electron microscopy (cryo-EM) have all provided insights into protein structure [1–3], with X-Ray Crystallography and NMR dominating for much of the 20^{th} century [4].

Recently, single-particle analysis (SPA) cryo-EM has transformed structural biology of proteins and RNA [5]. In this technique, a purified solution of the macromolecule is vitrified, trapping millions of individual copies in random orientations within a thin (< 100 nm) layer of vitreous (amorphous) ice. A transmission electron microscope is then used to capture thousands of two-dimensional projection images of these particles, which are computationally sorted and averaged to reconstruct a high-resolution, three-dimensional model. Recent hardware and software advancements have enabled the determination of purified protein and RNA structures near ($\lessapprox 2$

Å) or at (≈ 1.2 Å) atomic resolution in solution [6–10] – a 'resolution revolution' [11]– for which the Nobel Prize in Chemistry was awarded in 2017 [5].

Whilst valuable, these reductionist structural biology methods necessitate removing molecules from their native environment within the cell. This removal risks introducing non-physiological artefacts and prevents the study of the transient or context-dependent interactions that govern cellular function [12, 13].

The ultimate goal of structural biology is not merely to deduce the structure of a protein, but also to understand the protein's function in its cellular context. To achieve this, proteins must be observed *in-situ*. *In-situ* structural biology aims to determine the structures of macromolecules as they exist and function within the complex, crowded, and dynamic environment of the cell [14]. This approach is paramount to our understanding of how cellular architecture dictates function, how protein complexes assemble and disassemble in response to stimuli, and how pathological states arise from molecular dysregulation.

Furthermore, as artificial intelligence (AI) tools such as AlphaFold [15] and Rosetta [16] become increasingly proficient in predicting isolated structures, the demand for experimental structural biology shifts toward providing what these models lack: direct observation of the position, interactions, and functional states of a protein of interest within the cell.

At the forefront of this approach within *in-situ* structural biology is cryogenic electron tomography (cryo-ET). For simplicity, this thesis will refer to proteins as the target of interest, though it must be noted that the described workflow is broadly applicable to other biological macromolecules such as RNA, DNA, and their assemblies [17–19].

1.1.2 Cryo-ET: a Tool for *in-Situ* Structural Biology

Transmission Electron microscopy (TEM) offers a direct path to visualising the cell at high-resolution. However, historically, the intrinsic conflict between the high-vacuum conditions of the microscope column and the aqueous nature of biological matter has posed a barrier. Early EM protocols relied on destructive sample preparation, including chemical fixation, dehydration, embedding in plastic, and staining with heavy-metal salts [20]. While these methods provided foundational insights into cellular ultrastructure, they were known to induce significant artefacts, such as molecular aggregation, collapse, distortion, and an inability to observe high-resolution structural detail [21].

Cryo-ET is a three-dimensional imaging technique that could instead leverage vitrified cells for visualisation in a near-native state, without heavy-metal staining or plastic embedding. By acquiring a series of two-dimensional projection images as the sample is tilted relative to the electron beam, a three-dimensional reconstruction – or tomogram – of a cellular volume can be generated (see Figure 1.1).

Within these tomograms, individual macromolecules can be identified and their structures determined through a process known as subtomogram averaging (STA). Recent advancements in both hardware and software have enabled cryo-ET and STA to achieve high-resolution ($\lessapprox$ 4 Å) reconstructions of macromolecules in select cases and provide clear insight into molecular interactions, protein localisation, and functional dynamics [22–25]. Cryo-ET is the state-of-the-art technique for *in-situ* structural biology, offering capabilities currently unmatched by any other methodology.

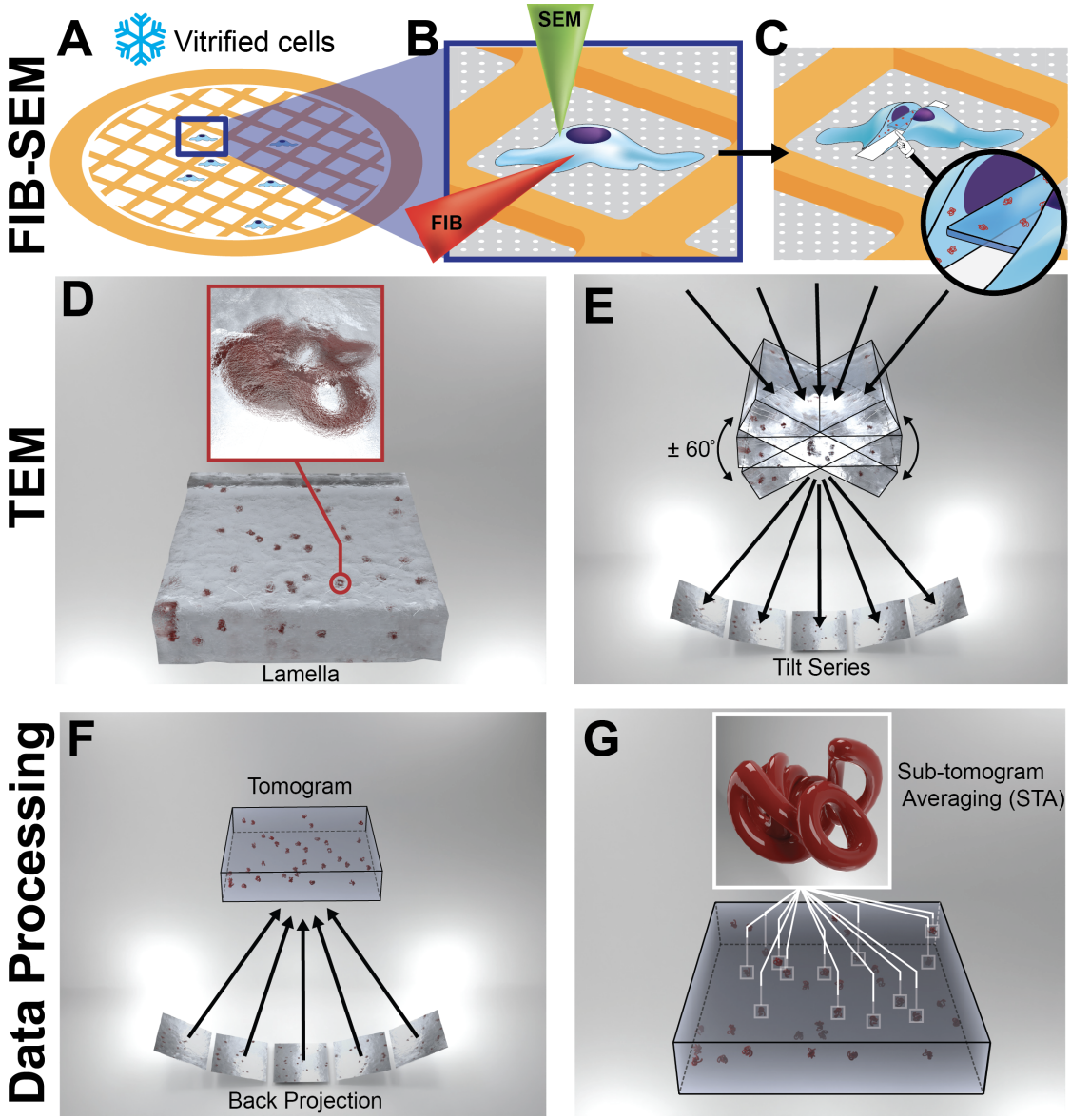


Figure 1.1: **Cryo-Electron Tomography (Cryo-ET) of vitrified cells**. **A** Cells cultured on gold grids are vitrified, preserving them in a near-native, hydrated state. **B** A focused ion beam-scanning electron microscope (FIB-SEM) is used to mill the (several microns) thick cell, creating an electron-transparent lamella (∼200 nm thick) that exposes the cellular interior, inside of which structural details may be seen (**C**). Moving into the Transmission Electron Microscope (TEM) allows high-resolution information to be collected. **D** Within the lamella, multiple copies of the target macromolecule (red) are shown embedded in the cellular environment. **E** The lamella is tilted at incremental angles (usually ± 60°) and projection images are recorded using the high-energy TEM electron beam, forming a 'tilt-series'. **F** The data processing steps then begin by computationally aligning and reconstructing these 2D images into a 3D volume, known as a tomogram. **G** Finally, subtomograms containing the protein of interest are computationally extracted, aligned, and averaged. This process, known as subtomogram averaging (STA), overcomes the low signal-to-noise ratio of the individual particles to produce a high-resolution 3D structure of the macromolecule.

1.1.3 Limitations for *in-Situ* Structural Biology with Cryo-ET and Current Solutions

Despite its strengths, cryo-ET still faces significant challenges and constraints. The primary constraint is the thickness of the sample; electrons cannot penetrate samples much thicker than a few hundred nanometres while retaining the high-resolution information of protein structure [26]. This is not an issue for cryo-EM SPA of isolated proteins; thin layers (< 80 nm) are easily produced by plunge freezing the protein solution in liquid ethane. Cells, however, are often more than two orders of magnitude thicker than vitreous ice in SPA. Thus, to achieve suitable electron transparency for effective imaging, cells must be thinned substantially following vitrification. In the most advanced workflow, a focused ion beam-scanning electron microscope (FIB-SEM) is used to remove material ('milling'). This forms a thin layer of the cell (approximately 100-300 nm in thickness), termed a 'lamella'.

While these advanced protocols in cryo-ET now make it possible to acquire data with fewer artefacts, a more fundamental challenge persists. Even after obtaining a high-quality tomogram, researchers are still faced with the 'needle in a haystack' problem. This refers to an inability to:

1. Identify the cellular region(s) of interest for targeted milling of lamellae;
2. Locate the area containing the protein(s) of interest within the fabricated lamellae for targeting cryo-ET data acquisitions and;
3. Pinpoint the protein(s) of interest in a crowded cellular environment within the generated tomograms.

A mammalian cell is estimated to express around 10,000 different proteins at any given time [27]. At present, only extremely large proteins – often proteins involved in multimeric complexes, or proteins in filamentous structures – have been solved to high-resolution using cryo-ET (primarily because they are the only

targets clearly visible in the tomograms with high signal-to-noise ratios (SNR) and distinct features).

To date, the minimum molecular mass at which untagged proteins can be reliably visualised by cryo-ET is estimated to fall within the 100-300 kDa range, although this is dependent on the thickness of the lamella [26, 28]. Therefore, tagging the protein of interest is extremely attractive for both *in-situ* structural biology and for wider cell biology.

1.1.3.1 Correlative Light and Electron Microscopy

The dominant strategy employed to overcome these challenges of localisation is cryo-correlative light and electron microscopy (cryo-CLEM). This workflow usually begins with imaging the vitrified sample under cryogenic fluorescence light microscopy (cryo-FLM) to generate a map of fluorescently tagged molecules of interest. To achieve targeted milling of the lamellae [29], this fluorescence map must be correlated with images acquired on the FIB-SEM. To ensure the fluorescently-labelled target has been retained, the lamella is re-imaged using cryo-FLM. At present, this verification step is performed either on an integrated light microscope within the FIB-SEM or by transferring the sample to a dedicated cryo-FLM. The resulting fluorescence map of the lamella is then used for correlation with the TEM images of the lamella.

Notwithstanding its utility, this correlative method exhibits notable limitations. Foremost among these is the fundamental gap in resolution between light and electron microscopy which compromises the accuracy of the targeting [29]. In general, cryo-CLEM has a (wavelength limited) resolution limit of approximately 250-300 nm in the lateral (x and y) directions, and 700 nm-1 μm in the axial (z) direction [29, 30]. This makes the technique useful for approximate correlation to the site of interest for acquiring a tilt-series using cryo-ET, but ineffective for localisation of the protein of interest within the tomogram.

Over the last decade, efforts have been made to improve the resolution of CLEM targeting. This includes the development of an array of super-resolution fluorescence light microscopy (SRFLM) methods such as stochastic optical reconstruction microscopy (STORM) [31], photoactivatable localisation microscopy (PALM) [32], and others [33]. Each of these techniques aims to push the boundary of resolution in the FLM beyond classic resolution limits (for an in-depth review of SRFLM applied to cryo-ET, see [34, 35]).

Despite these advances, the fundamental resolution limitation persists. Even under optimal conditions, the resolution of SRFLM applied to cryo-ET rarely exceeds 50 nm in the lateral direction [36–39] due to devitrification, melting, and even sublimation of the ice caused by the required high powered laser [40, 41]. This leaves a considerable resolution gap when compared to the sub-nanometre resolution achievable in cryo-ET. Additionally,these methods make use of a separate SRFLM, which necessitates further manual handling. This greatly increases the likelihood of surface ice contamination and means alignment issues are more common [42].

Beyond the challenge of localisation precision, a biocompatibility issue arises from the use of fluorescent tags. The most widely used fluorescent protein, GFP, is a considerable addition, often comparable in size to small protein domains (27 kDa, approximately 5 nm long, 2.5 nm diameter, and 25 nm^3 in volume [43]). This molecular addition can have significant and unpredictable consequences for the native behaviour of the target protein [44]. GFP's size can physically obstruct interaction sites (steric hindrance), prevent correct protein folding, aggregate, and even impede the conformational changes necessary for function. Consequently, there is a significant risk that the resulting structure does not represent the true functional state of the molecule, but rather an artefact induced by the observation method itself. This compromises the biological validity of the findings, underscoring the need for a smaller and less perturbing labelling strategy.

It is important to distinguish between genetically-encoded tags and externally introduced tags. A genetically-encoded tag is a protein (for example GFP) that the cell is engineered to produce from a provided genetic template. This is typically achieved by transfecting the cell with a plasmid, often leading to overexpression of the resulting fusion protein. In contrast, an extrinsic probe is a pre-synthesised labelling agent that is introduced to the cell from an external source. For FLM, these tags often comprise a range of small molecule (< 1 kDa) fluorescent dyes [45]. While many extrinsic probes, such as small-molecule fluorescent dyes, are significantly smaller (< 1 kDa) than protein-based tags like GFP, achieving specific intracellular targeting often requires a larger protein component. This is typically accomplished using one of two strategies.

The first is to create a complete bio-conjugate, where the dye is attached to a targeting protein (such as an antibody). Delivery of this large probe to an intracellular target typically requires the cell membrane to be permeabilised before the label is introduced. The second is a hybrid approach that utilises a genetically-encoded tag (such as a HaloTag [46]). In this system, the protein of interest is fused to the tag, which then serves as a specific handle to covalently capture a membrane-permeable small-molecule dye *in-situ*.

In both scenarios, while the component responsible for the signal (the dye) is small, the overall size of the complete labelling system remains significant. Therefore, the challenge of potential steric hindrance or size-based perturbation is not eliminated, but rather shifted to the targeting component of the system.

In summary, although CLEM has served the community well in correlating low-resolution cellular features with imaging targets, it lacks the spatial precision required to accurately localise individual proteins for subsequent STA. Furthermore, it adds additional transfer and imaging steps which can lead to devitrification and/or contamination.

1.1.3.2 Electron Dense Tags

An alternative strategy which bypasses the limitations of fluorescence-based correlation to the TEM data is to employ a tag that is directly visible in the EM. This approach relies on the generation of contrast between the tag and the background vitreous cellular milieu. This is achieved through the use of atoms with a high atomic number (Z) that scatter the incident electrons more than the light elements (carbon, nitrogen, oxygen, hydrogen, phosphorous) that constitute biological matter [47]. The greater the number of high-Z element atoms in a smaller volume, the stronger this effect is. Gold is the element most often used due to its extremely high Z and density, biocompatibility, and because it is chemically inert. By labelling a protein of interest with a small quantity of dense, high-Z material, a high contrast tag can be generated, which enables precise localisation directly within the EM and eliminates the resolution gap inherent to CLEM. To this end, several classes of electron dense tags have been developed.

Gold nanoparticles (AuNPs) are often used in cryo-ET. The most widespread historical application of AuNPs in cryo-ET has been not as a specific protein label, but as fiducial markers for tilt-series alignment [48]. In this case, 5-10 nm AuNPs are added to the sample before freezing. Their high contrast with independence of defocus, and well-defined spherical shape make them ideal landmarks for the computational alignment of the 2D projection images, which is a critical step in the generation of a high-quality 3D tomogram [49, 50].

With the advent of fiducial-less alignment software [51], the community's attention has turned towards using AuNPs as a protein tag. AuNPs ranging from 0.8[1] to 10 nm have been used to tag and target proteins using cryo-ET [53–55]. Although this size distribution does not seem to be large, a 10 nm AuNP consists of approximately

[1]Although the term 'nanoparticle' is officially defined as '*a particle with a diameter between 1 and 100 nm*' [52], for simplicity, collections of more than one heavy-element atom that are < 1 nm will also be referred to as nanoparticles throughout this thesis. They are often referred to as 'clusters' or 'nanoclusters' in other texts.

30,000 atoms, whilst a 0.8 nm diameter AuNP consists of approximately only 11 gold atoms [56]. This vast range in particle size highlights a fundamental trade-off in electron dense tagging. A larger tag provides a strong, easily detectable signal. However its intense electron scattering can obscure the structural details of the protein it is meant to identify, making STA difficult or even impossible [57, 58]. Additionally, the tag's electron dense nature can interfere with accurate contrast transfer function (CTF) estimation for high-resolution reconstruction [58]. By contrast, a smaller tag is less perturbing, although it risks being lost in the background noise of the thick, vitreous cell, thereby compromising its utility as a reliable marker.

To address the challenge of specific targeting, researchers have combined AuNPs with nanobodies, which are small (∼15 kDa) yet highly specific antibody fragments. For instance, 5 nm AuNPs have been successfully used to label extracellular adhesin proteins on *Pseudomonas aeruginosa* (a pathogenic bacteria species) by linking them to a specific anti-adhesin nanobody [54] (Figure 1.2A). This approach confirmed the identity of the target protein in its native context and validated the nanobody-to-nanoparticle conjugate as a viable labelling tool. However, by targeting a protein on the cell surface, this study did not address the challenge of intracellular delivery for this extrinsic tag and only acquired single images, not tilt-series.

Other work has focused on confirming the visibility of small gold tags in cryo-ET under the most favourable conditions. In one study, 2.2 nm AuNPs were successfully visualised after targeting them to integrin receptors on the cell surface [55] (Figure 1.2B). However, by targeting the outer cell membrane, the experiment was confined to the thinnest and most electron-transparent region of the sample, which represents a best-case imaging scenario. This avoids the significant challenges encountered within a typical thicker cellular lamella after FIB-milling, which is where most relevant biological processes occur. Therefore, while these studies collectively serve as valuable proofs-of-principles for tag detection in cryo-ET, they

do not offer a generalisable solution to the intracellular labelling problem at the heart of *in-situ* structural biology.

For intracellular targets, the physical size of the labelling species becomes a limiting factor. Even when using small nanoparticles (1-10 nm), the addition of a targeting ligand increases the overall hydrodynamic radius, which can be sufficient to sterically hinder or prevent translocation across size-selective barriers like membrane pores. Consequently, the development of minimally-sized tags is also essential for accessing the cell's cytoplasm.

Several studies have demonstrated the potential of using smaller AuNPs for intracellular labelling. For example, Groysbeck *et al.* successfully internalised 2 nm AuNPs into HeLa cells, observing them in both the cytoplasm and the nucleus of vitrified cells [53] (Figure 1.2C). However, these observations were made on thin cryo-sections (vitrified cells physically cut with a diamond knife, $\approx$ 100 nm thick), which provide a higher SNR than the thicker lamellae typically used for cryo-ET. The images acquired were also single, high-dose acquisitions (120 $e^{-}Å^{-2}$) and not part of a tomographic tilt-series. The same study established a practical lower limit for detectability, noting that 0.8 nm AuNPs were too small to be resolved under these same cryo-conditions, and highlighting the trade-off between tag size and visibility.

Azubel *et al.* demonstrated a more functionally relevant application by tagging a growth factor protein with $\sim$3 nm AuNPs and internalising it via endocytosis into human adipocyte cells [59] (Figure 1.2D). By identifying pairs of nanoparticles *in-situ* at a defined distance (8 nm) within their tomograms, the authors could track the journey of the functional protein dimer through the cell. Although these studies represent important proofs-of-principle, they do highlight the challenge of developing a truly general-purpose intracellular labelling strategy.

In the context of smaller nanoparticles, researchers using 1.4 nm AuNPs to label extracellular axoneme filaments of green algae (*Chlamydomonas reinhardtii*) were

only able to observe the gold densities after STA of the filament; the gold was not directly visible within the generated tomograms [60].

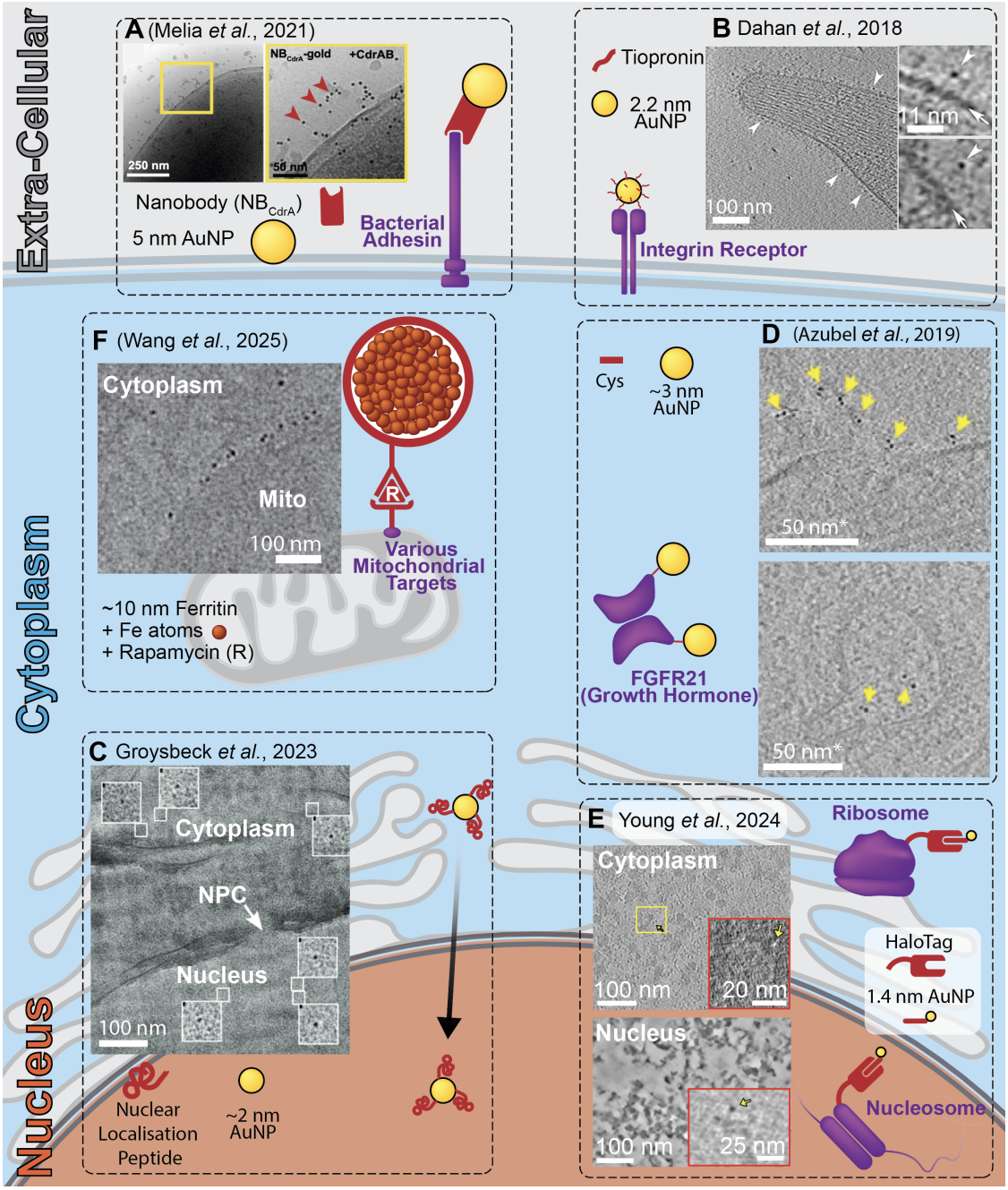


Figure 1.2: **Examples of electron-dense tagging for Cryo-ET**. The tagging strategy is shown in red, with the target in purple. The extra/intra-cellular region is indicated on the left. **A** 5 nm AuNP with nanobody (NB) targeted to extracellular bacterial adhesin proteins of *P. aeruginosa* [54]. **B** 2.2 nm AuNPs coated in Tiopronin molecules targeted to integrin receptors on platelet surfaces [55]. **C** shows free ∼2 nm AuNPs conjugated to nuclear localisation peptides (among others) for delivery to the nucleus, via the nuclear pore complex (NPC) [53]. **D** ∼3 nm AuNPs covalently linked to dimerised FGFR21, showing distinct pairs of AuNPs through various stages of the biochemical pathway [59] (**indicates estimated scale bar*). **E** 1.4 nm AuNPs targeted to ribosomes (cytoplasmic) and nucleosomes (nuclear) using a HaloTag system [61]. *Caption continued on the next page.*

Figure 1.2: *Continued figure caption*: **F** ∼ 10 nm diameter ferritin filled with iron, bound to a mitochondrial outer membrane protein (here, monoamine oxidase) using a rapamycin (R) induced coupling system [62].

The most significant recent advance in targeted intracellular labelling for cryo-ET was demonstrated by Young et al. [61]. In this preprint, the authors developed a multi-component tag consisting of a small AuNP (1.4 nm or 5 nm) covalently linked to both a fluorescent dye and a HaloTag handle. This nanoparticle-dye-halo construct was internalised into the cytoplasm of the cells by incubation with streptolysin-O toxins, which reversibly creates pores in the cell membranes [63] to allow influx of the tag construct. Once inside, the probe specifically bound the protein of interest - in this case, ribosomal and nucleosomal proteins, which were genetically engineered to include a HaloTag (Figure 1.2E).

This strategy provides a powerful, multimodal advantage. Firstly, the fluorescence signal enables initial, low-resolution targeting for lamella preparation and cryo-ET data acquisition. Secondly, the electron dense AuNP serves as a high-precision fiducial for identifying the molecule within the final tomogram. Finally, the specificity assured by the HaloTag system gives greater confidence in the accuracy of tagging the desired target. Despite these advancements, this approach highlights the persistent challenge of visibility: the authors noted that the SNR for the smaller 1.4 nm gold particles within the thick cellular lamella is extremely low, pushing the limits of detectability in cryo-ET.

An alternative to delivering electron dense synthetic nanoparticles, which requires a form of internalisation, as is the case with most nanoparticle-based methods, is to genetically encode a tag that can form an electron dense marker *in-situ*. The primary example of this technique present in the literature is the use of metallothionein: a small (6 kDa), cysteine-rich protein that is naturally produced to sequester toxic metal ions such as cadmium [64]. When expressed as a genetic fusion to a protein of interest, and upon exposure of the cell to various metal salts, metallothionein can form small electron dense clusters. This creates a built-in fiducial on the protein.

As each metallothionein molecule binds only a small number of metal atoms (typically 7 for the heaviest elements such as gold, bismuth and platinum [65]), the resulting metal clusters provide relatively low contrast. This often necessitates the fusion of multiple tags to generate a detectable signal [66]. Furthermore, the tag itself can be problematic; as with any genetically-encoded tag, it can interfere with the proper assembly of protein complexes, and can cause artificial oligomerisation or improper folding of the target [66]. A study which used metallothionein *in-vitro* to tag intermediate filaments attempted to move *in-situ* (into *E.coli*), but reported that overexpression of metallothionein-tagged filaments caused cell stress, preventing further progress [67]. Finally, the high concentrations of metal salts required to load the tag can be toxic to the cell and may even induce the expression of native metallothionein, which creates a confounding background signal that leads to false positive results [68].

A recent advancement over metallothionein was demonstrated by Jiang *et al.* who developed a method to induce synthesis of an AuNP *in-situ* using a cysteine-rich tag as a nucleation point [69]. The AuNPs in this case were between 3 and 6 nm in diameter, and the synthesis was initiated by introduction of a series of chemicals. This method has yet to be carried out under cryogenic conditions, and the necessary preparatory procedures may not be compatible with the physiological requirements of *in-situ* studies [69].

Another genetically-encoded strategy involves the iron-sequestering protein cage, ferritin. Early attempts to use ferritin as a tag fused directly to the protein of interest were impeded by its excessively large size (12 nm) and tendency to cause protein aggregation [62] (Figure 1.2F). To overcome this problem, a newer method, FerriTag, was developed in 2018. It uses the small molecule rapamycin to induce coupling of one tag to one protein of interest [70]. A recent preprint has now successfully adapted and optimised iron-loaded Ferritag for cryo-ET [62] - although it likely remains too large and electron-dense to be useful for downstream STA, owing to the size of the loaded iron core.

1.1.3.3 Shape-based Tagging Methods

This group of tags are distinguishable in tomograms because of their recognisable shape, rather than by their high SNR from electron dense materials. This approach has the advantages of avoiding potentially toxic metal-loading steps and contrast artifacts that can obscure nearby structures for downstream STA.

By excluding the iron-loading step, the 12 nm FerriTag cage can be used as a purely protein-based marker, identifiable by its distinct spherical shape. This strategy has been successfully used to locate clathrin-associated proteins in cryo-tomograms [71]. DNA origami [72] is assembled *in-vitro* to produce large 'signposts' that bind preferentially to a target at one end, thereby displaying a clear directionality of targeting within the tomograms [73]. To date, methods using DNA origami internalised to the intracellular space have not been reported. Furthermore, they are over 90 nm long which, by comparison to all other reported tags, is large.

An example of this strategy was developed by Fung *et al.* with an encapsulin-based scaffold [74]. Encapsulin is a large (25 nm) icosahedral protein shell, similar to FerriTag, and can be inducibly recruited to a target protein *in-situ*. Encapsulin's distinct and reliable shape allows for automated detection in tomograms using machine learning. This system has been successfully used to label proteins across a variety of organelles in human cells.

In principle, the absence of heavy-element atoms in shape-based tags makes STA practical compared to electron dense tags. Nevertheless, despite reported successes, the primary drawback of this entire class of markers is reliance on a large, recognisable shape. Whether it is the 12 nm diameter of FerriTag, the 25 nm diameter of encapsulin, or the 90 nm length of DNA origami structures - such tags represent a substantial increase in size compared to sub-5 nm electron dense tags. This steric bulk inherently increases the risk of perturbing the native function and interaction network of the studied protein.

Whilst these recent advances in tagging constitute significant technical breakthroughs, a crucial distinction must be made between their application in verification versus discovery. To date, most successful demonstrations have targeted proteins that are already large and identifiable, such as ribosomes [61], nucleosomes [61], filaments [60, 67], or proteins found anchored to the outside the cell [54, 55]. In these workflows, the tag serves to confirm the identity of a structure – or part of a structure [60] – that is already visible, rather than acting as a marker to find a previously invisible structure (see figure 1.2).

These verification studies are necessary steps towards creating a tagging system that has a discovery application. They have successfully proven that specific intracellular delivery and conjugation are possible. However, they have simultaneously highlighted a remaining obstacle; the confident *de novo* detection of small tags.

The transformative promise of *in-situ* tagging lies in its potential for true discovery: to label a protein of unknown location, use the tag's coordinates for *a priori* particle picking, and in turn, employ those positions to guide STA to solve a novel structure. This workflow, which would unlock the vast majority of the cellular proteome for structural analysis, remains an unrealised goal.

1.1.3.4 Defining the Ideal Tag for EM-Based Detection

The successful application of protein tagging for cryo-ET is a complex multidisciplinary challenge, spanning chemical synthesis, cellular and molecular biology, and microscopy.

While all these aspects are critical, this thesis will focus specifically on the fundamental principles of tag detection within the electron microscope. With this focus in mind, reviewing the limitations of current methods allows one to define the properties of an ideal *in-situ* tagging system from a detection standpoint. The labelling must be highly specific to reduce false positives and strictly monovalent,

meaning a single tag binds to a single target molecule, to ensure a one-to-one interaction and prevent aggregation. The tag must be able to access its intracellular target, which presents a significant biological challenge in itself. For integration into the correlative workflow, the tag should also incorporate a component detectable in the mesoscale (for example, fluorescence, or visibility by another modality) to guide targeted milling. Finally, and most critically for this work, the tag must be as small as possible to minimise steric interference with its target, while simultaneously generating sufficient SNR for confident detection above the background noise of a cellular lamella. This final requirement presents a substantial barrier and suggests that the solution lies not only in tag design, but in exploring EM modalities and strategies that could improve signal detection. It is this fundamental challenge that the following Chapters will systematically investigate.

1.2 The Toolbox: What Can Electron Microscopy Offer?

This thesis will discuss multiple electron microscopy modalities. To ensure clarity, the following terminology will be used throughout: TEM/EFTEM refers to a conventional mode of transmission electron microscopy, whereby electrons in a broad beam of illumination parallel to the optical axis pass through thin specimens (Figure 1.1A). The transmitted electrons are collected by all pixels of the detector within the same illumination time, which forms an image. This technique is sometimes referred to as conventional TEM (cTEM), bright-field TEM (bf-TEM), or phase-contrast TEM.

On the other hand, Scanning Transmission Electron Microscopy (STEM) refers to the use of a convergent electron beam. The beam is scanned across the sample and the electrons transmitted through may be collected using detectors for each scan position (Figure 1.1B). Although both conventional TEM and STEM fall under

the broader category of '*Transmission Electron Microscopy*', they will be referred to separately throughout this thesis according to these definitions.

Scanning Electron Microscopy (SEM), similar to STEM, uses convergent illumination. However, SEM typically detects electrons emitted from the sample surface rather than transmitted through the sample (Figure 1.1C). Consequently, it is used at lower acceleration voltage compared to the transmission methods. Further details of all the methods described will be provided in Chapter 2.

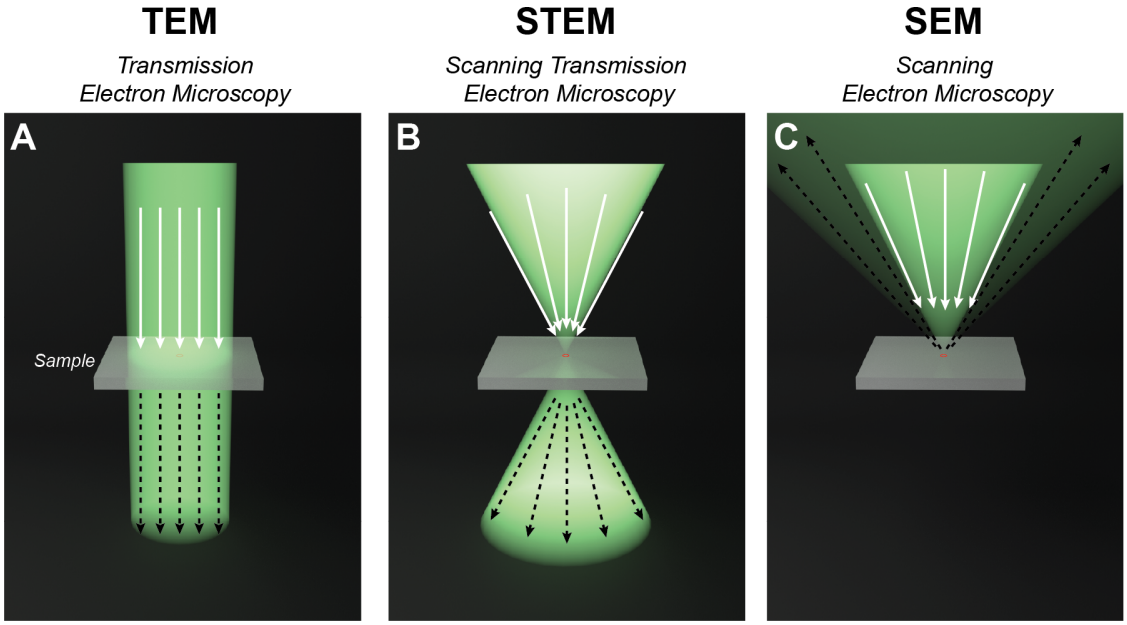


Figure 1.3: **Comparison between different electron microscopies**. Basic diagrams of each of the three main methods: **A** Transmission electron microscopy. Incident electron trajectories (white arrows) are parallel to the optical axis. Detected electrons containing information about the sample (black dotted arrows) are transmitted. **B** Scanning transmission electron microscopy. Incident electron trajectories are convergent, focused to a point on the sample and the resulting detected electrons are also transmitted. **C** Scanning electron microscopy. Incident electron trajectories are also convergent and so the illumination is similar to STEM, however the resulting detected electrons are not transmitted and are instead detected above the sample. An in-depth view comparing the lenses and their positions can be found in chapter 2, figure 2.8.

1.2.1 Energy-Filtered Transmission Electron Microscopy

Energy-Filtered Transmission Electron Microscopy (EFTEM), which forms the basis of conventional cryo-ET, generates contrast principally from coherent, elastically scattered electrons (termed 'phase contrast', introduced in-depth in Chapter 2, Sections 2.1 - 2.2).

However, especially in thicker samples, a significant fraction of electrons undergo inelastic scattering, where they lose energy and coherence. These electrons do not contribute to the useful phase contrast signal but instead produce background noise and blur in the final image.

The function of an energy filter is to physically remove these unwanted, inelastically scattered electrons. By selectively using only the coherent, 'zero-loss' electrons to form the image, EFTEM dramatically enhances phase contrast and is therefore essential for visualising biological structures in their near-native state. The physical principles of electron scattering and phase contrast are discussed in detail in Chapter 2.

Whilst EFTEM can provide high-resolution information for biological samples under cryogenic conditions, the low-dose imaging used to minimise radiation damage from the incident electrons creates a low SNR (typically < 0.1 for cryo-EM SPA [75, 76]), which is compounded for individual molecules within the crowded environment of a thick cellular lamella. Typically, this is overcome by averaging images from many identical particles, which boosts the signal relative to the background noise to reveal structural detail [77].

EFTEM has been revolutionised by the development of Direct Electron Detectors that eliminate the signal-blurring steps in converting electrons to light from previous detectors, and dramatically improve the detective quantum efficiency (DQE) [78]. Their high frame rates allow for the acquisition of data as a 'movie' composed

of many short exposures, rather than a single, long exposure. This movie-mode acquisition enables several image processing strategies.

Firstly, it enables the correction of beam-induced motion. As the high-energy electron beam interacts with the sample, it causes physical specimen drift and doming [79, 80], which blurs a single long exposure beyond recognition. By recording a movie, these movements can be tracked and computationally corrected. This alignment process restores the high-resolution information that would otherwise be lost [81].

Secondly, this approach facilitates fluence (dose) fractionation schemes [81, 82]. The total electron fluence required for imaging is distributed across the movie frames, allowing weighting of the frames during processing. The initial frames, captured before significant radiation damage occurs, contain the most reliable high-resolution information, while later frames contribute more to the lower-resolution signal useful for particle picking. It is this combination of movie-mode acquisition, motion correction, and dose-weighting that allows cryo-EM and -ET to achieve high-resolution from thousands of averaged, low-SNR particle images [83].

Despite these advanced image processing strategies, EFTEM faces a limitation for the specific task of locating single protein tags within a cell. This technique's reliance on phase contrast means that the signal is generated from the entire projected thickness of the specimen. Consequently, as noted earlier [53, 61], the weak signal from a single, small, high-Z nanoparticle is often overpowered by the 'noise' from the surrounding low-Z biological matrix (generally consisting of proteins, lipids, and ice). While powerful for determining the structure of isolated, abundant macromolecules through averaging, this projection imaging makes it exceptionally difficult to unambiguously identify a unique or rare tagged molecule. Therefore, other electron microscopy modalities that do not rely on phase contrast may be better suited to this niche.

1.2.2 Scanning Transmission Electron Microscopy

STEM, as introduced earlier, scans a beam of electrons focused to a point (termed 'probe') across the sample and forms an image from the scattered electrons. An image is built pixel-by-pixel, using one of several detection modalities, which offers flexibility. Therefore, STEM is an imaging technique that forms the basis for a multitude of different techniques, each with specific advantages and disadvantages.

The most widely used detection scheme, which was developed in the laboratory of Albert Crewe, is high-angle annular dark-field (HAADF) imaging [84]. Here, a ring-shaped monolithic detector with a central hole allows unscattered and low-angle scattered electrons to pass through, while electrons scattered to high angles are collected. In this context, 'high angles' are usually 3× the angle from the optical axis to the outer edge of the central beam (known as the convergence semiangle, α, see Figure 1.4). Other monolithic detectors can be employed to collect electrons scattered to lower angles outside of the beam using either an annular dark-field (ADF) detector (collecting from $> 1\times$ the convergence semiangle) or a bright-field (BF) detector (collecting up to the convergence semiangle). These detectors may be used in tandem to capture different angular ranges of the scattered or unscattered beam, depending on the detector's camera length[2].

[2]The camera length is not a real physical length in the electron microscope, but instead is related to the strength of the projector lenses magnifying the scattered intensity on the detector.

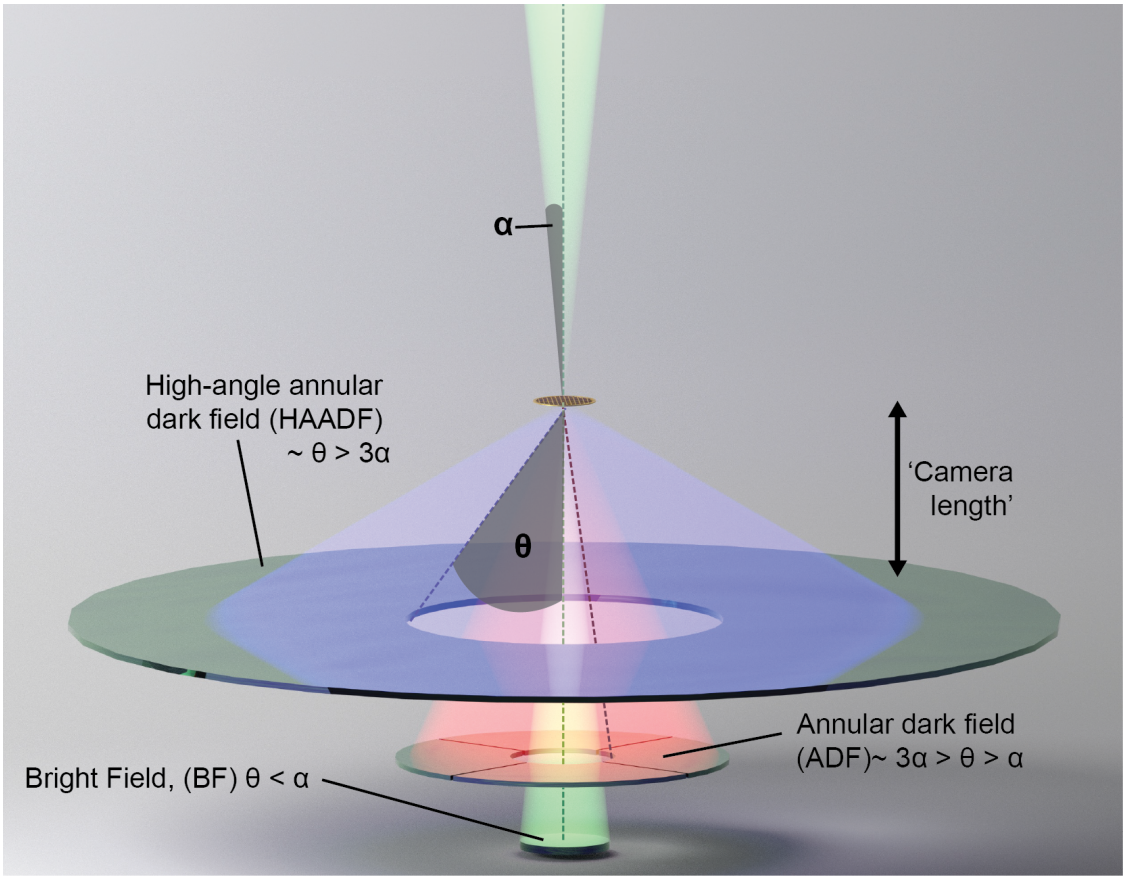


Figure 1.4: **Schematic of a typical STEM detection system**. A convergent electron probe is focused onto a thin specimen. The unscattered, directly transmitted beam (green) is collected by a central Bright-Field (BF) detector. Annular Dark-Field (ADF) and High-Angle Annular Dark-Field (HAADF) detectors collect electrons scattered to progressively higher angles (shown in red and blue, respectively). The inner collection semi-angle for each annular detector, which determines the image contrast, is indicated by the dashed lines.

The high angle scattering in HAADF is dominated by scattering from the atomic nucleus, such that the resulting image contrast is strongly dependent on the atomic number of the elements in the sample (approximately proportional to the atomic Z to the power of 1.6 - 2 [85]). This Z-contrast mechanism of HAADF provides an excellent basis for the detection of heavy elements (for example, the electron dense tags discussed in 1.1.3.2) within a background of light elements (the biological matrix of the lamella). In a constant-Z material (one that consists of an unchanging average elemental composition), the signal is directly proportional to the thickness

of the specimen [86].

Over 50 years ago, HAADF-STEM pioneered the visualisation of individual heavy atoms [84]. Since then, the technique has become an indispensable tool in materials science. Its dominance in this field, as opposed to the life sciences, arises from its capacity for high-resolution quantitative data of robust specimens, especially when paired with probe aberration correctors to push the resolution to sub-Å levels [87]. This allows for the quantitative characterisation of materials that are functionally relevant for catalysis, batteries, and semiconductors, among many others [88]. Initially, much of the use of STEM for biological specimens was restricted to observations of non-cryogenic and plastic-embedded or heavy element-stained samples [89–92]. An early biological application adapted this Z-contrast principle to directly measure the masses of dehydrated biological molecules [93].

While STEM is a versatile technique with broad applications, its application to *in-situ* structural biology necessitates its use under cryogenic conditions. Therefore, the following section will focus on the capabilities and challenges of cryo-STEM.

1.2.3 The Advantages and Limitations of Cryo-STEM for Biological Samples

Cryo-STEM offers several key advantages for biological imaging, including superior performance in thick specimens, more interpretable contrast in individual images, and the capacity for elemental analysis. However, these benefits are balanced by its primary limitation: an inability to visualise unstained proteins.

1.2.3.1 Thick Specimens

One advantage of STEM that has been leveraged for biological samples is its ability to produce high-quality images from relatively thick specimens, thus overcoming a key imaging limitation of TEM, as discussed in Section 1.1.3. The underlying reason

for this advantage stems from the different ways the two techniques form an image. In TEM imaging, the image is formed by an objective lens that must accurately focus the electrons which have passed through the sample. As a specimen gets thicker (beyond ∼300 nm), a larger fraction of electrons undergo multiple scattering events. A significant portion of these are inelastic collisions, where the incident electron transfers a small amount of energy to the sample. These electrons have lost energy, and so are focused differently by the post-specimen lenses compared to elastically scattered electrons. This chromatic aberration causes significant blurring and a loss of structural detail in thick samples.

In contrast, STEM forms an image by collecting electrons with a detector over a defined angular range, and does not rely on post-specimen imaging lenses, making STEM largely insensitive to chromatic aberration. This benefit allows STEM to generate tomograms from cellular samples up to – and even exceeding – 1 μm in thickness, a regime that is completely unattainable with TEM-based tomography methods [91]. This tolerance of thicker samples also negates the need for time-consuming (and often damaging) FIB milling of the samples to ensure their electron transparency.

Over the past decade, researchers at the Weizmann Institute (Elbaum and Wolf) have pioneered cryo-STEM tomography for biological samples [94]. In 2014, their breakthrough cryo-STEM tomography work successfully imaged an entire 600 nm-thick bacterial cell and thicker areas of human cells (which are normally inaccessible without milling) at 1-2 nm resolution [95]. The (TEM) cryo-ET tomograms of the same specimens show reduced image quality.

For imaging thick specimens (defined as $>$ 300 nm), a BF detector is typically implemented to mitigate the effects of beam broadening. As the electron probe traverses the sample, multiple[3] scattering events (which is when an incident electron is scattered more than once) cause the distribution of the electrons in the beam to

[3]Technically, scattering more than once is defined as 'plural scattering', while 'multiple scattering' is used for many events (>20) [96, 97], although the terms are often used synonymously

widen, degrading spatial resolution. However, as the BF detector is positioned on the optical axis, it collects only the central portion of this broadened beam. In doing so, it effectively acts as a filter, rejecting electrons that have scattered to higher angles and that would contribute the most to the blur in the image [98]. This results in an enhanced resolution compared to an ADF detector under the same conditions.

By observing thicker samples, this method also preserves more of the native cellular architecture, offering greater context that would otherwise be lost. This has allowed for the correlation of whole cell SRFLM data with high-resolution STEM maps, helping to bridge the gap between the two resolution scales [99, 100].

The first published application of cryo-STEM tomography on a biological lamella has been performed. The authors demonstrated that the milling process could be simplified by using thicker lamellae (300-500 nm) and proposed that this approach will make *in-situ* structural studies more accessible to the broader cell biology community [101].

1.2.3.2 Contrast and Interpretation

STEM imaging provides a distinct contrast mechanism, and one that is easier to interpret, than the phase contrast used in cryo-TEM. HAADF, BF, and other STEM detection modes largely bypass these complexities. In these techniques, the signal is a direct, positive, and non-oscillatory function of the local mass-thickness and atomic number [102]. This straightforward relationship between signal and structure makes the raw images easier to interpret visually, while also simplifying quantification.

In a crowded cellular environment, a phase-contrast TEM image is a complex superposition of overlapping features, further convoluted by the oscillatory nature of the contrast transfer function (CTF, which describes how different spatial frequencies are presented in the resulting images, reintroduced in Section 2.3.0.2). This means that the same object can appear with varied contrast depending on

the defocus applied, which necessitates computational corrections to make the image interpretable.

1.2.3.3 Elemental Analysis

STEM also has the capacity for nanoscale elemental analysis due to its use of a focused, scanning probe. As the probe dwells on each pixel, signals specific to individual elements, such as emitted X-rays and energy-loss electrons, can be collected to perform energy-dispersive X-ray spectroscopy (EDX) and electron energy-loss spectroscopy (EELS). These techniques can generate elemental maps with nanometre-scale resolution, providing chemical and bonding information that is largely inaccessible to other high-resolution imaging modalities. While EDX is challenging in cryo-conditions, due to the low signal and high fluence required, it has produced elemental maps under these conditions. For example, the technique mapped phosphorus granules in vitrified bacteria, albeit with an electron dose an order of magnitude higher than that used for standard cryo-ET [103].

Multiple studies using both biological [95, 103] and materials science samples [104] have demonstrated a qualitative decrease in observed radiation damage effects, such as bubbling, in cryo-STEM as compared to cryo-TEM. This effect will be reviewed later in Chapter 4.

1.2.3.4 Inability to Visualise Protein

The ability to visualise proteins in cryo-EM/ET, which is typically impeded in cryo-STEM, arises from their fundamentally different contrast mechanisms and signal-processing strategies. cryo-EM/ET is optimised for phase contrast, the ideal method for imaging a protein in ice [105]. A protein barely changes the intensity of the electron beam but does slightly alter its phase. By defocusing the microscope, this small phase shift is converted into an intensity difference (see Section 2.3.0.1).

Cryo-STEM, particularly in HAADF mode, is instead optimised for Z-contrast, which is highly sensitive to differences in atomic number and density. This is a major disadvantage for imaging unstained proteins, as the light atoms of the protein (carbon, nitrogen, oxygen) are nearly indistinguishable from the light atoms of the surrounding vitreous ice (hydrogen and oxygen). Without a strong initial contrast signal to detect, cryo-STEM is not well suited for visualising the faint signal of an untagged protein in its native state [102] – although phosphorous-containing species such as phosphorous granules, phospholipid membranes, and ribosomes are visible, as shown in [95, 100, 101, 103].

Outside the cell, cryo-STEM EELS was recently used with an SPA-type thin vitreous sample to attempt to reconstruct and localise individual metal-binding sites on two proteins (rabbit ryanodine receptor and worm haemoglobin), with limited success [106]. Furthermore, apoferritin (a classic test sample for cryo-EM) loaded with several zinc and iron atoms has been averaged, with results displaying putative binding sites for individual metal ions within [107]. Both of these advancements required averaging many copies of the STEM images to obtain their results. To combat this inability to visualise protein directly in vitreous samples using conventional STEM, new methods, proposed from the materials science fields, are beginning to have an impact when applied to biological samples.

1.2.3.5 Lack of Motion Correction

Another limitation of conventional cryo-STEM is the limited ability to correct for beam-induced sample motion, in contrast to cryo-TEM where motion correction is an integral part of high-resolution imaging. In cryo-TEM, images are typically recorded as dose-fractionated movies using fast, direct electron detectors. Each frame represents an instantaneous projection of the specimen, allowing rigid and non-rigid sample motion to be estimated and corrected post-acquisition, which is essential for achieving near-atomic resolution in radiation-sensitive biological specimens [108].

In STEM, by contrast, images are formed serially by raster-scanning a focused electron probe across the specimen, with the signal at each pixel acquired sequentially over time. A single STEM image therefore does not correspond to a single moment in time, but rather integrates specimen motion throughout the entire scan. While drift correction between successive STEM frames has been demonstrated, particularly in materials science where samples are more stable and higher doses can be tolerated [109–111], this approach does not address motion that occurs within an individual scan. Any beam-induced motion, deformation, or relaxation that takes place during the acquisition of a single STEM image is encoded irreversibly as geometric distortions and blurring.

For cryogenic biological specimens, which exhibit pronounced beam-induced motion and deformation, this lack of intra-frame motion correction fundamentally limits the achievable resolution in STEM [11]. Unlike TEM movies, STEM does not naturally provide a series of time-resolved frames that can be aligned and averaged without substantially increasing dose or scan time. As a result, motion artefacts are intrinsically coupled to the image formation process, making cryo-STEM more susceptible to motion-induced resolution loss than cryo-TEM.

1.2.4 Phase-Contrast STEM Techniques Applied to Biological Samples

This Section will provide the reader with a brief overview of recent developments in phase-contrast STEM-based imaging methods in the context of their application to biological samples.

1.2.4.1 Differential Phase Contrast Imaging

Differential Phase Contrast (DPC) is a technique that uses a circular or annular detector segmented into 4 (or more) quadrants to measure the deflection of the

electron beam as it passes through the sample [112]. By subtracting the signal from opposite quadrants, it extracts phase gradient information (how quickly the phase changes with respect to position) [113]. DPC images show real-time intensity changes due to electric or magnetic fields and sample thickness [114], offering phase contrast without inversions for lighter elements.

Integrated DPC (iDPC) further integrates phase changes to map atomic potential [115], which is useful for biological samples. Cryo-iDPC recently achieved high-resolution protein structuring of SPA samples (Tobacco Mosaic Virus and Keyhole Limpet Haemocyanin) at 3.5 Å and 6.5 Å [116], showing its potential for protein structures. The method provides quantitative phase contrast without defocus or contrast inversions, and may allow simultaneous elemental analysis via EDX (Section 1.2.3.3), supporting integrated structural and elemental characterisation. HAADF detectors could simultaneously enhance iDPC data collection by allowing sensitivity for heavier elements and thickness mapping [116]. The only published example of iDPC applied to cellular samples used chemically fixed, resin-embedded specimens, affecting the native state [117].

1.2.4.2 4-dimensional STEM

The evolution of STEM imaging is shifting from simple integrative monolithic detectors to the acquisition of complete electron scattering distributions at every probe position on the sample, enabled by high-speed pixelated detectors.

Rather than simply integrating the total number of electrons within a specific angular range, these new techniques record the entire distribution of scattered electrons for each probe position. This creates a four-dimensional dataset: two real-space (sample) dimensions, and two reciprocal-space (detector) dimensions that can be computationally analysed at a later date to reconstruct images with greater information content. These methods offer unparalleled flexibility. A comprehensive understanding of the workings of each of these methods is beyond the scope of this

introduction, and the reader is directed to [118, 119]. The following sections will briefly introduce the use of these emerging modalities for biological samples.

The use of a fast pixelated detector to take images of the full scattering intensity for each probe position allows for many different methods of data analysis. For example, virtual-BF, -ADF, or -HAADF can be completed by computationally masking the relevant pixels in the detector images. This confers the benefit of changing the positions of the virtual detectors *post factum* to find the optimal contrast for an image of a given specimen - and is not dependent on predetermined collection angles/camera lengths. Data can also be analysed by other methods, such as the DPC, iDPC, or centre of mass methods described earlier.

1.2.4.3 4D-STEM Tomography

By acquiring a full 4D-STEM dataset at each angle in a tomographic tilt-series, this technique is extended into three real-space dimensions, a method known as 4D-STEM tomography. The primary advantage of this technique is its flexibility to display the outputs of multiple data processing methods as full tomograms with differing information content. This method has been shown as a proof-of-concept for biological samples to visualise DNA inside bacteriophages under cryogenic conditions [120].

1.2.4.4 Electron Ptychography

Electron ptychography is a computational method which uses an overlapped probe on the sample to collect diffraction patterns in a 4D-STEM experiment. This allows determination of the phase of the electron wave [121].

By computationally iteratively reconstructing the phase information which is normally lost, ptychography can produce images with high contrast and resolution, even at a low electron dose [122]. This also allows for the removal of aberrations in images. Indeed, the materials science field have used this technique to achieve

the highest resolution images (0.23 Å) in an electron microscope [123]. This makes the technique one of the most promising for future high-resolution imaging of radiation-sensitive biological specimens, although there is some debate in the field as to whether regular EFTEM will outperform ptychography [124, 125].

The first attempts to reconstruct protein structure in cryo-EM SPA-type sample were completed in 2020 [126], and recent publications have improved the resolution to sub-nm level for several proteins [108, 127]. The structure of apoferritin has been resolved to 5.8 Å resolution with a limited number of particles, where cryo-TEM is able to reach $\sim$ 1 Å. There is still progress to be made to prove cryo-electron ptychography as a viable alternative to cryo-TEM-based methods for protein structure determination.

As of yet, there are no peer-reviewed publications which detail electron ptychography performed on a cellular sample under cryogenic conditions. However, one publication has applied electron ptychography to room temperature cellular sample [126]. Again, this technique could also be used to provide phase information for protein samples whilst localising heavy elements using Z-contrast principles with the HAADF. This process has been applied to the imaging of heavy iodine atoms on carbon nanotubes [128].

Another potential benefit electron ptychography may present is the ability to decouple the 'pixel size' of the real-space scan from the field of view. This would enable extremely large-scale field of view at a small pixel size [129], aiding in the search for the 'needle in the haystack' issue which usually hinders cellular imaging in the TEM (as detailed in Subsection 1.1.3).

1.2.4.5 Tilt-Corrected Bright Field STEM

Another method of processing 4D-STEM data acquired by the same experimental setup of ptychography is tilt-corrected bright-field STEM [130, 131], also known as parallax [132]. This method works by treating each individual pixel in the detector

plane as its own TEM detector. Recent work has identified tilt-corrected bright field STEM as the optimal method for processing 4D-STEM tomography data, citing its superior performance over ptychographic reconstruction in thick specimens [133, 134]. Comparisons to EFTEM for thick (∼500-800 nm) samples show its potential in retaining a greater proportion of the signal in the final image [130].

In summary, while EFTEM-based cryo-ET has driven an *in-situ* resolution revolution, its reliance on phase contrast and extensive averaging is a poor match for the 'needle in a haystack' problem of localising tagged proteins. In contrast, STEM offers several advantages. These include superior performance in thick samples, interpretable Z-contrast, and the capacity for elemental analysis - all of which are factors that make it an ideal candidate for a tag-based discovery workflow. However, the inability of STEM to visualise unstained protein has limited its application. The recent development of advanced, phase-sensitive STEM modalities – like iDPC and ptychography – now presents a compelling opportunity to combine the high-SNR detection capabilities of STEM with the high-resolution imaging required for *in-situ* structural biology.

1.2.5 SEM and Volume Imaging

Beyond the transmission imaging modalities of TEM and STEM, the Focused Ion Beam-Scanning Electron Microscope (FIB-SEM) is an instrument that has enabled the routine application of cryo-ET to thick biological specimens such as eukaryotic cells and tissue [135, 136]. The SEM is usually operated normal (90°) to the sample, with the FIB at (∼ 52°). In this 'dual-beam' system, the FIB uses a beam of heavy ions (typically Gallium or a plasma of argon, xenon, oxygen, or nitrogen) to 'mill' material from a bulk sample, making thin, electron-transparent lamella for downstream EFTEM [17, 137]. The SEM uses a low acceleration voltage (typically 1-30 kV) and forms an image by collecting signals that originate from the sample

surface [138]. The primary signal used for biological samples is formed from low-energy secondary electrons, which are generated from inelastic interactions in the sample [139]. The images formed using SEM on biological samples are usually much lower resolution ($\sim$ 10 nm resolution) than those formed in TEM and STEM [140].

In a standard cryo-ET workflow, SEM can be used to provide real-time feedback during the milling process [141, 142]. This live imaging is useful for monitoring the progress of the milling, ensuring the integrity of the lamella by detecting cracks, and qualitatively assessing when a desired thickness has been reached.

This combination of FIB milling and SEM imaging also presents a powerful technique for volumetric imaging (or volume EM, vEM) of large ($>$ 1 µm) sample thicknesses [143]. By sequentially removing thin layers from a bulk sample with the ion beam and acquiring an SEM image of each newly exposed block-face, a complete 3D volume of a cell or tissue can be reconstructed [144, 145]. This approach, termed serial FIB-SEM, allows the user to navigate through much larger volumes of cellular ultrastructure than cryo-ET (albeit at a reduced resolution) in a near-native state.

Despite its power for providing mesoscale context, the SEM is limited in resolution, which prevents it from solving the molecular-scale issue of protein identification (point 3 in Section 1.1.3). The achievable resolution on vitrified biological samples is typically limited to 10 nm in the xy-axes, and $\sim$20-50 nm in the z-axis [146–148].

This volumetric imaging capability has recently been leveraged as a label-free strategy for identifying a region of interest [147–150]. By progressing through the reconstructed 3D volume, a researcher can identify a rare or specific morphological region without the need for fluorescent tags. Once the region of interest is located, serial milling can be stopped to prepare a lamella by milling the remaining bulk sample below the region of interest [147, 148]. This lamella created on the region of interest can then be transferred to TEM for high-resolution cryo-ET.

Thus, FIB-SEM is a valuable tool for bridging the gap between the micrometre scale of light microscopy and the sub-nanometre scale of electron tomography, enabling label-free targeting at the level of whole organelles or large cellular features. However, it cannot provide the final step of molecular localisation. This leaves a clear need for a workflow that can pinpoint the position of individual proteins within the prepared lamella. The proposed workflow in the following section will address this challenge.

1.3 A Proposed Workflow

By combining the requirements of an ideal tag with the capabilities of modern electron microscopy, this thesis proposes and investigates the foundational aspects of a novel hybrid workflow for the future of *in-situ* structural biology.

Its central strategy involves a multi-component label designed to combine three key functions: a targeting component for high specificity, a fluorescent component for mesoscale guidance, and a small high-Z nanoparticle for detection in the electron microscope. While the biological challenges of delivering such a tag to an intracellular target are significant, this work focuses specifically on the subsequent physical and imaging challenges of the workflow.

The initial preparation of a targeted lamella can be achieved via two complementary routes (Figure 1.5). The first is a standard correlative workflow where fluorescence from the tag guides the FIB milling (Figure 1.5A). Alternatively, for the label-free identification of rare cellular events or a specific morphology, a cryo-serial FIB-SEM approach can be employed to navigate the cellular volume before a targeted lamella is prepared (Figure 1.5B). Regardless of the targeting method used to produce the lamella (Figure 1.5C), it is subsequently transferred to the cryo-TEM system for a two-stage data acquisition strategy.

Firstly, a standard low-dose cryo-ET tilt series is collected in EFTEM mode (Figure 1.5D). This initial step captures the high-resolution structural information of the proteins in a near-native state - before any significant radiation damage has occurred.

Only once these radiation-sensitive structural data are acquired is the microscope illumination changed to STEM mode (Figure 1.5E). The same positions are revisited to obtain high-dose ADF images. This second step is dedicated exclusively to localising the AuNP tags, thus leveraging the superior SNR for high-Z materials in STEM-ADF. Because the structural data has already been collected, there are no strict low-dose limits on this search. The electron fluence can be maximised to improve tag detection, but it is ultimately limited by the dose threshold at which significant beam-induced motion of the tag or structural degradation of the vitreous ice begins to occur. Finally, the high-precision coordinates of the tags from the STEM images are correlated back to the EFTEM tomograms to guide the STA of the target protein.

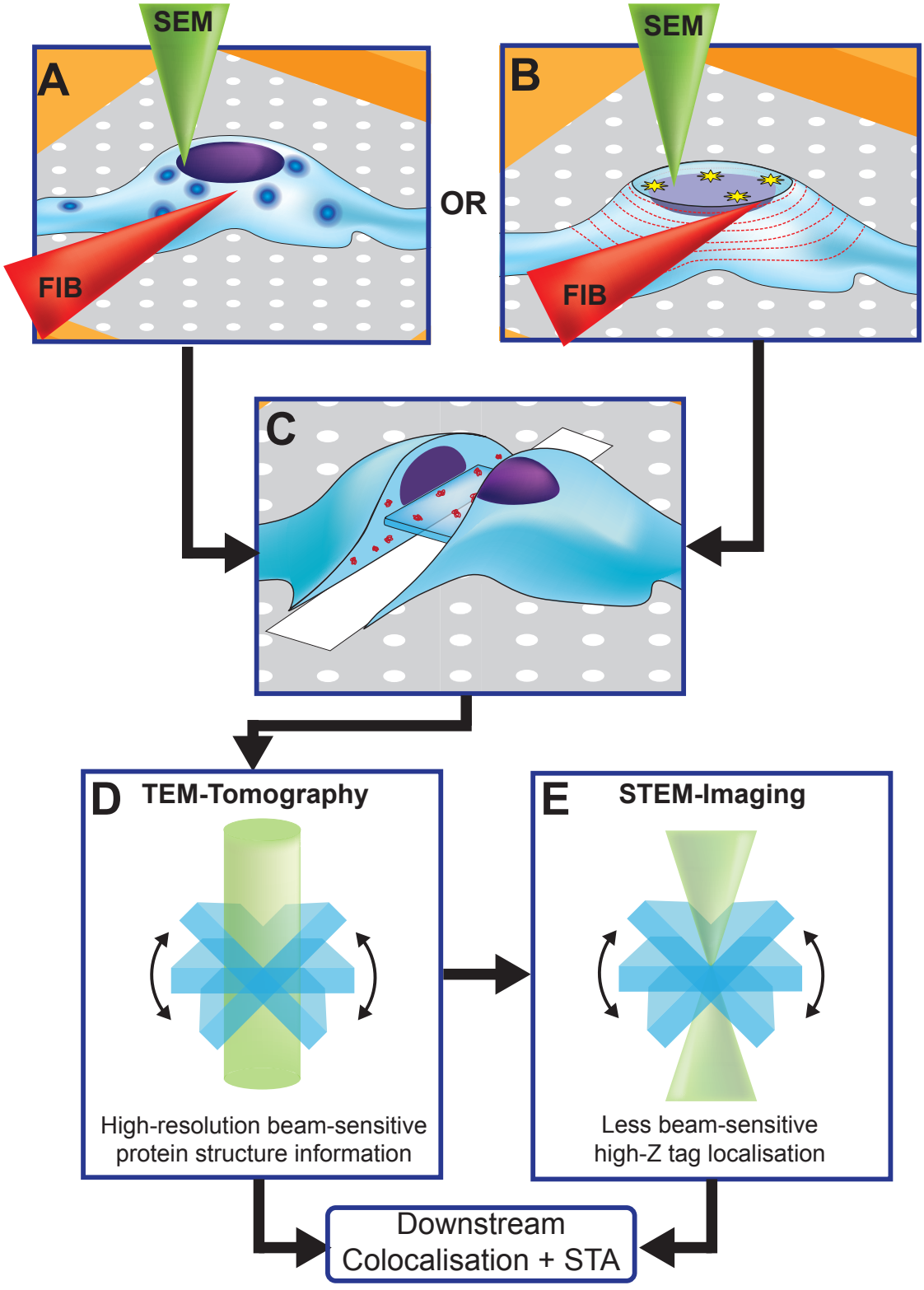


Figure 1.5: **Proposed hybrid workflow for targeted *in-situ* structural biology**. A vitrified cell can be targeted at the mesoscale via two complementary routes: **A** The first is a conventional fluorescence-guided approach, with the blue regions showing fluorescent puncta. Alternatively, for identification of specific nanoscale cellular components or morphology (yellow stars, **B**), *caption continued on the following page.*

Figure 1.5: *continued caption*: cryo-serial FIB-SEM can be used to navigate the cellular volume by sequentially milling and imaging. After mesoscale targeting, a lamella may be fabricated (**C**) for subsequent TEM-tomography to collect high-resolution information of the radiation-sensitive protein structure within the lamella by EFTEM cryo-ET (**D**). Only once this information has been collected can the lamella be exposed to further high-dose ADF-STEM imaging to locate the positions of high-Z electron-dense tags for following colocalisation and data processing steps **E**.

While this two-stage imaging strategy is sound in principle, its practical implementation was ultimately hampered by upstream challenges in reliably delivering the tags to their intracellular targets. As detailed in the preliminary investigation documented in Appendix Section A.1.1, the extremely low efficiency of tag internalisation made consistent target identification unfeasible (see Figures A.1 and A.2). This experience highlighted a crucial point: even with a perfect biological tag, the success of any high-resolution correlative workflow to image minimally-sized tags is fundamentally constrained by the physics of the imaging process itself.

However, the practical implementation of this workflow is predicated on addressing a central and significant challenge in cryo-electron microscopy: beam-induced radiation damage. This fundamental physical barrier, detailed in the following Section, prevents the straightforward application of the high electron fluences required for tag detection. Therefore, this primary obstacle must be systematically investigated before the workflow can be implemented. This thesis is dedicated to that investigation.

1.4 The Overarching Barrier: Radiation Damage in Cryo-EM

To put this challenge into perspective, the electron dose administered during a typical low-dose cryo-EM exposure ($\sim$50 $e^{-}Å^{-2}$) is sufficient to theoretically break every peptide bond within a protein sample three times over [151]. The detailed

physical principles of the electron-specimen interactions discussed in this section are provided in the Background (Chapter 2).

1.4.1 Damage Processes in Electron Microscopy

The two primary damage mechanisms in high-energy electron microscopy (TEM and STEM) are knock-on and radiolysis, which are based on elastic or inelastic interactions of the incident electrons with the nucleus of the atom or its electron cloud, respectively [152, 153]. A variety of other secondary and tertiary effects can take place as a result of the aforementioned primary mechanisms in beam-induced radiation damage of vitreous ice. These include charging, beam-induced motion, bubbling, and mass loss. These processes are each respectively outlined and discussed throughout the following.

1.4.1.1 Knock-on

Knock-on damage is the result of a direct, elastic collision between an incident electron and an atomic nucleus (see Section 2.2). In this type of interaction, if the energy transferred exceeds the atom's displacement threshold, the atom can be physically ejected from its position in the material [154]. While knock-on damage is possible at the 300 kV accelerating voltage used in this thesis, its contribution to the overall damage of a vitrified biological specimen is negligible [153]. The primary reason for this is the vast difference in probability between the two damage mechanisms. The likelihood of high-angle elastic scattering from light elements, such as those found in water, is extremely low (see Figure 3.6). In contrast, the likelihood for an inelastic interaction, which transfers energy to the sample and causes radiolysis, is an order of magnitude greater [155]. For this reason, radiolysis is considered the main fluence-limiting damage mechanism in cryo-EM of biological samples [155, 156].

1.4.1.2 Radiolysis

Radiolysis is a process initiated when an incident electron is inelastically scattered by the sample (see Section 2.2). For materials composed of light elements, such as vitreous ice and proteins, the most common energy transfer that occurs is around 20 eV [157] and excites a plasmon (a collective oscillation of the valence electrons in the sample). This energy loss is greater than the excitation energy for a water molecule of 7.4 eV [104, 158].

The plasmon is unstable and is thought to decay on a femtosecond timescale [151, 159]. The decay of the plasmon ejects an electron from an atom in the sample and creates an electron-hole pair (a positively charged molecular ion and a free secondary electron). This is believed to be the primary ionisation event of radiolysis [160].

The consequence of such an event is twofold. Firstly, the remaining molecular ion is in an unstable, excited state. Therefore, in an insulating material like vitreous ice, where there are no free conduction electrons to neutralise the charge, the ion relaxes (lowers its energy) by breaking covalent bonds [160]. This process generates highly reactive free radicals (such as $OH^{\bullet}$,$OH_2^{\bullet}$, $O_2^{\bullet}$, and $H^{\bullet}$) [161, 162]. Secondly, both the generated secondary electrons and the charged/radical species of the sample molecules may diffuse away from the initially irradiated area. As these secondary electrons move throughout the sample, they have sufficient energy to cause further secondary ionisations [163], spatially propagating more radiolysis effects. Together, these processes lead to the destruction of the specimen's high-resolution structure [164].

1.4.1.3 Charging

The diffusion of secondary electrons away from the irradiated site leads to a depletion of electrons at the irradiated position and a build-up of electrostatic charge where samples and supports are non-conductive [153, 163, 165, 166]. In STEM and SEM,

this region of concentrated positive charge generates a radial electric field that points outwards, away from the centre of the beam, and may exert a force on any other charged particles within the sample. Similar effects have been observed in cryo-TEM, and influenced the proposal that charging was the main cause of beam-induced motion in the sample [167, 168].

1.4.1.4 Beam-Induced Motion

Although charging was initially presented as the cause of beam-induced motion of particles in cryo-EM SPA samples, the TEM beam has been shown to create a stable charge distribution on the ice. This forms almost instantly at a fluence orders of magnitude less than is used in typical exposures ($\sim 10^{-3}$ – $10^{-1} e^{-} Å^{-2}$) [169, 170].

Instead, to explain beam-induced motion, evidence for a mechanical model originates from observations tracking the movement of large, symmetric rotavirus proteins [171]. These experiments revealed that particles not only translate but also undergo rotations, a phenomenon not easily explained by simple electrostatic forces [171]. This led to the current understanding of beam-induced motion being caused by a physical doming of the vitrified ice and its support film – likely as the electron beam relaxes mechanical stress from vitrification [79, 157, 172].

1.4.1.5 Bubbling

A common manifestation of radiation damage in vitrified biological samples is the formation of microscopic bubbles within the ice. This phenomenon is attributed to the build-up of molecular hydrogen (H_2) gas, a terminal product of radiolysis [173]. The process begins with the radiolysis of water molecules, which generates highly reactive hydrogen ($2H^{\bullet}$) and hydroxyl ($OH^{\bullet}$) free radicals. In pure vitreous ice, these radicals can readily recombine to reform water ($H^{\bullet} + OH^{\bullet} \longrightarrow H_2O$). However, in the presence of a biological macromolecule, a secondary reaction pathway becomes

dominant. The radicals can react with the organic molecules of the protein by abstracting a hydrogen atom, resulting in the formation of stable, insoluble H_2 gas ($OH^{\bullet} + R{-}H \longrightarrow R{-}O^{\bullet} + H_2$) [173, 174]. This mechanism is strongly supported by the experimental observation that bubbles form preferentially at the protein-ice or carbon-ice interfaces [162, 175].

As mentioned in Section 1.2.2, multiple reports in the literature investigate the phenomenon of bubbling by comparing different levels of fluence, flux, and illumination methods [95, 104, 171, 176].

1.4.1.6 Mass Loss

Mass loss is defined as the physical thinning of the specimen under electron irradiation. This form of damage is readily visible as an increase in electron transparency in transmission EM images. Although heating is an appealing explanation for the loss of mass in cryogenic radiation-sensitive samples, several publications have independently concluded that electron beam-induced heating is minimal at the typical fluence and flux used in typical cryo-TEM or cryo-STEM ($\sim$1 – 10 K increase) [104, 138, 139, 156, 177, 178]. Mass loss must instead be caused by radiolytic processes [177], such as the evolution of hydrogen and oxygen gases, and potentially water molecules from the surfaces of the vitreous ice layer.

Early investigations by Heide [179] revealed a crucial insight into the mechanism of mass loss, demonstrating that the rate of mass is independent of the sample's thickness. By comparing a thin (5 – 200 nm) layer of vitrified ice supported on a carbon substrate to one suspended over a hole, the researchers observed that the suspended ice (which is exposed to the vacuum on both sides) lost mass at twice the rate.

This experiment demonstrates that mass loss is a surface-limited phenomenon. This does not imply that the initial radiolytic events are confined to the surface,

but instead highlights that, for the products of radiolysis to be 'lost' from the sample, they must first diffuse to a surface and then desorb into the surrounding vacuum [179, 180].

1.4.2 Damage Mitigation Strategies in Electron Microscopy

As covered in Section 1.4.1, beam-induced radiation damage encompasses a number of (largely unavoidable) physical mechanisms. These therefore establish the ultimate limiting factor in the high-resolution structural analysis of vitrified biological specimens. Consequently, strategies to mitigate damage and use the fluence as efficiently as possible are of paramount importance to the field. The following Sections will provide a brief discussion of the primary experimental parameters which can be manipulated to this end.

1.4.2.1 Energy of the Incident Electron Beam

One fundamental parameter that can be adjusted to alter the beam-induced damage is the accelerating voltage of the electron beam. However, the effect of this voltage on the two primary damage mechanisms, knock-on and radiolysis, is opposite.

As discussed previously, knock-on damage has an energy threshold. Knock-on events can effectively be eliminated by reducing the accelerating voltage of the electron beam below this threshold [139]. This finding has motivated the development of low-kV microscopes for specific materials where knock-on is the primary concern for beam-induced damage [181].

However, this strategy is counterproductive in the context of biological specimens where radiolysis is the dominant damage mechanism. This is because the probability of a damaging inelastic interaction is inversely related to the electron's energy [182].

Electrons from a lower-energy beam (such as in the SEM) have a greater probability of inelastic scattering, which increases their likelihood of depositing energy into the sample. Consequently, the radiation sensitivity of biological material increases as the accelerating voltage is reduced [183]. Lowering the voltage to prevent the minor issue of knock-on damage only exacerbates the far more severe problem of radiolysis. In addition to increasing radiolytic damage, reducing the accelerating voltage also alters the balance between elastic and inelastic scattering, which has direct implications for image formation efficiency. Peet *et al.* introduced the elastic-to-inelastic scattering ratio as an information coefficient, providing a framework to evaluate the amount of usable structural information obtained per unit radiation damage as a function of beam energy and specimen composition [183]. While lower accelerating voltages increase total scattering cross-sections, this increase is dominated by inelastic events that contribute disproportionately to specimen damage rather than image contrast. For light-element, radiation-sensitive biological specimens, this results in a decrease in information efficiency at lower voltages, with the information-per-damage metric favouring higher accelerating voltages. This analysis reinforces the conclusion that operating at 100–300 kV represents a practical optimum for maximising structural information while mitigating radiolysis in cryogenic biological electron microscopy of thin vitreous samples [183–185].

1.4.2.2 Conductive Sample Coating and Structural Support

Another class of mitigation strategies aims to reduce beam-induced charging by the addition of conductive layers at the sample preparation stage. For example, a continuous layer of graphene may provide a conductive pathway that can effectively dissipate charge away from build-up on the sample - although no publications have explicitly shown an improvement in damage reduction using graphene [186–189]. It has also been suggested that graphene can offer a degree of mechanical stabilisation and protection for the vitrified specimen [190].

As cryo-FIB milled lamellae are electrically isolated from the main grid, they are more susceptible to beam-induced charging than standard SPA samples. A direct solution is to sputter-coat the sample with a thin (∼5 nm) layer of conductive platinum, which is believed to create a path to dissipate charge and maintain stable imaging conditions during cryo-ET [191, 192]. A preprint publication has shown an increase in attainable resolution of ribosomes using this method [191] although this has yet to be validated elsewhere. However, this approach also introduces drawbacks: the conductive layer reduces the SNR of the biological specimen, and the sputtering process itself can be inconsistent, leading to an inhomogeneous coating of unreliable thickness.

1.4.2.3 Reducing the Sample Temperature

At liquid nitrogen temperatures ($\lesssim$97 K), the vitrified ice forms a rigid, amorphous matrix that is thought to physically trap the larger free radicals generated by radiolysis at or near their point of origin. This is known as the 'cage effect', and has been supported in simulation [152, 193]. It is this mechanical restraint – preventing larger radicals from migrating and interacting with neighbouring molecules – that allows the specimen's high-resolution structure to persist to a greater electron fluence, thereby extending the usable fluence budget.

Although the primary stages of electron beam damage (radiolysis and knock-on) are not affected by temperature, the use of temperatures lower than liquid nitrogen has long been proposed as beneficial to electron-beam induced damage reduction due to the cage effect [194].

The principle that lower temperatures may reduce radical mobility has motivated ongoing research into the use of liquid helium temperature for cryo-EM (∼4 - 17 K). The central question is whether it is possible to achieve a further reduction in the diffusion of the radicals at these extreme temperatures, a feat which could offer another improvement in sample preservation.

Recent works both advocate for [157, 195] and dispute [196–198] the benefit of operating far below liquid nitrogen temperature in cryo-TEM of proteins. The most recent of these appears to uncover an effect of increased beam-induced motion at liquid helium temperatures. By using different grid supports, this effect can be counteracted, yielding the expected improvement of approximately 1.5 × lower radiation sensitivity [157, 199].

1.4.2.4 Alternative Illumination Strategies

Another set of mitigation strategies is to optimise the illumination itself by altering the spatio-temporal delivery of the electron fluence. In their focus on either the temporal or spatial characteristics of the beam, these approaches aim to minimise damage without reducing the total number of electrons used for imaging.

1.4.2.5 Flux Optimisation

One possible temporal approach is to alter the flux (also referred to as dose-rate) of the illumination. For any given total fluence, a balance must be struck between the practical need for high-throughput data collection (which favours a high electron flux over a short time) and potential dose-rate effects on damage [200]. For example, in cryo-EM SPA, a standard fluence of 40-60 $e^{-}Å^{-2}$ is typically delivered over a few (∼3-10) seconds. This gives a flux somewhere between 4-20 $e^{-}Å^{-2}s^{-1}$, a compromise that balances data quality with sample throughput and stage stability. Using a higher flux can have detrimental effects to the sensitive high-resolution structures of proteins [176, 178].

1.4.2.6 Pulsed Electron Beams

The temporal distribution has also been explored through the use of pulsed electron beams. This is when fluence is delivered in short (femtosecond to picosecond) bursts

separated by longer (picoseconds to nanoseconds) beam-off periods.

While some work suggests a potential damage reduction for extremely radiation-sensitive crystalline samples [201–204], a recent preprint on a more relevant cryo-EM SPA-type sample (plunge-frozen vitreous Tobacco Mosaic virus) did not find any such reduction in radiation damage [205].

Since primary radiolytic damage is effectively an instantaneous event, the probability of damage at any given point is governed by the average electron arrival rate. At a fixed total fluence, this average rate is the same for both pulsed and continuous beams. The consensus viewpoint is that grouping electrons in time is not expected to reduce the overall rate of primary damage events [125, 151].

1.4.2.7 Spatial Distribution of the Electron Beam

While the aforementioned strategies focus on altering the temporal properties of the electron beam, a more significant consideration is the spatial distribution of the electron fluence.

This principle was explored over 30 years ago using TEM through 'spot scanning' techniques, which attempted to mimic the scanning exposure of STEM with a small (approximately 40-50 nm) diameter TEM beam over the specimen. These techniques revealed an improvement to beam-induced motion [206, 207].

In a similar vein, it is important to note the difference between the parallel 'floodlight' illumination used in TEM and the convergent scanning probe used in STEM.

Several studies have reported a superior 'dose resistance' in samples imaged in STEM mode compared to a continuous TEM beam [95, 104, 208]. This suggests that irradiating a given pixel for a very short dwell time, followed by a much longer 'relaxation' period as the beam scans other areas, may be less damaging than continuous illumination [200].

The field of material sciences has experimented with altering the scanning strategy to visit pixels out of the standard 'raster' scanning order for STEM. Spiral scans [209–211], interleaved scans [212–214], random scans [215, 216], and more [217], have been proposed in material sciences as a means to address various issues with standard raster scans.

Of particular relevance are interleaved and random scans, both of which may have implications for reducing damage to radiation-sensitive biological samples.

Random-sparse scanning (where the probe visits a subset of the probe positions needed to construct the full image, in a random order), combined with compressed sensing (a method for reconstructing the image by filling in missing pixels) is a clear way to reduce damage. This is because the probe visits only a subset (usually 5-30%) of positions [215, 216]. However, this technique is best suited to repeating, atomic material science-type samples where there is very little heterogeneity in images. In fact, this method has been applied to STEM tomography of non-vitreous cryogenic samples - to the detriment of image quality [218].

In the interleaved scanning geometry (also known as 'leapfrog' [214]), once the first probe position is visited, the probe skips a predefined number of positions along the x-axis to visit the next position until the line is completed. The probe repeats this sequence by skipping the same number of lines along the y-axis until the bottom of the frame is reached. The probe then returns to the top of the frame to repeat the pattern for the previously skipped pixels, until the entire scan is complete [212]. This approach has been shown to reduce mass loss of beam-sensitive zeolite samples at atomic resolution [212].

Recently, an interleaved scan was applied for the first time in the SEM for cryogenic biological samples to reduce charging artefacts [219]. This interleaved scan will form the basis of experimental investigations in Chapter 4, and exploratory investigation in Chapter 5.

1.5 Thesis Aims and Outline

The central challenge of this thesis, therefore, is to investigate the foundational barrier of radiation damage within the specific context of the proposed STEM and SEM workflows.

Before experiments can be justified, the theoretical limits of the approach should be established. It is important to determine the minimal nanoparticle size that is theoretically detectable above the noise of a thick cellular lamella and to determine how this is affected by key imaging parameters, such as electron dose and detector collection angles. Therefore, Chapter 3 of this thesis will develop a theoretical framework to define this parameter space, in doing so providing a foundation for the experimental work that follows. This theoretical analysis results in a clear obstacle: the confident detection of small tags is essentially a challenge of the electron fluence budget.

As such, Chapter 4 will investigate the practical consequences of this fluence. It will examine the damage to vitreous ice caused by a focused electron beam in STEM mode, and explore alternative scanning strategies to determine if the fluence can be delivered more efficiently to minimise sample damage.

It is necessary that this concern for fluence-induced damage also extends to the sample preparation stage. Repeated SEM imaging, which is employed in advanced targeting workflows such as cryo-serial FIB-SEM represents another significant, yet largely unquantified, source of radiation damage. Therefore, Chapter 5 explores the impact of SEM imaging on the high-resolution structure of proteins, using the SPA of apoferritin as a sensitive damage reporter.

Finally, Chapter 6 concludes this thesis by synthesising the findings on STEM- and SEM-induced damage from the preceding Chapters. The implications of these results will be discussed in the broader context of correlative microscopy and the

pursuit of high-resolution *in-situ* structural biology. Ultimately, this work aims to provide a comprehensive and foundational analysis of the requirements and consequences of a high-SNR heavy tag-based discovery pipeline.

2

Background Information

Contents

2.1 Wave Properties of Electrons 53
2.1.1 Imaging with Electrons 53
2.1.2 Electron Wavelength 53
2.2 Electron-Specimen Interactions 56
2.3 Principles of Image Formation and Contrast 59
2.4 Electron Optics and Microscope Components 65
2.4.1 The Electron Source 65
2.4.2 The Electron Lenses and Apertures 66
2.4.3 Beam Deflection and Correction Systems 69
2.5 Image Formation and Detection System 72
2.5.1 Magnification 74
2.5.2 Energy Filter 75
2.5.3 Detectors 75
2.6 Resolvability 77
2.6.1 The Third Dimension 82

This Chapter establishes the fundamental principles of electron microscopy that form the basis for the work presented in this thesis. The Chapter begins with an introduction of the wavelike properties of electrons that make electron microscopy useful for imaging. Following this, the Chapter explores the primary ways that an

electron interacts with a specimen, which is the origin of all of the image contrast and damage. With this physical foundation established, the theoretical principles of image formation and contrast generation in the microscope will be explained. Finally, it will cover the specifics of the instrumentation used that is essential to this research.

2.1 Wave Properties of Electrons

2.1.1 Imaging with Electrons

In 1876, Ernst Abbe postulated that the resolution of optical microscopy could only be improved by the use of shorter wavelengths of light [220]. 24 years later, a negatively charged subatomic particle was discovered: the electron [221]. However, it took another 24 years for the wave-particle duality of electrons to be posed by Louis de Broglie in his doctoral thesis, with the equation $\lambda = h/p$ [222]. Here, λ is the wavelength of the electron, h is Planck's constant, and p is the momentum, a particle-based property. This realisation paved the way for the use of electrons in imaging - and in less than a decade, the first electron microscopes were invented [223, 224].

This section will introduce key concepts and terminology for electron imaging, which will be referred to throughout this thesis.

2.1.2 Electron Wavelength

For electrons accelerated by high voltages (as in the EM), their wavelength cannot be accurately described by classical mechanics. Relativistic effects begin to apply when the electron is accelerated to 10% the speed of light (c). This equates to an electron accelerated through a potential difference of approximately 2.5 kV. The relativistic equations[1] will be used for all calculations of the electron properties.

[1] As the velocity tends towards 0, the relativistic equations give the same value as the (non-relativistic) equations in classical mechanics.

In this framework, the velocity is given by [225]:

$$v = c \times \sqrt{1 - \left(\frac{1}{\gamma^2}\right)} \ , \tag{2.1}$$

and the wavelength is given by:

$$\lambda = \frac{h}{m_0 c \sqrt{\gamma^2 - 1}} \ , \tag{2.2}$$

where γ is the Lorentz factor, which describes how physical properties change due to relativistic effects:

$$\gamma = 1 + \frac{eV}{m_0 c^2} \ , \tag{2.3}$$

e is the charge on an electron (1.60×10^{-19} C), m_0 is the rest mass of the electron (9.11×10^{-31} kg), and c is the speed of light (3×10^8 ms^{-1}).

An acceleration voltage of 300 kV is used for all TEM and STEM work in this thesis (Chapters 3 and 4), while the SEM-damage Chapter (Chapter 5) uses acceleration voltages of 5, 3, and 1.2 kV. Table 2.1 contains calculated parameters of the electrons under these acceleration voltages, using equations 2.1 - 2.3.

Table 2.1: Calculations of the properties of electrons used for imaging in this thesis.

Acc. Voltage (V)	λ **(m)**	v **(ms^{-1})**	v/c	γ	**E (J)**
3×10^5	1.97×10^{-12}	2.33×10^8	0.78	1.587	4.8×10^{-14}
5×10^3	1.73×10^{-11}	4.16×10^7	0.14	1.010	8.0×10^{-16}
3×10^3	2.24×10^{-11}	3.23×10^7	0.11	1.006	4.8×10^{-16}
1.2×10^3	3.54×10^{-11}	2.05×10^7	0.07	1.002	1.9×10^{-14}

To understand how an electron microscope forms an image, particularly of a low-contrast biological sample, the electron is considered as a wave. The following sections will guide the reader through the formation of contrast for phase-contrast imaging.

2.1.2.1 Phase and Amplitude

A sinusoidal wave (such as an electron wave) has two fundamental properties: amplitude (A) and phase. The amplitude is defined as the displacement of the wave from its equilibrium position, and its square is the intensity recorded by a detector. Phase describes the position of the wave in its oscillatory cycle.

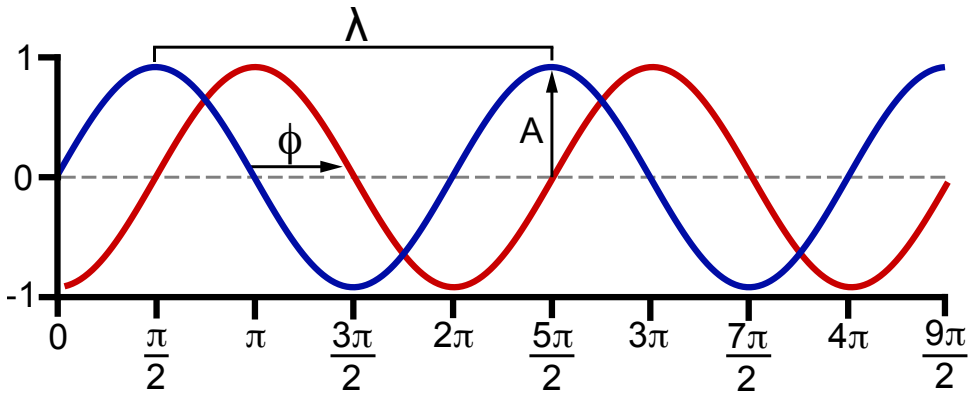


Figure 2.1: **Schematic of a sinusoidal wave.** The blue line displays a sine function with the labelled wavelength (λ) and amplitude (A). The red line shows the same sine wave, with a difference in phase (phase shift, ϕ).

2.1.2.2 Coherence and Interference

The generation of phase contrast for high-resolution imaging is based on predictable interference of electron waves, a phenomenon that requires a highly coherent beam. Two types of coherence are important: 'Temporal coherence' ensures the electrons have a highly uniform wavelength, achieved through a low energy spread in the electron source. 'Spatial coherence' ensures that the wave travels as a uniform plane wave, achieved through use of a point-like source.

When coherent electron waves overlap, they interfere. The nature of this interference depends on their relative phase difference (phase shift, ϕ). As shown in Figure 2.2, constructive interference occurs when the waves are in phase ($\phi = 0$ radians, 0°), increasing the final amplitude (Figure 2.2A). Conversely, if one wave is phase shifted

relative to the other by π radians (180°), the waves cancel, and the resulting wave has no amplitude (Figure 2.2C). If a phase shift occurs, the interference results in a new wave with an amplitude given by $2A\cos\frac{\phi}{2}$ (Figure 2.2B). The ability to manipulate this interference is the basis of phase contrast imaging, explained in section 2.3.0.1.

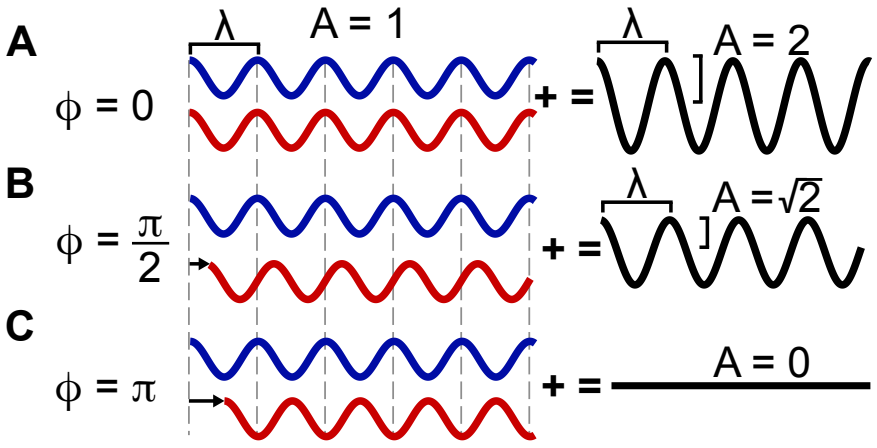


Figure 2.2: **Interference between waves.** The blue lines display the same sine function (amplitude = 1) as in Figure 2.1. The red lines are phase shifted from the blue wave by **A** $\phi = 0$, **B** $\phi = \pi/2$, and **C** $\phi = \pi$, displaying the interference generated and the resulting amplitudes.

Amplitude contrast occurs when the specimen absorbs or scatters electrons away from the objective aperture and from the optical axis, thereby reducing the amplitude (and thus the intensity) of the electron wave reaching the detector. These properties of the electron are the primary reason electron microscopes can achieve atomic resolution. However, the ability to form an image depends not only on the properties of the electron itself but also on how it interacts with the atoms of the specimen.

2.2 Electron-Specimen Interactions

When the high-energy incident electron strikes the atoms of a sample, several different interactions may occur between them, as depicted in Figure 2.3. These interactions result in signals that can be collected to form an image. They are

also the source of irreversible radiation damage. The interactions can be broadly classified into two main types: elastic scattering and inelastic scattering.

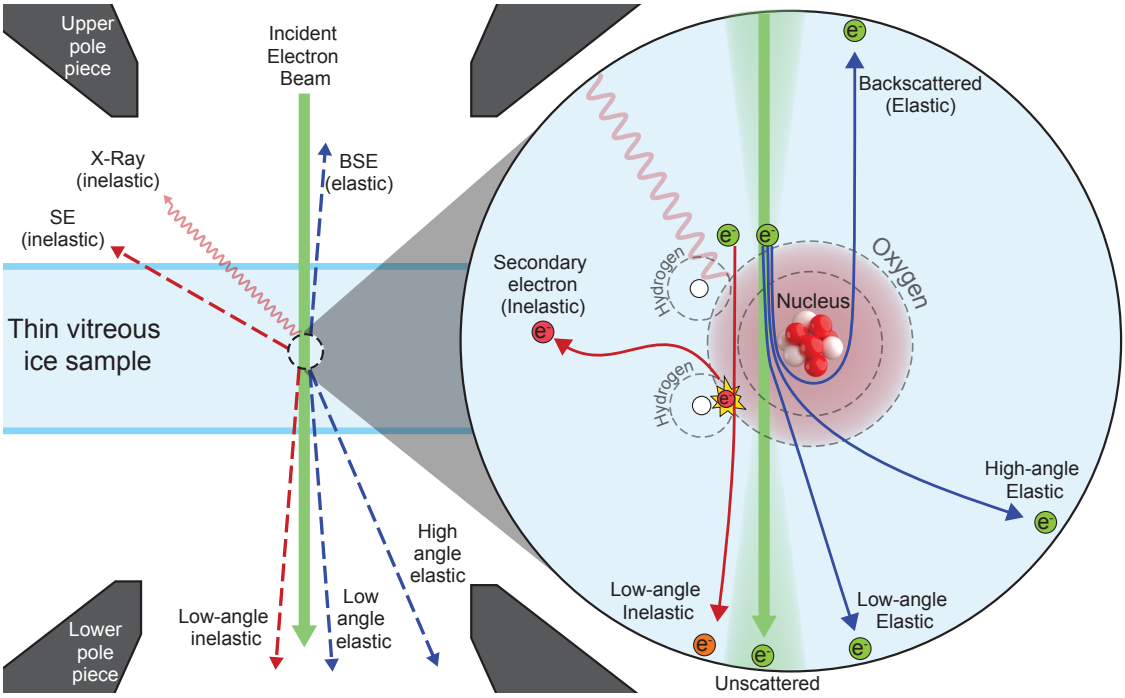


Figure 2.3: **Electron-specimen interactions within the electron microscope**. A beam of incident electrons can be seen (green, left arrow) travelling out of the objective pole piece and through a thin sample of vitreous ice. A multitude of signals can be produced. Those on the left (red dashed arrows) are inelastic processes and on the right (blue dashed arrows) are elastic processes. The interaction of the electron with the atoms of a molecule of H_2O is enlarged on the right, which shows that most of the incident electrons travel through without interacting with the molecule (as is the case for most high-energy electrons). The elastic interactions can be seen on the right, interacting with the nucleus of the oxygen atom. The incident electrons are coloured green both before and after the interaction to indicate that they have not lost energy (they retain their wavelength). The electrons on the left (red arrows) are the inelastic processes, which lose energy to the sample. A green incident electron interacts with and deposits energy to an electron in the bond of the water molecule, causing it to break (damage, yellow star). This can produce a low-energy secondary electron (red to reflect low energy) that may diffuse away, while the incident electron has lost some of its energy and is scattered to a low angle (orange). The energy transferred to an electron by an inelastic scattering process can also produce X-Rays characteristic of the elements involved.

2.2.0.1 Elastic Scattering

Elastic scattering is the deflection of an incident electron by the electrostatic (Coulomb) field of an atomic nucleus [226]. In this interaction, the electron's trajectory is changed, but it loses a negligible amount of kinetic energy; its wavelength remains effectively constant.

In TEM, elastically scattered electrons are the primary source of information and are focused by the objective lens to form the phase-contrast image. In STEM, High-Angle Annular Dark-Field (HAADF) detectors are specifically designed to collect electrons that are elastically scattered to high angles. The resulting signal is approximately proportional to $Z^{1.7}$, providing strong Z-contrast [227]. This is the principle used to detect high-Z nanoparticle tags against a low-Z biological background, as modelled in Chapter 3. Similarly, in low-energy SEM, elastically backscattered electrons (BSEs) provide compositional contrast of the specimen surface [138].

2.2.0.2 Inelastic Scattering

Inelastic scattering occurs when an incident electron interacts with the electrons within the specimen's atoms, transferring a significant amount of energy to result in atomic excitations or ionisations. In contrast to elastic scattering, the trajectory of the incident electron is only slightly deviated [226].

Inelastic scattering has both advantages and disadvantages in electron microscopy. For high-resolution imaging, inelastic scattering is often detrimental. In TEM, inelastically scattered electrons have a different wavelength and are focused to different planes along the optical axis by the magnetic lenses, an effect known as chromatic aberration, which blurs the final image [96]. The energy deposited in the sample during inelastic events breaks chemical bonds and causes radiation

damage in sensitive samples (see Figure 2.3) [139, 164]. Mitigating this damage is the central theme of Chapters 4 and 5.

Inelastic scattering does provide information. For example, in SEM, the most common imaging mode relies on detecting secondary electrons. These are low-energy electrons ejected from the sample atoms by the primary beam. Because they can only escape from close to the top surface, secondary electrons provide high-resolution topographical contrast [138]. The energy lost by the primary electron can also be measured using an energy filter or an X-Ray detector to perform elemental analysis via Electron Energy Loss Spectroscopy (EELS) or Energy Dispersive X-Ray Spectroscopy (EDX), respectively.

2.3 Principles of Image Formation and Contrast

This thesis employs both coherent and incoherent electron imaging.

TEM is treated as a coherent technique that primarily utilises elastic scattering to form images, especially when an energy-filter is used (EFTEM). Conversely, in the scanning methods (STEM and SEM), signals from both elastic and inelastic scattering are important for different methods of detection. While advanced coherent STEM modalities exist (Introduction section 1.2.4.2) [118], all STEM analysis in this thesis is treated as incoherent.

However, the vast majority of contrast in cryo-EM of proteins in vitreous ice arises from phase contrast [228]. Thin biological specimens composed almost entirely of light elements (∼99% = H, C, N, O, and P [47]) are considered 'phase objects' because they do not significantly alter the amplitude of the electron wave [229, 230]. Instead, the electrostatic potential of the atoms within a protein slightly advance the electrons that pass through it. This advancement results in a small phase shift (ϕ) relative to the wave that passes through the empty ice.

Detectors are only sensitive to intensity (the square of the amplitude), not phase. Consequently, a pure phase object is invisible in a perfectly focused microscope. To generate contrast, this undetectable phase shift must be converted into a measurable change in amplitude. This process forms the basis of TEM-phase contrast imaging and will be described in the next section to aid understanding of later Chapters.

2.3.0.1 The Weak Phase Object Approximation

To understand how the phase contrast image is formed, the incident coherent electron beam is first described using complex notation, expressing both the amplitude (real) and phase (imaginary). An incident wave travelling along the optical axis (z-axis) is described by:

$$\Psi_{incident} = Ae^{ikz} \tag{2.4}$$

where k, the wave number, is $2\pi/\lambda$. For simplicity, the amplitude (A) is assumed to be 1.

When this wave passes through the sample, it is phase shifted by a small amount, ϕ. To model this situation, the Weak Phase Object Approximation (WPOA) is used. Under the WPOA, the complex wave function that exits the specimen (Ψ_{exit}) is the sum of two parts: A large amplitude, unscattered wave (approximated as $\Psi_{incident}$), and a small amplitude scattered wave ($\Psi_{scattered}$) [228–230].

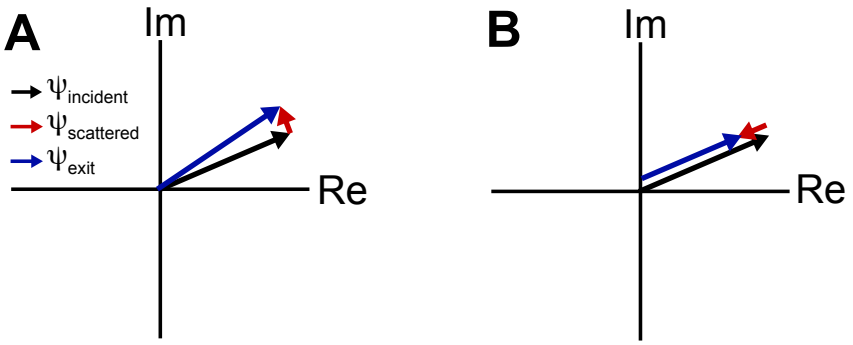


Figure 2.4: **Argand diagrams of the incident ($\psi_{incident}$), exit (ψ_{exit}) and scattered ($\psi_{scattered}$) waves**. **A** the incident electron wave function has an indistinguishable difference in amplitude from the exit wave function, after incorporating a phase shift of $\phi = \pi/2$ from the incident wave. **B** Once the phase is shifted by an additional $\pi/2$ ($\phi = \pi$) the resultant amplitude may be detected as a change in intensity in the exit wave

The phase is modelled as being shifted by $\pi/2$ in the complex plane, as shown by an Argand diagram (Figure 2.4A). The exit wave is given by:

$$\Psi_{exit} = \Psi_{incident} \cdot e^{i\phi}. \tag{2.5}$$

Because the phase change is small, the exponential term for the phase shift can be approximated using the first two terms of a Taylor expansion:

$$e^x = 1 + x + \frac{x^2}{2!} + \frac{x^3}{3!} + \frac{x^4}{4!} + \dots$$
$$e^x \approx 1 + x \quad \text{(for small values of } x\text{)}$$
$$\Rightarrow e^{i\phi} \approx 1 + i\phi.$$

This can then be substituted back into equation 2.5:

$$\Psi_{exit} \approx \Psi_{incident} \cdot [1 + i\phi], \tag{2.6}$$

and rearranged [225]:

$$\Psi_{exit} \approx \Psi_{incident} + i\phi\ \Psi_{incident}. \tag{2.7}$$

The resultant vector in the Argand diagram (the exit wave, in blue, Figure 2.4A) has almost the exact same length (amplitude) as the incident, unscattered wave (black). Since the detector measures intensity (amplitude squared), this small change is undetectable.

Each of these small-amplitude scattered waves is scattered at an angle depending on the spacing of the feature in the sample (d). Bragg's law states that the angle of this scattering (θ) is given by:

$$\sin(\theta) = \lambda/d\ . \tag{2.8}$$

The objective lens focuses waves scattered at the same angle to points in the back focal plane of the microscope. As the waves continue, they interfere with the unscattered wave in the final image plane to form the image (Figure 2.5A). However, due to defocus (and lens aberrations), there is now a path length difference between the unscattered and scattered electron waves. This path difference introduces an additional phase shift that is dependent on both the amount of defocus and the scattering angle. When this path difference equals a quarter of a wavelength, it adds a further $\pi/2$ phase shift to the resultant wave, combining with the initial $\pi/2$ shift from the WPOA to give a phase shift of π. This creates an observable change in amplitude, shown by the CTF (Figure 2.5B).

To maximise this effect, the microscope is often operated at the 'Scherzer defocus'. This specific defocus value balances the negative phase shift of the defocus against the positive phase shift caused by spherical aberration (C_s). This creates a region where the phase shift remains approximately constant, resulting in maximal destructive interference and a detectable change in amplitude at lower spatial frequencies.

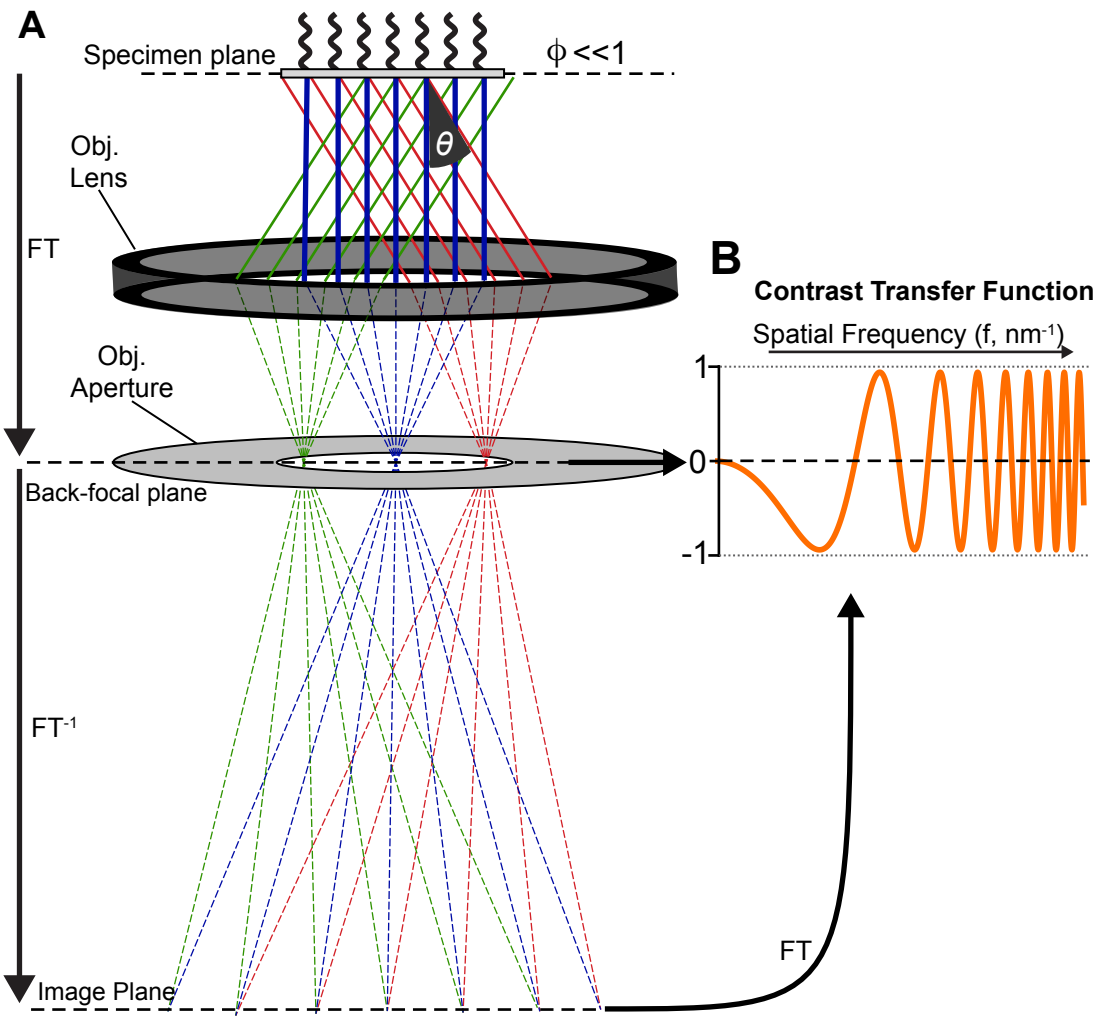


Figure 2.5: **Diagram of image formation in the TEM (phase contrast imaging)**. **A** Black electron waves are seen at the top of the diagram, incident on the thin sample. A phase shift occurs at the sample plane and the electron wave is separated into the unscattered wave (blue) and the waves scattered to many separate angles (θ, coloured green and red). The objective lens acts as a Fourier transformer, creating a diffraction pattern in the back focal plane that separates the scattered waves by their spatial frequency (f). An objective aperture can be inserted to block high-angle scattered electrons to enhance contrast. The waves then continue and interfere at the image plane, forming the first real-space image, which is subsequently magnified by the projector lenses. This recombination is effectively a second Fourier transform (FT^{-1}). **B** An ideal Contrast Transfer Function (CTF), which describes the phase shifts applied in the back focal plane and thus dictates the contrast in the final image.

2.3.0.2 Contrast Transfer Function

The level of detail in an image is described by spatial frequency, denoted by f. It is the reciprocal of the spacing d in the specimen from equation 2.8 ($f = 1/d$). High-resolution details have a small d and therefore a large f.

This concept of spatial frequency is central to image formation because the objective lens physically sorts scattered electrons by their angle, performing a Fourier Transform (FT). This action converts the image information from real space (position) into reciprocal space (spatial frequency) in the back focal plane, as illustrated in Figure 2.5A. It is in this reciprocal space that lens-induced phase shifts occur. The phase shift $\chi(f)$ introduced by defocusing the objective lens is given by [228, 231]:

$$\chi_z(f) = -\pi\lambda\Delta z f^2, \tag{2.9}$$

where Δz is defocus (weakening of the objective lens, underfocus).

An ideal lens would focus all parallel rays to a single point. However, real electromagnetic lenses are imperfect and suffer from spherical aberration (C_S). This aberration causes electrons scattered at higher angles (those carrying high-resolution information, with a large f) to be focused more strongly than those scattered at lower angles, effectively blurring their contribution.

This over-focusing also creates an additional path length difference, introducing an additional phase shift that is always present. This effect is most pronounced at high spatial frequencies because it scales with the fourth power of the scattering angle [228, 229]. The phase shift from spherical aberration is given by [228, 231]:

$$\chi_s(f) = \frac{1}{2}\pi\ C_s\ \lambda^3 f^4. \tag{2.10}$$

The total phase shift, $\chi(f)$, introduced by the objective lens is the sum of these two effects. The final image contrast is generated by the interference between the unscattered wave and the scattered wave, which has been phase-shifted by this total amount. This conversion from phase to amplitude at every spatial frequency is described by the Contrast Transfer Function (CTF). For a WPO, the CTF is a sine function of the addition of both $\chi_z(f)$ and $\chi_s(f)$ [228, 231]:

$$CTF(f) = \sin\left(-\pi\lambda\Delta z f^2 + \frac{1}{2}\pi\ C_s\ \lambda^3 f^4\right). \tag{2.11}$$

An example of a CTF curve can be seen in Figure 2.5B. The above equation describes how contrast varies with spatial frequency for any given defocus, forming the characteristic oscillating curves that must be corrected for in cryo-EM data processing. Chapter 3 outlines the specifics of STEM image formation applied to vitreous biological samples.

Understanding the theoretical basis for contrast generation, as described by the CTF, is only meaningful in the context of the physical instrument that generates the electron beam and manipulates it with electromagnetic lenses. The following sections will therefore describe the fundamental components and operational principles of TEM and STEM, from the electron source to the detector.

2.4 Electron Optics and Microscope Components

2.4.1 The Electron Source

A suitable source of electrons is essential to the generation of sufficient contrast and for resolving fine structural details in electron microscopy.

'Thermionic' sources rely on materials capable of stably emitting electrons when heated to high temperatures [232]. 'Field emission' sources, commonly referred

to as field emission guns (FEGs), use an atomically sharp tungsten wire from which electrons are extracted by a strong electric field [96]. Unlike thermionic sources, FEGs are able to operate at lower temperatures. A variant of this approach is the Schottky field emission gun (SFEG), where thermal assistance improves electron emission efficiency. SFEGs provide electrons with a greatly reduced energy spread compared to thermionic sources, which is important for image formation described later [233, 234].

For even lower energy spread, electrons can be extracted without thermal assistance using a cold field emission gun (CFEG), which operates at lower temperatures than an SFEG [7]. However, CFEGs require ultra-high vacuum conditions (10^{-6} to 10^{-9} Pa) and periodic flashing at high current to eliminate contamination. A CFEG is used for the STEM and TEM imaging in this thesis, whilst an SFEG is used for the SEM imaging.

The application of a potential difference between the filament of the electron emitter (a cathode) and a metal cylinder with a small selective aperture at the base (an anode) directs electrons downward through the aperture. As they are accelerated by the created electric field, the electrons gain kinetic energy. Subsequently, a series of accelerator coils step up the potential difference to further accelerate the electrons down toward the lenses and specimen.

2.4.2 The Electron Lenses and Apertures

After exiting the gun aperture, the electrons are focused by a series of electromagnetic lenses, depending on the required illumination. These lenses consist of coiled copper wires that generate a strong, azimuthally symmetric magnetic field when a current is passed through the wire (Figure 2.6).

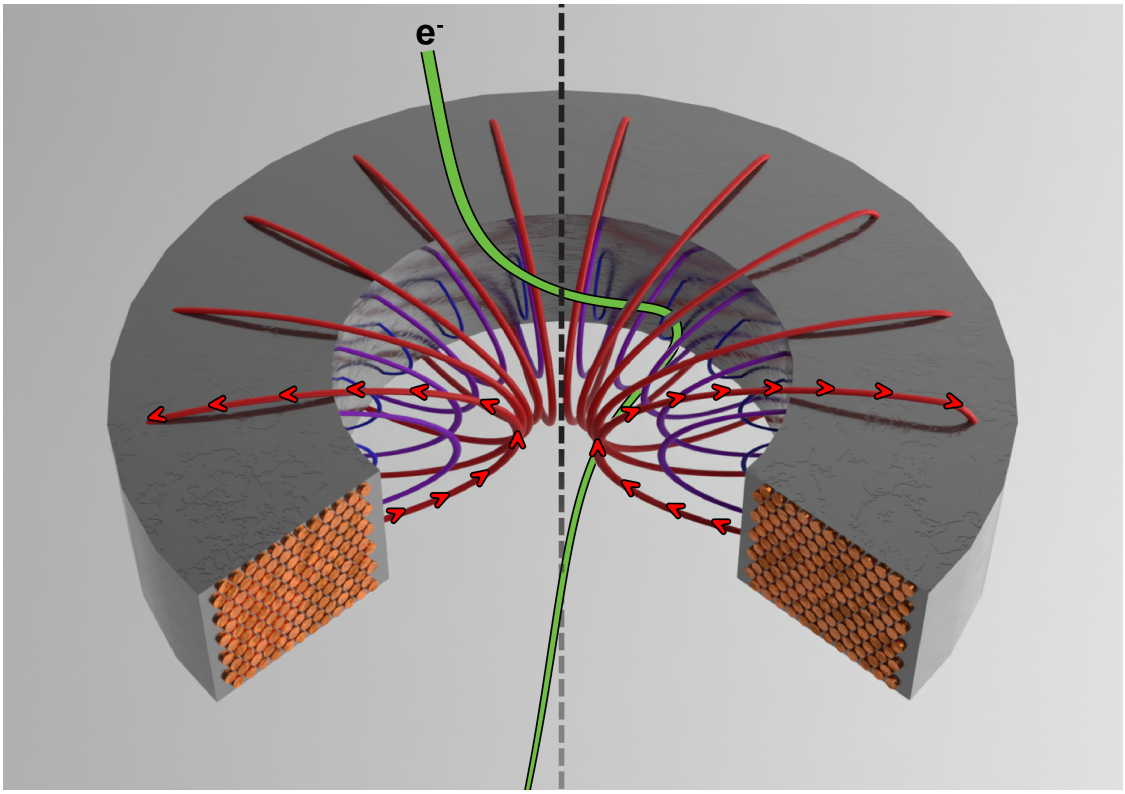


Figure 2.6: **A cross-section of a magnetic lens used for focusing electrons**. A current passing through the symmetrical copper windings (coils) generates a strong magnetic field (field lines in red, purple, and blue). This field acts as a convex lens, forcing electrons into a helical trajectory (green path). The electrons are brought to a focus on the optical axis. The strength of the current directly controls the focal length of the lens. Note that the exit position of the electron is rotated about the optical axis.

Electrons, as moving charged particles, experience a Lorentz force in the presence of this magnetic field. This force acts perpendicularly to both the electrons' velocity and the magnetic field direction, causing the electrons to follow helical trajectories around the optical axis. As the electrons circle, the Lorentz force is continuously directed towards the centre of the lens. This results in a net convergence of the electron beam towards the optical axis, effectively focusing it toward a crossover point [235].

Once the electrons have moved far enough down the microscope that they are no longer meaningfully affected by the lens, their trajectory remains unchanged.

The amount of current passing through an electromagnetic lens must be carefully

controlled, as this current generates the magnetic field responsible for focusing the electron beam. However, the same current also produces Joule heating within the lens coils. Variations in temperature alter the magnetic properties of the lens and lead to thermal expansion of mechanical components, both of which change the effective focusing strength and optical alignment. To ensure a stable magnetic field – and to minimise thermally induced focus drift and specimen displacement – electron microscope lenses are actively cooled, maintaining a constant temperature and hence a consistent force acting on the electrons.

Electron microscopes have several lenses before the specimen plane, which are designed to give even, parallel illumination over a desired area of the sample for TEM, or a finely focused probe in STEM and SEM. Condenser lenses (CLs) are used to condense the wide beam from the electron gun down into a smaller area suitable for irradiating the sample plane.

The STEM/TEMs used in this thesis have different numbers of CLs; the JEOL microscope (used in Chapters 3 and 4) has 2 CLs. By contrast, the Titan Krios (used in Chapters 3 and 5) is a 3-CL system with a condenser mini-lens which ensures that parallel illumination is reached over a wide range of magnifications in TEM mode, and allows an adjustable convergence semiangle in STEM mode.

Condenser apertures are also used to select a specific range of electrons from the central portion of the beam's cross-sectional area. This serves both to reduce the number of electrons incident on the sample and to block incoherent electrons that would not contribute meaningfully to the final image in TEM or STEM. The condenser stack, therefore, prepares the illumination for the specimen either as a broad, parallel beam in TEM mode or a finely focused probe in STEM mode.

2.4.3 Beam Deflection and Correction Systems

Integrated within this lens stack are other electromagnetic coils that perform specific functions. This is particularly relevant for Chapters 4 and 5, which use scanning deflector coil systems to irradiate the sample with non-standard patterns.

2.4.3.1 Beam Shifting

In both STEM and SEM, the image is formed by systematically moving a focused probe across the specimen. To achieve this without altering the illumination angle at the sample, a double-deflection system is employed, which consists of two pairs of magnetic scan coils (two quadrupoles) [235]. The upper scan coils first deflect the beam, tilting it away from the optical axis by a specific angle. This is followed by the lower scan coils, which apply an equal and opposite deflection. This two-step action cancels the initial tilt, resulting in a beam shift: the electron probe is displaced laterally to a new (x,y) position on the specimen but continues to travel parallel to the optical axis (Figure 2.7A).

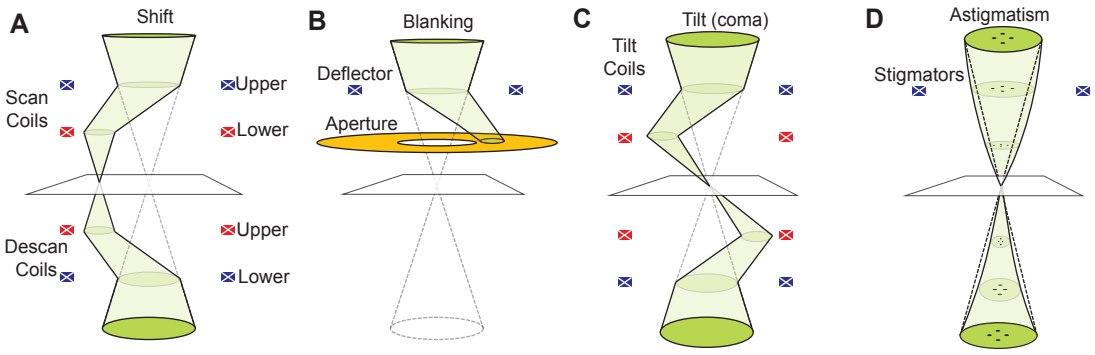


Figure 2.7: **Beam Deflection in the electron microscope**. Dashed lines indicate the unaltered trajectory of a STEM beam for reference. **A** A shift in the beam (scanning in STEM and SEM) may be induced by a pair of coils (here only one axis is shown). The first set moves the beam off axis with a tilt, and the second reverses the tilt, ensuring the beam is parallel to the optical axis with a displacement. Below the sample plane, descan coils can be used to re-correct for this shift. **B** Blanking uses a strong deflector to rapidly divert the beam away from the optical axis (here, into an aperture), shielding the sample from irradiation. **C** For beam tilt, a similar situation is observed to the shift coils in **A**. This is created when the lower deflector coil's strength is doubled relative to the upper coil, which causes the beam to pivot at the sample plane. This is used for coma (tilted illumination) correction. **D** Astigmatism is an aberration caused by an asymmetrical lens field that focuses the beam to different points in orthogonal directions. This results in an elliptical probe, which is corrected using stigmator coils to restore a circular beam shape.

After the primary scan coils deflect the beam to illuminate an off-axis area of the specimen, a second set of 'descan' coils located after the sample can be used to apply an equal and opposite beam displacement. This action reverses the initial shift, ensuring that the transmitted beam remains stationary on the detector regardless of which area of the sample is being illuminated [236]. In addition to their use in forming a scanning probe, deflection coils are also employed for high-throughput imaging in TEM through a technique known as beam shifting. By eliminating the need for slow, mechanical stage movements between exposures, this electromotive beam-shifting method can substantially increase the speed of data acquisition [237].

2.4.3.2 Beam Blanking

Similarly, beam deflectors allow the sample to be quickly and effectively shielded from the beam to prevent unnecessary radiation damage. An electrostatic deflector, when activated, applies a strong electric field to rapidly divert the electron beam away from the optical axis and into an aperture, effectively shielding the sample (Figure 2.7B). This allows the beam to be blanked almost instantaneously (within nanoseconds) without having to stop emission from the source or move a slow mechanical shutter [238, 239]. Beam blanking is particularly important for cryo-STEM and SEM, where it prevents the stationary, high-current density probe from damaging the sample before and after an acquisition is performed.

2.4.3.3 Beam Tilting

Coma is an off-axis aberration that occurs when the illuminating beam is not perfectly parallel to the objective lens's optical axis. This misalignment causes electrons passing through the lens at different azimuths to have different focal lengths. This results in a comet-shaped, asymmetrical blurring of the image points. Coma can be corrected by applying a controlled beam tilt with the deflection coils to realign the illumination with the true optical axis of the lens (Figure 2.7C).

2.4.3.4 Beam Astigmatism and Aberrations

Astigmatism is an aberration caused by an asymmetry in the magnetic field of a lens, as illustrated in Figure 2.7D. This imperfection causes the lens to have different focal lengths in orthogonal directions. The resulting electron probe is elliptical rather than circular, which severely degrades image resolution. Astigmatism is corrected using stigmators that apply a weak, compensating field to restore the rotational symmetry of the focusing field and produce a round probe.

While astigmatism is a primary, correctable aberration, the ultimate resolution of the microscope is often limited by a more fundamental, higher-order imperfection known as spherical aberration (C_S), that arises due to the limitations with a round lens geometry [240]. C_S correctors are complex multipole lens systems [87], typically composed of either sextupoles or quadrupoles and octupoles, that are placed within the microscope column [241].

These correctors are designed to generate a negative spherical aberration through the introduction of other aberrations that cancel out the inherent, positive spherical aberration of the round objective lens [240]. This can result in a much smaller, more convergent, and higher-current electron probe, dramatically improving the achievable resolution in STEM - as will be shown in section 2.6.

2.5 Image Formation and Detection System

The components described up to this point – the electron source, condenser lenses, and some deflection systems – are common to all modes of high-resolution electron microscopy, as they are required to generate and control the primary electron beam. However, the path of the electrons after the specimen plane marks the fundamental divergence between an SEM and the transmission modes (TEM and STEM).

In an SEM, all signals are generated from the top surface of the specimen and collected by detectors placed above it; there are no post-specimen lenses. In a conventional setup, the electrons emitted from the sample travel in straight lines to detectors positioned around the chamber. In high-resolution 'immersion' mode, the sample is raised to sit within the strong magnetic field of the final objective lens. This field not only focuses the incoming beam to a finer spot but also acts as a funnel for the electrons emitted from the surface to travel back up the column to in-column detectors.

Conversely, in TEM and STEM, the information is carried by the transmitted and scattered electrons that pass through the specimen. These electrons must be manipulated by a system of post-specimen lenses and detectors to form the final image. The following sections will detail these post-specimen components.

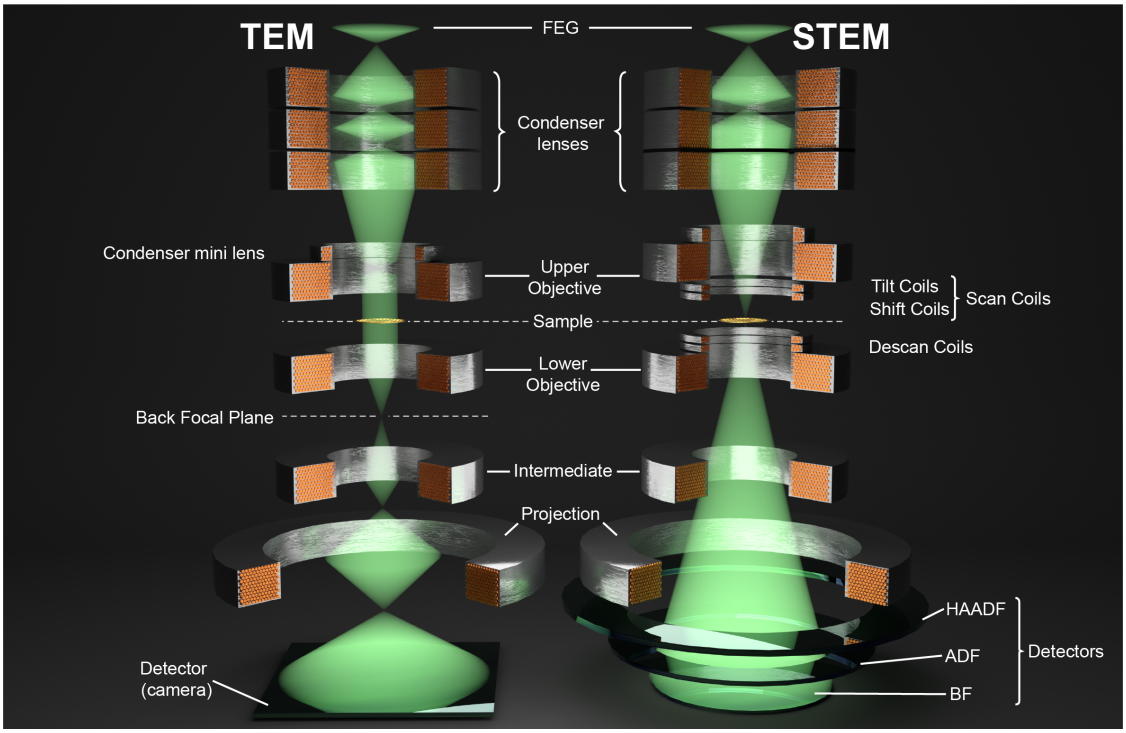


Figure 2.8: **Simplified diagram of a Transmission Electron Microscope**. TEM is displayed on the left, and STEM mode on the right. Although most of the physical components are the same, the key differences between these modes of operation is the various strengths of the lenses involved. For example, in STEM, a weakened condenser lens system is used to focus the beam to a probe at the sample plane, whereas in TEM, the beam is parallel over the sample to allow maximal phase contrast. STEM also requires scan coils and often, descan coils. The post sample lenses in TEM each form a magnified image, while in STEM, the post sample lenses are used to magnify a diffraction pattern on the circular/annular detectors. SEM illumination is similar to STEM illumination without the post-sample components, as signals are usually only detected above the sample.

The objective lens, located immediately after the sample, is the most critical lens for determining image quality in TEM [242].

2.5.1 Magnification

In a TEM, magnification is achieved through a multi-lens projection system. The objective lens forms an initial magnified image which is then passed through a series of intermediate and projector lenses to form a final, highly magnified image on the detector (Figure 2.8). The magnification (M) for a single lens in this system is given by the ratio of the image distance (v) to the object distance (u), as described by the thin lens equations:

$$\frac{1}{f} = \frac{1}{u} + \frac{1}{v}\ , \quad \mathrm{M} = \frac{v}{u} \tag{2.12}$$

where f is the focal length of the lens. In TEM, therefore, the final magnification on the detector is controlled by altering the current in the post-specimen intermediate and projector lenses, which modifies their focal lengths and thus the overall magnification of the projection system.

Magnification in scanning modes (SEM and STEM) is achieved in a fundamentally different way. Instead of projecting a magnified image, magnification is simply the ratio of the (fixed) display width to the scanned area width:

$$M = \frac{\mathrm{Width}_{\mathrm{display}}}{\mathrm{Width}_{\mathrm{scan}}}. \tag{2.13}$$

Consequently, increasing the magnification is achieved by decreasing the size of the area scanned on the sample.

This reliance on a focused probe in STEM provides an image known as a Ronchigram. A Ronchigram is a 'shadow image' of an amorphous specimen formed by the beam, and provides a real-space map of the aberrations in the probe. When the focus point of the probe is adjusted to be at the same z-height as specimen, the magnification of this shadow image becomes effectively infinite [243]. Although this state is not used to form a standard image, it is essential for aberration correction [244].

2.5.2 Energy Filter

An energy filter separates electrons based on the kinetic energy they retain after passing through the specimen. The primary purpose of an energy filter in TEM imaging is to remove the inelastically scattered electrons, which are responsible for chromatic aberration and a reduction in the final image contrast, especially for thicker samples. This filter uses a strong magnetic prism to bend the electron beam by 90 degrees. Electrons that have lost energy (and thus have a slightly longer wavelength) are bent less strongly than the zero-loss, elastically scattered electrons. This process spreads the electron beam into a spectrum according to its energy, and an adjustable energy-selecting slit is placed at the end of the prism.

For EFTEM, this slit is narrowed to select only the zero-loss electrons, which are then passed on to the detector. This 'zero-loss filtering' dramatically improves the signal-to-noise ratio and sharpness of the final image. Alternatively, by collecting the entire energy spectrum at each pixel, the filter can be used for analytical techniques like EELS to map elemental composition and bonding states [106, 162].

2.5.3 Detectors

The final stage of the electron microscope is the detector, which converts the electron signal into a digital image. The type and geometry of the detector are varied dependent on the mode used, as they determine which electrons are collected and the type of information recorded.

2.5.3.1 STEM Detectors

In STEM, the standard detector arrangement consists of a small, central BF detector surrounded by one or more ring-shaped ADF detectors. This geometry allows multiple signals to be acquired simultaneously. The BF detector collects

the unscattered and low-angle scattered electrons, while the ADF detectors collect electrons scattered to higher angles. Specifically, a HAADF detector is positioned to capture electrons scattered to very high angles, which are predominantly elastically scattered. This provides the strong Z-contrast signal, as introduced in section 1.2.2.

A common technology used for these detectors is the scintillator-photomultiplier tube (PMT) system. This is an indirect detection method that provides significant signal amplification, making it highly sensitive. The process occurs in two stages: firstly, an incident electron strikes a scintillator crystal, generating a burst of photons. Secondly, these photons are guided into a PMT, where they are converted back to electrons and amplified through an avalanche effect, resulting in a large, measurable signal [245, 246]. This also integrates the signal over a large area, which is ideal for fast STEM or SEM detection.

2.5.3.2 SEM Detectors

SEM detectors are similar in design to STEM detectors (generally scintillator-PMT detectors), but are instead designed to collect the signals that originate from the sample surface as the beam is scanned.

The choice of detector used to collect these signals is largely dictated by the working distance (WD, the distance between the final lens and the sample). At a long working distance (>5-10 mm), the most common detector is the side-mounted Everhart-Thornley Detector (ETD). A positive bias within the opening of the ETD attracts low-energy SEs (see Figure 2.3) to generate a topographical image [138].

To achieve higher resolution, a shorter working distance (typically <5 mm) is required, which places the sample within the magnetic field of the final lens in immersion mode. In this configuration, a Through-the-Lens Detector (TLD), located inside the column, may be used. The lens's magnetic field efficiently funnels the SE signal up to the TLD for high-resolution topographical imaging.

By adjusting the detector's bias, a TLD can also be configured to detect BSEs for compositional analysis [138].

2.5.3.3 TEM Detectors

Modern high-resolution cryo-EM relies on Direct Electron Detectors (DEDs), a technology that prompted the 'resolution revolution' in structural biology [11]. DEDs are capable of directly sensing the charge of each electron as it hits the sensor. This direct detection mechanism offers exceptional sensitivity, a very low noise profile, and a higher Detective Quantum Efficiency (DQE, a measure of a detector's SNR performance across a range of spatial frequencies).

The most significant advantage of DEDs is their rapid readout speed, which enables full images to be recorded as high-frame-rate movies [81]. This is critical for cryo-EM, as it allows for the computational correction of beam-induced motion, a primary factor that previously limited resolution [171]. By aligning the individual frames of the movie, any physical movement of the specimen during the exposure can be corrected.

Furthermore, this movie mode allows for sophisticated data processing strategies. For instance, electron counting can localise each electron impact to sub-pixel accuracy, maximising resolution [247]. Additionally, the frames can be dose-weighted, where the information from later frames, which have suffered more radiation damage, is down-weighted to improve the quality of the final reconstruction [248].

2.6 Resolvability

The resolution of a microscope is defined as the smallest distance at which two distinct features can be reliably resolved under ideal imaging conditions. This section will focus on understanding the resolvability of STEM systems used in Chapters 3

and 4. In STEM, this limit is determined by the properties of the electron probe itself, including its size, diffraction, coherence, and the presence of lens aberrations.

Assuming a Gaussian spatial distribution for the STEM probe is a simplification that achieves reasonable agreement between theory and experimental results [249]. The diameter of the probe in STEM is the main determinant of the resolution. However, different measurements of diameter can be derived from a Gaussian distribution, depending on how much or little current is to be included in the measurement. The full width at half maximum (the diameter of the probe containing 50% of the current, FWHM) is the most commonly used definition of resolution in STEM and will be used here throughout [250]. The FWHM of the probe in vacuum, D_{probe}, is determined by the quadratic sum of FWHM from four individual Gaussian distributions, each of which contribute to the overall diameter of the probe.

The first of these contributions (D_D) arises from the physical diffraction limit of electrons passing through the edge of the condenser aperture. The most often used criterion for resolution at the diffraction limit is given by the overlap of two Airy disks (the diffraction-limited image of a single point, see Figure 2.9)[2] [251, 253, 254]:

$$D_D = \frac{0.61\,\lambda}{\alpha}, \tag{2.14}$$

where λ is the wavelength of the incident electrons, and α is the convergence semiangle.

[2]It should be noted that the constant of 0.61 is not a separation of the FWHM of this contribution, which would use a constant of 0.51 (see Figure 2.9E). The choice of 0.61 as the constant in this equation reflects the maximum of one Airy disk coinciding with the first-order minima of the other, also known as the Rayleigh limit, is the most commonly accepted value for diffraction-limited resolution [251, 252].

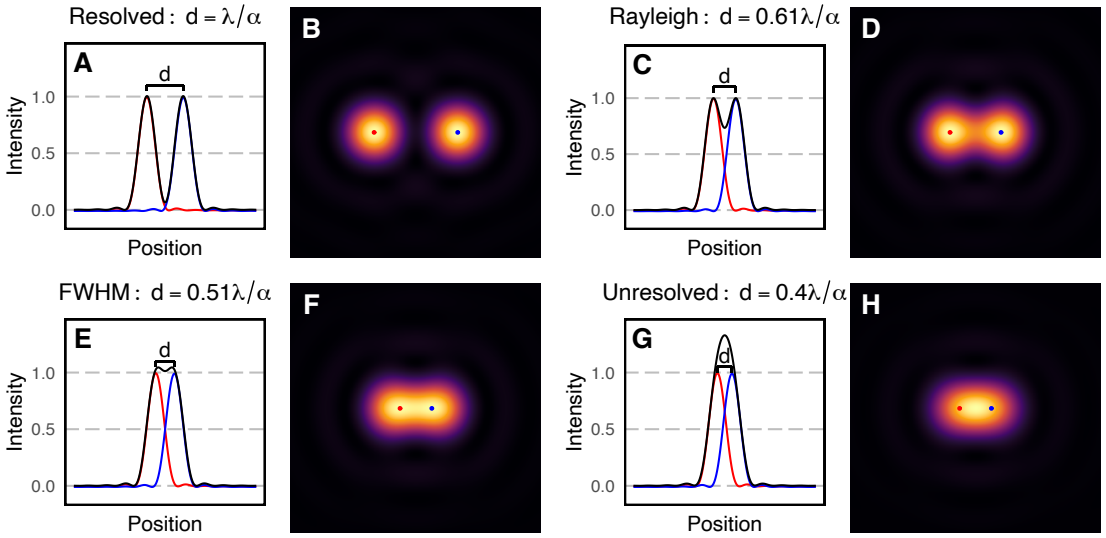


Figure 2.9: **Resolution criterion used for diffraction limited imaging**. Graph of intensity of two Airy disk bessel functions with varying λ/α overlaps of **A** = 1, **C** = 0.61 (Rayleigh limit), **E** = 0.51 (FWHM), and **G** = 0.4. The black line is the sum of the intensities of the blue and red overlapping curves. **B**, **D**, **F**, and **H** show the resultant plotting of the summed intensity as would appear in an image, with the centre of the red and blue features plotted as dots at d distance from one another.

The spherical aberration is the most important contributor to probe diameter, as it is often the limiting factor to attaining high spatial resolution. With symmetric lenses, this aberration is unavoidable and always positive [240, 243]; the electrons that pass through the extremities of the lenses in the microscope are overfocused compared to those that travel closer to the optical axis. This contribution from spherical aberration (D_S) is given by:

$$D_S = \frac{1}{2} C_S \alpha^3, \tag{2.15}$$

where C_S is the spherical aberration coefficient [254, 255]. The chromatic aberration contribution (D_C) reflects the spread of the incident electron energy, and gives a spatial broadening as electrons with different energies will be focused to different z axis planes in the microscope. This contribution is:

$$D_C = C_C\,\alpha\,\frac{\Delta E}{E_0}, \tag{2.16}$$

where C_C is the chromatic aberration coefficient, ΔE is the energy spread from the electron gun, and E_0 is the accelerating voltage used on the microscope. Finally, the effective diameter of the source, D_I, is given by [250, 254, 255]:

$$D_I = \frac{2}{\pi\alpha}\sqrt{\frac{I_{probe}}{\beta}}, \tag{2.17}$$

where I_{probe} is the current in the probe and β is the brightness of the electron gun. This equation follows the same $1/\alpha$ dependence on the convergence semiangle as the diffraction limit.

If each of these contributions is approximated as a Gaussian profile of the probe, then the ideal probe size, D_{probe}, in vacuum is the addition of each of these contributions in quadrature [243, 250, 254]:

$$D_{probe} = \sqrt{({D_D}^2 + {D_S}^2 + {D_C}^2 + {D_I}^2)}. \tag{2.18}$$

In the Titan Krios G4, the magnitudes of both C_S and C_C are 2.7 mm, and ΔE is 0.3 eV when E_0 is set to 300 keV. The brightness, β, of the CFEG is 1×10^8 A/m^2 sr [96]. The probe current is maintained at a low level of 3 pA, which is consistent with cryo-STEM analysis - where minimising fluence, and therefore current, is often required.

In the JEOL ARM300F2, the C_S can be minimised with the corrector to < 1 µm whilst the C_C of the 'ultra high-resolution' configuration is 1.6 mm, and ΔE = 0.35 eV at an E_0 = 300 keV [256]. β and the current are the same as in the Titan Krios. Calculating these values for the two microscopes used in this thesis in STEM mode gives Figures 2.10 A and B.

Instead of using the addition of quadrature to find the maximum attainable resolution (the so-called 'geometric method'), the optimum resolution for an uncorrected system can be found by balancing defocus with spherical aberration [240, 243]. This 'Scherzer defocus' ($\Delta f_{Scherzer}$) can be found using:

$$\Delta f_{Scherzer} = -\sqrt{C_S\ \lambda}\ . \tag{2.19}$$

Using 300 kV and 2.7 mm of C_S (as on the Titan Krios) gives a $\Delta f_{Scherzer}$ of -72.9 nm (note the negative, which indicates a defocus above the sample). At this defocus value, a tolerable phase shift is allowed over the flat region of the ronchigram of $\pi/2$, in turn leading to the derivation of the optimal convergence semiangle (α_{opt}), and the optimal FWHM probe size at α_{opt} (D_{opt}) [243, 257]:

$$\alpha_{opt} = \left(\frac{4\lambda}{C_S}\right)^{\frac{1}{4}} \tag{2.20}$$

$$D_{opt} = (0.43\ C_S)^{\frac{1}{4}}\ \lambda^{\frac{3}{4}}. \tag{2.21}$$

For Titan Krios, D_{Probe} (using the above quadrature addition steps) is 2.9 Å, at an α of 4.8 mrad, while the optimal FWHM probe size D_{opt} is 1.6 Å, at an α_{opt} of 7.4 mrad.

For JEOL ARM300 F2, D_{Probe} (using the above quadrature addition steps) is 0.6 Å, at a α of 26.5 mrad. Note that the wave-optical treatment can be applied to a C_S-corrected system. However, the theoretical gain in resolution would be minimal at an inconsequentially small defocus for the work in this thesis and would almost certainly require correction of higher-order aberrations. Considering the probe size as an approximation for resolution is valid primarily for extremely thin samples, where only single scattering applies. It ignores potential multiple scattering and probe broadening within the specimen, which are considered in Chapter 3.

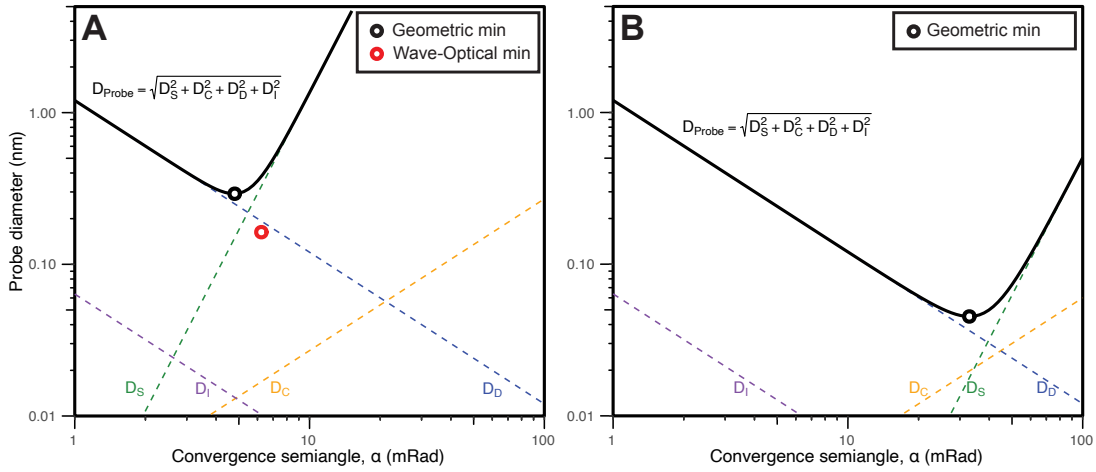


Figure 2.10: **Probe diameter (FWHM) as a function of the convergence semiangle, α, for the two microscopes used in this thesis in STEM mode**. **A** The non-C_S corrected Thermo Fisher Scientific Titan Krios G4, and **B** JEOL ARM300F2 with a C_S corrector. Note that the effect of the C_S corrector effectively shifts the contribution of the spherical aberration (D_S, dashed green line) to greater α, with a resultant decrease in probe diameter beyond the limited α of the uncorrected system in **A**. The geometric and wave-optical minima are marked with black and red points, respectively.

2.6.1 The Third Dimension

The nature of three-dimensional localisation means that emphasis is not solely placed on lateral resolution, but also on resolution along the z axis. The distance in the z axis over which there is a decrease to $\approx 80\%$ intensity along the optical axis of the probe at the specimen height (at 0 defocus), assuming ideal conditions, is given by [258, 259]:

$$\Delta z = \frac{2\lambda}{\alpha^2}. \tag{2.22}$$

This is a similar criterion to the Rayleigh criterion, where the intensity falls to $\approx 81\%$ of its maximum value. This equation holds when α is below the optimum (before the effects of spherical aberration dominate). The probe can be computationally

simulated using a propagation of the aberration function from an aperture with a known convergence semiangle, across a range of z values. The aberration function ($\chi(\alpha)$) is given as an addition of all the rotationally symmetric aberration terms [259]:

$$\chi(\alpha) = \frac{1}{2}\,\Delta z\,\alpha^2 \;+\; \frac{1}{4}{C_S}^3\alpha^4 \;+\; \frac{1}{6}{C_5}^3\alpha^6 \;+\; \frac{1}{8}{C_7}^3\alpha^8 ... \tag{2.23}$$

Higher order terms than the third order spherical aberration (C_5, C_7, *etc.*) are ignored. By substituting the spatial frequency f, using the small-angle approximation ($\alpha \approx f\lambda$), the shape of the focused STEM probe is determined by the same coherent aberration function, $\chi(f)$, that governs the CTF in TEM. This is a direct consequence of the Helmholtz principle of reciprocity, which states that the wave amplitude at a detector point is unchanged if the positions of the point source and the detector are interchanged [260, 261]. Therefore, the total phase shift from defocus and spherical aberration can be described using the function previously defined in Equation 2.9 [262].

The wave function at the aperture, Ψ_{Ap}, is then:

$$\Psi_{Ap}(f) = A(f)\; e^{i\chi(f)}, \tag{2.24}$$

where $A(f)$ is 1 if the convergence semiangle is less than the aperture edge, or 0 if it is outside, e is Euler's number, and i is the imaginary unit. To find the intensity at the sample plane ($\Delta z = 0$), the Fourier transform (FT) is taken and the resulting absolute amplitude is squared [262]:

$$I = |\mathrm{FT}(\Psi_{Ap})|^2. \tag{2.25}$$

By altering Δz in steps of 1 nm, the probe intensity may be calculated over a range of z values to build a cross section of the xz probe slice (Figures 2.11 A-D).

It is important to note that the current within the probe and chromatic aberration have not been considered in this method. As highlighted by the geometric method, these factors are insignificant with the use of a cold FEG and low current for cryo-STEM and are therefore negligible compared to the spherical aberration and diffraction limited terms. Assuming the probe is symmetric around the Z axis allows the profile of the probe to be plotted in the xy plane at 0 defocus (Figures 2.11E-H[3]).

[3]The author acknowledges Dr. Jon Barnard's guidance in calculation of these simulated probe profiles.

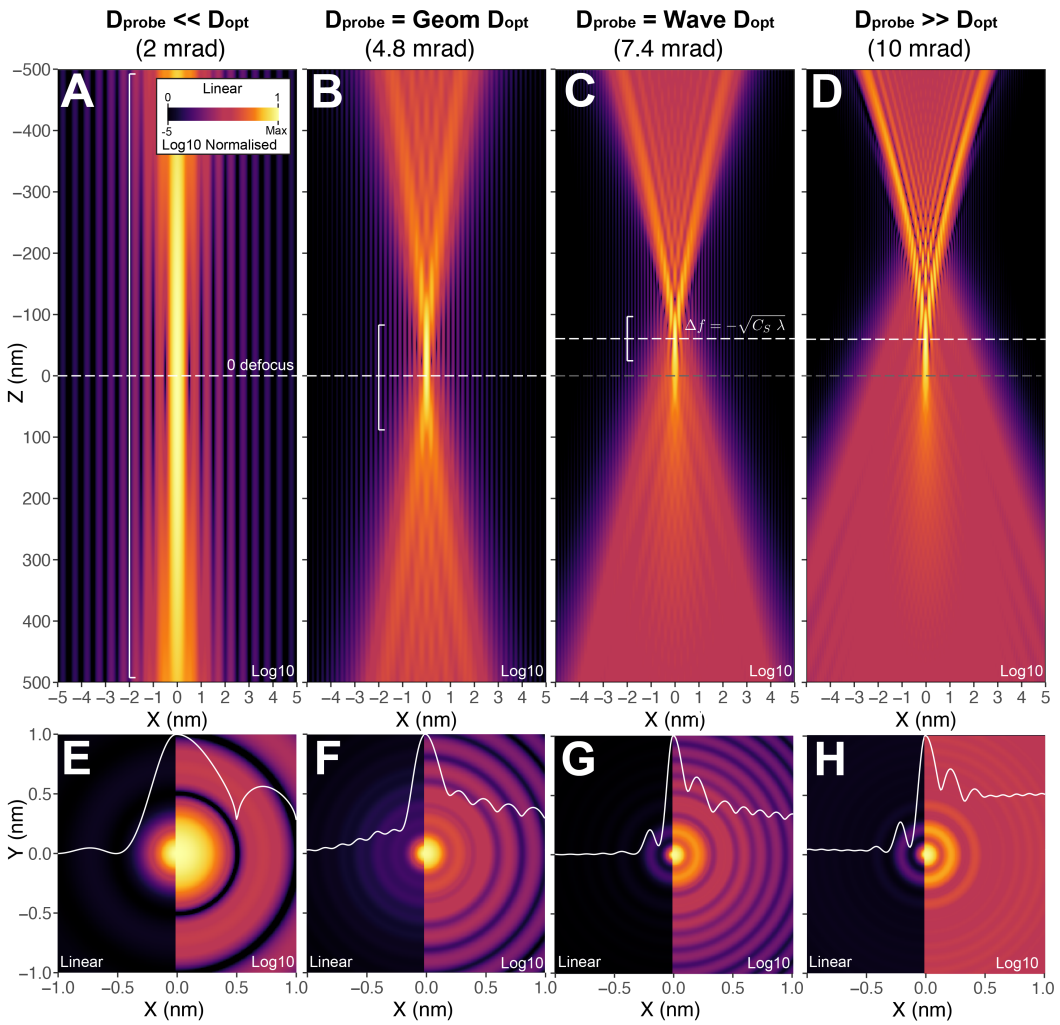


Figure 2.11: **Simulations of the probe in STEM mode using the non-C_S corrected Thermo Fisher Scientific Titan Krios G4, assuming ideal imaging conditions**. **A-D** show xz cross sections of the probe at a convergence semiangle far below the optimum, at the geometric optimum, at the wave optimum, and far above the optimum, respectively (each calculated in 2.10 A). The intensity is displayed by colour according to the normalised log scale to better display weaker intensities, from the maximum intensity to a cutoff of -5. The depth of focus according to $\Delta z = 2\lambda/\alpha^2$ is displayed as a vertical white line to the left of the probe in **A-C**. For **A** and **B**, a horizontal dashed line indicates 0 defocus (the Gaussian imaging plane): for **C** and **D**, this denotes the Scherzer defocus for optimal imaging. **E-H** show xy cross sections of the probe at each of the dashed horizontal white lines from **A-D**. The left side of each image is displayed in linear scale, and the right side in log scale to better display weaker intensities (C_S = 2.7 mm).

3

Theoretical Considerations for STEM Nanoparticle Localisation

Contents

3.1 Introduction 87
3.2 Considerations for the Theoretical Model 89
3.2.1 3-Dimensional Localisation Approaches 89
3.2.2 Geometry of STEM on Lamellae 97
3.2.3 Beam Broadening 99
3.3 Theoretical Model for Nanoparticle Detection 102
3.3.1 Detectability - Scattering Cross Section 102
3.3.2 Application to Thicker Samples 106
3.3.3 Model Results 111
3.4 Experimental Application of the Model 117
3.4.1 Experimental Methods 118
3.4.2 Experimental Results 121
3.5 Discussion 123
3.5.1 Approach for 3D-localisation and Geometry of the STEM 123
3.5.2 Beam Broadening Limits the Achievable STEM Resolution in Lamellae 124
3.5.3 Theoretical Model and the Detectability of Nanoparticles in Vitreous Ice 125
3.5.4 Conclusion 128

3.1 Introduction

The success of tagging proteins with heavy-element nanoparticles for STEM analysis fundamentally depends on the reliable detection of nanoparticles. Specifically, high-atomic Z nanoparticles must be distinguished against a low-atomic Z ice background of substantial comparative thickness. This detection challenge necessitates establishing an experimental framework that can achieve detection with sufficient statistical confidence while accounting for the complex interplay of multiple experimental parameters.

To address this challenge, the analysis in this Chapter focuses on ADF-STEM imaging. This modality was selected for its intuitive Z-contrast mechanism, which is highly effective at visualising high-atomic Z tags against an amorphous, low-atomic Z background. ADF imaging offers a directly interpretable and reliable signal for the foundational detection model developed here that may be integrated with other STEM-based techniques in the future (see section 1.2.3.3). Furthermore, this analysis is framed within the context of a correlative workflow, whereby STEM is used to locate tags within a larger volume reconstructed by EFTEM tomography. The explored parameters are therefore constrained by the need for compatibility with the low-dose (relative to materials science methods) and cryogenic protocols typical of this workflow.

Within this ADF-STEM framework, several critical parameters directly influence the successful resolution and detection capability. For example, the convergence semiangle (α) governs both achievable resolution and depth of focus. This places fundamental limits on nanoparticle resolvability (see section 2.6).

Secondly, sample tilt angles in a tilt series affect the effective thickness through which the electron beam must travel, altering SNR. The optimal high-atomic Z nanoparticle size should satisfy requirements of both resolution (resolvability) and signal-to-noise limitations at practical collection angles (detectability). Critically,

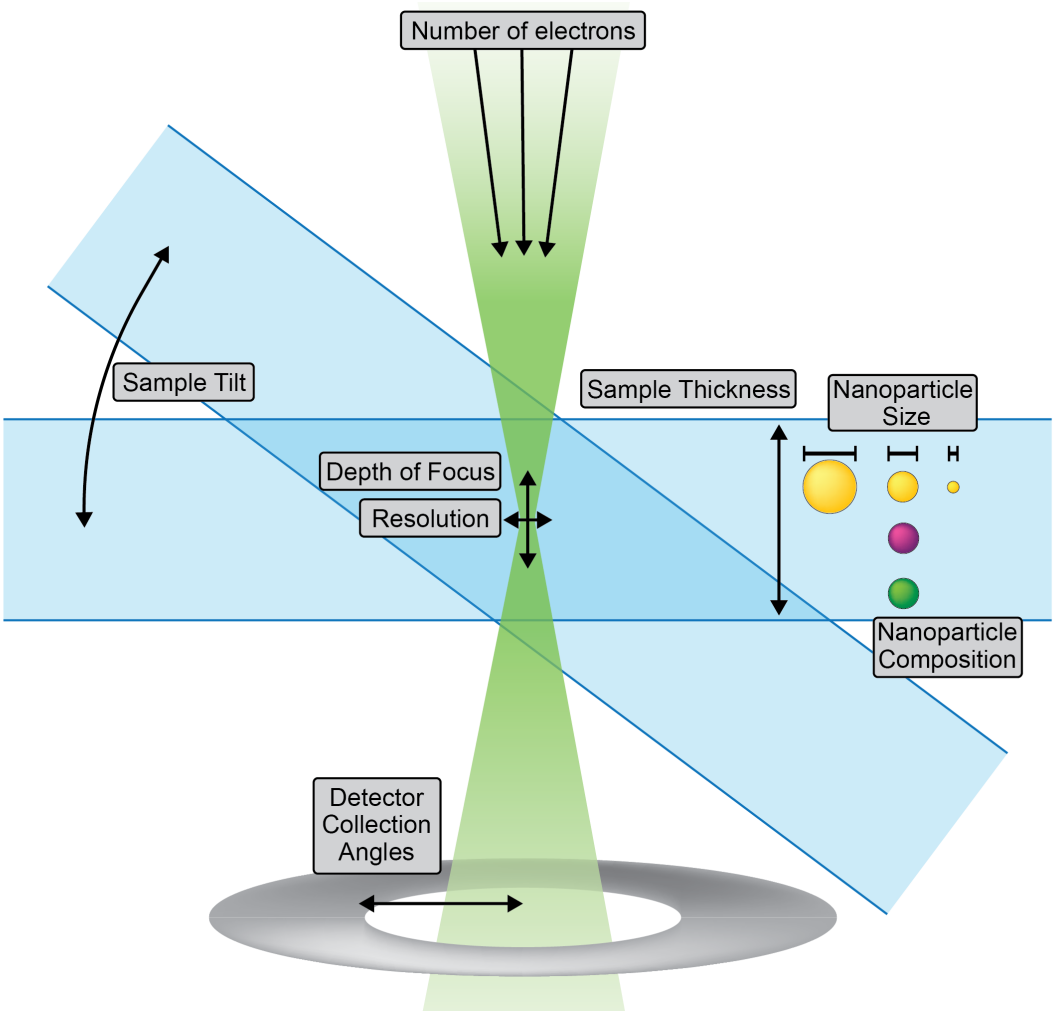


Figure 3.1: **Parameters for Nanoparticle Detection in STEM.** This chapter systematically investigates the key parameters governing the detection of a high-Z nanoparticle in STEM. A conceptual overview of the factors addressed herein is shown, including sample properties (tilt, thickness, nanoparticle size and composition), beam characteristics (number of incident electrons, resolution, and depth of focus), and instrument settings (detector collection angles).

the electron fluence incident on the sample ultimately determines the detection threshold whilst balancing against radiation damage limitations.

This Chapter presents a series of theoretical analyses designed to systematically constrain experimental parameter space. By establishing the relationships between imaging parameters and detection performance, a framework for identifying optimal experimental conditions can be created, reducing the scope of empirical testing required (see Figure 3.1).

Section 3.2 of this Chapter will first consider methods of achieving the desired three-dimensional localisation outcome to select a geometry and workflow for the STEM. Next, section 3.3 will guide the reader through the construction of a model of detectability based on scattering cross section theory, and subsequent application to a nanoparticle in a thick layer of vitreous ice. Section 3.4 will compare this model to examples of experimental data, with a discussion of these results in section 3.5.

3.2 Considerations for the Theoretical Model

3.2.1 3-Dimensional Localisation Approaches

The acquisition of three-dimensional structural information is essential for accurate protein/tag localisation within vitreous ice. Each available methodology presents distinct advantages and limitations in both experimental implementation and subsequent data analysis.

This next section evaluates four potential approaches for obtaining three-dimensional information using STEM mode from cryo-milled lamellae. For comparison, a standard EFTEM tilt series acquisition, suitable for tomogram reconstruction and high-resolution STA, usually employs conditions similar to the following: 300 kV acceleration voltage, a pixel size of ∼1.5-2 Å per pixel, which translates to a ∼600-800 nm untilted field of view for a 4096 × 4096 image. 41 images are usually taken per tilt series between ± 60° and 3 $e^{-}Å^{-2}$ per tilt (total fluence of around 120 $e^{-}Å^{-2}$). A single tilt series of this type takes approximately 24 minutes to complete using a Titan Krios G4 (Thermo Fisher Scientific), without additional beam-shift tilt series [263, 264].

3.2.1.1 Cryo-STEM Tomography

As introduced in section 1.2.3, Cryo-STEM tomography refers to the process akin to cryo-ET, which takes images at each specific tilt angle of the lamella (θ_{tilt}). In total, 30 to 50 images are usually taken, often with a 2° to 4° tilt between them, which covers a θ_{tilt} between ± 40 to ± 60°. This approach requires the entire lamella thickness to remain in focus across all tilt angles, making selection of the convergence semiangle (α) critical. The chosen convergence semiangle must provide sufficient depth of focus to encompass the full lamella thickness at maximum tilt (see Figure 3.2A).

This constraint also necessitates dynamic focus, with the scan rotation aligned orthogonal to the stage tilt axis. By modifying the STEM focus throughout the scan, the probe position in the z-axis is continuously adjusted during acquisition. The dynamic focusing correction assumes a perfectly flat sample, with the focus adjustment calculated as the tangent of the tilt angle multiplied by the y-axis displacement from the horizontal centre of the untilted field of view ($\theta_{tilt} = 0°$).

While this approach can theoretically image the entire lamella thickness in focus, practical implementation faces significant challenges. Sample thickness variations, non-planar lamellae, and calibration difficulties often compromise robust execution [265]. Consequently, successful cryo-STEM tomography implementations usually use a much larger depth of focus (achieved through smaller convergence semiangles) to maintain the entire lamella thickness in focus without requiring dynamic focusing or autofocus, albeit at the cost of a greatly reduced lateral and axial resolution [95, 101, 266].

This well-established methodology offers many advantages. It has a robust data processing pipeline which follows a process similar to the usual EFTEM tomography data; automation for cryo-samples is built into several microscope control software programmes.

However, the amount of time spent acquiring each of the tilt series images in STEM renders this method undesirable for a high-throughput workflow. To demonstrate, a typical STEM scan with a matching 4096 × 4096 pixels and a relatively short dwell time of 5 µs, would take approximately 1 minute 24 seconds per image. This equates to over 1 hour per tilt series (assuming 41 images are taken as with the EFTEM tilt series).

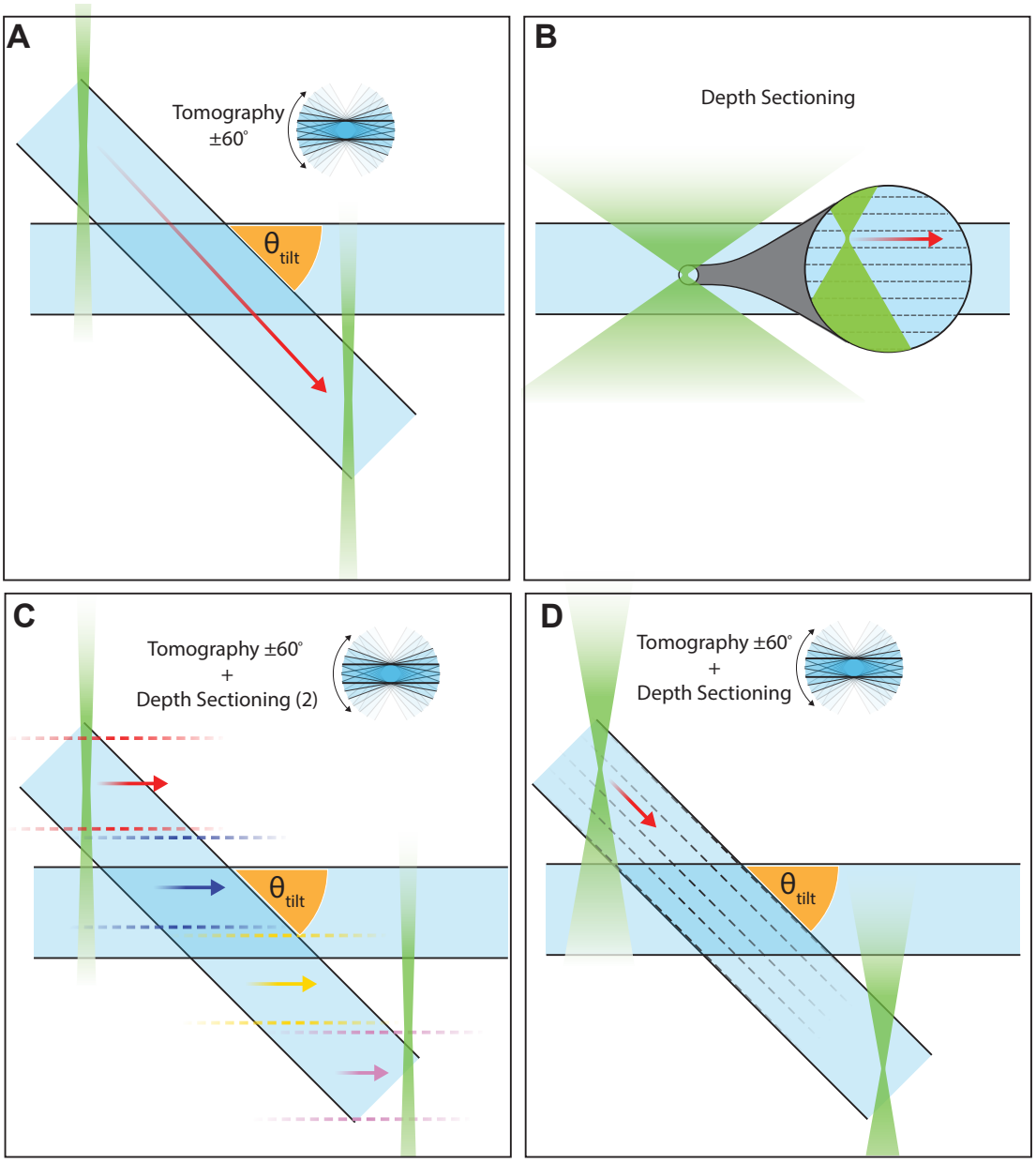


Figure 3.2: **STEM 3D localisation methods**. An xz view of the lamella is shown for **A** Standard STEM-tomography, accomplished either using a very weakly convergent beam at the expense of lateral resolution, or with dynamic focusing at a higher convergence angle and resolution. ($t(\theta_{tilt})$). **B** Depth sectioning, using a C_S-corrected probe to isolate a shallow depth of focus of the lamella. **C** Previously proposed hybrid-depth sectioning and tomography [267, 268] (without dynamic focusing), and **D** hybrid-depth sectioning and tomography with dynamic focusing.

3.2.1.2 Depth Sectioning STEM

Depth sectioning utilises a sufficiently narrow depth of focus to isolate a single plane of the untilted lamella, then systematically alters the focus in discrete steps to image successive slices. This produces a z-stack of images. In stark contrast to STEM-tomography, depth sectioning requires maximisation of the convergence semiangle to achieve the shallowest possible depth of focus. The primary benefit of this method is the high spatial resolution in the x- and y-axes, because the probe diameter is minimised at these broad convergence semiangles. The resolution of the z-axis is entirely dependent on minimising the depth of focus (see Figure 3.2B).

To obtain a sufficient z-axis resolution of 1 nm, the required convergence semiangle is >40 mRad, which necessitates spherical aberration (C_S) correction. At this convergence semiangle, the ideal lateral resolution would be on the order of 1 Å.

Another advantage of this method is that the stage remains stationary between successive images, and requires minor alignments for data reconstruction (such as corrections for drift between frames).

The primary disadvantage of depth sectioning is the substantial number of scans required to comprehensively map the entire thickness at adequate z-axis resolution. For instance, targeting 1 nm z-axis resolution on a perfectly flat 200 nm lamella requires at least 200 scans to image the complete volume. Using 4096 × 4096 pixel images with 5 µs dwell time translates to 4 hours and 40 minutes per imaged site. Even more relaxed parameters – 2 nm z-axis resolution (31 mrad convergence semiangle) and a thinner 120 nm lamella – would still require 60 images, with a total duration of 2 hours and 37 minutes per site.

Beyond the impractical time investment, this extensive imaging protocol results in an immense cumulative electron fluence. For localising small nanoparticles, where higher fluences are needed per image, this level of irradiation would cause

substantial mass loss from the vitreous sample (as detailed in Chapter 4), rendering the structural data meaningless.

However, even if these limitations of time and fluence could be tolerated, the method presents a hardware incompatibility with the proposed workflow. Achieving a useful z-axis resolution necessitates a spherical aberration (C_S) corrected STEM. This is a feature not typically available on the high-resolution EFTEM platforms required for the initial tomography step. While instruments combining both capabilities exist [130, 133], their limited availability precludes their consideration as the basis for a generalisable workflow.

3.2.1.3 Hybrid Depth Sectioning STEM Tomography

This method is a hybrid of the two previously outlined methods: tomography and depth sectioning. During Hybrid Depth Sectioning STEM Tomography, the specimen is tilted in increments, as with tomography, except, at each tilt increment, dynamic focusing can be applied at the optimum convergence semiangle (for a non-C_S-corrected instrument) to serially depth section through the lamella at each tilt angle for optimal resolution. This is similar to previously proposed methods Figure 3.2C, [267, 268], although it includes dynamic focusing, which was not considered previously (Figure 3.2D). As an example, the non-C_S-corrected Titan Krios generates an idealised lateral (xy) resolution of 1.6 Å and a depth of focus of approximately 50 nm (see sections 2.6 and 2.6.1).

A 200 nm thick lamella could be scanned four to eight times at each tilt angle with dynamic focusing to image the entire lamella at the uncorrected system's optimum resolution. This neglects more complex interactions such as beam broadening and aberrations, both of which would deteriorate the practically achievable resolution. Once again, hybrid depth sectioning STEM tomography suffers from the distinct disadvantage of needing many images per complete tilt series, with 41 tilt angles × 4-8 images per tilt. This produces a total of around 150-300 images per site.

Thus, this method is limited by the same constraints as depth sectioning of a prohibitively large fluence applied to the sample (upward of 1000 $e^{-}Å^{-2}$) and the length of time taken to image.

3.2.1.4 Sparse-Tilt STEM Triangulation

The methods covered earlier each produce an entire three-dimensional volume for correlation with the identical volume obtained from EFTEM. However, these approaches are largely redundant. Rather than reconstructing a complete three-dimensional STEM volume, the 3D position of each marker (x, y, and z coordinates) can be determined by triangulation from a small set of projection images.

Since comparable images have already been acquired in the EFTEM tilt series, STEM images taken at matching tilt angles could enable marker position inference from only a few individual tilts. This requires sufficient features in individual images to allow accurate alignment between the STEM and EFTEM datasets. The positions of markers in the reconstructed volume can then be determined through triangulation or direct correlation with the EFTEM tomogram (Figure 3.3).

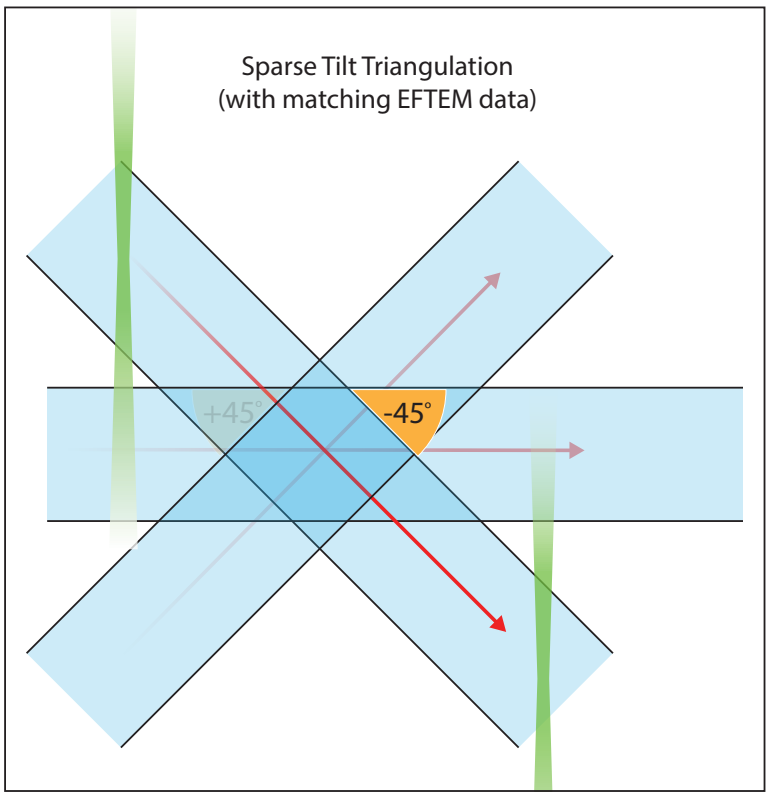


Figure 3.3: **Sparse-Tilt STEM Triangulation Strategy**. Using a minimum number of tilts (for example 3 at +45°, 0°, and - 45°) enables a maximal fluence to be used for each individual image, with correlation to the EFTEM images at the chosen tilt angles. This method minimises the time taken to image whilst maximising the SNR within the given fluence budget.

For example, if the EFTEM tilt series comprises 41 images spanning θ_{tilt} of ± 60°, the STEM acquisition could be limited to only three images at, for example, θ_{tilt} = +45°, 0°, and -45°. These STEM images would correlate with the EFTEM tilt series images at matching angles. This would allow determination of marker positions in the corresponding EFTEM tomogram, through triangulation along those specific angular projections. This three-tilt scheme is a pragmatic example, chosen to provide strong geometric constraints for triangulation while minimising acquisition time; other schemes with more tilts could also be envisioned.

This approach offers significant advantages in acquisition speed and allows maximisation of the electron fluence in each image, because only a minimal number

of STEM images are required, increasing the SNR in each. As an example, three images acquired at the aforementioned tilt angles would likely only take less than 20 minutes total to record. This is similar in speed to the EFTEM tilt series, and so could be included in a workflow to reach high-throughput for targeting. However, the method critically depends on successful image registration between EFTEM and STEM datasets and thus the precision of triangulation is limited by the precision of feature matching across the different imaging modalities. This challenge may be mitigated by using the bright-field STEM signal for alignment, as its contrast mechanism is more directly comparable to that of the EFTEM images, though uncorrectable sample warping could remain a fundamental limitation.

This comparative analysis of the four potential 3D localisation strategies reveals that only one is compatible with the goals of a high-throughput, high-resolution correlative workflow. Both Cryo-STEM tomography (and its hybrid variants) and depth-sectioning are ruled out by their prohibitively long acquisition times, which are incompatible with practical experimental throughput, and high fluences. Furthermore, depth-sectioning requires C_S-corrected optics that are not usually present on the standard instruments used for EFTEM tomography.

Therefore, the 'Sparse-Tilt Triangulation' method is selected as the most promising and viable strategy. Its primary advantages are its acquisition speed and, most critically, its ability to concentrate the entire electron fluence budget into a minimal number of images, thereby maximising the SNR for detecting the smallest possible tags.

3.2.2 Geometry of STEM on Lamellae

With the selected approach to achieve three-dimensional localisation in mind, a framework to establish the geometry for STEM is now possible. A requisite condition is that the convergence semiangle should provide a depth of focus sufficient to encompass the entire lamella along the z-axis, if not using depth sectioning.

Alternatively, if depth sectioning is utilised, the convergence semiangle should be configured to the optimal angle for non-C_S-corrected systems. Furthermore, the resolution exhibits a strong dependency on the convergence semiangle, as described in section 2.6. Thus, a convergence semiangle that permits the entire lamella to be imaged in focus might simultaneously be inadequate for achieving the highest-resolution imaging.

From this point onwards, the non-C_S-corrected Titan Krios will be considered as the basis for the rest of the calculations as it is a tomography-focused instrument and the most widely used for structural determination in the cryo-ET to date [EMDB].

The projected thickness of the lamella (t) at a given angle of tilt (θ_{tilt}) is related to the thickness of the lamella at 0° tilt (t_0) as:

$$t = \frac{t_0}{cos(\theta_{tilt})}, \tag{3.1}$$

which may then be substituted into the equation for depth of focus in STEM (equation 2.22), and rearranged for the maximum usable α for that tilt angle and thickness of the lamella:

$$\alpha_{max} = \sqrt{\frac{2\lambda \cos(\theta_{tilt})}{t_0}}. \tag{3.2}$$

Taken altogether, this results in a hierarchical approach to selecting the best convergence angle for any given sample thickness and tilt:

- If the projected thickness is smaller than the depth of focus provided by the wave-optical optimum (α_{opt}, from equation 2.20), then α_{opt} is used to achieve the best possible resolution. Practically, this is only possible for very thin samples (<50 nm thick) using the setup described here.

- If the projected thickness exceeds the depth of focus at α_{opt}, the angle must be reduced to keep the sample in focus. The largest possible angle that can be used within this regime is the geometric optimum α, using equation 2.18.

Using this system to find the maximum convergence angle at the desired maximum tilt, it is possible to relate this information to the minimum probe diameter, and therefore the expected maximum resolution, for a given experimental setup.

3.2.3 Beam Broadening

It is unrealistic to predict the maximum achievable resolution with the equation for the probe in vacuum. Due to the effects of multiple scattering, the diameter of the probe spreads as it traverses the thickness of the layer (Figure 3.4A). Note that this will result in the well-documented top-bottom effect of resolution in STEM of thick samples [269, 270]; the resolution at the top surface is better than at the bottom surface. This beam broadening in xy for a given z in an amorphous material, has been characterised previously [98, 225, 250, 271, 272]. The beam broadening also varies slightly depending on the specific derivation used - but all share the dependence on thickness to the exponent of 3/2. Here, the equation that considers the FWHM will be used for consistency with equations 2.14 - 2.18:

$$D_B = 1.3 \times \left(\frac{\lambda^2}{2\pi a_0}\right) t^{3/2} \times \sqrt{\frac{N_A\ \rho_s}{3\pi\ A_s}} \times Z\gamma, \tag{3.3}$$

where a_0 is the Bohr radius, t is the thickness of the sample, N_A is the Avogadro constant, ρ_s is the density of the sample, A_s is the atomic weight of the sample, Z[1] is the effective mean atomic Z (proton number) of the sample, and γ is the Lorentz factor. For water, Z is approximately 4.7 for electrons in the keV energy range, and a value in this range has demonstrated good agreement between simulations and experimental data [98, 273–275].

[1]Capital Z is used throughout the text to distinguish between atomic Z of the sample and the lowercase z for z-axis measurements.

This leads to a modified version of the equation for the diameter of the probe in vacuum (equation 2.18), whereby the full probe diameter for a given α and thickness traversed can be calculated by quadrature addition of the FWHM diameters of beam broadening and the probe in vacuum:

$$D_{probe}(t) = \sqrt{{D_{probe}}^2 + {D_B}^2}. \tag{3.4}$$

Plotting equation 3.4 for several tilt angles and thicknesses of the sample gives Figures 3.4B-D.

The attainable resolution must be maximised when considering the convergence semiangle and the proposed method of 3-dimensional localisation. This analysis has specified a range over which acceptable resolution is likely to be achieved, given an infinite SNR. The plots in Figures 3.4B and D show that the diameter of the probe increases substantially depending on the position of the feature within the thickness of the sample. If the bottom surface of the lamella (Figure 3.4D) is considered as the maximum achievable resolution, encompassing the entire sample thickness at a given a tilt angle, the entire cryo-FIB-milled lamella can be resolved (typical thickness 200 nm) at a resolution of $\approx$ 1 nm. This is only if a maximum tilt angle of 45° is used.

Increasing the tilt angle to 60° will give better performance in terms of localisation in the z-axis. This is because a larger angular separation between tilted views provides greater parallax, creating a more robust geometric constraint for triangulation. However, the caveat is that the projected thickness is now double the untilted thickness, which gives substantially more beam-broadening. Consequently, it is unlikely that $\approx$ 1 nm features at the bottom surface of the sample will be resolved (Figure 3.4).

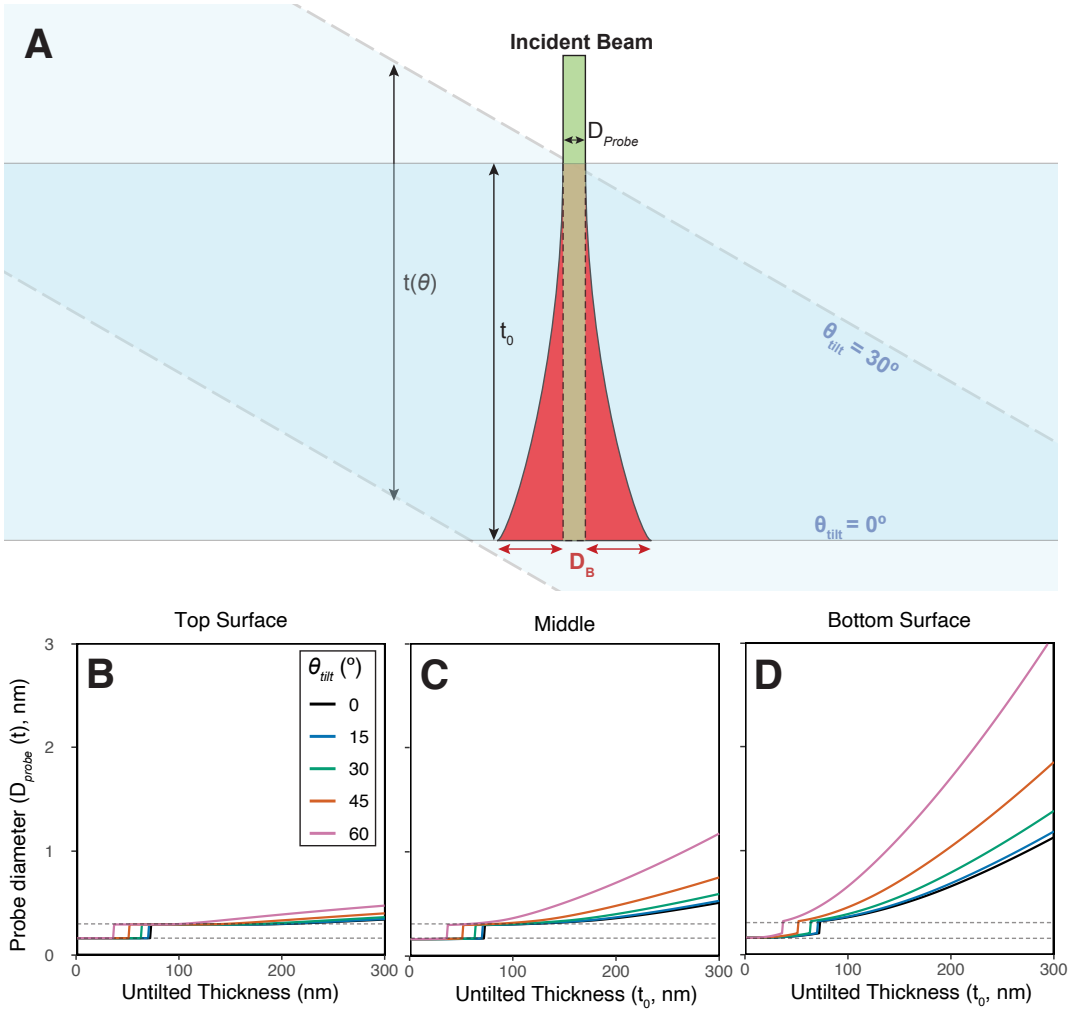


Figure 3.4: **Expected probe diameter for different combinations of sample thickness and tilt angle. A** Schematic view of the beam broadening shown for two sample tilt angles. The incident beam (with FWHM diameter D_{probe}) is broadened by D_B, shown in red. The thickness of the untilted sample (t_0) and tilted sample ($t(\theta_{tilt})$) have different projected thicknesses, and so will undergo different degrees of beam broadening. Using equations 3.2-3.4, Figures **B**,**C**, and **D** show this total probe diameter with the effects of beam broadening as a function of the untilted sample thickness and the tilt angle used, for the top, middle, and bottom of the sample, respectively. Dashed horizontal lines indicate the sharp change from probe diameter at α_{opt} and the geometric optimum α.

This section has analysed 3D localisation methodologies, and established that a limited-tilt acquisition strategy, such as the 'Sparse-tilt STEM triangulation' approach, represents the most viable balance between acquisition time, electron fluence, and the need for three-dimensional information. The geometric constraints

of this strategy show that the achievable spatial resolution is limited by a trade-off between the required depth of focus and the probe's convergence angle. Furthermore, it is known that beam broadening within the thick, tilted vitreous ice severely degrades this resolution. This places a practical limit of approximately 1 nm on the ability to resolve features at the exit surface of a typical 200 nm lamella (see discussion section 3.5).

Having established the practical limits of resolvability, the subsequent challenge is to determine the detectability of a nanoparticle tag. Achieving a 1 nm resolution is meaningless if the tag cannot first be reliably detected against the background noise. Therefore, the following section will develop a theoretical framework to analyse this detection capability by modelling the SNR as a function of collection angles, electron fluence, nanoparticle characteristics, and thickness of the vitreous ice background.

3.3 Theoretical Model for Nanoparticle Detection

3.3.1 Detectability - Scattering Cross Section

Where the resolvability and depth of focus are determined by the pre-specimen convergence semiangle (α, see section 2.6), the post-specimen collection angles (denoted by θ) are the ranges over which the STEM detectors are able to capture scattered electrons. The SNR is dependent on the inherent sample parameters, namely: the thickness and composition of the low-atomic Z background, the elemental composition and size of the nanoparticle, and the input fluence. For any given sample, maximising the SNR for detection is therefore a matter of optimising these collection angles.

The effective probability of an atom scattering an incident electron is represented by a scattering cross section, denoted by σ and expressed in units of area. These

cross sections are more usefully displayed by the differential scattering cross section, which describes the distribution of scattering into a solid angle (Ω, see Figure 3.5).

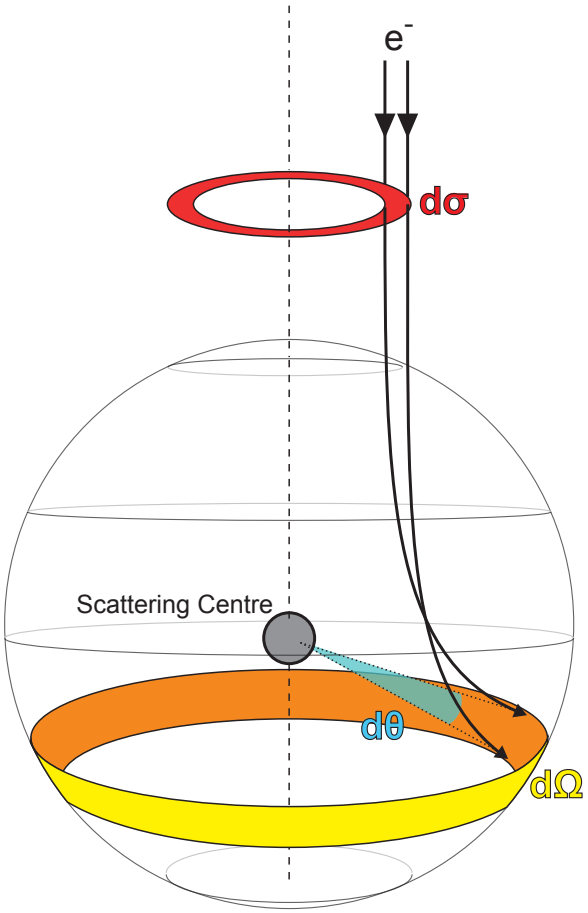


Figure 3.5: **Schematic representation of the differential scattering cross section**. The differential cross section ($d\sigma$) is depicted in red, illustrating electrons traversing through it and being scattered into the differential solid angle ($d\Omega$), indicated in yellow. The scattering centre, shown in grey, does not necessarily correspond to the nucleus of the atom but represents the point from which scattering appears to originate from, with a differential scattering angle ($d\theta$, blue). Note the electron passing through closer to the centre of the scattering cross section is deflected at a larger angle.

As covered in Section 2.2, scattering can be elastic or inelastic, depending on the energy of the scattered electron. Therefore, the equation for the differential scattering cross section of the atom is:

$$\frac{d\sigma_{total}}{d\Omega} = \frac{d\sigma_{el}}{d\Omega} + \frac{d\sigma_{inel}}{d\Omega} \ , \tag{3.5}$$

where σ_{el} is the elastic cross section, and σ_{inel} is the inelastic cross section. Several ways to calculate the differential scattering cross section exist, using tabulated data or different parametrisations [276–278]. The equations used here are from Reimer [231]. The differential cross section for elastic scattering is:

$$\frac{d\sigma_{el}}{d\Omega} = \frac{4Z^2R^4\gamma^2}{{a_0}^2} \times \frac{1}{[1+({\theta}/{{\theta_0}^2})]^2}, \tag{3.6}$$

where Z is the effective mean atomic Z number of the sample, a_0 is the Bohr radius of the hydrogen atom, and θ is the scattering angle. The Wentzel atomic radius, R, is the range of the electrostatic potential of the atom. This represents the approximate distance at which the positive nuclear charge is 'shielded' by the surrounding negative electron cloud:

$$R = a_0 Z^{-\frac{1}{3}}, \tag{3.7}$$

while θ_0 is a shielding angle that sets the angular boundary for large-angle scattering from the unshielded nucleus [231]:

$$\theta_0 = \frac{\lambda}{2\pi R}. \tag{3.8}$$

The differential cross section for inelastic scattering is:

$$\frac{d\sigma_{inel}}{d\Omega} = \frac{Z\lambda^4\gamma^2}{4\pi^4{a_0}^2} \times \frac{1-[(1+{\theta^2}/{{\theta_E}^2})/{\theta_0}^2]^{-2}}{(\theta^2+{\theta_E}^2)^2}, \tag{3.9}$$

here, θ_E is the characteristic angle for inelastic scattering:

$$\theta_E = \frac{\Delta E}{\gamma m_0 v^2} \tag{3.10}$$

where ΔE is a typical energy loss in an inelastic scattering process. Here 20 eV is used, similar to experimentally acquired data [183, 231].

Calculation of these differential scattering cross sections for gold (an example high-atomic Z element) and carbon and oxygen (example low-atomic Z elements) is shown in Figure 3.6A.

The total scattering cross section from a given atom (Total σ_{atom}) is therefore the total differential cross section (equation 3.5) integrated from 0 to $\pi/2$ rad (representing all forward scattering), multiplied by 2π and $\sin(\theta)$ to account for the change from a 3-dimensional solid angle to 2-dimensional angle:

$$\text{Total } \sigma_{atom} = \int_0^{\frac{\pi}{2}} \frac{d\sigma_{total}}{d\Omega} \, 2\pi \sin(\theta) \, \mathrm{d}\theta \tag{3.11}$$

Here, the focus is on calculating the scattering cross section (and consequently, the probability of an electron being scattered from a certain element) within a specified angular range, bounded by an inner and outer angle. Therefore, the differential cross sections can be integrated over this range θ_{inner} to θ_{outer}:

$$\sigma_{atom}(\theta) = \int_{\theta_{inner}}^{\theta_{outer}} \frac{d\sigma}{d\Omega} 2\pi \sin(\theta) \, \mathrm{d}\theta. \tag{3.12}$$

This model simplifies the calculation by treating the incident beam as a single ray and the detector acceptance angles as sharp cut-offs. In reality, the convergence angle of the probe is convolved with the scattering distribution, effectively blurring these detector edges. In the context of this analysis, this was considered negligible.

The plot of the scattering cross section can be found in Figure 3.6B.

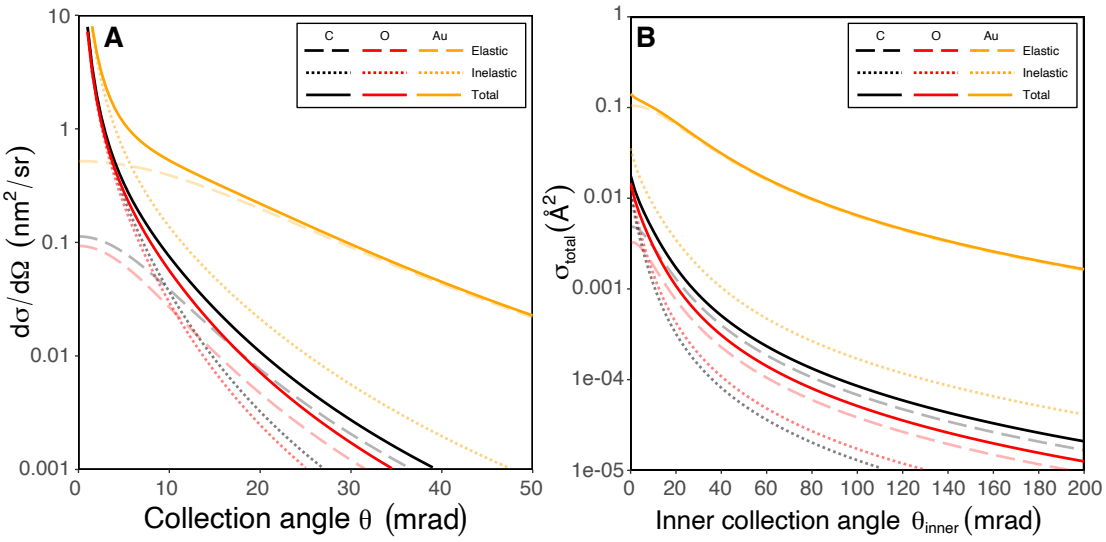


Figure 3.6: **Differential scattering cross sections and scattering cross sections plotted from equations 3.5 - 3.10 for selected elements**. **A** The elastic, inelastic, and total differential scattering cross sections plotted as a function of the collection angle, θ, for gold, carbon, and oxygen. **B** The elastic, inelastic, and total scattering cross sections plotted as a function of the integrated collection angle, from the inner collection angle θ_{inner} to $\pi/2$ rad (representing the total forward scattering), for gold, carbon, and oxygen.

It is clear from Figure 3.6 that inelastic scattering is localised almost entirely to low collection angles ($<$ 10 mrad), whereas elastic scattering dominates at higher collection angles, beyond 10 mrad. Practically, this results in a purer elastic scattering signal at higher collection angles in STEM-ADF, and a greater contribution from inelastically scattered electrons for lower-angle detection, such as STEM-BF or TEM. Tabulated data from the National Institute of Standards and Technology (NIST) for elastic scattering of electrons with carbon and gold were also plotted (Appendix Figure A.4), and showed reasonable agreement with equations 3.5 - 3.10.

3.3.2 Application to Thicker Samples

Thus far, the cross section equations used have been limited to individual atoms scattering incident electrons. To extend the applicability to larger systems, such as

vitreous ice samples, the number of atoms for a given thickness must be considered.

The mean free path (Λ) represents the characteristic distance after which the number of unscattered electrons in the beam has been reduced to $1/e$ (37%). The mean free path for elastic, inelastic, or total scattering can be calculated using [231]:

$$\Lambda = \frac{A}{\sigma_{atom}\ \rho N_A}, \tag{3.13}$$

where A is the molecular weight of the sample, N_A is the Avogadro constant, ρ is the density of the sample, and σ_{atom} is the relevant scattering cross section.

To briefly verify that this equation gives values similar to those experimentally determined for EFTEM or STEM-EELS, the inelastic mean free path of water/vitreous ice can be calculated. Typically, this falls in the range between 300 - 400 nm at 300 keV [279–282]. Using equation 3.13 gives an inelastic mean free path length (Λ_{inel}) in vitreous ice of 305 nm([2]). This is close to the most rigorous experimentally measured value of 314 nm [279]. Reducing the incident electron energy for equations 3.5 - 3.13 to 120 kV gives a Λ_{inel} of 230 and 195 nm, which align well to the experimentally determined values of 232 and 203 nm for the respective experimental setups of [281] and [282].

The inelastic mean free path is also related to the signal recorded and the thickness (t) of the sample [279]:

$$-\frac{t}{\Lambda} = \ln\left(\frac{N}{N_0}\right), \tag{3.14}$$

where t is the thickness of the sample, N_0 is the total intensity of the incident electrons, and N is the intensity of the scattered electrons. Therefore the number of electrons scattered to within a given angular range (between θ_{inner} and θ_{outer}) is [225]:

[2]Using a suitable outer collection angle of 10 mrad, to simulate an objective aperture typically employed in EFTEM imaging [26, 183, 279, 283, 284].

$$N = N_0(1 - e^{-t/\Lambda}) \tag{3.15}$$

where Λ is the mean free path of the sample (calculated using the scattering cross section σ for scattering integrated between θ_{inner} and θ_{outer} from equation 3.12).

For a heavy element (high Z) nanoparticle suspended in vitreous ice, the resulting SNR in the STEM image may be derived from a comparison between the number of electrons detected in the full thickness of vitreous ice, and the number detected in the thickness of vitreous ice with a nanoparticle of a certain thickness.

Where electron counting is taking place, noise levels follow Poissonian statistics. The SNR for electron counting in these calculations is defined as [285]:

$$\text{SNR} = \frac{|N_{Sig} - N_{Bck}|}{\sqrt{N_{Bck}}}, \tag{3.16}$$

where the background signal (N_{Bck}, the signal from the full thickness of vitreous ice) is [225]:

$$N_{Bck} = N_0 \left(1 - e^{-\left(\frac{t_i}{\Lambda_i}\right)}\right), \tag{3.17}$$

and the N_{Sig} is the signal from a nanoparticle (of diameter t_{np} and mean free path Λ_{np}) suspended in vitreous ice (of thickness t_i-t_{np} and mean free path Λ_i) given by [98, 225]:

$$N_{Sig} = N_0 \left(1 - e^{-\left(\frac{t_{np}}{\Lambda_{np}} + \frac{(t_i - t_{np})}{\Lambda_i}\right)}\right). \tag{3.18}$$

$\sqrt{N_{Bck}}$ is also the approximate 'shot noise' which is inherent when counting a finite number of electrons[3]. The Detective Quantum Efficiency (which describes how

[3]Note that this is not strictly the SNR of the sample, but the signal of the nanoparticle and the ice to the signal of the ice matrix alone.

efficiently counted electrons are represented as signal) is assumed to be unity, as is possible with modern monolithic STEM detectors. As a result, this measure is not considered for this model [286].

The theoretical model calculates the signal based on the maximum thickness of the nanoparticle, equivalent to its full diameter, t_{np}. However, an experimental measurement based on the mean intensity averages the signal over the nanoparticle's entire circular projection, where the thickness of the nanoparticle is variable. To account for this difference between the theoretical and experimental approaches, a concept of mean projected thickness is used (Figure 3.7).

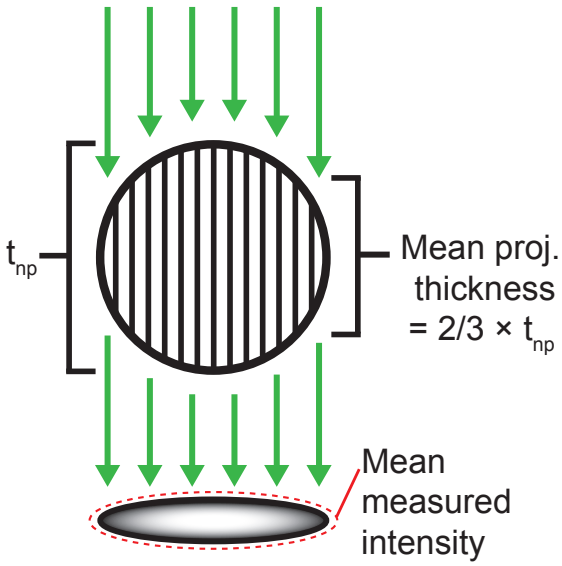


Figure 3.7: **Schematic representation of the mean projected thickness**. Intensity in the images is measured across the entire nanoparticle diameter. Therefore the mean projected thickness is used to measure one SNR value for each nanoparticle.

For a perfect sphere, the mean thickness is its total volume divided by its projected circular area. With a nanoparticle diameter of t_{np} and radius r, this is derived as:

$$\text{Mean thickness} = \frac{\text{Sphere Volume}}{\text{Projected Area}} = \frac{4/3\pi r^3}{\pi r^2} = \frac{4}{3}r$$

Expressed in terms of the nanoparticle diameter ($2r = t_{np}$), this simplifies to:

$$\text{Mean thickness} = \frac{2}{3} \times t_{np}$$

Therefore, to accurately compare the model's prediction with an experimental SNR derived from the mean particle intensity, the nanoparticle thickness in the theoretical calculation is replaced by its mean thickness ($2/3 \times t_{np}$). This leads to the modified equation used for the comparison:

$$N_{Sig} = N_0 \left(1 - e^{-\left(\frac{(2/3\ t_{np})}{\Lambda_{np}} + \frac{t_i - (2/3\ t_{np})}{\Lambda_i}\right)}\right). \tag{3.19}$$

Extending the mean-free path model to single atoms requires a special consideration for the density term, which is fundamentally a bulk property of a material.

To maintain consistency within the model's analytical approach, an effective density was calculated for each element. This was derived from the atomic mass and the atomic volume, assuming a perfect sphere with a defined atomic radius (144 pm for gold).

It is important to note that this effective density is distinct from the bulk crystal density, as it does not account for the interstitial spacing inherent in a crystal lattice. However, it provides a self-consistent parameter that allows the scattering model to be applied to the single-atom limit. The values for gold are not substantially different from that of bulk crystalline gold ($\rho = 2.5 \times 10^{-20}$ and 1.9×10^{-20} g nm^{-3} for a gold atom and bulk crystalline gold, respectively). The thickness (t_i) of heavy atoms used in the model is their diameter as measured in STEM-HAADF images of approximately 0.1 nm.

3.3.3 Model Results

To define the minimal size for a high-Z tag in a variety of experimental conditions, equation 3.16 was plotted for several representative diameters of AuNPs and thicknesses of the vitreous ice, as a function of the inner collection angle, gives Figure 3.8. The AuNPs are assumed to be perfect crystalline gold, with a density (ρ) of 19.32 g cm^{-3}, molecular weight (A) of 197 g mol^{-1}, and with an atomic Z of 79, embedded in vitreous ice of varying thickness. The number of incident electrons (N_0) used here is 100, which corresponds to a typical low-fluence cryo-STEM experimental setup of 3 pA and 5 µs dwell time per pixel.

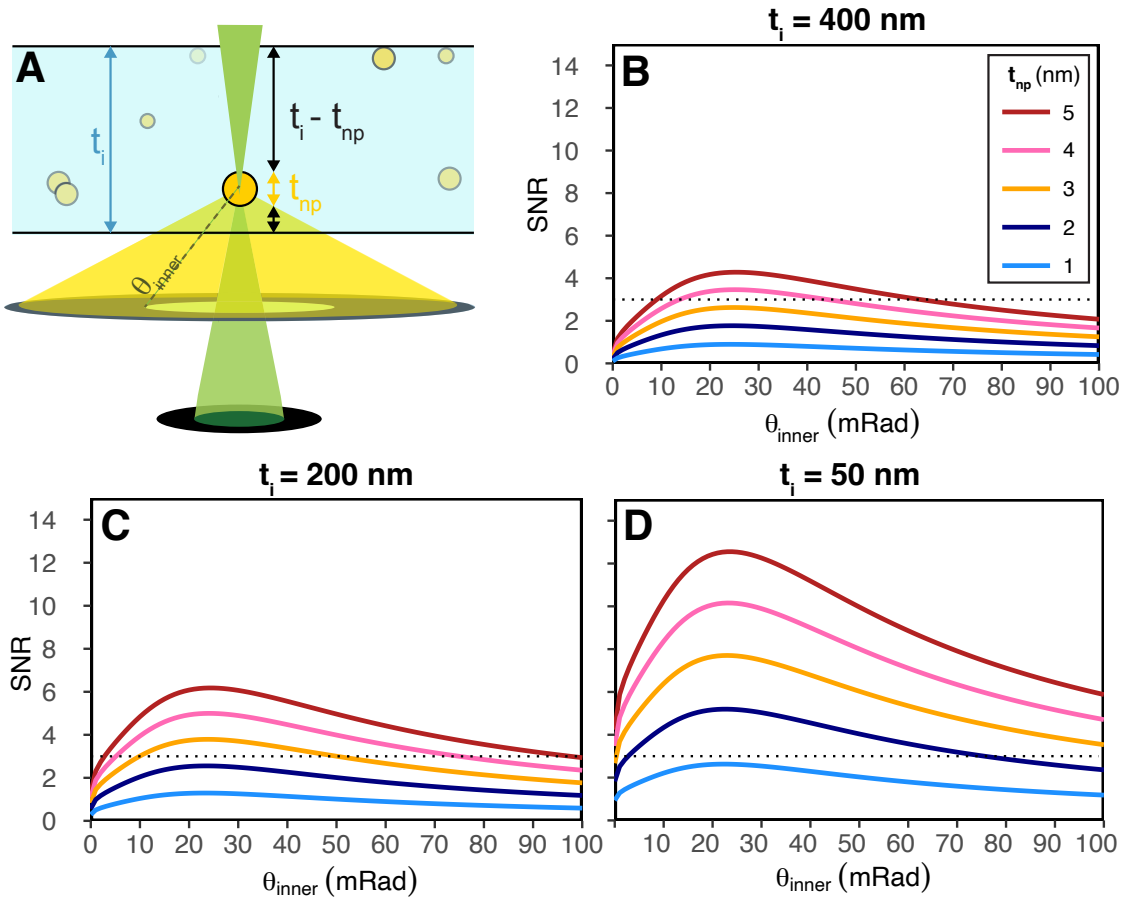


Figure 3.8: **Finding the optimal collection angle for the ADF detector**. **A** A schematic of the simple model used to find the signal and background. t_i represents the thickness of the vitreous ice while t_{np} is the diameter of the nanoparticle. The scattered intensity is then integrated between θ_{inner} to $\pi/2$ rad, and the resultant SNR may be calculated. These calculated curves are shown in **B** -**D** for t_i = 50, 200, and 400 nm, respectively, with lines plotted for representative crystalline AuNPs with diameters (t_{np}) between 1 and 5 nm. The incident number of electrons (N_0) is 100 in each case. The dashed horizontal line indicates the rose criterion, at an SNR of 3.

As expected, in thinner layers of vitreous ice, the SNR increases across all particle sizes. In each case, this is a direct result of the AuNP scattering more electrons compared to the vitreous ice.

As the inner collection angle increases, the SNR also increases to a maximum value at approximately 20-25 mrad, before decreasing again at higher inner collection angles (>30 mrad). This peak represents an optimal balance between maximising contrast

and minimising noise. Although using a higher collection angle improves the contrast between gold and ice, it drastically reduces the total number of electrons that reach the detector. Beyond 30 mrad, the inherent shot noise – the statistical fluctuation in the electron count – becomes comparable to, or even larger than, the absolute signal difference between the gold and the ice. Consequently, so few electrons are collected that the signal difference is statistically insignificant, in turn causing the SNR to fall.

By analysing the peak of each SNR curve, the required number of incident electrons (N_0) to detect a nanoparticle of a given size within a certain ice thickness can be determined. These results are presented in terms of total incident electrons rather than electron fluence (electrons per unit area). This choice was made because fluence is dependent on specific experimental conditions, such as the electron probe size or pixel area. Presenting the data using N_0 provides a more fundamental value from the model, which, by dividing by the area relevant to a specific experimental setup, can be readily converted to a practical fluence (see Equations 2.18-3.4, and discussion section 3.5).

Several commercially produced small diameter AuNPs are available - for example, 2.2, 1.8, 1.4, and 0.8 nm. The 2.2, 1.8, and 1.4 nm diameter nanoparticles are each assumed to be perfect crystalline gold. The specifications of the 0.8 nm nanoparticle product state that it is composed of 11 gold atoms in a 0.82 nm diameter spherical arrangement [56, 287]. This results in a different calculated density of around 64% from that of crystalline gold. This is in line with another recently published estimate which concerns the packing of heavy metal atoms in a cluster [288].

Plotting the peak SNR for each of these nanoparticles and single atoms – for a variety of incident electrons and ice thicknesses – gives Figure 3.9.

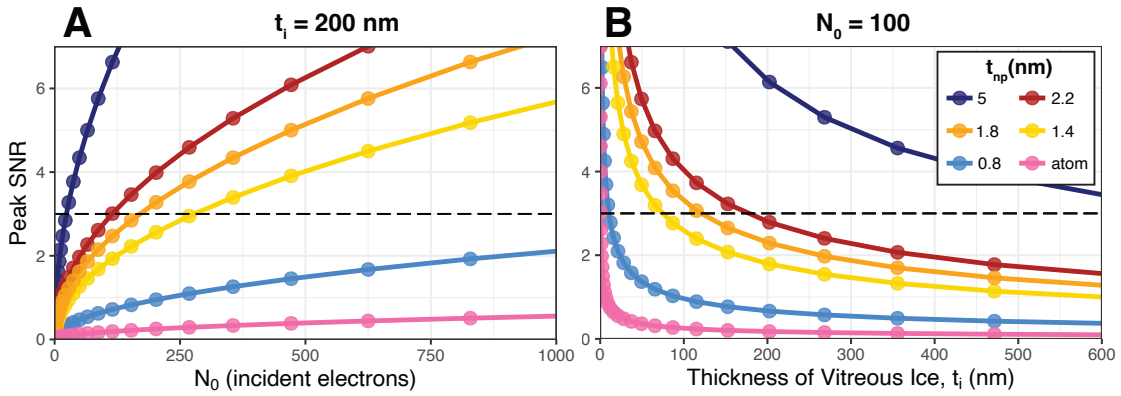


Figure 3.9: **Peak signal to noise ratio calculated for various nanoparticle sizes and experimental conditions. A** Peak SNR for a fixed thickness of vitreous ice ($t_i = 200$ nm) with increasing number of incident electrons (N_0). **B** Peak SNR for a fixed number of incident electrons ($N_0 = 100$) with increasing thickness of vitreous ice (t_i). The dashed horizontal line indicates the Rose criterion, at an SNR of 3. Further examples across wider ranges of t_i and N_0 may be seen in Appendix Figures A.7 and A.8, respectively.

3.3.3.1 Elemental Composition

Finally, this section analyses the elemental composition of the heavy-atom tag itself. The ideal candidate must possess: 1) a high atomic number (Z) for strong electron scattering, 2) high density to maximise number of scattering centres for a given particle size, and 3) established low cytotoxicity to avoid perturbing the native cellular environment.

Gold has long been the conventional choice for labelling in electron microscopy, a practice which has been established for decades [289]. Its suitability stems from a combination of excellent electron scattering properties due to its high atomic number (Z=79), atomic weight (A = 197 g mol^{-1}), density (ρ = 19.3 g cm^{-3}), and its chemical inertness, which also makes it highly biocompatible with low cytotoxicity (see section 1.1.3.2).

However, several other dense, bio-compatible heavy elements are viable alternatives for nanoparticle labels. Platinum (Pt: Z = 78, A = 195 g mol^{-1}, ρ = 21.5 g

cm^{-3}), Iridium (Ir: Z = 77, A = 192 g mol^{-1}, ρ = 22.6 g cm^{-3}) and Bismuth (Bi: Z=83, A = 209 g mol^{-1}, ρ = 9.8 g cm^{-3}) share many of the beneficial attributes of gold. Uranium (U: Z = 92, A = 195 g mol^{-1}) may also be a strong candidate for nanoparticle synthesis, for it has a density (ρ = 19.1 g cm^{-3}) comparable to that of gold. The cytotoxicity of uranium is unlikely to cause issue at the low concentrations needed for nanoparticle delivery [290].

Whilst Osmium (Os: Z = 76) is the densest naturally-occurring element [291], its high toxicity makes it unsuitable for the purpose of biological nanoparticle labelling *in-situ* [292].

The selection criteria for an element to be used as a potential tag shifts when considering single-atom tags. As mentioned earlier, an individual atom's bulk density is no longer a relevant physical parameter. Instead, the signal is primarily governed by the atom's scattering cross section, which increases significantly with atomic number. This makes elements with a higher atomic Z than gold particularly desirable. For example, Bismuth (Bi: Z=83) and Uranium (U: Z=92, the highest-Z naturally-occurring element), are both compelling candidates for potential single-atom detection.

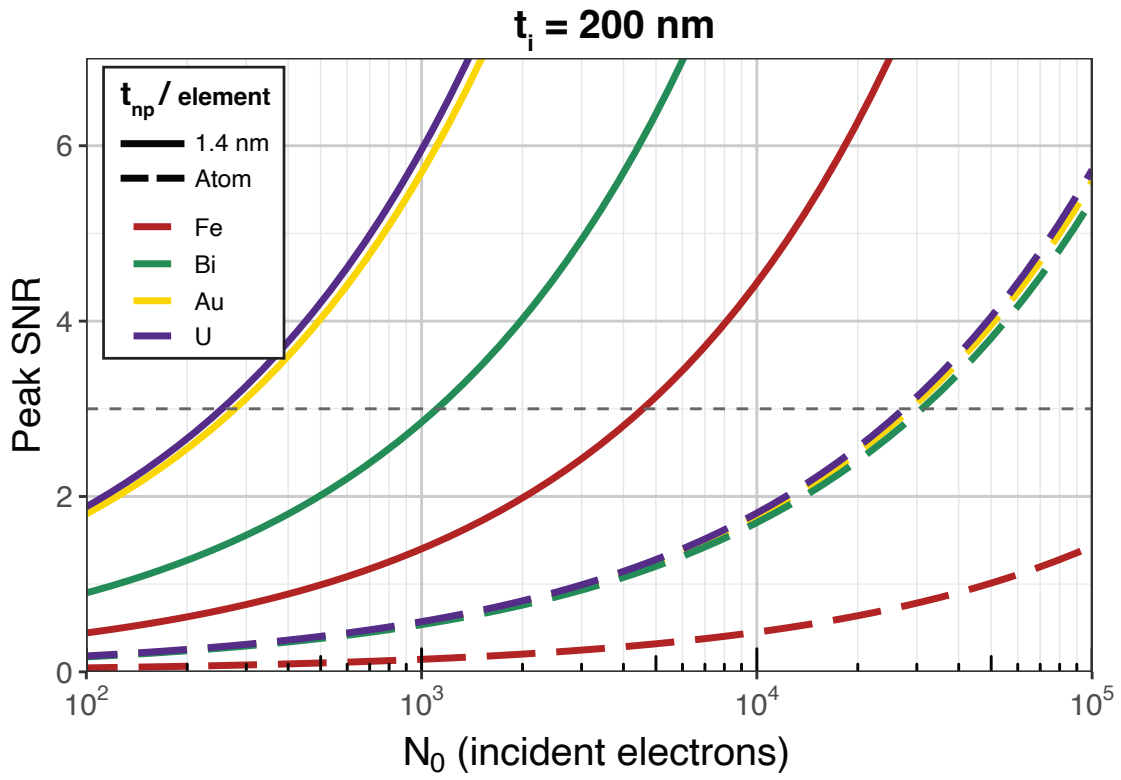


Figure 3.10: **Peak SNR calculated for iron, bismuth, gold, and uranium tags.** Peak SNR for a fixed thickness of vitreous ice (t_i = 200 nm) plotted against increasing number of incident electrons (N_0). The iron, bismuth, gold, and uranium are each displayed as both 1.4 nm diameter nanoparticles (solid lines) and as single atoms (dashed lines). The dashed horizontal line indicates the Rose criterion, at an SNR of 3.

The low bulk density of elemental bismuth (ρ = 9.8 g cm^{-3}) results in its 1.4 nm nanoparticles having a significantly lower peak of SNR than AuNPs for a given electron fluence. However, this disparity is no longer true for single atoms. As a single bismuth atom (Z = 83) is very similar to a gold atom (Z = 79) or a uranium atom (Z = 92) in both atomic number and size, the calculated peak SNRs of these atoms are nearly indistinguishable from each other. The low density and elemental Z of iron (Fe: Z=26, A = 55.8 g mol^{-1}, ρ = 7.9 g cm^{-3}) makes it a poor choice for use as a small nanoparticle or a single-atom tag, compared to heavier elements, despite its use in previous cryo-ET and -STEM works [62, 70, 107].

Based on these principles, uranium is predicted to be the most effective choice

for nanoparticle or single-atom tagging of all the elements, as shown in Figure 3.10. In a 200 nm thick layer of vitreous ice, a single uranium atom is predicted to require approximately 10,000 incident electrons to reach a peak SNR of 2, rendering it only just visible [293].

3.4 Experimental Application of the Model

To validate the predictions from this model, the SNR was measured from experimental STEM images containing 0.8 and 5 nm AuNPs. While the theoretical SNR is calculated using the presence or absence of electrons striking the ADF detector (using equation 3.16), a practical measurement from an image requires a different, though analogous, approach.

Experimentally, the SNR is determined using the mean intensity of the feature of interest ($\bar{I}_{Sig}$) and the surrounding background ($\bar{I}_{Bck}$), and the standard deviation of the intensity of background pixels ($\sigma(I_{Bck})$) [294]:

$$\mathrm{SNR}_i = \frac{|\bar{I}_{Sig} - \bar{I}_{Bck}|}{\sigma(I_{Bck})}. \tag{3.20}$$

This experimental definition is directly comparable to the theoretical SNR in equation 3.16 [294]. The numerator, which represents the signal contrast, is the experimental equivalent of the difference in electron counts, because the recorded pixel intensity is proportional to the number of detected electrons.

The primary difference lies in the denominator, which represents the noise. The theoretical model assumes that the noise is purely the ideal shot noise ($\sqrt{N_{Bck}}$) arising from Poissonian statistics [293]. In contrast, the measured background standard deviation $\sigma(I_{Bck})$ is a metric which accounts for the total noise in the acquired image [294]. This total noise encompasses not only the fundamental shot noise but also additional contributions from the experimental setup, such

as detector gain and electronic read-out noise. Therefore, equation 3.20 provides a direct measure of image quality, quantifying the signal against all competing noise sources that are present in a real-world experiment. As such 3.20 will be used for comparison to the modelled SNRs.

3.4.1 Experimental Methods

To validate the theoretical model, the SNR was measured directly from experimental datasets. The images were acquired with the Titan Krios G4 (non-C_S-corrected and the JEOL ARM300F2 (C_S-corrected); the latter dataset will be used in the analysis presented in Chapter 4.

3.4.1.1 Sample Preparation

The sample preparation was consistent for both instruments. Holey carbon R2/2 grids were prepared with AuNPs suspended in pure water. For the Titan Krios G4 (Thermo Fisher Scientific) sample, a colloidal mixture of nanoparticles with nominal diameters of 0.8 and 5 nm (Nanoprobes) was used. Only 5 nm nanoparticles (Nanopartz) were used for the ARM300F2 (JEOL). The grids were vitrified by plunge freezing into liquid ethane using a Vitrobot Mark IV (Thermo Fisher Scientific), with a 2.5 second blot time at a blot force of +10.

3.4.1.2 Electron Microscopy

STEM-ADF images were acquired on the Titan Krios G4 at 300 kV with a probe convergence semiangle of 7.4 mrad (α_{opt}). The sample was kept at constant 80 K for cryogenic imaging. The probe current was set to 3 pA with a pixel dwell time of 10 µs, which resulted in 188 incident electrons per pixel. The pixel size was 0.9 Å, giving a total electron fluence of 232 $e^{-}Å^{-2}$ measured per pixel (or 38.2 $e^{-}Å^{-2}$ measured per probe area for each position). The annular dark-field detector was configured with

a nominal camera length of 275 mm, with a calibrated inner collection angle of 37.8 ± 0.8 mrad, and an outer collection angle of 217.6 ± 8.8 mrad (see section A.2.1).

Additionally, STEM images on the ARM300F2 were acquired at 80 K and 300 kV, with a probe convergence semi-angle of 16 mrad. The probe current was set to 15.5 ± 0.78 pA with a pixel dwell time of 5 µs. This resulted in an average of 484 incident electrons per pixel. The pixel size was 3.4 Å, and gave a total electron fluence of 42 $e^{-}Å^{-2}$. The HAADF detector was configured with a calibrated inner collection angle of 89.3 ± 1.1 mrad and an outer collection angle of 343 ± 10 mrad (limited by the differential pumping aperture). This microscope setup was used to acquire all data in Chapter 4, which outlines a more detailed description of the electron microscopy settings.

A prerequisite for this analysis is an accurate measurement of the local ice thickness. This was achieved (after nanoparticle imaging) using a tilt-pair hole, similar to the methods described previously [197, 281].

First, the microscope stage was tilted to -30°, and during a one minute exposure, the stationary electron beam created a hole in the ice. Following this, the beam was blanked, the stage tilted to +30°, and the area imaged. The thickness of the ice was determined from the projected separation of the entrance and exit surfaces of the hole.

A schematic of this process, with measurements for the Titan Krios dataset, is shown in Figure 3.11. Two thickness measurements can be made from each image: from the initial decrease in intensity to the second 'sharp' edge of the hole (t_{i1}), and the first 'sharp' edge of the hole to the return to full intensity (t_{i2}). A similar method was implemented for the ARM300F2 dataset, as detailed in section 4.2.8.

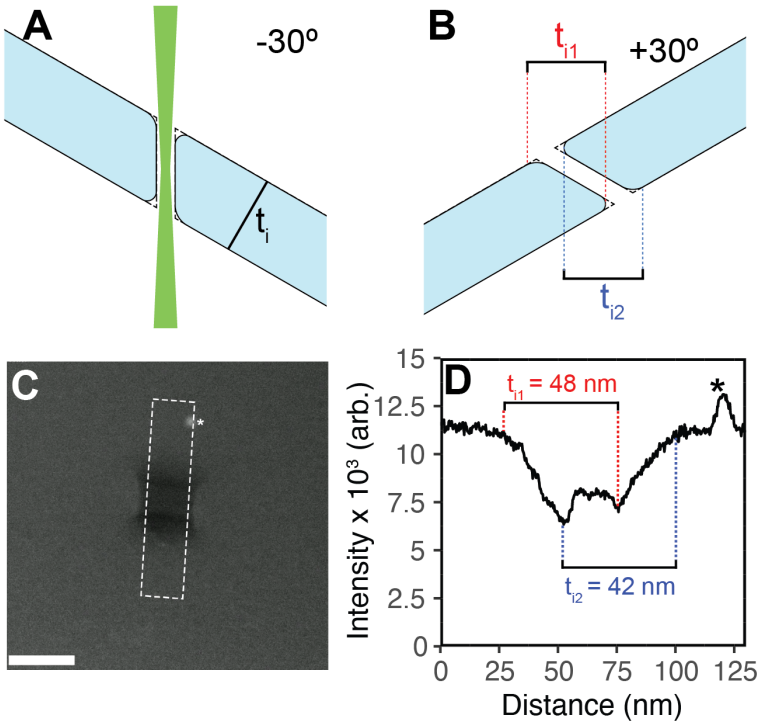


Figure 3.11: **Measuring the vitreous ice thickness for plunge frozen sample.** **A** Hole created at -30° using the stationary electron beam, with the thickness of the ice (labelled t_i). **B** Hole imaged at +30°. Two measurements of the thickness of the ice (t_{i1} and t_{i2}) are made. **C** Imaged hole at +30°, with a dashed line rectangle indicating the line profile taken (**D**), and asterisk showing the position of the AuNP around which the experiment was centred (see Figures 3.12A and B). Scale bar 50 nm.

3.4.1.3 Data Processing

To accurately measure the diameters of the AuNPs, a Gaussian blur filter (σ = 1.5 px) was applied to smooth the image, at a threshold which covered all nanoparticles present in each image.

Assuming the nanoparticle's projection is perfectly circular, the area (A) of each nanoparticle was then converted to a diameter (d), using

$$d = 2\sqrt{\frac{A}{\pi}}. \tag{3.21}$$

The diameter and intensity measurements of the nanoparticles can be extracted (from the non-Gaussian-filtered image). The former is used as t_{np} in the subsequent SNR

calculation (Equation 3.16), and the latter is used as $\bar{I}_{Sig}$ in the calculation SNR_i (Equation 3.20). $\bar{I}_{Bck}$ was taken from a region free from all nanoparticles. Assuming the nanoparticle density remains constant, and the nanoparticle diameter in the xy plane is the same as the diameter of the nanoparticle in the z-axis (projected thickness), this allows for calculation of the SNR expected for this range of nanoparticle diameters (± 1 standard deviation) using the model presented (Figure 3.12).

3.4.2 Experimental Results

The mean measured diameter of the 0.8 nm-diameter AuNPs is 0.8 ± 0.1 nm (Figure 3.12A and B). In vitreous ice (at a thickness of 45 nm), and at the inner collection angle of 37.8 mrad, this translates to an expected SNR of 1.70 ± 0.22, according to the model presented. The experimentally obtained SNR_i is 1.46 ± 0.13, plotted in Figure 3.12C.

The sizes of the (nominal) 5 nm-diameter AuNPs (acquired from two different sellers) varied. The 5 nm AuNP dataset, taken on the Titan Krios (Figures 3.12D-F), have a mean diameter of 5.0 ± 1.0 nm. Using these values for t_{np} in the model gives expected SNRs of 16.2 ± 3.2. The experimentally measured values for the SNR in Figures (Figures 3.12D and E) is 13.2 ± 0.7.

The nominal 5 nm-diameter nanoparticles from the dataset on the ARM300F2 have a mean diameter of 4.0 ± 0.8 nm. The model predicts their SNR to be 3.3 ± 0.7, while the experimentally measured value is 2.8 ± 0.4 (Figures 3.12G-I).

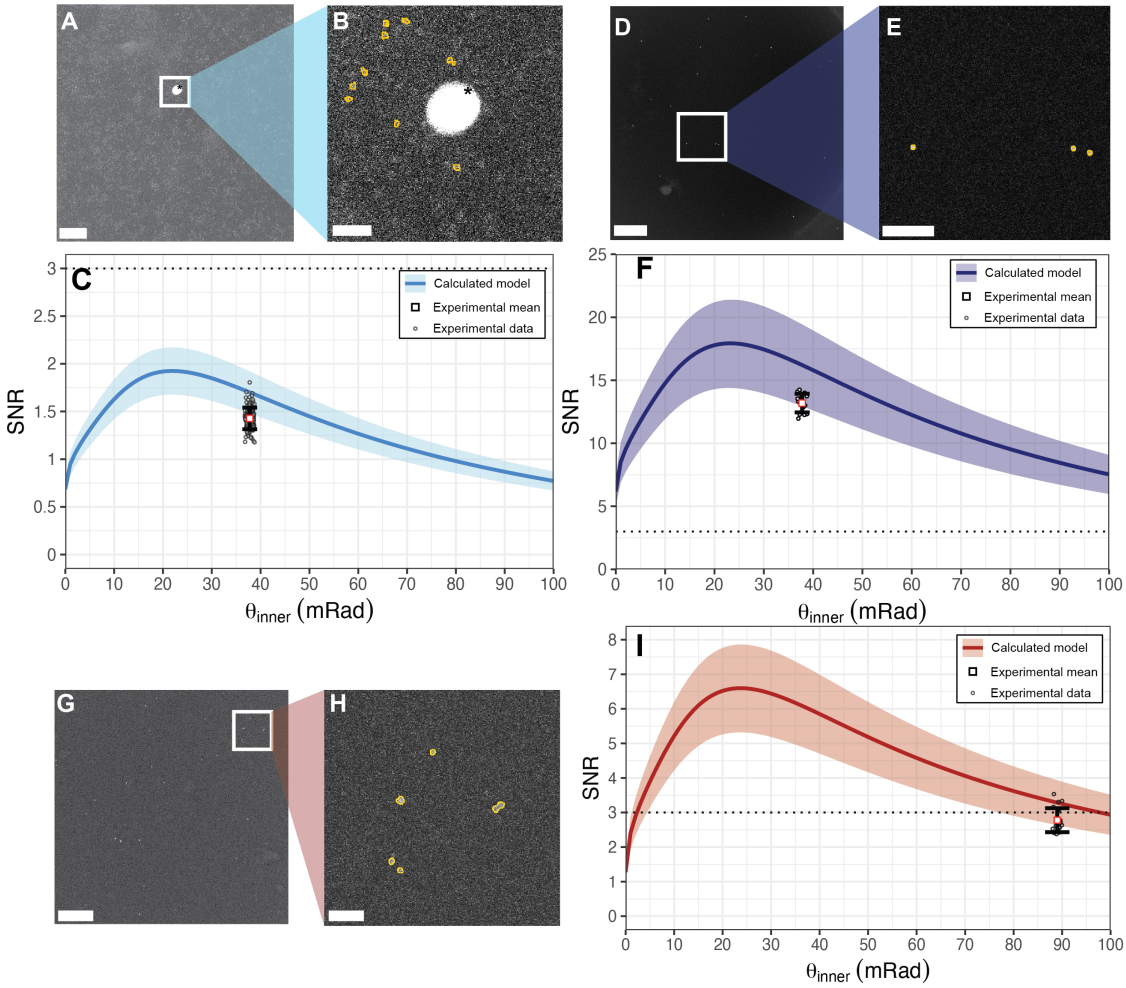


Figure 3.12: **Experimentally determined SNR results. A-C** for the Titan Krios dataset, with 0.8 nm AuNPs for a small inner collection angle (37.8 mrad) in thin ice (45 nm) using a low number of electrons per pixel ($N_0 = 188$). **A** An overview image of one 6.3 nm AuNP, and many (approximately 1500) 0.8 nm AuNPs (scale bar 10 nm). **B** A magnified region of A, showing example highlighted regions of the 0.8 nm AuNPs in yellow (scale bar 5 nm). **C** Graph of Inner collection angle against SNR. The predicted model is shown as a blue solid line, with the shaded area representing the model as applied to nanoparticles of the mean diameter ± 1 SD. Data points for individual nanoparticles can be seen, plotted with the overall mean and error bars. The pattern of **A-C** is repeated for 5 nm AuNPs, on the same sample and hole at a lower magnification in **D-F**, and in **G-I** for the ARM300F2 5 nm AuNP dataset at a greater inner collection angle and thicker sample (ICA = 89 mrad, thickness = 230 nm). (Scale bars: **D** = 200 nm, **E** = 50 nm, **G** = 100 nm, **H** = 25 nm).

3.5 Discussion

3.5.1 Approach for 3D-localisation and Geometry of the STEM

Initial analysis concluded that a sparse-tilt triangulation approach is likely to be the most feasible method for 3D nanoparticle localisation within the high-throughput workflow that is needed to align with cryo-ET. By requiring only a few projections, this strategy minimises the prohibitively long acquisition times associated with full STEM tomography and depth sectioning, making it theoretically compatible with the timescale of a standard EFTEM tilt series. However, the practical implementation of any tilt-based cryo-STEM method still faces significant challenges, especially on radiation-sensitive and amorphous sample.

A large depth of focus (and therefore a small convergence semiangle) is required to ensure the entire projected thickness of the lamella remains in focus. This directly conflicts with the goal of achieving the highest possible lateral resolution, which necessitates a large convergence semiangle.

Autofocus in STEM often biases toward the top surface of the lamella, where the probe is narrowest and resolution is best. Typically, a 'stepped-image' method is used, capturing images at varying defocus heights along the z-axis to determine the optimal focus. This approach reduces resolution for features at the lamella's bottom, as they lie outside the focal plane and are imaged by a broadened during its passage through the sample. Possible strategies to alleviate this may include using a sacrificial area to one side of the region of interest. This would improve autofocus routines by using the point of 'blow-up' of the ronchigram. This method may yield better results in terms of ensuring that adequate focus is reached before each image is taken.

Despite these challenges, the sparse-tilt approach theoretically remains the most viable strategy for 3D nanoparticle localisation within a high-throughput workflow. To overcome some of the focusing limitations in a practical setting, the optimal implementation could incorporate limited depth-sectioning.

At each of the discrete tilt angles (for example, -45°, 0°, +45°), a limited depth-sectioning series of 4-5 scans could be acquired (each encompassing ∼50 nm over the z-axis, using dynamic focusing). This would ensure that the entire thickness of the lamella is sampled with a shallow depth of focus, maximising lateral resolution for a non-C_S-corrected microscope, and guaranteeing that all nanoparticles are imaged in focus, regardless of their z-axis position. This strategy, while slightly increasing acquisition time, theoretically represents a solution for achieving reliable, high-resolution 3D localisation using STEM for biological applications.

3.5.2 Beam Broadening Limits the Achievable STEM Resolution in Lamellae

The analysis of beam broadening reveals the practical limits of resolution in a thick, tilted lamella, moving beyond the ideal in-vacuum probe size.

For a typical 200 nm lamella, the model (Figure 3.4) predicts that the probe diameter at the exit surface is approximately 1 nm at a 45° tilt, and 0.8 nm at a 30° tilt. This has a direct consequence for the detection of the smallest tags. While a 0.8 nm AuNP could be resolved at the entrance surface of the ice, if it were located near the exit surface, it would effectively be blurred beyond recognition. This phenomenon is a well-documented characteristic of STEM [269].

This establishes a zone in the z-axis over which the tagging strategy within a standard lamella is likely viable. The probe size in the middle of the ice (∼0.3 nm) is sufficient. However the goal of tagging a protein with a 0.8 nm nanoparticle is only practically feasible for, at best, the top half of a typical 200 nm sample volume.

Tags located in the bottom half are likely to be unresolved due to the resolution limit imposed by beam broadening. This is also supported by the images taken of 0.8 nm AuNPs in 45 nm of ice (Figures 3.12A and B); The nanoparticles are barely visible in this thickness of ice, let alone in the first top half of a 200 nm thick sample.

While the intuitive solution would be simply to prepare thinner lamellae, this has been shown to be detrimental to the quality of the final STA reconstruction, due to FIB-induced damage [17, 295]. Therefore, a compromise must be made; a lamella thickness that is optimal for the biological structure of interest may also render the smallest tags undetectable in the lower half of the volume of ice under typical cryo-STEM scanning conditions (without manually flipping the grid by 180°).

3.5.3 Theoretical Model and the Detectability of Nanoparticles in Vitreous Ice

It is important to acknowledge the limitations of the theoretical model presented here.

Key assumptions, such as the single-scattering approximation and the application of the mean free path, begin to break down in the regimes of much thicker specimens or isolated atomic scatterers. Consequently, the absolute SNR values predicted by the model should be considered semi-quantitative, rather than perfectly accurate, allowing for relative comparison between all the different model parameters.

An important approximation in the model for single atoms is the use of a pseudo-density for calculating the mean free path. While this simplification may introduce a systematic offset in the absolute calculated values, it provides a method for comparative analysis between different atomic species. The validity of this approach is demonstrated by applying the model to the experimental parameters reported by Sheader *et al.* [288]. For an incident number of electrons (N_0) of 40,000, and a sample thickness of 70-100 nm, the model predicts an SNR in the range of 2.5–3.1.

This result is in approximate agreement with the experimental images presented in their work, lending confidence to the model's predictive power for relative SNR when applied to single atoms in thicker vitreous ice.

The theoretical model also provides insights into the practical limits of nanoparticle detection. The analysis of peak SNR as a function of incident number of electrons reveals that AuNPs with diameters of > 1.4 nm are likely to be good candidates for tagging and STEM detection. Within a 200 nm thick vitreous ice lamella, 1.4 nm AuNPs are predicted to reach the Rose criterion for unambiguous detection with less than ~ 250 incident electrons, or to reach an SNR of 2 using ~ 100 electrons. This suggests that for larger tags, detection is not a significant challenge.

The 0.8 nm nanoparticle, in contrast, requires approximately 2000 incident electrons to achieve the same SNR under identical conditions (see Appendix figure A.7 for full plots).

One aspect not accounted for by the SNR-based output of the model is the sampling of the nanoparticle. In this context, sampling is the number of probe positions which a typical diameter of a nanoparticle takes up in the final image. For example, if a nanoparticle is magnified upon to the point where it is 20 pixels across in the image at a SNR of 2, this is much more likely to be recognisable as a particle than a nanoparticle at the same SNR which is only 10 pixels across (see Figure A.6 for a comparison).

Using this idea, it is also important to consider a realistic fluence calculation that is based on the sampling needed. For example, according to the model for single-atom scattering in a thick layer (Figure 3.10) to achieve a SNR of ~ 3, a gold atom would require 30,000 incident electrons. However, to resolve the atom within the image, the atom should be sampled to at least 5 pixels across in the final image.

Calculating the fluence using the diameter of the gold atom in this way gives a required fluence on the order of $\sim 10^5$-10^6 $e^-Å^{-2}$. This is on the same order

of magnitude as, and in line with, experimentally-determined fluence for atomic STEM localisation in recent work which used aberration-corrected STEM to resolve platinum atoms in 70-100 nm sections of cryofixated tissue [288]. This also renders single-atom localisation in individual STEM images within a native cryo-ET context likely impossible, especially if multiple scans at different tilt angles are required to cover the entire volume. While detection may be theoretically possible, the impact on vitreous ice is likely to be catastrophic, with mass loss and beam-induced movement of the nanoparticles, as described in [288].

The experimental validation showed that the model appears to agree relatively well with the experimental data on both large (5 nm) and small (0.8 nm) AuNPs in thick and thin vitreous ice. However, the model appears to systematically overestimate the SNR of the tag in question by a factor of approximately 1.2 (1.18 for 0.8 nm AuNPs, and 1.21 for both 5 nm AuNP datasets). The origin of this overestimation could be due to a number of factors.

First, the assumption used in the model that the noise is only caused by the shot noise in the image is unlikely to be accurate, as other sources of noise will also be present. The approximation of the scattering cross sections by equations 3.5-3.12 are not perfect, and many different parametrisations exist (although the equations used in this Chapter appear to give similar results to other published work, see Figure A.5 from [103]).

Additionally, the model depends on assumed values for the effective Z of water. This quantity is known to change at different acceleration voltages [98, 273] and is often modified to give a good fit to the experimental data, with 4.7 being used here throughout. Small errors in these input constants will propagate through the calculation and affect the final predicted SNR. In order to give a better agreement to the limited experimentally acquired data here, the effective Z of water should be raised to around 5.3. The cellular matrix is not water; the average cellular

density and effective atomic Z will likely be higher, making these calculations an overestimation of the achievable signal for *in-situ* work.

3.5.4 Conclusion

This Chapter has established that, while a sparse-tilt STEM strategy is likely the most practical approach for 3D tag localisation in STEM, the success of this approach is fundamentally constrained by the physics of electron scattering. The combined challenges of beam broadening and low SNR create a compromise; a tag must be large enough to be resolved and detected with a tolerable fluence, but small enough to avoid perturbing the target.

The primary conclusion is that for the smallest, most desirable tags, the electron fluence required for confident detection is incompatible with the preservation of typical biological specimens under near-native cryogenic conditions. This identifies the electron fluence budget as the central, limiting factor for the entire workflow. Therefore, the next logical step, and the focus of Chapter 4, is to directly investigate the consequences and mitigation of this high fluence in vitreous ice.

4

Cryo-STEM Radiation Damage Mitigation Using An Interleaved Scanning Pattern

Contents

4.1 Introduction 130
4.2 Materials and Methods 131
4.2.1 Sample Preparation 131
4.2.2 Raster and Interleaved Pattern Creation 132
4.2.3 Trench Patterns 134
4.2.4 STEM Microscopy Hardware and Alignment 136
4.2.5 Scan Generator 138
4.2.6 Sample Screening 138
4.2.7 Experimental Data Collection 139
4.2.8 Thickness Measurements 141
4.2.9 Data Analysis 142
4.3 Results 146
4.3.1 Scanning Methods Affect Mass Loss in Vitreous Ice . . 147
4.3.2 Statistical Analysis Across All Datasets 150
4.3.3 Trench Experiments and Directional Mass Loss of Vitreous Ice 158
4.4 Discussion 164
4.4.1 Findings 164
4.4.2 Future Directions and Conclusion 170

The work presented in this Chapter was performed in collaboration with Dr. Abner

Velazco-Torrejon. The author gratefully acknowledges his contributions to the experimental work and the preparation of the resulting manuscript.

4.1 Introduction

The preceding Chapter established that the confident detection of minimally-sized high-Z tags in cryo-STEM is fundamentally fluence-limited. Achieving a sufficient SNR, particularly for sub ∼2 nm particles, necessitates a substantial electron fluence. This requirement, however, is in direct conflict with the primary constraint of imaging radiation-sensitive biological specimens: the need to preserve sample integrity. Therefore, any strategy that can extend the usable 'fluence budget' presents a major advantage. This Chapter will address this challenge directly by investigating how the fluence can be delivered in cryo-STEM using an alternative scanning method designed to minimise beam-induced damage. Its success is examined by quantification of the mass loss from the sample.

While the individual mechanisms of radiation damage were reviewed in Chapter 1 section 1.4, the specific contributions of all of these separate effects are complex and not fully understood [162]. The initial ionisation event of radiolysis is known to trigger a cascade of secondary processes such as charging, bond breakage, secondary electron generation, and the diffusion of reactive radicals that can result in structural changes and loss of mass [153, 166, 177, 200]. This complex interplay is thought to be the basis for the superior 'dose resistance' observed in samples imaged in STEM mode compared to a continuous TEM beam, where a short dwell time followed by a long 'relaxation' or 'healing' period appears to be less damaging [95, 104, 162]. However, the physical evidence for this effect, particularly in vitreous ice, remains an active area of investigation. Whilst the materials science field has explored alternative scanning strategies to mitigate damage in other beam-sensitive materials [212, 296], these concepts have not yet been systematically applied or quantified for cryogenic biological samples. To summarise the main findings of alternative

scanning strategies employed previously, a reduction in mass loss was observed when scanning a radiation-sensitive zeolite sample using a variety of different scanning methods in a pair of seminal papers published from the group of Verbeek [212, 213]. It was found that an interleaved pattern (as will be described in section 4.2) appeared to maximise the damage reduction (up to 11% reduction in loss of mass) [217]. Alternative scanning patterns have also been utilised in the FIB-SEM to alter the milling and charge dissipation characteristics [219, 297]. Taken together, these findings suggest that a more complex relationship exists between damage and the distribution of the fluence in time and space for a finite fluence budget. STEM offers the flexibility to investigate this through the dwell time of the probe at each scan position and the scan pattern.

This Chapter addresses this challenge directly. It aims to first systematically quantify the damage, measured as mass loss, induced in pure vitreous ice by a high-dose STEM probe. Secondly, it will test the central hypothesis that this damage can be actively mitigated by altering the spatio-temporal distribution of the fluence. In general, the distances over which a reduction in damage is expected to be effective considering different scan types is between 10 and 100 nm in length. An interleaved scanning pattern is implemented and its effectiveness is systematically compared against a conventional raster scan across a range of dwell times and sample thicknesses. To make the effects of damage more evident and quantifiable, an electron fluence approximately 100× greater than that used in standard cryo-ET was used.

4.2 Materials and Methods

4.2.1 Sample Preparation

AuNPs with a mean diameter distribution of 5 ± 2 nm and a citrate capping agent (Nanopartz) were supplied in deionised water at 3.3 µM. The solution was washed with 0.22 µm filtered reverse osmosis grade I pure water, concentrated to 16.5 µM

and sonicated before application onto glow-discharged (30 s at 180 mA, Gloqube, Quorum Technologies) copper 200 mesh Quantifoil R2/2 grids (Agar Scientific). The grids were subsequently plunge frozen using a vitrobot (mk IV, Thermofisher Scientific) using a blot time of 2.5 seconds and blot force of +10 at 95 % humidity and 4°C. Grids were left unclipped and stored under liquid nitrogen. The AuNPs were used to ensure that the experimentally acquired images were adequately focused, and their size and concentration were chosen to give a clear signal of sparse nanoparticles in the ice background (as can be seen in many figures within this Chapter).

4.2.2 Raster and Interleaved Pattern Creation

The raster scanning pattern sequence is created using the following minimal loop in python:

```
x_size=512
y_size=512
index = 0

for y in range(y_size):
    for x in range(x_size):
        print(x,y,index,'\n')
        index += 1
```

Where `x_size` and `y_size` denote the dimension in the x direction or y direction of the scanned frame, respectively. `index` is the order in which the probe visits a position (in `[x,y]`, for example, 1 for the first probe position, 2 for the second, and runs up to `x_size` × `y_size`).

As introduced in section 1.4.2.7, the interleaved scanning geometry visits the first probe position and then the probe skips a predefined number of positions along the x-axis to visit the next position until the line is completed. The probe repeats this sequence by skipping the same number of lines along the y-axis until the

bottom of the frame is reached. The probe then returns to the top of the frame to repeat the pattern for the previously skipped pixels, until the entire scan is complete [212]. The interleaved scanning pattern sequence is created using a slightly modified loop of the raster scan code:

```
x_size = 512
y_size = 512
index = 0
interleave_jump=3

for y_round in range(interleave_jump):
    for x_round in range(interleave_jump):
        for y in range(y_round, x_size, interleave_jump):
            for x in range(x_round, y_size, interleave_jump):
                    print(x,y,index,'\n')
                    index += 1
```

This introduces a new variable, `interleave_jump`, which specifies the number of every n^{th} pixel irradiated along both the x and y directions when generating the scan coordinates.

It is important to clarify the semantic distinction between the terms '*jump*' and '*skip*' in the context of interleaved scans. Jump describes the distance between consecutively scanned pixels, whereas skip [212, 213, 219] refers to the count of pixels that the probe does not dwell upon between sequentially scanned pixels (jump $=$ skip $+ 1$).

In practice, it is more useful to refer to the interleaved scan with jump. Thus, this thesis will exclusively use jump (j) to avoid ambiguity. In this Chapter, interleaved scanning patterns always use a jump of $j = 3$.

It is also important to note that a jump of $j = 1$, or a jump of $j =$ `x_size` are equivalent to a regular raster scan. The interleaved scan will also cover the entire area of the region to be scanned multiple times in separate 'passes'. For all the

work outlined in this Chapter, this number of passes in an interleaved scan is equal to j^2, or 9. A schematic version of selected interleaved and raster scans can be found in Figure 4.1 to demonstrate the order of scanning.

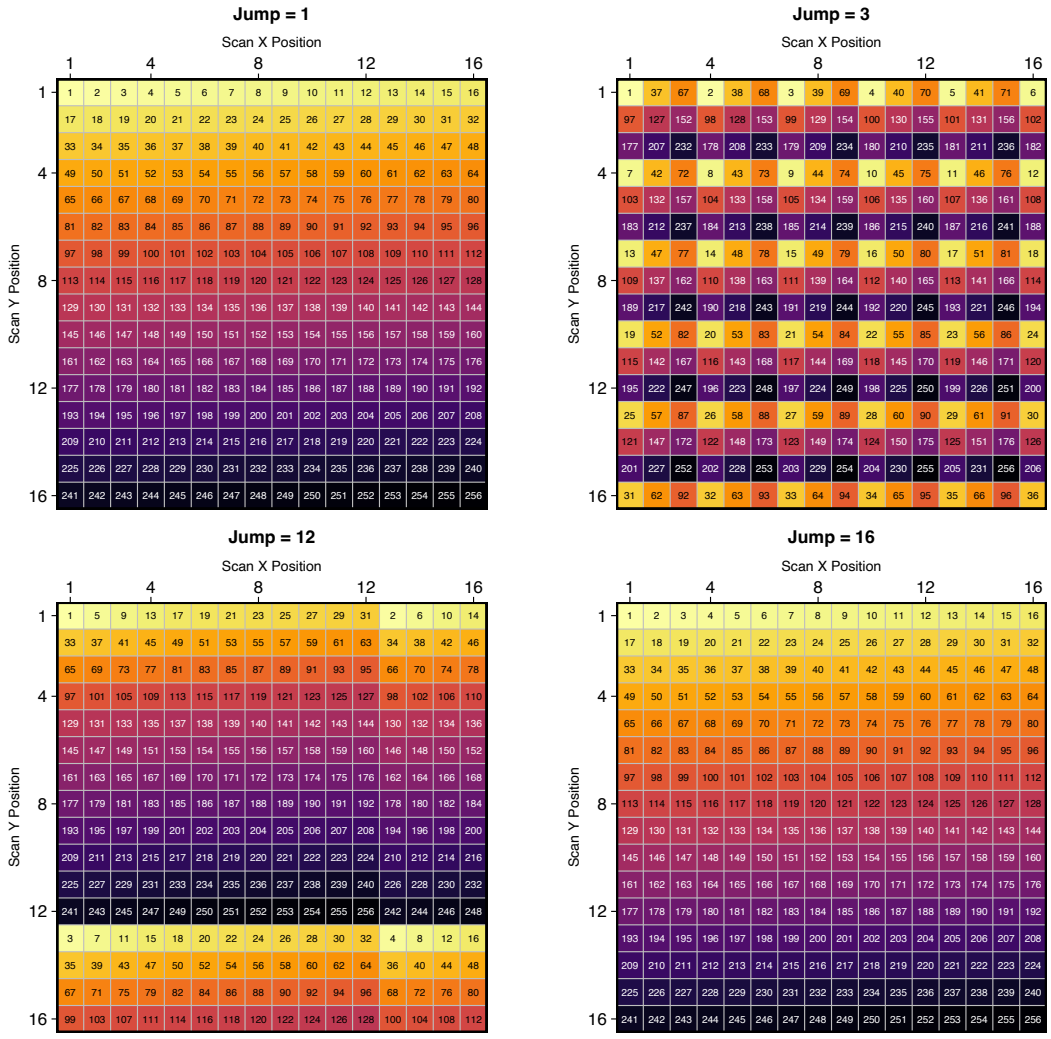


Figure 4.1: **Examples of 16 × 16 interleaved scans with differing 'jump number'.** Numbers within each pixel are the index or order in which the position is scanned. **A** $j = 1$, which is equivalent to a standard raster scan, **B** $j = 3$, used for work in this Chapter, **C** $j = 12$, and **D** $j = 16$, which is equivalent to a standard raster scan.

4.2.3 Trench Patterns

This work involved designing structured test patterns. These consisted of small rectangular boxes, referred to as 'trenches', and each used standard raster scanning

sequences. The trenches were arranged in vertical columns along the y-axis and scanned sequentially.

To examine how beam damage propagates both within and between trenches, the spacing between trenches was varied systematically for each column.

As shown in Figure 4.2, two types of trench patterns were used. Both patterns are fixed at 3072 × 3072 pixels in total. In Figure 4.2A, each trench was 512 pixels wide (x-axis) and 128 pixels tall (y-axis), with a 512 pixel spacing between columns along the x-axis. Within each column, five trenches were spaced vertically. In the first column, the vertical spacing between trenches was 512 pixels, halved to 256 pixels in the second column, and quartered to 128 pixels in the third column.

Figure 4.2B shows use of a denser variant of the pattern. Each trench was 256 pixels wide and 128 pixels tall, and the column spacing was 256 pixels. This pattern included five columns and eight trenches per column. Each column's trenches were spaced by 40 pixels less than the previous column - from 256 pixel spacings in the first column to 96 pixels in the 5^{th} column.

All trench patterns were scanned using consistent microscope alignment (section 4.2.4), but acquired with a range of magnifications and dwell times. For each experiment, specific magnifications and dwell times are stated, determining the spacing distances.

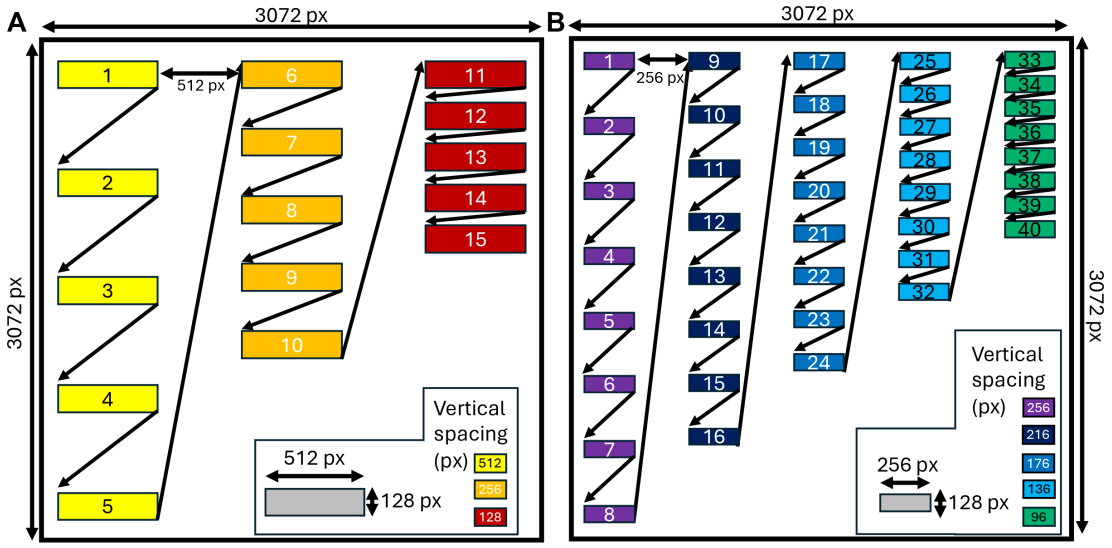


Figure 4.2: **Schematic of 'trench' experiment patterns used**. The black single-headed arrows indicate the trajectory of the probe between trenches. Black double-headed arrows indicate distances in pixels. Each trench is scanned with a standard raster pattern. **A** The first pattern used, with 512×128 trenches, and a halving of the distances between each trench in each subsequent column, as indicated in the key at the bottom right of the panel. **B** 256×128 trenches with shorter distances between trenches and columns, indicated in the key at the bottom right of the panel. Note that the true distances (in units of nm) require multiplication with the specific pixel size at the magnification used.

4.2.4 STEM Microscopy Hardware and Alignment

The C_s-corrected JEM-ARM300F2 (JEOL) was used in STEM mode. A 20 µm condenser aperture was used, giving a convergence semiangle of 16.0 ± 0.2 mrad. The camera length was set at 8 cm, which corresponded to an inner collection semiangle of 90 mrad, well within the HAADF regime. [227, 298]. This gives an ideal probe size of approximately 0.8 Å and a depth of focus of 15 nm (calculated using the method presented in section 2.6) [259, 299].

The alignment of the optical system was performed on a standard polycrystalline gold cross-grating (EMS) and the resolution was confirmed to be approximately 1 Å. This was supported by high-resolution acquisitions after aberration corrections using the JEOL Cosmo software (Figures 4.3A and B). The beam current was

measured using a Faraday cup and adjusted to be 15.5 pA using the gun extraction voltage. The beam current was also measured over 12 hours (longer than one usual experimental session length, Figure 4.3C) and was stable over this time period to an acceptable 5% of the set-point (15.8 ± 0.8 pA). The vitreous ice samples were kept stable at 97 K, during the experiments using a cryo-holder (model 2550, Fischione). Au cross gratings were used at room temperature for alignment. Figure 4.3D is a plot of the drift in mean ADF intensity observed in an image taken over vacuum for each experimental session.

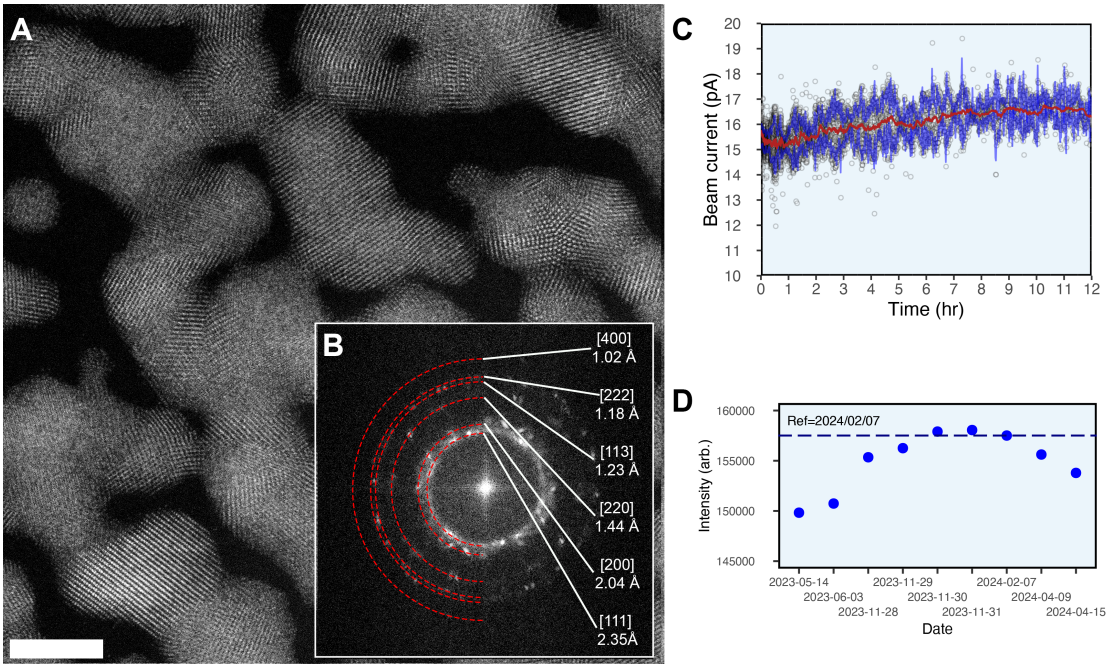


Figure 4.3: **Alignment and beam current stability over time periods corresponding to one experimental session. A** HAADF image of gold cross-grating at a pixel size of 0.167 Å, taken with the 20 µm condenser aperture (convergence semiangle = 16 mrad ± 0.2 mrad. **B** FFT of **A** with red dashes to indicate the lattice spacings of the gold sample and spatial frequencies reached with the alignment. **C** The probe current is shown over 12 hours, measured using a Faraday cup on the fluorescent screen. The mean current over this period was 15.79 ± 0.78 pA. **D** Mean ADF signal readout from images taken over vacuum once alignment was reached before each session. Offsets used for each experimental session are calculated from the deviation from the reference line (reference = experimental data taken on 2024/02/07).

4.2.5 Scan Generator

In this work, an external scan generator (DE-freescan, Direct Electron) was used to control the scan coils of the microscope to generate raster and interleaved scans. In both cases, a lookup table with the aforementioned x- and y-coordinates of the desired scanning sequence, in a formatted .xy file, were provided to the external hardware for the purpose of controlling the scan coils.

While flyback delays are commonly implemented in raster scanning (to give time for the electron beam to return to the beginning of a line in a raster scan), their application to interleaved scanning patterns is non-trivial. Consequently, to exclusively test the influence of the scanning acquisition pattern, flyback delays were deliberately omitted in the experimentally acquired scans. Additionally, following the initial experimental evaluations, a minimum dwell time of 20 µs was established. This condition was necessary to maintain the geometric proportions of the scanned region exhibiting mass loss. More specifically, to ensure that the scanned region remained square. At lower dwell times ($\leq$10 µs), an observable contraction appeared in the x-direction. This is presumed to result from the probe's failure to reach the extremities of the scanning area without the enforcement of a flyback delay.

The response of the probe to the scanning system was also characterised at the experimental conditions (described in appendix section A.4).

4.2.6 Sample Screening

Initial screening to find suitable grid squares was performed at low fluence by defocusing the illumination incident on the sample. To achieve this, the specimen stage was moved upward (toward the source) along the optical axis, the condenser aperture was removed, and the resulting illumination was observed on the fluorescent screen (covering an area of approximately 1×10^5 µm^2 on the grid). The search for

suitable holes filled with thin vitreous ice was completed using a focused probe with a 5 µs dwell time at a relatively low magnification (20 k×). Overall, the fluence during the screening process did not exceed 1 $e^{-}Å^{-2}$ on areas of the sample used for subsequent experiments.

Focusing was performed on AuNPs on the edges of the holes by selecting a small region of the field of view to be scanned. This prevented unnecessary irradiation of the region where the experiments were performed. The grid holes were then centred in the field of view by moving the stage. The beam was blanked immediately. The entire screening process was performed using the DigiScan system and Gatan Microscope Suite (GMS) software. The experimentally-acquired data was collected at a greater magnification from central regions of the holes to ensure a uniform ice thickness across the field of view.

4.2.7 Experimental Data Collection

Each experimentally scanned area (raster or interleaved) was scanned with 512×512 pixels, at a pixel size of 3.4 Å. This corresponded to an area of 174×174 nm^2. Importantly, the raster and interleaved scanned areas were spaced by another 174 nm between each other to ensure no damage interaction occurred. Using the 'spot' mode in GMS, the beam (whilst blanked) was positioned at different locations outside the predetermined scanned regions to ensure that these areas did not experience any additional fluence before, during, or after the scan.

All results of interleaved and raster scanning described in this Chapter equate to experiments with a raster on the left and interleaved on the right - in that order. For this purpose, two separate .xy coordinate files (created as described in section 4.2.2) were loaded into the external scan generator. The position of the scans were also swapped to confirm that the order of scanning had no effect.

For both raster and interleaved scans, the total fluence was fractionated into sequential frame acquisitions (with the number of acquisitions dependent on the dwell time used). The acquisition schemes are shown in Table 4.1.

Table 4.1: Imaging conditions used for HAADF STEM acquisitions. Fluence and flux are reported: in total, and per each pass of the probe, for the specific acquisition dwell time and number.

Dwell time, µs	No. of acquisitions	Total fluence, $e^{-}Å^{-2}$	Total flux, $e^{-}Å^{-2}s^{-1}$	Fluence per acquisition, $e^{-}Å^{-2}$
20	25	4280	32	171
100	5	4280	32	856
250	2	4280	32	2140
500	1	4280	32	4280

After performing raster and interleaved scans in each hole filled with amorphous ice, overview images were taken at a lower magnification, with a pixel size of 5 Å and 5 µs dwell time, corresponding to a fluence of 19.4 $e^{-}Å^{-2}$. These overview images were used to quantify the mass loss at the scanned regions[1]. All experiments were repeated in holes with different amorphous ice thickness. A flowchart of the screening and experimental process can be seen in Figure 4.4.

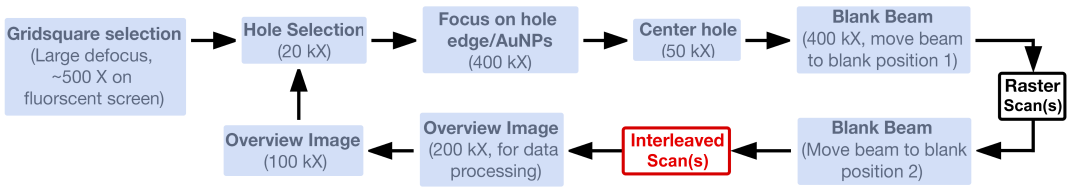


Figure 4.4: **Flow diagram of the screening and data acquisition steps in order**. Care was taken to irradiate the experimentally scanned areas as little as possible before each experiment. Changes in magnification are noted.

[1]Note that total damage during experiments cannot be assessed directly from the individual raster or interleaved STEM images, as once the intensity corresponding to a given scan position is recorded as a pixel in the corresponding image, any further damage originating from a later position in the scan sequence is ignored (often referred to as 'dark progression' [213, 300]. Therefore, only the overall damage is considered here after all experimental scanning is completed.

4.2.8 Thickness Measurements

Thickness measurements were made by directly measuring the projection of the face of the void generated by the electron beam resulting from the mass removal.

In this process, similar areas were raster scanned at 0.8-1 ms dwell time to remove almost all of the vitreous ice in a specific region. Clear, sharp boundaries between vacuum and intact vitreous ice were obtained at the bottom of the scanned areas (Figure 4.5).

The sample was then tilted to 25-30°, with the tilt axis parallel to the x-scan direction. An image was taken at 0° tilt to obtain a reference intensity near the scanned regions, as shown in Figure 4.5. The thickness was subsequently calculated from the measured projected length of the sharp boundary of the 3D volume. This procedure was repeated in several holes in a sample grid showing different vitreous ice thicknesses, and the estimated values of the thickness were plotted with respect to the reference intensities (All thickness calibration graphs can be found in Appendix Figure A.11). Since the HAADF signal is proportional to thickness in an amorphous material, these data were fitted using a linear function. The derived fit parameters then act to produce a thickness calibration curve for subsequently acquired data from different sample grids, when using the same beam current with identical gain and offset settings of the analogue HAADF detector (Figure 4.3D). This procedure accounts for the experiment-specific offset which corresponds to a baseline reference signal acquired in vacuum. The error in the thickness measurements was calculated as the standard error of the fitted values and the standard deviation of the reference intensity measurement.

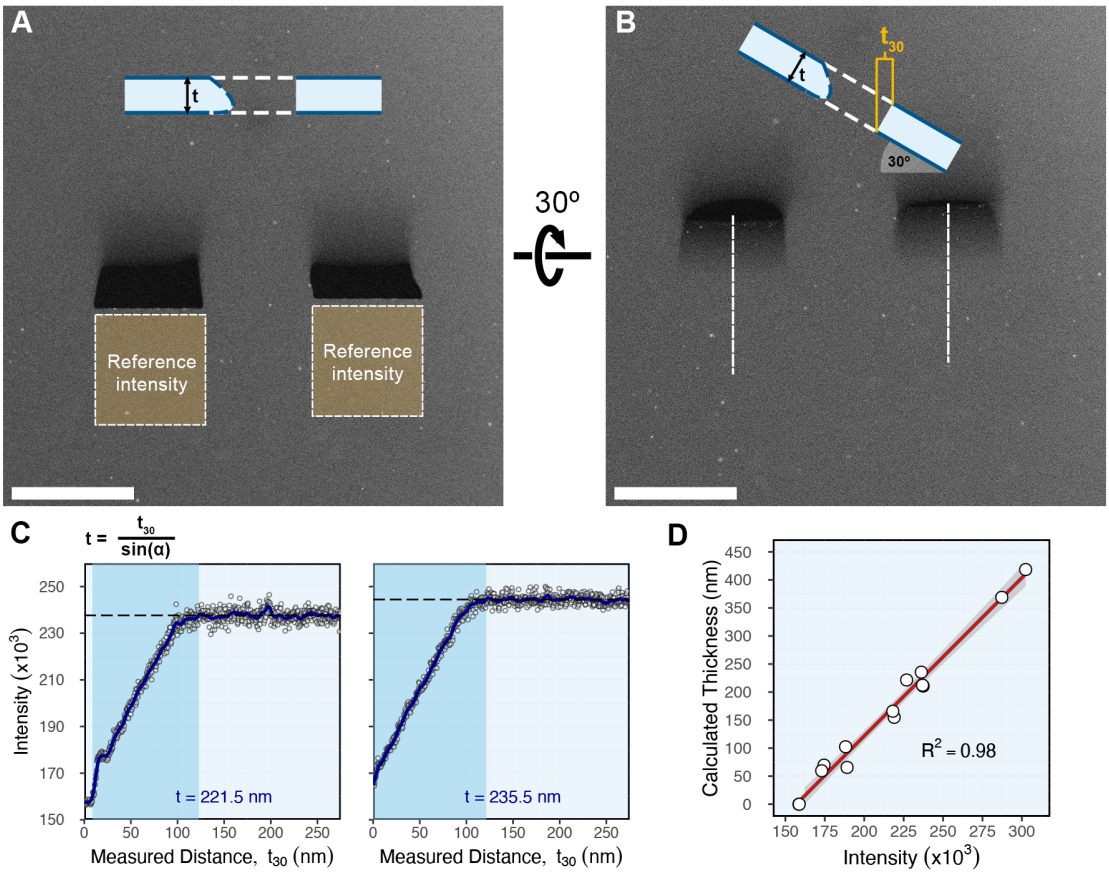


Figure 4.5: **Projected thickness measurement and thickness calibration curve.** **A** images taken at 0° for reference intensity, post removal of all mass in the scanned area using a pixel size of 3.4 Å and a long dwell time, 800 µs to 1 ms. Above is a yz schematic of the removed ice. **B** the stage is then tilted through α =30°, and images taken of the projection. Dotted white lines indicate the positions of line profiles. **C** Plotted line profiles of the projected distance at 30° tilt (t_{30}). The dashed black horizontal line indicates the plateau of intensity (full thickness), with a dark blue region showing the size t_{30}. Thickness of the vitreous ice can then be calculated using $t = t_{30}$ / $sin(\alpha)$. **D** Calibration curve of all experiments, showing an expected linear trend of intensity (I_0) to thickness (t): $t = I_0 \times\ 0.28 \times 10^{-3} - 443$. All thickness calibration graphs can be found in Appendix Figure A.11. Scale bars 200 nm.

4.2.9 Data Analysis

Datasets with significant surface ice contamination, cracks visible in the ice, or AuNPs visibly out of focus were excluded from further processing. In addition, the intensity variation of the ice background in the overview images was analysed

in order to consider only data acquired over areas of uniform thickness. Details of the measurements of the variation in the intensity of the ice background can be found in Appendix Figure A.10.

Out of 146 experiments, 87 were of suitable quality for analysis (n = 87). This reflects the variability of conditions introduced during the sample preparation method.

Line profiles of 600 nm in length (y-scan axis) averaged over 150[2] nm in width (x-scan axis) were measured across experimentally scanned regions in overview images (Figure 4.6A). To compare the results on areas of similar vitreous ice thickness and describe assessment metrics, normalisation of the intensity of the line profiles was calculated as

$$N_I = \frac{I_{exp} - I_{vac}}{I_{ref} - I_{vac}}. \tag{4.1}$$

N_I is the normalised intensity, I_{exp} is the intensity of the line profile, I_{ref} is the mean intensity of undamaged reference regions in the line profiles, and I_{vac} is the mean intensity of the vacuum. Regions of the line profiles used as undamaged references correspond to the sections outside the scanned areas, 150 nm from the top and bottom of the line profiles. This analysis gives 1.0 as full thickness and 0.0 as vacuum intensity.

The vitreous ice thickness was finally estimated in each line profile by applying the thickness calibration curve to the raw intensity values (Figure 4.5D). The thickness of the undamaged ice was determined by the application of the mean intensity values from unscanned reference regions within the line profiles.

A locally estimated regression (locally estimated scatter plot smoothing, LOESS) was fitted to the raw data of the line profiles using RStudio [301]) to reduce the effects of noise and unwanted signal originating from the nanoparticles (Figures 4.6B and C).

[2]The line profiles were averaged over a width of 150 nm in the x-axis, narrower than the intended scanned distance (174 nm). This width was selected as the largest possible for averaging that remained unaffected by any distortions at the scan peripheries, as will be discussed later.

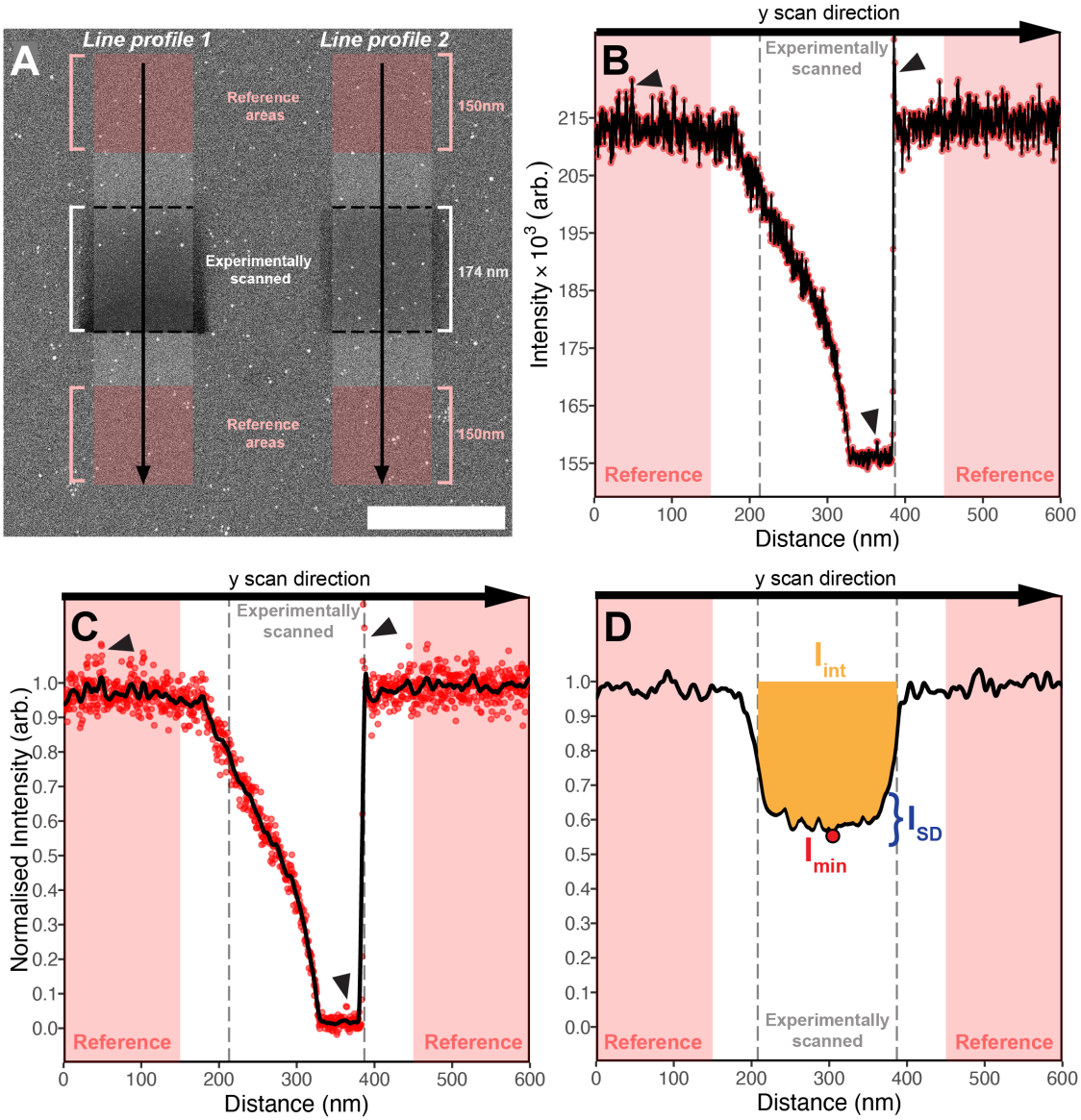


Figure 4.6: **Line profile data processing and analysis**. **A** Schematic view to illustrate the positions of the line profiles, with overlays to represent the undamaged reference areas for an assessment of the thickness. Dashed black lines indicate the boundaries of the experimentally scanned regions (raster or interleaved). The black arrows denote the direction of the y scan axis. The scale bar is 200 nm. **B** Raw line profile, and **C** LOESS-smoothing implemented line profile, as taken over 600 nm in length (y-scan axis direction) and averaged over 150 nm in width (x-scan axis direction). As indicated by the arrows at the top of each graph, increasing distance on the graph's x-axes correspond to progression in the y-axis of the image. Variations in signal are displayed in **B**, demonstrating the need for smoothing. Black triangles indicate deviations in the signal that may alter the subsequent data processing steps, which are lessened in **C** whilst still maintaining an accurate representation of the raw data (red circles). **D** plot of the LOESS-smoothed and normalised data of Line profile 2 (in **C**). The reference and experimentally scanned areas (from **A**) are highlighted. The metrics I_{min}, I_{SD}, and I_{int} are displayed in the experimentally scanned area.

These values were then used to estimate the minimum intensity, I_{min}, the integrated intensity along the y-scan axis, I_{int}, and the standard deviation of the intensity, I_{SD}, in the scanned areas (Figure 4.6D).

I_{min} gives an indication of the minimum thickness of ice at any point on the y-axis after scanning, in units of nm, with 0 nm being vacuum. I_{int} allows a calculation of the total volume remaining as the product of the intensity for each step in the y-axis the scan width (in units of nm^3). The mass loss, in femtograms (fg), is then determined by subtracting the mass of this remaining volume from the initial mass of the unscanned volume, which is calculated from the reference thickness. I_{SD}, however, does not give a measurement of the damage directly. It instead shows the anisotropy of mass removal within the scanned area over the y-axis. Figure 4.7 provides simplified schematic representations of the metrics used. They are vital in providing measurement diagnostics: a large I_{int} indicates a greater total mass loss from the sample, while a large I_{SD} indicates more anisotropic mass loss in the slow scan direction, and I_{min} provides a measure of the thinnest point across the scanned region. These assessment metrics were chosen to distinguish between different profile behaviours with respect to thickness, scan type, and number of acquisitions/dwell time. Figure 4.7 shows two schematic examples to demonstrate the situations in which the assessment metrics are most useful.

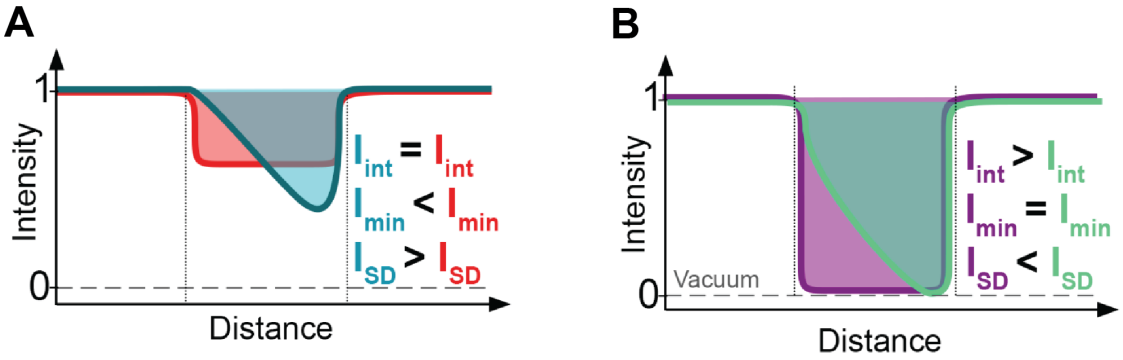


Figure 4.7: **Schematic views of hypothetical damage profiles to demonstrate the use of the assessment metrics**. Dotted vertical lines indicate the experimentally scanned area, a horizontal dashed line indicates vacuum at 0. **A** The red curve shows a hypothetical line profile with a very even mass removal across the entre scanned area. The blue line shows an uneven mass removal across the scanned area. Their I_{int} values (the shaded areas) are equal, therefore the I_{min} and I_{SD} both show that the blue line reaches a thinner ice layer and is more uneven in the mass removal. **B** Both the purple line and the green line reach vacuum meaning their I_{min} value is the same. The purple line profile clearly has a greater I_{int}, indicating total mass removal is also greater. The I_{SD} of the purple curve is lower as it reached vacuum more quickly than the green curve.

Assessment metrics (total mass loss from I_{int}, I_{min}, and I_{SD}) were each plotted against thickness for every dwell time and acquisition scheme, with linear regressions fitted to these data. Differences between raster and interleaved scanning were evaluated based on whether the regression lines exhibited statistically significant changes. All data was analysed using Python scripts (version 3.8.8) to first filter the datasets according to the thickness variation, FIJI (version 2.9.0) to obtain the line profiles, and RStudio (Version 4.2.2) for all subsequent data processing steps.

4.3 Results

This section presents the main experimental results obtained using the measurement and analysis techniques outlined in the preceding section. The first set of results concern measurements of mass loss to determine the differences between the raster and interleaved scanning methods, which is followed by a presentation of the

trench scanning experiments to give more evidence in identifying the nature of damage as mass loss in vitreous ice.

4.3.1 Scanning Methods Affect Mass Loss in Vitreous Ice

To systematically investigate damage in vitreous ice using cryo-STEM, two different scanning methods were tested on plunge frozen samples of 5 nm AuNPs in pure water (Figure 4.8A).

Since HAADF scattering intensity is related to the thickness and atomic Z of the sample, AuNPs appear as bright spots against the vitreous ice background of low atomic number. A decrease in intensity of the vitreous ice background corresponds to a thinner sample region.

Imaging parameters were chosen to find suitable conditions that showed clear loss of mass, indicating damage in experimentally scanned regions. An overall fluence and flux of 4280 $e^{-}Å^{-2}$ and 32 $e^{-}Å^{-2}s^{-1}$, respectively, were used for these reasons in the experimentally scanned regions, to show clear damage as mass loss. Conversely, imaging parameters for the acquisition of post-experiment overview HAADF images were chosen with a fluence of 19.4 $e^{-}Å^{-2}$ and a flux of 0.9 $e^{-}Å^{-2}s^{-1}$, to minimise additional damage in the regions of interest or the surrounding ice background.

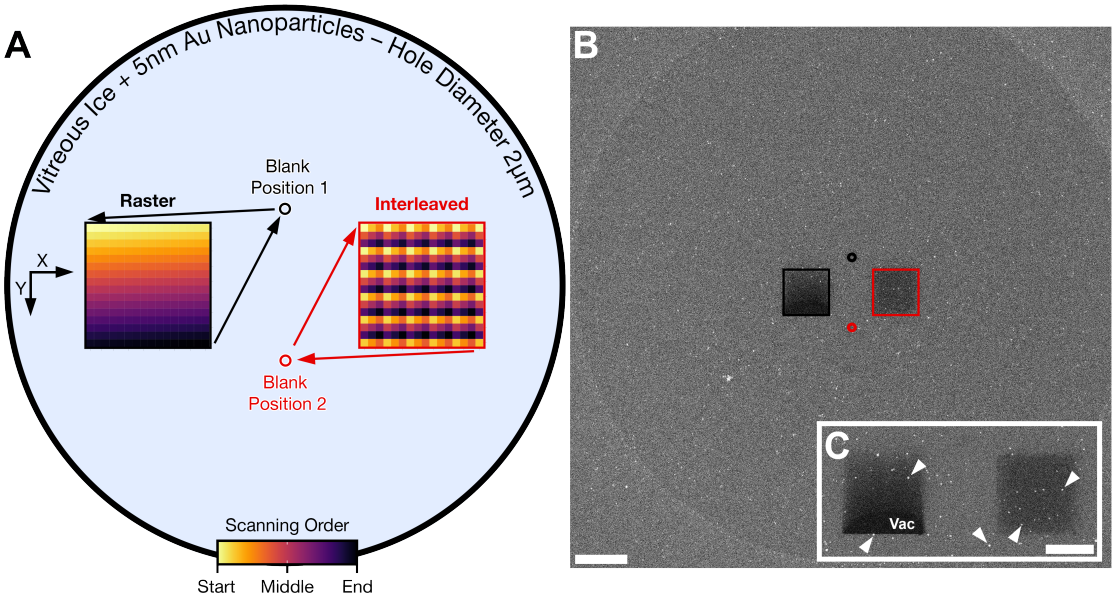


Figure 4.8: **Experiment schematic comparing raster and interleaved scanning in amorphous ice**. **A** Scanning sequence represented as a gradient of colour. The raster scan (left, black outline) and interleaved scan (right, red outline) are positioned near the centre of the hole. The electron beam was positioned at 'blank positions' before and after scanning, ensuring no overlap with scanned areas. **B** A completed experiment at 250 µs×2 acquisitions, in approximately 130 nm thick vitreous ice at the centre of a 2 µm diameter hole in a quantifoil grid. Raster (black) and interleaved (red) overlays show the positions of the experimentally scanned regions and corresponding blanked probe positions. Scale bar 200 nm. **C** Magnified region from the same experiment. White triangles indicate positions of 5 nm AuNPs embedded in the vitreous ice. 'Vac' indicates a vacuum region, where all ice was removed. Scale bar 100 nm.

Figure 4.9 shows representative experimental results with line profiles from regions of vitreous ice of comparable thickness. Overall, a 20 µs × 25 acquisitions raster scan appears to produce a uniform loss of mass across the entire scanned region (Figure 4.9A). This is indicated by a lack of a gradient in that region and the flat intensity of its corresponding line profile.

In contrast, interleaved scanning appears to produce a thinner region of ice at the top of the scanned area, demonstrated by the darker region towards the top and the lower minimum intensity at the start of its line profile.

The experiments performed at 100 µs × 5 acquisitions show similar damage profiles

to each other, with no markedly discernible change in intensity across the scanned areas for the different scanning methods (Figure 4.9B). There is, however, a slight increase in intensity towards the bottom of the interleaved scanned area, as shown by the interleaved line profile (shallow positive gradient). Figures 4.9C and 4.9D show 250 µs × 2 acquisitions and 500 µs × 1 acquisition experiments. Both these experiments exhibit considerable and uneven mass loss under raster scanning, manifesting as a strong intensity gradient from the top to the bottom of the raster scanned areas. This is also shown by a steep negative gradient in the line profiles. Both show clear evidence of a mass removal to vacuum, where the width of the missing ice appears to be around twice as large for the single 500 µs acquisition with respect to the 250 µs × 2 µs case. Conversely, interleaved scans at both of these dwell times show a uniform thin layer of ice across the entire area.

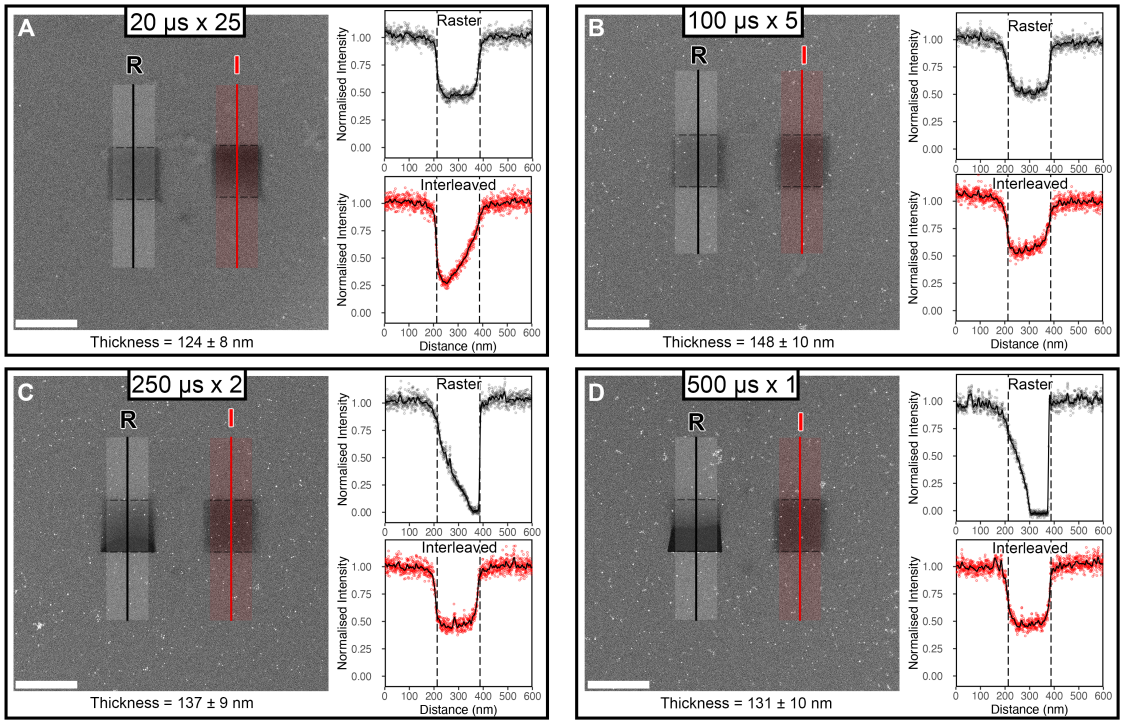


Figure 4.9: **Overview HAADF images acquired after sequential acquisitions in similar thicknesses of ice.** All experiments used the same beam current and images were acquired using the same brightness and contrast settings for the HAADF detector. Overview images (left of each panel, **A**-**D**) with accompanying line profiles (right of each panel). Solid vertical lines on the overview images indicate positions of the raster (black) and interleaved (red) line profiles, averaged over a width of 150 nm and with intensities normalised with respect to the unscanned regions. Data points correspond to the normalised line profiles and the solid lines to a local regression fitted to this data. Two vertical dashed lines on each line profile indicate the start and end of the scanned region in the y-direction. The images and graphed line profiles show varied damage profiles for different dwell times, number of acquisitions, and probe scanning sequences. **A** 20 µs dwell time, 25 acquisitions. **B** 100 µs dwell time, 5 acquisitions. **C** 250 µs dwell time, 2 acquisitions. **D** 500 µs dwell time, 1 acquisition. A vacuum is observed at the bottom of the raster scanned region on **C** and more clearly from the central part to the bottom of the raster scanned region on **D**. All scale bars 200 nm.

4.3.2 Statistical Analysis Across All Datasets

The previously introduced assessment metrics, I_{int} (as total mass loss), I_{min}, and I_{SD}, were plotted against thickness in order to determine their relationship to damage using different acquisition schemes (combinations of scan patterns, dwell

time, and number of acquisitions).

The plots of mass loss and I_{min} for all acquisition schemes are shown in Figure 4.10. For mass loss plots, the theoretical maximum mass loss can be calculated by multiplying the scan area (3×10^3 nm^2) with both the thickness and density of amorphous ice. This accounts for the complete removal of mass corresponding to a specific ice thickness. For the thinnest ice (less than 80 nm, see darker blue curves in Columns 1 and 2 of Figure 4.10), all acquisition schemes resulted in mass loss close to the maximum mass loss limit.

To facilitate direct comparison between experiments across a wide range of vitreous ice thicknesses (from approximately 40 to 300 nm), the reported change for the statistical analysis of each assessment metric was calculated at the mean ice thickness across all experiments (155 nm, n = 87). See statistical summary tables (Tables 4.2: mass loss (calculated from I_{int}, 4.3: I_{min}, and 4.4: I_{SD}).

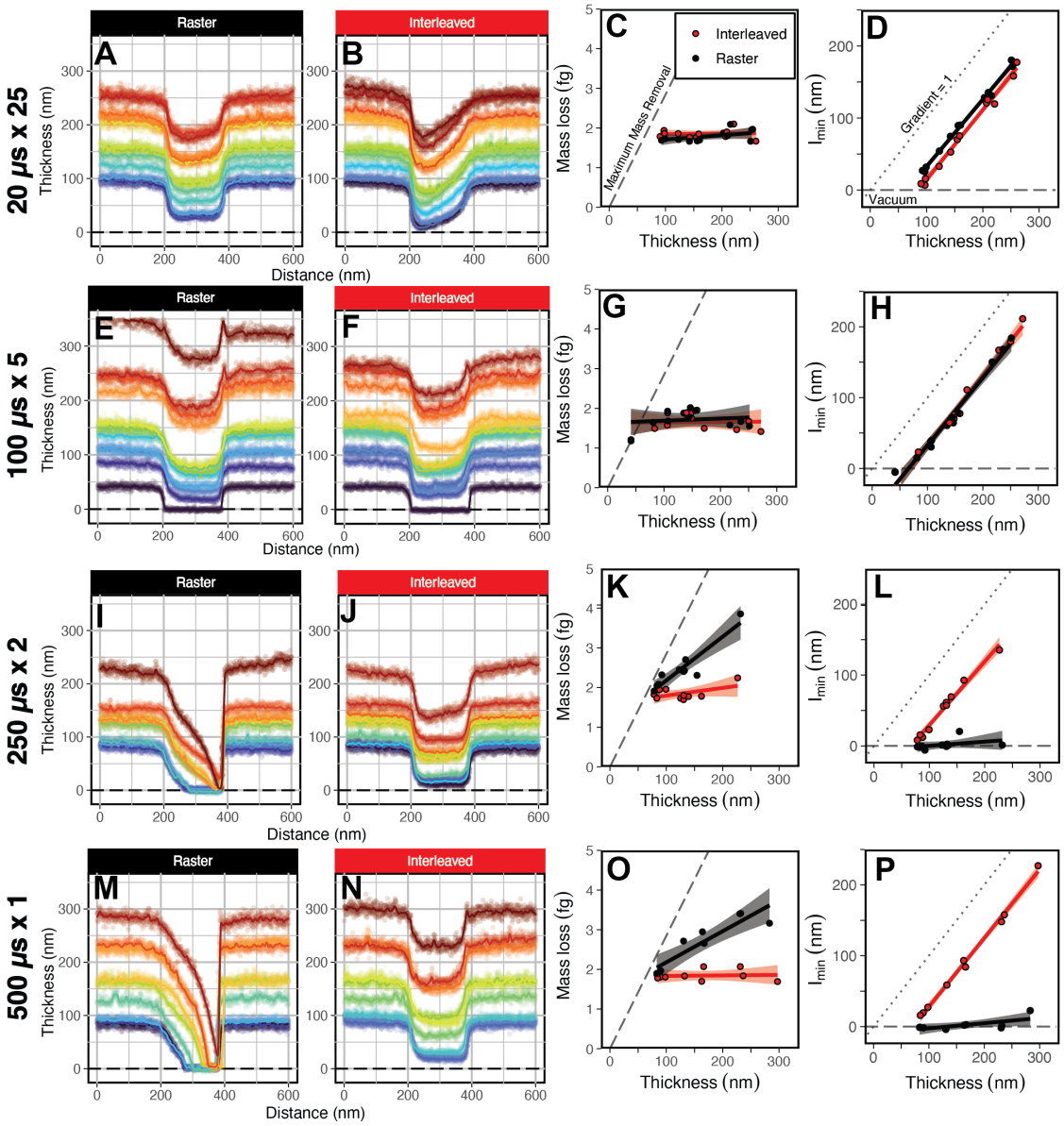


Figure 4.10: **Line profiles from all experiments and comparisons of mass loss and I_{min} between raster and interleaved scanning across all thicknesses of vitreous ice**. **A-D** 20 µs × 25 acquisitions, **E-H** 100 µs × 5 acquisitions, **I-L** 250 µs × 2 acquisitions, and **M-P** 500 µs × 1 acquisition. **Columns 1 and 2** show pairs of line profiles from all experiments, alternating between raster and interleaved. Colours represent thickness of the undamaged ice for visualisation purposes (red = thicker, blue = thinner). Dashed horizontal line at 0 nm thickness indicates vacuum. **Column 3** shows plots of mass loss, calculated from I_{int}, against thickness of vitreous ice at 20, 100, 250, and 500 µs dwell times, respectively. The shaded area around the line indicates the standard error in the fit of the line. The dashed line represents the theoretical maximum mass loss. **Column 4** shows plots of minimum intensity (I_{min}) against thickness at 20, 100, 250 and 500 µs dwell times, respectively. A lower minimum intensity corresponds to a thinner layer of ice. Dashed horizontal line indicates vacuum. Dotted line represents a gradient of 1 where thickness = I_{min}.

4.3.2.1 Line Profiles

The 20 µs × 25 acquisitions line profiles show that raster scanning at this dwell time acquisition scheme results in an even mass removal across the scanned area (Figure 4.10A). By comparison, interleaved removes more mass at the top, and less mass towards the end of the scanned region (Figure 4.10B).

For the 100 µs × 5 acquisitions (Figures 4.10E and F), no difference can be clearly observed between raster and interleaved scanning from the line profiles. The opposite is true for the longer dwell time acquisition schemes, where both the 250 µs × 2 acquisitions (Figures 4.10I and J) and the 500 µs × 1 acquisition line profiles (Figures 4.10M and N) appear to be similar in overall trend. The raster scanning exhibits an uneven mass loss across the scanned area. More mass was removed at the end compared to the beginning of the scanned area. Vacuum was reached in all but the thickest vitreous ice. Interleaved scanning, however, appeared to lose a consistent amount of mass across all thicknesses. In all cases, the mass loss appears to be even across the scanned areas. These observations are clearly consistent across the whole thickness range of vitreous ice tested.

4.3.2.2 Mass Loss (calculated from I_{int})

For the thinnest ice (less than 70 nm), all acquisition schemes resulted in mass loss close to the maximum mass removal limit. This suggests that the thinnest ice is unable to withstand the high fluence used - regardless of the two different acquisition schemes investigated.

Over all thicknesses of vitreous ice, scanning at shorter dwell times (20 µs × 25 and 100 µs × 5, Figures 4.10C and 4.10G, respectively) showed no statistical difference in total mass loss between the raster and interleaved scanning methods.

Experiments at longer dwell times (500 µs × 1 and 250 µs × 2, Figures 4.10K and 4.10O, respectively), however, indicated that raster scanning removed significantly more mass than interleaved scanning.

In the context of long dwell time, apparent mass loss in raster scanning occurs at greater thicknesses (as there is a larger volume available for removal). At the same time, the effects of interleaved scanning become more evident as the ice thickness increases, where mass loss remains constant.

Quantatively, for 250 µs × 2 acquisitions, raster scanning removed 1.5 times more mass (2.79 ± 0.072 fg) at the mean thickness than interleaved scanning did (1.90 ± 0.072 fg). At the maximum thickness tested (≈ 230 nm), raster scanning showed approximately 3.7 ± 0.16 fg mass loss. In contrast, interleaved scanning showed no increase in mass loss with increased thickness. Similarly, for 500 µs × 1 acquisition, raster scanning resulted in a mass loss at the mean thickness of 2.60 ± 0.073 fg. This represents a 1.4-fold increase in the mass lost compared to interleaved scanning, which showed a significantly lower mass loss of 1.84 ± 0.074 fg. Table 4.2 contains the relevant data used in determining the mass loss for each specific measurement.

Table 4.2: Statistical results of the linear regression model for mass loss (data from column 3 in Figure 4.10) for the different acquisition schemes, with respective standard errors in the fit of the line. All statistics were calculated at the mean thickness for all experiments (155 nm, n=87). Asterisks (*) and **bold** indicate statistical significance. ***= $p < 0.05$, ****= $p < 0.01$, *****= $p < 0.001$.

Acquisition Conditions (Dwell time × Acquisitions)	**Mass loss** (fg)		
	Raster (±SE)	Interleaved (±SE)	Δ (p-value)
20 µs × 25	1.77 (±0.036)	1.85 (±0.036)	-0.09 (0.163)
100 µs × 5	1.69 (±0.071)	1.65 (±0.068)	0.04 (0.628)
250 µs × 2	2.79 (±0.072)	1.90 (±0.071)	**0.89*** (<0.001)**
500 µs × 1	2.60 (±0.073)	1.84 (±0.074)	**0.76 *** (<0.001)**

4.3.2.3 Minimum Thickness (I_{min})

The minimum intensity values, I_{min}, plotted against ice thickness, are shown in Figures 4.10D, H, L, and P. Images for interleaved scanning at 20 µs × 25, showed a resulting layer of ice that was slightly thinner than in raster scanning that was statistically significant. Specifically, this difference was approximately 16 nm across all thicknesses (I_{min} = 84 ± 2 nm and 68 ± 2 nm for raster and interleaved, respectively, at the mean ice thickness across all experiments of 155 nm).

At 100 µs × 5, no statistically significant difference was observed between either scanning method (I_{min} = 86 ± 3 nm and 87 ± 3 nm for raster and interleaved, respectively).

For the 250 µs × 2 and 500 µs × 1 acquisitions, raster scanning consistently removed sufficient mass to reach vacuum, regardless of the thickness (I_{min} = 3 ± 2 nm, and 1 ± 2 nm for 250 µs × 2 acquisitions and 500 µs × 1 acquisition, respectively). Interleaved scanning, however, did not reach vacuum for these longer dwell time acquisitions, retaining some notable ice thickness (I_{min} = 79 ± 4 nm for 250 µs × 2 acquisitions, and 81 ± 2 nm for the 500 µs × 1 acquisition). Table 4.3 contains the relevant data used in determining the minimum thickness for each specific measurement.

Table 4.3: Statistical results of the linear regression model for I_{min} (data from column 4 in Figure 4.10) for the different acquisition schemes, with respective standard errors in the fit of the line. All statistics were calculated at the mean thickness for all experiments (155 nm, n=87). *= p < 0.05, **= p < 0.01, ***= p < 0.001.

Acquisition Conditions (Dwell time × Acquisitions)	I_{min} (nm)		
	Raster (±SE)	Interleaved (±SE)	Δ (p-value)
20 µs × 25	83.9 (±1.5)	67.8 (±1.5)	**16.1** (0.004)**
100 µs × 5	86.2 (±2.8)	86.8 (±2.7)	-0.5 (0.816)
250 µs × 2	3.3 (±2.4)	78.8 (±2.4)	**-75.4*** (<0.001)**
500 µs × 1	1.5 (±2.0)	81.3 (±2.0)	**-79.7 *** (<0.001)**

4.3.2.4 Standard Deviation (I_{SD})

For interleaved scanning at 20 µs × 25 acquisitions, no significant difference in mass loss was observed between interleaved and raster scans (Section 4.3.2.2). However, compared to raster scanning, a slightly thinner minimum point (I_{min}) in the ice was reached. This suggests that mass removal is less uniform, and resembles the pattern shown in schematic Figure 4.7A, which compensates for the mass loss.

This finding is corroborated by the plots of standard deviation (calculated from I_{SD}) across the scanned region shown in Figure 4.11. The standard deviation for interleaved scanning is double that for raster scanning at this dwell time (I_{SD} = 10 ± 1 nm and 20 ± 1 nm for raster and interleaved scans, respectively, at the mean ice thickness across all experiments). This is consistent with more even mass removal for a raster scan at this dwell time.

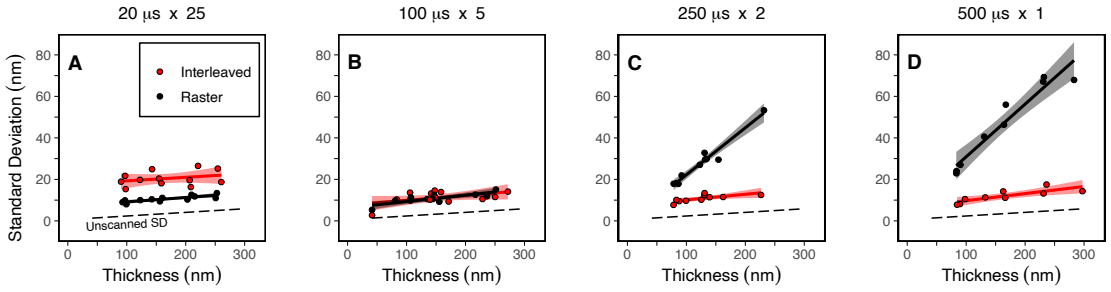


Figure 4.11: **Standard deviation of the experimentally scanned regions plotted against thickness.** The standard deviation of the scanned region shows the unevenness of the scanned region, highlighting anisotropic mass loss for **A** 20 µs × 25 acquisitions, **B** 100 µs × 5 acquisitions, **C** 250 µs × 2 acquisitions, and **D** 500 µs × 1 acquisition. The dashed line indicates the standard deviation level of the unscanned reference areas, taken as the first and last 150 nm of the line profile.

Similar to the mass loss and I_{min} plots (Columns 3 and 4 in Figure 4.10, respectively), no significant difference was observed in the 100 µs × 5 acquisition experiments between raster and interleaved scans (I_{SD} = 10 ± 1 nm and 11 ± 1 nm, respectively). At longer dwell times, the steep negative gradient of thickness in raster acquisitions

contributed to significantly increased standard deviations. For 250 × 2 acquisitions, the raster and interleaved standard deviations were found to be $I_{SD} = 35 \pm 1$ nm and 12 ± 1 nm, respectively. Similar values were observed for the standard deviation for 500 × 1 acquisition, $I_{SD} = 44 \pm 1$ nm and 12 ± 1 nm for raster and interleaved scans, respectively.

The data suggest that interleaved scans at the extended dwell time acquisition schemes (250 µs × 2 acquisitions and 500 µs × 1 acquisition) facilitate a more uniform removal of mass compared to raster scans. Additionally, interleaved scanning under these longer dwell time acquisition schemes reproduce the effects of shorter dwell times and repeated raster scanning.

The extended dwell time acquisitions demonstrate a significantly greater standard deviation within the scanned region across the entire spectrum of thicknesses for raster scanning, as opposed to interleaved scanning. This observation was anticipated, as the I_{min} frequently reaches vacuum before the completion of the scan. In contrast, interleaved scanning maintained a low constant level at approximately $I_{SD} \approx 5$ nm across all thicknesses, which closely aligns with the base undamaged I_{SD}. This signifies a more uniform mass removal throughout the scanned area.

Table 4.4 contains the relevant data used in determining the standard deviation in mass removal for each specific measurement.

In summary, a reduced dwell time of 20 µs × 25 acquisitions gave no significant change in mass loss for raster or interleaved scanning. However interleaved scanning appeared to remove mass in a more uneven fashion than raster scanning. Similarly, 100 µs × 5 acquisitions showed no significant differences between the two scanning methods by all metrics. In contrast, both 250 × 2 acquisitions and 500 µs × 1 acquisition showed that interleaved scanning resulted in a marked decrease in mass loss compared to raster scanning. This was confirmed across every measurement metric. The outcomes of interleaved scanning with longer dwell time and reduced

Table 4.4: Statistical results of the linear regression model for I_{SD} (data from 4.11) for the different acquisition schemes, with respective standard errors in the fit of the line. All statistics were calculated at the mean thickness for all experiments (155 nm, n=87). *= $p < 0.05$, **= $p < 0.01$, ***= $p < 0.001$.

Acquisition Conditions (Dwell time × Acquisitions)	I_{SD} (nm)		
	Raster (±SE)	Interleaved (±SE)	Δ (p-value)
20 µs × 25	10.3 (±0.8)	20.2 (±0.8)	**-9.9*** (<0.001)**
100 µs × 5	11.0 (±0.7)	11.2 (±0.6)	-0.2 (0.570)
250 µs × 2	34.7 (±0.7)	11.6 (±0.7)	**23.1*** (<0.001)**
500 µs × 1	44.8 (±1.4)	11.7 (±1.4)	**33.1*** (<0.001)**

repetitions (250 µs × 2 and 500 µs × 1) were comparable to acquisition schemes using raster scanning with shorter dwell time and increased repetitions (20 µs × 25). This indicates that similar levels of damage, in terms of mass loss, are reached under both these scan acquisition schemes.

4.3.3 Trench Experiments and Directional Mass Loss of Vitreous Ice

To investigate the nature of beam-induced damage in cryo-STEM further, trench test patterns were developed, as detailed in section 4.2.3. Here, the spacing along the y-axis between adjacent scanned areas was varied across different x-axis columns. The initial experiment was conducted at a magnification of 250 k× (2.7 Å pixel^{-1}) with a dwell time of 800 µs. This yields a fluence used of 1.06×10^4 e$^-$Å^{-2}.

For the left and middle columns within this experiment (Figure 4.12A), the spacing between adjacent trenches in y is 140 nm and 70 nm, respectively. Minimal mass loss is evident between each 140 nm-spaced trench in the image (Figure 4.12B), as confirmed by the line profiles (Figure 4.12C) reverting to 1.0 on the normalised intensity scale on regions between the scanned areas. However, when the gap between adjacent trenches decreases to 70 nm, the line profile shows a slight and

consistent lowering of intensity in the unscanned regions. This effect is increased at 35 nm-separated trenches, where substantial mass removal is observed in the regions between the intended scanned areas. These large gap areas are only briefly irradiated by the probe during its transition between trenches, a duration estimated to be around 290 µs (see Appendix section A.4). This brief exposure is insufficient to account for the observed damage, which would require a cumulative fluence several orders of magnitude greater.

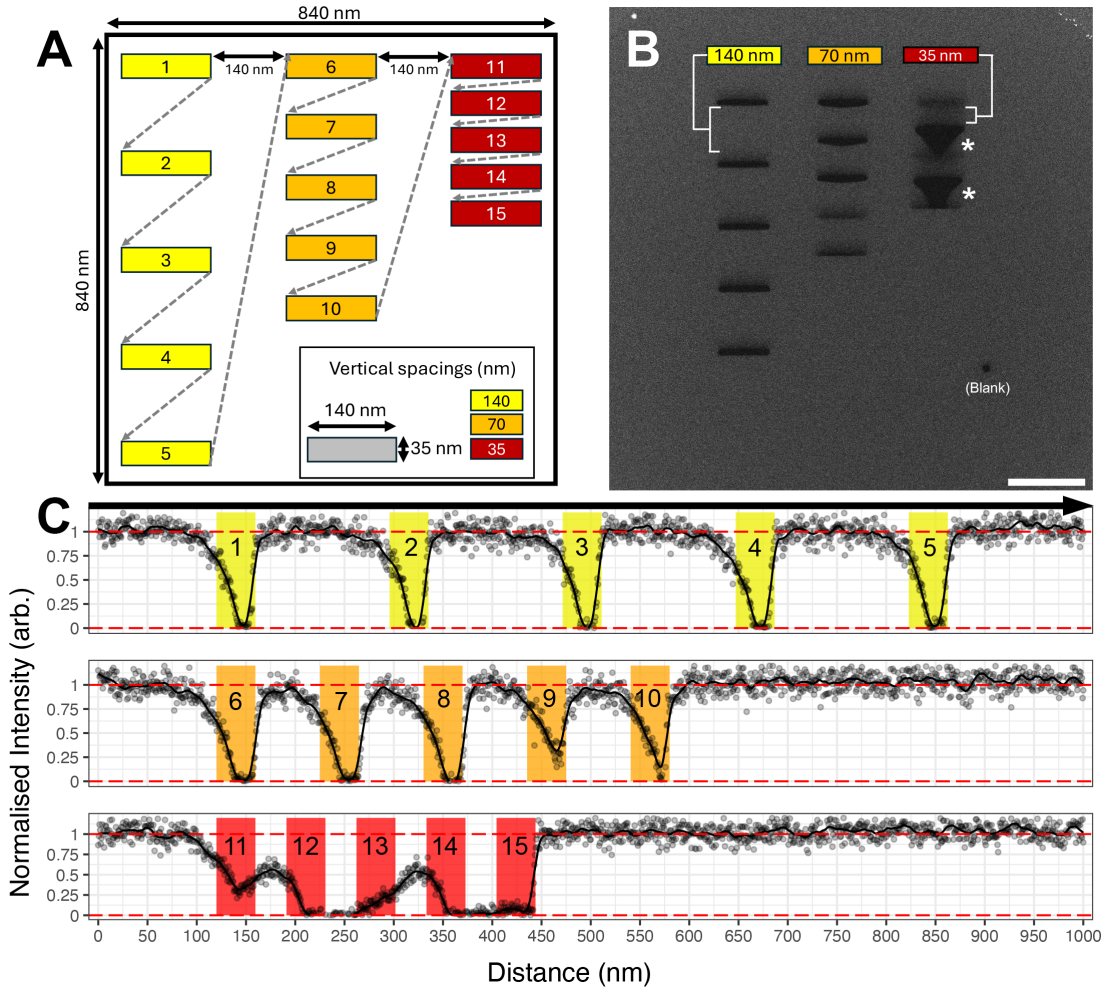


Figure 4.12: **Trenches experiment at 250 k× magnification (2.74 Å pixel^{-1}) and a dwell time of 800 µs.** **A** A schematic view of this experiment using the pattern from 4.2, in dimensions of nm. Trenches are numbered according to the order in which they were scanned and coloured according to the vertical spacings between each trench. Dashed grey lines indicate the trajectory of the probe between scanned trenches. **B** Overview image taken at 200 k× of the completed experiment. Vertical spacings are indicated with corresponding colour above each column. Scale bar 200 nm. **C** Normalised line profiles taken vertically from top to bottom and numbered, as shown in **A**. Asterisks (*) mark the 'inverted triangles'.

Additionally, a straight and abrupt edge is observed at the bottom of each scanned region for the 140 nm separated trenches, indicating a consistent mass removal to vacuum. However, when the distance between the scanned trenches is decreased to 70 nm, the bottom edges of the first three trenches in this example (numbered 6-8 in Figure 4.12A) appear to bow slightly downwards in the middle.

Unlike the first three trenches in this column, the fourth trench (number 9) does not appear to have removed as much mass to reach vacuum by the end (bottom) of the trench. The fifth trench (number 10) does reach vacuum however, and has a clear and abrupt bottom edge similar to each of the trenches in the 140 nm separated column (numbers 1-5).

Most notably, the 35 nm separated trenches (numbers 11-15) differ from those discussed thus far, and seem to follow an entirely unexpected repetitive pattern. The first trench (number 11) has not removed enough mass to reach vacuum, in which around 25% of the initial thickness remains at the thinnest point. In comparison, the second trench (number 12) has removed enough to reach vacuum, and forms an inverted triangular geometry of mass loss across the transverse plane (evident in Figure 4.12B). This pattern extends into the next trench (number 13). Some mass loss is observed between trenches 13 and 14, in a fashion similar to that occurring between trenches 11 and 12. The triangular pattern of mass loss present between trenches 12 and 13 is repeated for trenches 14 and 15. The final trench (number 15) has a straight and abrupt edge at the bottom of the scan (similar to trenches 1-5 and 10).

Further examples of this effect can be found in the appendix Figure A.13, which displays the clear repeated pattern of mass loss.

This relationship between the distance of scanned areas is further exemplified by the trenches in Figure 4.12. These were observed at a higher magnification (400 k×, 1.67 Å pixel^{-1}) and a reduced dwell time of 250 µs, equating to a fluence of 8.7×10^{3} e^{-}Å^{-2}.

Consistently, the final trench in each column exhibits a distinct and sharp transition from vacuum to intact vitreous ice of nominal thickness at the base of the scanned area (trenches 8, 16, 24, 32, and 40). Within each column, the trenches (1-7, 9-15, 17-23, 25-31, and 33-39) appear to have lost mass from a broader region than the

intended scanned region sizes. They also display bowing of the bottom edge (Figure 4.13B), with increasingly shorter distances between the trenches.

Notably, the column with 29 nm spacings between each trench provides another instance of a recurring pattern of alternating downward bowed mass removal and reduced mass removal (observed between trenches numbered 17-24, in Figure 4.13B).

When transitioning from the left column to the right, a progressive change in the morphology between damaged trenches and the intermediary scanned regions is clearly visible. In general, a greater mass loss occurs in the unscanned regions between adjacent trenches as the trench spacing decreases. The line profiles highlight that a smooth transition occurs from the consistent mass removal upon large trench separation (purple, 43 nm), to a more asymmetric mass removal profile as the spacing approaches the trench width (light blue, 23 nm). This culminates in the complete removal of all mass – both in the scanned trenches and the unscanned separation regions – when the trench separation becomes small enough (green, 16 nm).

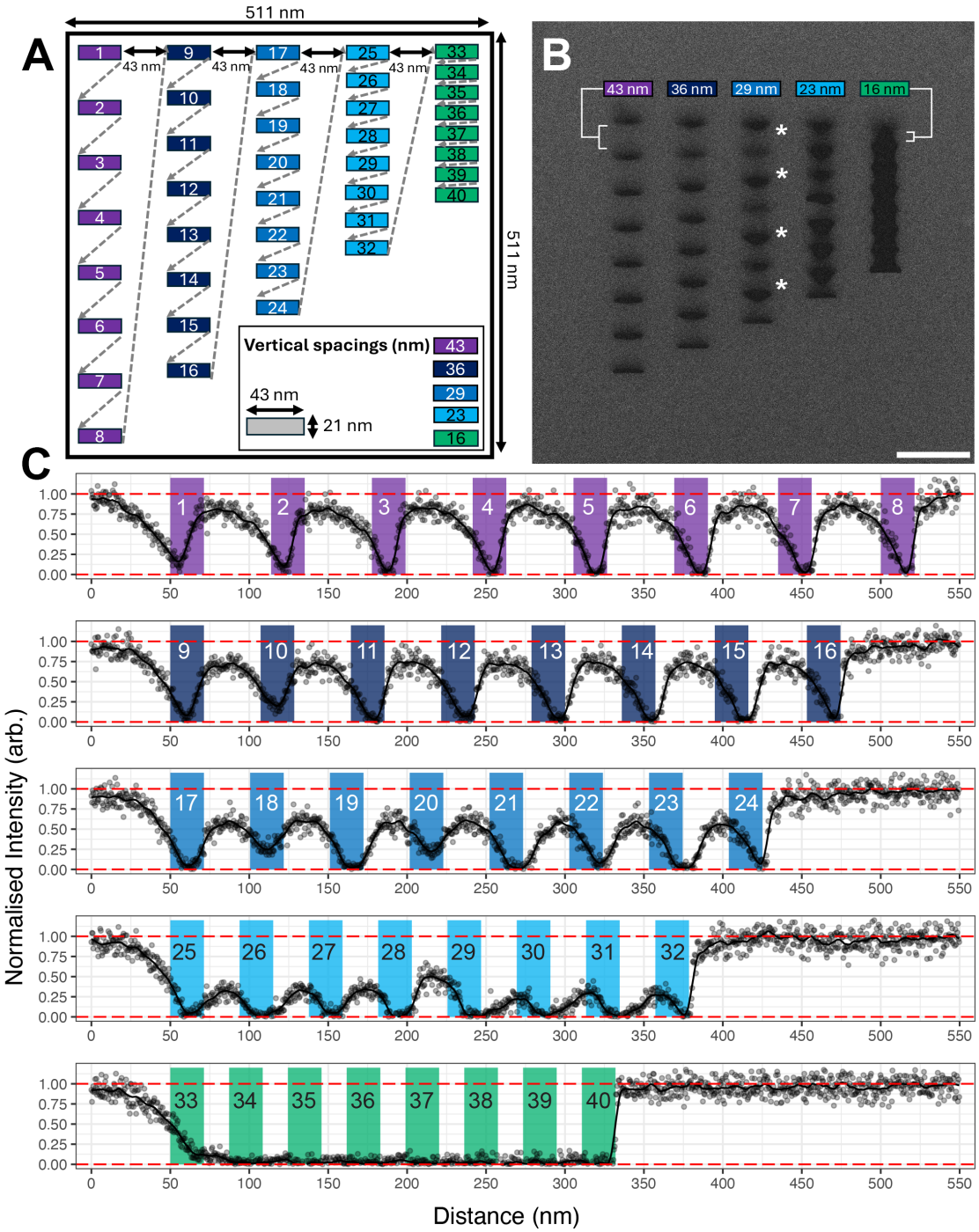


Figure 4.13: **Trenches experiment at 400 k× magnification (1.67 Å pixel^{-1}) and a dwell time of 250 µs. A** A schematic view of this experiment using the pattern from Figure 4.1, in dimensions of nm. Trenches are numbered according to the order in which they are scanned and coloured according to the vertical spacings between each trench. Dashed grey lines indicate the trajectory of the probe between scanned trenches. **B** Overview image taken at 300 k× of the completed experiment. Vertical spacings are indicated with corresponding colour above for each column. Scale bar 100 nm. **C** Normalised line profiles taken vertically from top to bottom and numbered as shown in **A**. Asterisks (*) mark the 'inverted triangles'.

An important observation is that the final trench in each column consistently terminates with a sharp, flat edge, in contrast to the downward-bowed damage front of the preceding trenches. This shows that the mass loss is not an artefact of a single scan, but rather is influenced by the irradiation of the next trench.

With the results of two different experimental investigations into the radiation damage of vitreous ice under a novel analytical scanning scheme presented and described, the next section is dedicated to their interpretation and critical evaluation.

4.4 Discussion

The experiments presented in this Chapter were conducted on pure vitreous ice in order to isolate radiation damage as clearly quantifiable mass loss, avoiding the confounding secondary reactions that can occur with biological macromolecules. This approach also facilitates a more direct interpretation of the results and aligns with other foundational studies in the field [162, 179, 180]. The damage induced by both interleaved and raster scans was assessed across a thickness range of approximately 50-300 nm. This range thus renders this work highly relevant to *in-situ* cryo-ET and cryo-EM SPA-type samples.

4.4.1 Findings

The experimental results presented in this Chapter reveal a complex relationship between the chosen scanning strategy and the resulting beam-induced mass loss in vitreous ice, see Figures 4.8 to 4.13. The core finding is that neither a raster nor an interleaved scan is universally superior: rather, their effectiveness is dependent on the temporal distribution of the fluence.

Although interleaved scanning reduced mass loss effect for few-pass long dwell time exposures, conventional raster scanning produces an equal uniform and predictable

damage profile under more fractionated, short dwell time conditions with the same fluence. This apparent contradiction demonstrates that the total accumulated fluence and flux are not the sole determinants of damage.

An explanation that incorporates at least two distinct physical processes is required in order to account for these results. The first is the diffusion of mobile radiolytic products. Following the initial fast ionisation events, a high concentration of reactive species is generated locally. The hypothesised 'relaxation time', that gives STEM an apparent fluence resistance compared to TEM, can be attributed to this process; it provides a rest period that allows these damaging species to either quench or, if they are small enough, diffuse away from the irradiated volume. This results in a reduction of cumulative damage, which is viewed as the tertiary effects of mass loss or bubbling [95, 104, 156]. This concept aligns with recent descriptions in materials science, which have found it necessary to include a diffusion term to describe the benefits of alternative scanning strategies [212, 213, 296, 302].

These seemingly conflicting results, where interleaved scanning is protective at long dwell times but detrimental at short fractionated dwell times, can be explained by a model based on two competing timescales: the re-irradiation time of a local area and the dissipation time of the damage-inducing species (see Figure 4.14).

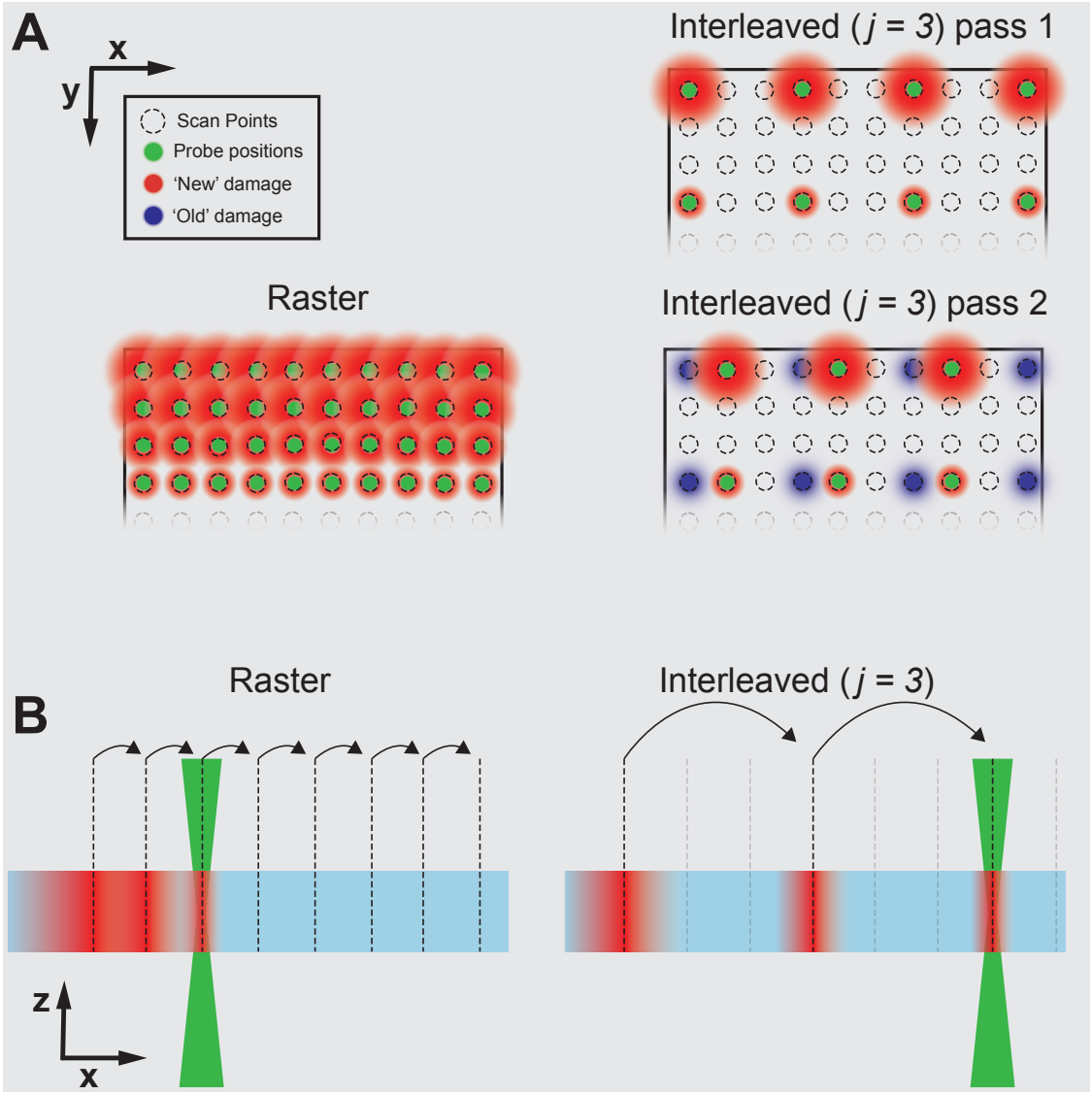


Figure 4.14: **Schematic for explanation of the damage patterns observed**. **A** xy view of the raster (left) and interleaved (right) scanning, showing the probe positions (dashed circles), the completed scanned positions in green, and their respective zones of 'new' irradiated damage extending outward from each scanned position. Where the damage is sufficiently diffused to no longer cause a runaway effect ('old' damage), the circles are coloured blue. **B** xz view of the raster (left) and interleaved (right) scanning in ice, demonstrating the zones of new damage that are overlapping in raster scanning, but are sufficiently spaced in interleaved scanning. Further, more detailed diagrams to aid understanding can be found in the appendix, Figures A.14 and A.15.

In the case of long dwell time and single-pass acquisitions (for example 500 µs × 1), the re-irradiation time is defined as the interval between irradiating two

adjacent probe positions. This could be the next position of the scan in either x or in y. For a raster scan, this length of time is 500 µs in the fast (x) scan direction, and 265 ms in the slow (y) scan direction. This is too short for the localised products of radiolysis to diffuse or quench, and creates a propagating front of damage which leads to runaway mass loss - particularly towards the end of the scan. The interleaved scan is superior here because it introduces a delay between the irradiation of adjacent positions (14.5 s in the fast (x) scan direction, and 43.7 s in the slow (y) scan direction). This timescale is sufficient for local damage to dissipate, thus stopping a runaway mass loss.

However, the situation is inverted for highly fractionated, short dwell time acquisitions (e.g., 20 µs × 25). Here, the damage is thought to be outrun using the raster scanning, as the time between adjacent pixels is 20 µs in x and 10 ms in y scan directions. Therefore, the dominant timescale becomes the inter-acquisition time. For a raster scan, the time before the same local area is re-irradiated is the full acquisition time (∼5.2 s in this work). This provides a long relaxation period. For the interleaved scan, however, the re-irradiation of an adjacent pixel occurs much sooner - in the subsequent 'pass' (after 580 ms). This is much closer to the aforementioned y-axis delay using 500 µs raster scanning which results in damage. The experimental data strongly suggest that this shorter delay is insufficient for the sample to fully relax, and leads to the observed non-uniform damage for short dwell time interleaved scanning.

A simple explanation of isotropic diffusion is insufficient to explain the damage observed in the trench-scanning experiments. Specifically, the downward 'bowing' of the damage front between closely-spaced trenches, and the fact that mass loss occurs in regions that the beam does not dwell upon (for a considerable period of time), suggests a directional driving force, as opposed to random diffusion.

It is therefore proposed that a secondary process is the creation of a localised electrostatic field. Two potential mechanisms could account for this. The first

is that as the insulating vitreous ice is irradiated, and the ejection of secondary electrons leaves behind a net positive charge. This charge creates a local electric field that extends into the surrounding ice, exerting a force on mobile, charged radiolytic fragments and other secondary electrons in the surrounding area.

An alternative hypothesis might involve the newly generated secondary electrons themselves being attracted to or repelled by the charged radiolytic products left from a previous scan. However, this scenario is inconsistent with the relevant timescales of the damage process. The migration and absorption of secondary electrons is a rapid process, likely completed within picoseconds [202]. In contrast, the experimental re-scanning of a damaged region and the delay in transitioning to a subsequent scan both operate on millisecond-to-second timescales, which are many orders of magnitude slower. Given this temporal mismatch, it is highly unlikely that the secondary electrons are the cause of variations observed between the different scanning methods. This distinction in timescales strongly suggests that the slow, observable evolution of non-local damage is not likely to be governed by secondary electrons. Instead, it may be driven by the much slower diffusion and migration of the larger and heavier charged radical products of the initial radiolytic events. Therefore, the model of a static positive charge attracting these slower-moving species provides a physical mechanism that is more consistent with the experimental observations (see Figure 4.15).

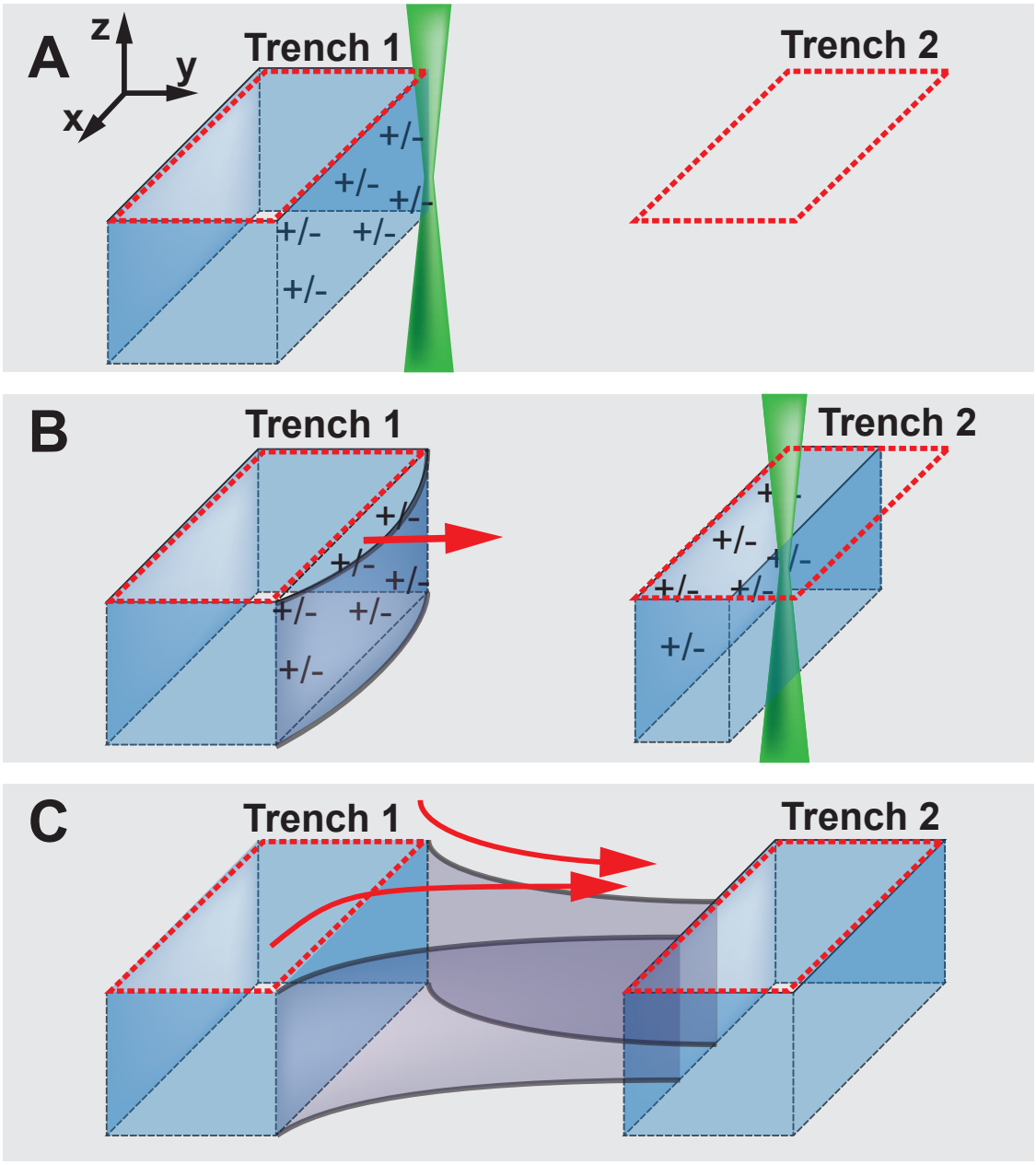


Figure 4.15: **Possible mechanism for the observed trench damage patterns**. **A** The first trench is scanned by the probe, resulting in mass loss, and the generation of charged species at each surface (only the bottom surface is shown) with unconfirmed identity. **B** The probe moves on to begin scanning the next trench. The new mass loss generates further charged species as the probe scans, beginning the 'downward bowing' of the bottom edge of the previous trench (red arrow). **C** If the subsequent trench is spaced a sufficiently short distance away, an 'inverted triangle' of mass loss may appear from the migration of the charged species through the amorphous ice (red arrows).

4.4.2 Future Directions and Conclusion

The findings presented in this Chapter, which establish a clear link between scan strategy and radiation damage, are promising for applications where minimising damage is important for observing native biological structures. Beyond this, several new avenues for future investigation are opened. These can be broadly categorised into: the direct testing of the proposed damage model, the practical optimisation of scanning strategies, and the integration of these findings with more sensitive damage metrics.

A primary future direction would be to directly test the hypotheses presented. To do so, the role of radical diffusion could be investigated through kinetic isotope effect experiments [303]. Repetition of trench-scanning experiments in vitrified ice using different isotopic forms of water ($^{2}D_2O$ and $H_2{}^{18}O$)), one could directly test the hypothesis that the diffusion of a hydrogenous species or an oxygenated species is a rate limiting step. Furthermore, the electrostatic component could be directly visualised using 4D-STEM techniques such as iDPC. By mapping the phase shifts in the ice surrounding an irradiated area, it may be possible to directly measure the proposed localised electric field that could be responsible for driving the anisotropic mass loss, or the mass loss between scanned trenches.

On a practical level, the work could also be extended to optimise the interleaved scanning strategy. This would involve systematically varying the jump (j) between successively irradiated pixels to determine the optimal balance between the inter-pass time and the total acquisition time over a range of dwell times. Furthermore, this technique could be refined through the use of scan engine protocols that incorporate beam blanking during the longer jumps of an interleaved scan, eliminating the small (but non-zero) fluence imparted by beam flyback.

Finally, while mass loss is a simple metric for examining catastrophic damage, future work must connect these findings to more subtle damage to the high-resolution

protein structure. This will be the focus of Chapter 5, which will explore the role of single particle analysis as a more sensitive reporter and how it can be used to investigate the impact of SEM scanning on protein structure. Ultimately, the goal is to combine these damage mitigation strategies to create a workflow that extends the usable fluence budget for beam-sensitive biological samples.

5

SEM Damage for High-Resolution Cryo-Electron Tomography Workflows

Contents

5.1 Introduction 173
5.2 Materials and Methods 174
5.2.1 Simulations of SEM Conditions in Vitreous Ice 174
5.2.2 Protein Purification 175
5.2.3 Sample Preparation 176
5.2.4 Scanning Electron Microscopy 176
5.2.5 Transmission Electron Microscopy of Single Particle Analysis Data Collection 178
5.2.6 Single Particle Analysis Data Processing 179
5.3 Results 182
5.3.1 Simulation of low-energy SEM electrons in Vitreous Ice 182
5.3.2 Dose Applied to the Sample 185
5.3.3 SEM Exposure Causes Loss of High-Resolution Information 186
5.3.4 Exploratory Damage Mitigation Using Interleaved SEM Scanning 200
5.4 Discussion 205
5.4.1 Practical Considerations for Biologists: Workflow and Instrumentation 208
5.4.2 Limitations of the Methods Used 210

5.1 Introduction

The search for rare biological features for high-resolution cryo-ET has been advanced by the adoption of volumetric cryo-serial FIB-SEM [140]. As described in Section 1.2.5, this technique maps the 3D cellular ultrastructure through sequential milling and imaging, enabling the preparation of a targeted lamella at a precise location of interest [30, 147, 148, 150]. While this workflow has shown proof-of-concept success for downstream STA [147], its viability hinges on a critical yet unquantified assumption: that embedded protein structures can survive the repeated electron exposures from the SEM.

This is a significant concern, as the low accelerating voltages used in SEM (typically 1-5 kV) result in a high inelastic scattering cross-section [138]. Consequently, each incident electron is more likely to deposit damaging energy into the sample compared to a high-energy (100-300 kV) electron in a TEM/STEM. While the total fluence (electrons applied per unit area) during SEM imaging is extremely low (typically 0.1-1 $e^{-}Å^{-2}$) [304], it is the absorbed dose (energy absorbed per unit mass) that dictates damage to the sample [182].

Despite this, the potential for SEM-induced structural degradation of proteins has been largely overlooked. A landmark study by Klumpe *et al.* was the first to demonstrate the complete serial FIB-SEM to STA pipeline, resulting in a 24 Å resolution structure of a ribosome [147] from two tomograms and ∼4000 subtomograms. The authors acknowledge the potential for damaging the structures within the lamella by ablating an additional 50-100 nm from the top of the final lamella surface to remove a presumed damage layer, yet the actual depth and nature of this damage to protein structure have not been systematically characterised.

This Chapter provides the first systematic and quantitative analysis of SEM-induced damage on high-resolution protein structures under cryogenic conditions. Using SPA of apoferritin as a sensitive reporter for structural degradation, the presented work aids in assessing the impact of SEM irradiation as a function of accelerating voltage and beam current. Furthermore, this investigation extends the findings from Chapter 4 by directly comparing conventional raster scans with an interleaved pattern to evaluate its potential for damage mitigation.

This work provides the first quantitative framework for understanding the limits of SEM imaging for correlative, high-resolution cryo-ET workflows. Its output provides evidence that will allow researchers to make informed decisions about SEM irradiation in these advanced correlative workflows for *in-situ* structural biology. It will also provide the community with further evidence of electron beam-induced damage in radiation-sensitive specimens.

5.2 Materials and Methods

5.2.1 Simulations of SEM Conditions in Vitreous Ice

Electron scattering simulations were performed using the CASINO Monte Carlo software package (WinCasino v3.3.0.4) [305]. The model substrate was defined as a 100 nm-thick slab along the Z-axis, and 100 × 100 nm^2, with the elemental composition and density corresponding to vitreous ice using a molecular weight of 18 g mol^{-1} and a density of 0.94 g cm^{-3} [306].

Beam conditions were simulated for three acceleration voltages (1.2, 3, and 5 kV), with a fixed initial beam diameter of 3 nm at the sample surface, for direct comparison. The number of incident electrons per pixel was set to 384, 768, and 1536 (for probe currents of 6.25, 12.5, and 25.0 pA and an overall dwell time per pixel of 10 µs. See section 5.2.4.1 for further details on the chosen conditions).

The full lateral spread of electron trajectories was captured by extending the modelled x-axis from –100 nm to +100 nm. Output trajectory data, including spatial coordinates and energy loss per inelastic event, were exported for further analysis.

Data processing and visualisation were conducted in R [301]. Three-dimensional trajectory plots were rendered to illustrate the behaviour at each voltage and current. Energy deposition maps were generated from the simulation output.

The absorption of energy by position is also calculated using the CASINO software. It is important to note that the software normalises these energy deposition data by the total number of simulated trajectories. The resulting maps therefore represent the average energy deposited per incident electron. This renders the result independent of the number of electrons used for the simulation. These patterns were viewed as xz cross-sections, and percentile-based contours (10, 25, 50, 75, and 90%) were calculated to quantify and identify regions of energy deposition within the sample volume.

5.2.2 Protein Purification

Plasmids containing the sequence for a human heavy-chain apoferritin-glutathione fusion protein with a Tobacco Etch Virus (TEV) protease cleavage site were transformed into DH5α competent *E. coli* (New England Biosciences) and induced at an optical density (at 600 nm) of 0.16 with 40μM iPTG (Sigma Aldrich) to express the protein fusion construct overnight at 20°C. Cells were subsequently lysed using a cell disruptor with 1 mM EDTA 0.5 % Triton-X100 (v/v in PBS) (Sigma Aldrich).

The 0.45 µm filtered lysate was added to a 50% Glutathione S-transferase bead-ethanol slurry (ThermoFisher Scientific) and allowed to equilibrate at 4°C for 4 hours on rollers before being washed with Tris buffer (50 mM Tris, 100 mM NaCl, and 0.5 mM TCEP). TEV protease was added to the mixture and the cleavage allowed to proceed overnight at 20°C before separation using gel filtration (a Superdex 25

ml S200 SEC column). Confirmation of separation was achieved by electrophoresis before concentration using a molecular weight cutoff of 10 kDa (Sartorius). The purified apoferritin was aliquoted (10 µl) and flash frozen in liquid nitrogen for storage at -80°C and a concentration of approximately 5 mg ml^{-1}.

5.2.3 Sample Preparation

The apoferritin was diluted in Tris buffer to a concentration of 2 mg ml^{-1} and NaCl was added to a final concentration of 0.5 M. 3 µl of the resulting protein solution was pipetted onto glow discharged (at 20 mA for 45 s, Quorum) UltrAuFoil 200 mesh R 2/2 London finder grids (Quantifoil Micro Tools). The protein solution was vitrified using the Vitrobot mkIV (ThermoFisher Scientific) with a blot time of 2.5 seconds, wait time of 10 seconds, and blot force of +10 at 95 % humidity and 4°C. Grids were then clipped into Auto grids (Thermofisher Scientific) and stored in liquid nitrogen. Two separate experimental sessions were used to acquire all of the data for this Chapter, on two separately produced grids. The sample was produced using the same batch of grids, and sample preparation steps were identical.

5.2.4 Scanning Electron Microscopy

The clipped grids were loaded into a Helios 5 Hydra DualBeam pFIB-SEM (ThermoFisher Scientific) for exposure to the SEM beam. Each accelerating voltage was aligned to give the best possible imaging conditions in immersion mode on a sacrificial imaging area at a pixel size of 3.85 nm. Using a low-magnification SEM atlas, grid squares suitable for TEM imaging were selected. Ideal squares were chosen based on their proximity to one another and the presence of uniform ice, with occasional empty holes indicating optimal ice thickness. The SEM atlas images were acquired at 1.2 kV, using extremely low fluences (due to the low magnification) of less than 1×10^{-6} $e^{-}Å^{-2}$. This acceleration voltage clearly showed the difference between thin and thick ice as a noticeable decrease in contrast in the centre of the

filled holes. This was attributed to electrons that escaped from the bottom surface of the thin ice (see Appendix Figure A.16 for an example).

All SEM imaging was carried out with the incident beam normal (90°) to the surface of the grid, collecting images using the 'though the lens' detector (TLD), at a working distance of 4 mm. The quoted value from the supplier for the probe FWHM at low current (pA range) is approximately 2 nm.

Using the MAPS software (v3.27, ThermoFisher Scientific) tileset function, each selected grid square was exposed to a sequence of different SEM conditions. The scan axis was rotated so that the scan frame was aligned to the grid bars for maximal efficiency in tiling the SEM exposures. Each captured image had dimensions of 4096 x 6144 pixels (height x width), with a horizontal field width of 23.6 μm. To cover the approximate area of 100^2 μm per grid square, this required 7 x 5 SEM exposures, with 5% overlap between each tile.

5.2.4.1 SEM Regular Scanning Conditions

In total, 9 separate conditions of SEM exposure were used for three acceleration voltages (1.2, 3, and 5 kV) at three beam currents (6.25, 12.5, and 25 pA). The dwell times for all exposures were kept constant at 100 ns x 100 line integrations, resulting in a 10 μs overall dwell time. These conditions were chosen to reflect commonly-used experimental conditions implemented in acquiring high-resolution images at the highest possible magnifications for vitreous biological samples in SEM [147, 148, 150]. Each grid square took approximately 2.5 hours to image at these conditions (∼4 minutes per image). Focus for each grid square was manually set for the first tile of each tile set with a fixed focus throughout the rest of the exposures.

To ensure consistency, most of the SEM-exposed conditions (8 of 9) and their negative control were collected from a single vitrified grid (Grid 1). A second grid (Grid 2) was prepared using identical protocols to acquire additional data for the

1.2 kV (6.25 pA) condition, another negative control, and also the scanning pattern experiments (interleaved and raster, section 5.2.4.2).

5.2.4.2 SEM Alternative Scanning Conditions

For exposure to the SEM in different scanning sequences, the MAPS software could not be used. As described in our recent work on charge mitigation in the SEM [219], an external scan engine (Quantum Detectors) was used to control the scan coils of the microscope, with scripting using AutoScript (ThermoFisher scripting software) to control the scanning coils. The pattern for the interleaved scanning was modified from the pattern presented in section 4.2.5, to incorporate a jump of $j = 10$ pixels. This was changed to give a distance between subsequently scanned pixels that gave no overlap in Monte-Carlo simulations at the SEM conditions used (see section 5.3.1). For this exploratory comparison of interleaved scanning, SEM imaging was performed exclusively at an accelerating voltage of 5 kV and a beam current of 6.25 pA. Additionally, the dwell time distribution was 100 ns and 100 frame integrations to match the methods used in our previous work [219]. To ensure that all images were acquired with the same electron fluence between the different scanning conditions, the experiment did not incorporate any flyback delays.

5.2.5 Transmission Electron Microscopy of Single Particle Analysis Data Collection

Grids exposed to SEM were loaded into a Titan Krios G4i (ThermoFisher Scientific) operated at 300 kV for TEM imaging. The TEM was used in nanoProbe mode, with a Selectris energy filter (slit width of 10 eV) for data acquisition. Zero Loss Peak centring and tuning of the energy filter were conducted using the Sherpa software. Coma and astigmatism correction were performed using EPU.

Data were acquired at nominal magnification of 165 k×, corresponding to a nominal pixel size of 0.758 Å. The fluence applied to the sample was confirmed to be 40 $e^{-}Å^{-2}$ over vacuum. The Falcon IV detector was used in counting mode to collect ∼1368 EER detector frames over a 4.45 second exposure time (flux = 8.99 $e^{-}Å^{-2}$ s^{-1}). In total, 20,908 images were acquired across all SPA experiments (11,776 from grid 1, and 9,132 from grid 2). Data were acquired between a nominal defocus of -1.6 to -3.0 µm in 0.2 µm increments.

5.2.6 Single Particle Analysis Data Processing

All datasets were processed independently within a single RELION 4 project to ensure consistency. A flowchart of processing steps is shown in Figure 5.1. All micrographs (approximately 1500 per condition) were imported and beam-induced motion corrected using RELION's implementation of MotionCorr [307]. CTF correction was then applied using CTFfind 4.1 [308].

Using RELION, ∼1000 apoferritin particles were manually picked from the negative control dataset and a 2D classification job was used to create a template for subsequent template-based automatic picking on all micrographs. Particles were picked across all micrographs (approximately 500,000 per condition). These particles were extracted in Bin4 (3.03 Å $pixel^{-1}$) and subjected to an initial 2D classification into 50 classes to remove obvious non-particle classes and artefacts. 2D classes that clearly represented apoferritin particles were selected (approximately 350,000 per condition) for 3D classification into 5 classes at Bin4. The reference structure was an initial model created from a subset of 10,000 negative control particles, and low-pass filtered to 60 Å. 3D classification was completed both in octahedral (O) symmetry, and without symmetry (C1) for comparison.

An initial refinement was completed after selecting classes which exhibited clear secondary structure in C1. In all classification steps, the aim was to pick approximately similar numbers of particles from each dataset (taking the control as a

reference to define the number), to facilitate an approximately equal comparison between the conditions during data processing (the numbers of particles in each class can be found in Appendix Tables A.2 and A.3). The classifications were generally completed in C1, as this enabled clearer distinction between particle classes with and without visible structural features.

Further 3D classification and CTF refinements were completed at Bin2 to ensure the negative control dataset reached the Nyquist resolution (3.02 Å). At Bin1, another C1 3D classification, followed by several rounds of CTF refinement and 3D auto-refine, were performed to obtain a final structure. A script was applied to calculate the Henderson and Rosenthal B-Factor for each dataset, as a measure of particle quality independent of the number of particles used [309]. This process was repeated 3 times for each dataset (technical replicates) in order to give an error measurement for each B-factor. The B-factor was fitted to the straight-line portion of the plot, from a minimum of >1600 particles. This ensured that no overestimation of the B-factor took place due to low resolution estimates based on small numbers of particles, and is the standard method for computing the B-factor [157, 196, 248, 310].

The standard error of the B-factor was determined by propagating the standard error of the slope from the linear model. For conditions with multiple technical replicates, the final reported B-factor and its associated standard error are the mean and standard error of the mean (SEM) of the values calculated from each individual replicate.

To determine if the observed differences in B-factors between experimental conditions were statistically significant, an Analysis of Covariance (ANCOVA) was performed. This test compares the slopes of the regression lines across all groups. The slopes of all conditions were compared in a pairwise fashion using the Tukey test.

To visually assess the quality and local fit of each reconstruction, the atomic model of human heavy-chain apoferritin (PDB: 8CPV, [311]) was fitted into the cryo-EM

density using Chimera [312]. This allowed for a direct, residue-specific evaluation of the map quality and damage. A near-identical data processing workflow was also employed for the Raster and Interleaved datasets, as presented in section 5.3.4.

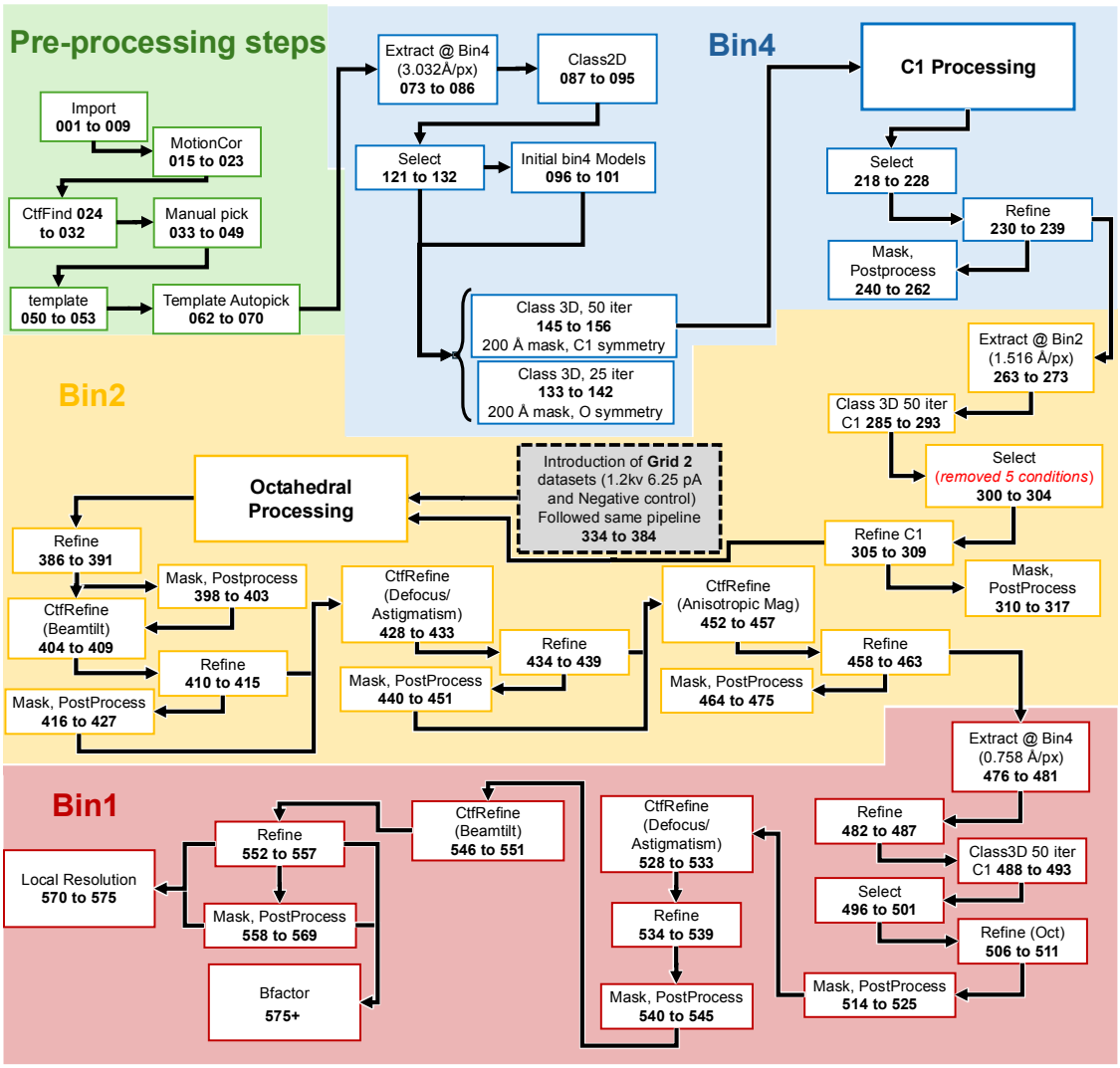


Figure 5.1: **Schematic of processing workflow for presented data**. The Pre-processing steps (green), Bin4 (blue), Bin2 (yellow), and Bin1 (red) are outlined. Bold numbers indicate job numbers, for comparison to the table and supplementary figures for individual job results (Tables A.2 and A.3). Note the inclusion of the Grid 2 data in the Bin2 section (**334** to **384**).

5.3 Results

5.3.1 Simulation of low-energy SEM electrons in Vitreous Ice

Monte-Carlo simulations of electrons interacting with 100 nm of vitreous ice are shown in Figure 5.2. Figures 5.2A-I show a matrix of the three acceleration voltages and three currents used in this work for exposure in the SEM. The three different acceleration voltages simulated (1.2 kV, 3 kV, and 5 kV) show a varied distribution of energy in the vitreous ice, and a different pattern of electron trajectories.

The 1.2 kV acceleration voltage deposits the most energy per electron, with a mean of 1.04 keV deposited per incident electron (approximately 87% of the energy of each incident electron). This appears to extend over approximately 60 nm in the z-axis. In contrast, both the 3 kV and 5 kV acceleration voltages deposit their energy throughout the entire 100 nm thickness of the vitreous ice in z, with a lower mean energy deposition per incident electron of 0.68 keV and 0.39 keV (22% and 8% of incident electron energy, respectively).

The energy deposition contours depicted in Figures 5.2J-K indicate that, as expected, the greater the acceleration voltage, the less energy is deposited in this thin amorphous sample per incident electron. The lateral spread of energy deposition (visualised through the white-coloured 90% energy contours) also varies with voltage. The 1.2 kV beam deposits energy in a diameter of approximately 55 nm at its widest point, at a depth of $\sim$ 40 nm.

At 3 kV, the lateral spread is over the entire z-axis, and has a diameter of almost 90 nm at the bottom surface of the 100 nm thick vitreous ice. The 5 kV deposits 90 % of the energy in a narrower x range, with a diameter of around 30 nm at the bottom surface.

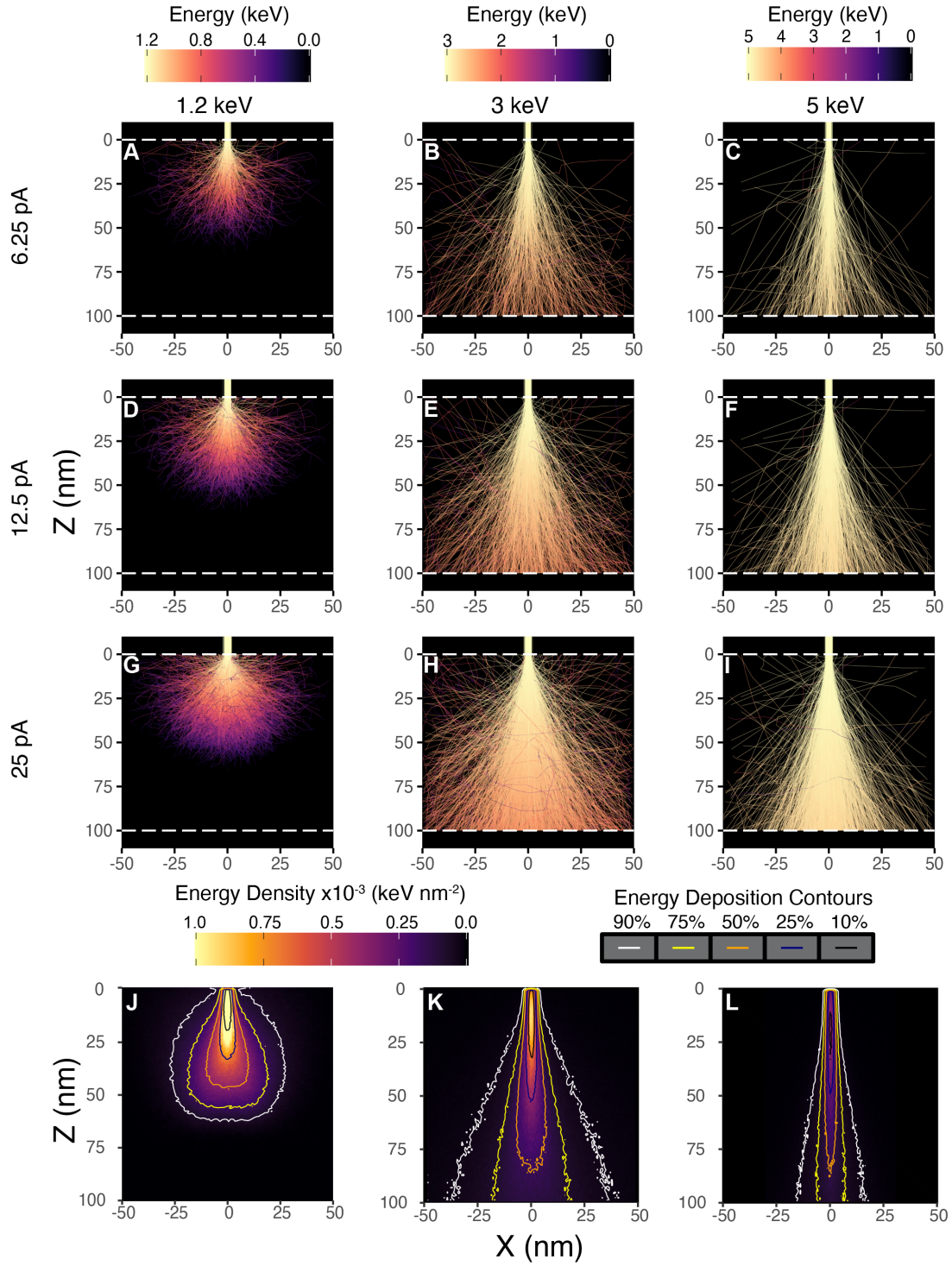


Figure 5.2: **Monte Carlo simulations of electron trajectories and energy deposition at combinations of SEM acceleration voltages and currents applied to a sample of 100 nm thick vitreous ice.** Panels **A-I** show all electron trajectories plotted as lines, projected and viewed in the xz plane. Each electron trajectory is coloured by the energy the electron has as it moves through the sample. Columns indicate the different incident electron energies used. (*Figure caption continued on the next page*).

Figure 5.2: (Column 1 (**ADG**) = 1.2 keV, column 2 (**BEH**) = 3 keV, and column 3 (**CFI**) = 5 keV). Rows 1 (**ABC**), 2 (**DEF**), and 3 (**GHI**) indicate the different number of electrons used for each dwell time, corresponding to 6.25 pA (384 incident electrons), 12.5 pA (768 incident electrons), and 25 pA (1536 incident electrons), respectively. Dashed horizontal white lines at 0 and 100 nm indicate the top and bottom surfaces of the simulated vitreous ice. Note that each colour scale of energy is adapted to include the incident energy. The final row (**JKL**) consists of energy density maps from 2000 simulated electron trajectories for 1.2 keV (**J**), 3 keV (**K**), and 5 keV (**L**) electrons, coloured by the absorbed energy density. The legend is common to all three plots. The contours show the boundaries within which 10, 25, 50, 75, and 90 % of the absorbed energy is located.

The less-than-complete energy deposition (1.04 out of 1.2 keV, = 87%) observed at 1.2 kV acceleration voltage is primarily due to the substantial multiple scattering and backscattering of incident electrons from the top surface of the vitreous ice. At greater acceleration voltages, this effect diminishes. Instead, transmission through the 100 nm ice layer becomes the dominant path, with most electrons passing through the sample without depositing their full energy.

The inelastic scattering cross section also offers an explanation of these simulations (as discussed in section 3.3, and using equations 3.5 - 3.13).

The physical basis for this difference in penetration depth between acceleration voltages is the energy-dependence of the inelastic mean free path (Λ_i, the average distance an electron travels between damaging inelastic scattering events). Using the scattering model established in section 3.3 (equations 3.5 - 3.13), the calculated Λ_i values for amorphous ice at 1.2, 3, and 5 keV are approximately 4.2, 9.0, and 13.9 nm, which agree well with the Monte Carlo simulated Λ_i values of 2.4, 7.2, and 13.0 nm (the consistent underestimation of the calculated Λ_i values with respect to the Monte-Carlo simulated values can likely be attributed to inaccuracies in the cross-section equations at low incident electron energies).

These findings confirm that the shallow penetration of the 1.2 keV beam is a direct consequence of its extremely short mean free path, which causes the majority of its energy to be deposited near the sample surface.

5.3.2 Dose Applied to the Sample

To compare sample damage across different acceleration voltages, electron fluence (e^{-}Å^{-2}) is an unsuitable metric on its own. A direct comparison using only fluence is misleading because the energy deposited per incident electron is strongly energy dependent.

As demonstrated by the simulations in Section 5.3.1, electrons at lower acceleration voltages transfer significantly more energy to the sample. Therefore, to enable a meaningful comparison between the SEM conditions tested in this work and established 300 kV TEM benchmarks [157, 248, 313, 314], the incident fluence was converted to absorbed dose (energy per unit mass, measured in MGy). This conversion follows the methodology established by Henderson [313, 315].

The fluences applied to the sample in SEM are 0.26, 0.53, and 1.05 e^{-}Å^{-2} for the 6.25, 12.5, and 25 pA, respectively. Using the continuous slowing down approximation range data from ICRU, the range (r_0) for electrons in water [316] (Table A.3 '$\rho\ r_0$') can be converted to amorphous ice using density ($\rho = 0.94$ g cm^{-3} [306]):

$$r_0\ (\text{cm}) = \frac{\rho\ r_0}{\rho}\ \left(\frac{\text{g cm}^{-2}}{\text{g cm}^{-3}}\right). \tag{5.1}$$

The product of the range, the fluence (f, in e^{-}Å^{-2}, converted to electrons cm^{-2} by multiplying by 1×10^{16}), charge of the electron ($e = 1.6 \times 10^{-19}$ C), and acceleration voltage (V in JC^{-1}), gives the energy deposited in units of Joules per cm^3:

$$\text{Energy Density (J cm}^{-3}) = \frac{f \times 10^{16}\ eV}{r_0}\ \ \frac{(\text{Å}^{-2})(\text{C})(\text{JC}^{-1})}{(\text{cm})}. \tag{5.2}$$

Division by the density (in g cm^{-3}) and multiplication by 1×10^3 gives the result in Joules per kilogram, also known as Gray (Gy), the measurement of dose:

$$\text{Dose (J kg}^{-1}, \text{Gy}) = \frac{\text{Energy Density}}{\rho} \times 10^3\ \ \frac{(\text{J cm}^{-3})}{(\text{g cm}^{-3})}. \tag{5.3}$$

The results of the fluence, flux, and dose applied using each condition of SEM scanning is given in Table 5.1[1].

[1]To put the magnitude of these figures into perspective, the calculated doses in SEM are

Table 5.1: Calculated electron interaction and radiation dose parameters for various beam conditions. The table compares low-voltage SEM at different beam currents against a standard acquisition for a 300 kV TEM in amorphous ice. The mass thickness range (ρr_0) is derived from the ICRU database [316]. † The value for 1.2 kV is a linear interpolation, as this energy is between the database values of 1 kV and 1.5 kV. The final column estimates the equivalent fluence of 300 kV TEM irradiation needed to match the calculated SEM doses.

Accel. Voltage (kV)	Current (pA)	Fluence (e^-/Å^2)	Range (ρr_0, [316]) (g cm^{-2})	Density [306] (g cm^{-3})	Stopping Dist. (cm)	Stopping Dist. (nm)	Energy Density (J cm^{-3})	Dose (Gy)	Dose (MGy)	300kV Equiv. Fluence (e^-/Å^2)
1.2	6.25	0.26	†6.00×10^{-6}	0.94	6.38×10^{-6}	64	7.93×10^{4}	8.43×10^{7}	84.3	15.2
1.2	12.5	0.53	†6.00×10^{-6}	0.94	6.38×10^{-6}	64	1.59×10^{5}	1.69×10^{8}	168.7	30.4
1.2	25	1.05	†6.00×10^{-6}	0.94	6.38×10^{-6}	64	3.17×10^{5}	3.37×10^{8}	337.3	60.8
3	6.25	0.26	3.10×10^{-5}	0.94	3.30×10^{-5}	330	3.84×10^{4}	4.08×10^{7}	40.8	7.4
3	12.5	0.53	3.10×10^{-5}	0.94	3.30×10^{-5}	330	7.68×10^{4}	8.17×10^{7}	81.7	14.7
3	25	1.05	3.10×10^{-5}	0.94	3.30×10^{-5}	330	1.54×10^{5}	1.63×10^{8}	163.3	29.4
5	6.25	0.26	7.54×10^{-5}	0.94	8.02×10^{-5}	802	2.63×10^{4}	2.80×10^{7}	28.0	5.0
5	12.5	0.53	7.54×10^{-5}	0.94	8.02×10^{-5}	802	5.26×10^{4}	5.60×10^{7}	56.0	10.0
5	25	1.05	7.54×10^{-5}	0.94	8.02×10^{-5}	802	1.05×10^{5}	1.12×10^{8}	111.9	20.0
300	NA	40.00	8.65×10^{-2}	0.94	9.20×10^{-2}	9.20×10^{5}	2.09×10^{5}	2.22×10^{8}	222.1	40.0

5.3.3 SEM Exposure Causes Loss of High-Resolution Information

The resolution achievable in cryo-EM SPA depends on a number of factors, including sample quality, ice thickness, microscope alignment, and imaging conditions.

To validate the direct comparability of data between these two grids, two controls were implemented. Firstly, negative control SPA datasets were collected from both Grid 1 and Grid 2. Secondly, to estimate potential variations in ice thickness, the mean intensity of the raw EFTEM micrographs (converted by the acquisition software as 'dose on camera', analogous to the fluence on camera) was plotted for

conceptually equivalent to the radiation absorbed less than 1 metre from the epicentre of a nuclear explosion. This analogy highlights the extreme energy density delivered by a focused electron beam and the violent nature of the imaging process at the molecular scale.

each dataset (Appendix Figure A.17). This value is used as a proxy for comparative ice thickness and was found to be relatively consistent across all experimental conditions from both grids (19.4 ± 2.7 $e^{-}Å^{-2}$). Therefore, the data from both grids are considered to be comparable for this analysis.

To test the impact of SEM exposure, different grid squares of an apoferritin single-particle grid were exposed to a matrix of SEM imaging conditions, leaving squares unexposed as negative controls. An overview of the experimental grid, indicating the location of each SEM exposure condition, is shown in Figure 5.3.

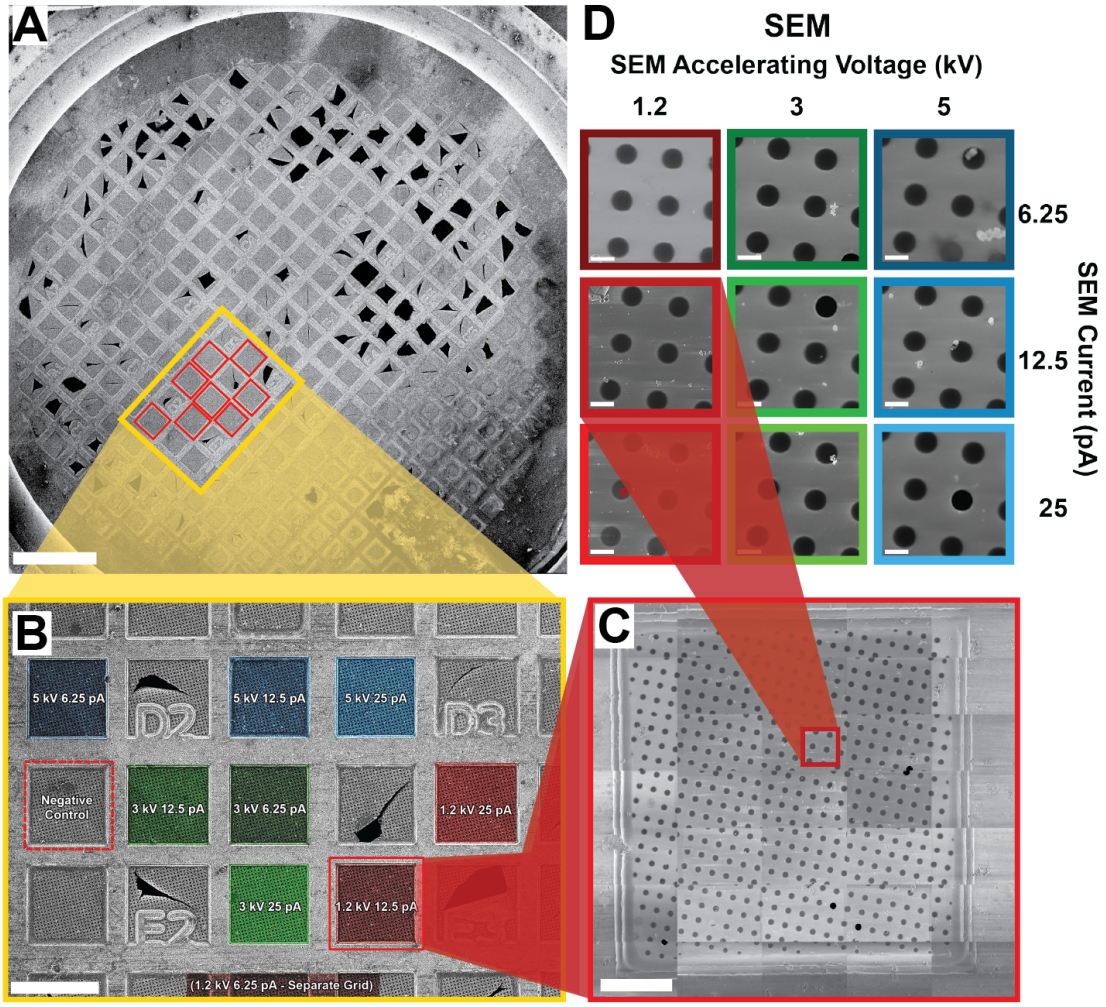


Figure 5.3: **Workflow for exposure to SEM beam. A** Overview of the finder grid in SEM to locate suitable non-broken grid squares with relatively thin ice that are suitable for downstream TEM imaging. Chosen region indicated with a yellow box and magnified in **B**. The selected grid squares are coloured for their respective SEM exposure parameter, with red (1.2 kV), green (3 kV), and blue (5 kV) at 6.25 pA, 12.5 pA, and 25 pA. Note that the images have been mirrored to allow the numerals to be read. The 1.2 kV 12.5 pA grid square from **B** is magnified in **C**, showing the experimentally-scanned entire grid square 7×5 montage, taken using MAPS software. Each tiled exposure is 6144×4096 pixels. **D** shows an enlarged region from one tile of the 1.2 kV 12.5 pA. A similarly enlarged region from the middle of all SEM imaging conditions is also shown, demonstrating that focus is achieved and maintained throughout the imaging. Scale bars are **A** 300 µm, **B** 100 µm, **C** 20 µm, **D** 2 µm.

Following SEM irradiation, each of these grid squares were relocated in the TEM, using the finder grid to ensure the locations were correct, and a full SPA dataset was

collected (detailed in section 5.2.5). When compared to the negative control by eye, the TEM micrographs do not appear to show any immediately observable damage to the apoferritin, as demonstrated in Figure 5.4. Additionally, no bubbling is observed, as is common with large electron fluences in TEM of biological molecules in vitreous ice. The Thon rings of the collected data are fitted up to a spatial frequency of $\sim$1/0.17 Å^{-1} ($\sim$6 Å), and also display the 'water ring' (a ring of brightness in the CTF), consistent with ice thicker than $\sim$50 nm [317, 318].

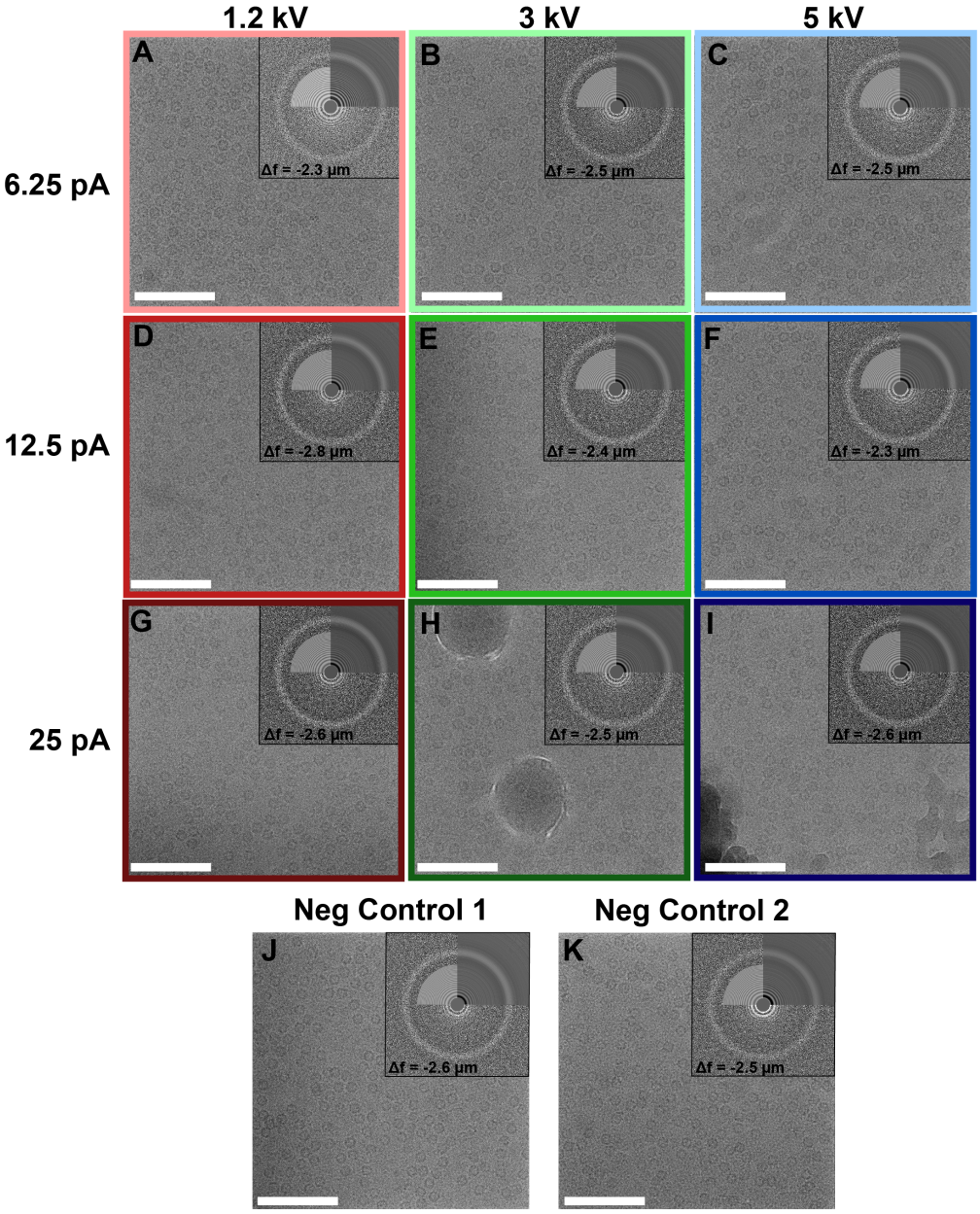


Figure 5.4: **Results of the CTF estimation on motion-corrected micrographs from each dataset.** All micrographs were chosen at the same defocus ∼2.5 µm, displaying Thon rings fitted up to a spatial frequency of 1/0.17 $Å^{-1}$ (∼6 Å), inset in the top right of each micrograph. The 'water ring' is visible at 1/0.25 $Å^{-1}$ (3.9 Å). Apoferritin molecules are clearly visible at this defocus as circular densities. Scale bars all 100 nm.

To select a homogeneous particle set for high-resolution refinement, multiple rounds of 3D classification were employed. A key methodological decision was to perform

these classifications without imposing the known octahedral (O) symmetry all datasets. Initial tests revealed that applying high symmetry was problematic in two ways: firstly, it averaged out and effectively masked localised, non-symmetrical damage on the particles in the classes. Secondly, for datasets with significant damage, it created artificial 'symmetrised noise' classes (Figure 5.5A) that appeared coherent but lacked any genuine high-resolution structural information. Therefore, to obtain an unbiased and more interpretable assessment of particle quality, all critical 3D classification steps were performed in C1 (Figure 5.5B).

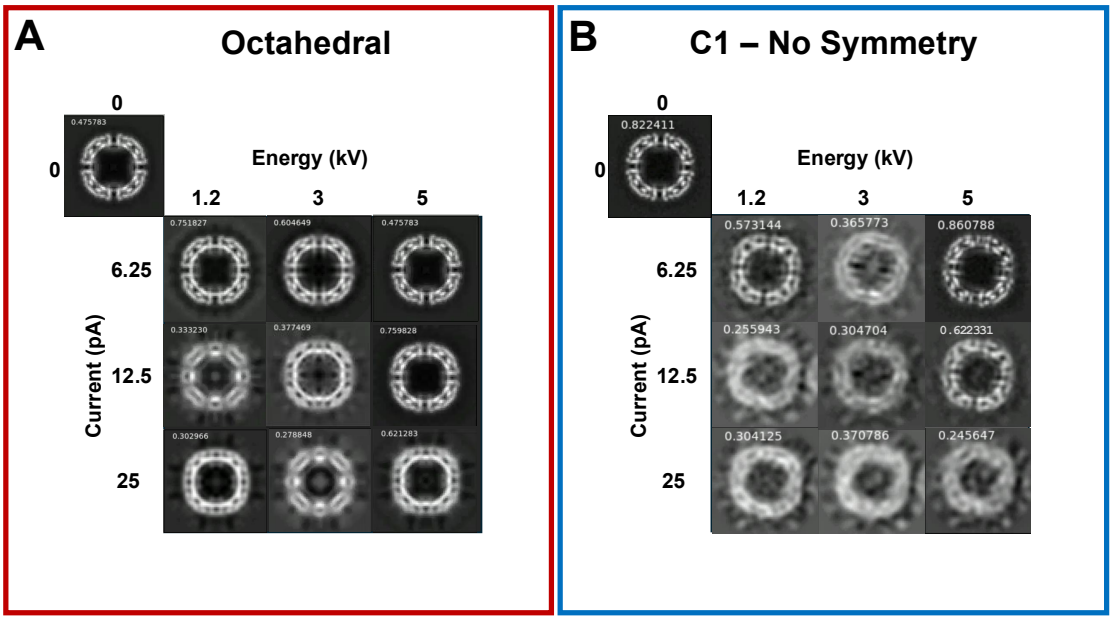


Figure 5.5: **Results of initial 3D classification at Bin4**. Images are displayed in a matrix of their respective SEM irradiation. Each image displayed is the most populated class (with the number corresponding to the fraction of the total population in the top left of each image). A clear difference is shown between the results of 3D classification using octahedral symmetry (**A**), and without symmetry applied (**B**). The negative control for grid 1 can be seen in the top left (0 kV, 0 pA). The entire 3D class data can be seen in Appendix Figures A.18 and A.19.

This approach, applied initially to particles binned by a factor of four, immediately revealed the extent of the structural degradation across the different SEM-irradiation conditions. The full ensemble of these initial 3D classes is shown in Figure 5.5. Crucially, for the most heavily irradiated datasets – specifically the 1.2 kV (12.5

and 25 pA), 3 kV (12.5 and 25 pA), and 5 kV (25 pA) conditions – no classes could be identified that contained sufficient secondary structure detail to permit stable alignment. Consequently, these datasets could not be aligned during the refinement. This represented a practical dose limit beyond which structural information was irrecoverable. These classes were therefore not processed any further.

Following this initial sorting, only the viable particle sets from the remaining conditions – those that produced well-resolved classes with clear secondary structure – were selected for further analysis. After re-extraction at the calibrated pixel size (Bin1, 0.758 Å pixel^{-1}) and further rounds of classification (see Figure 5.1 and Appendix Table A.2), these curated datasets were subjected to final rounds of high-resolution 3D refinement and CTF refinement with octahedral symmetry imposed, to produce the final map for each condition.

The resulting reconstructions, presented in Figure 5.6A, reveal a clear trend: increasing the SEM exposure generally leads to a progressive degradation in the achievable resolution, from ∼2.7 Å in the non-irradiated control, to ∼4.2 Å in the most damaged – yet still successfully refined – dataset. This loss of high-resolution information is quantitatively confirmed by the corresponding Fourier Shell Correlation (FSC) curves to estimate the resolution shown in Figure 5.6B.

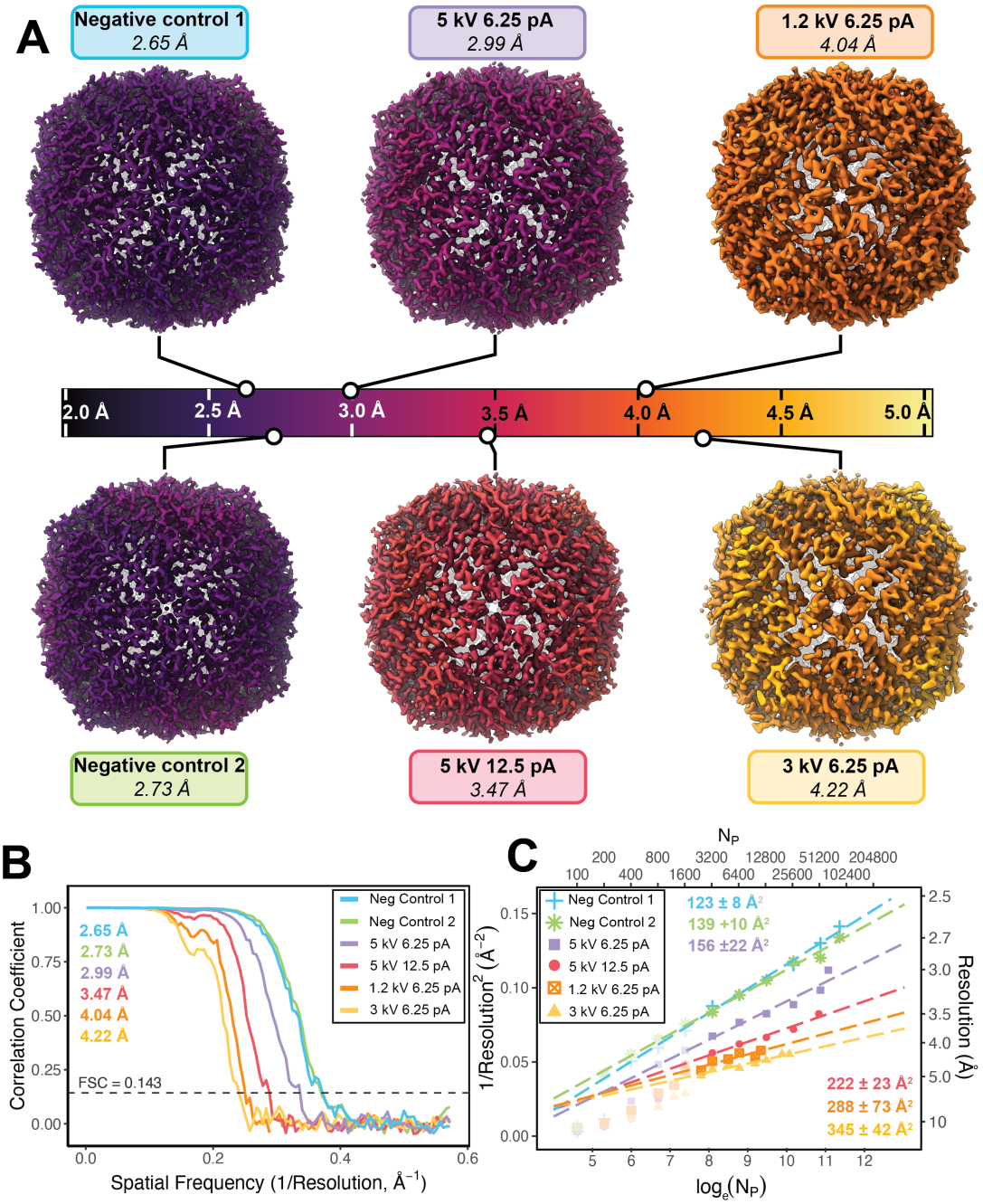


Figure 5.6: **Damaged apoferritin reconstructions from separate SEM-exposed grid squares**. **A** Refined cryo-EM maps of apoferritin (all displayed at the mean threshold + 4σ) from data acquired with different pre-exposure to SEM, coloured by their local resolution on the scale shown. The condition of SEM exposure (or negative control) and estimated resolutions are indicated in the label of each reconstruction. The numbers of particles used for each final model are (clockwise from Negative control 1, $\times 10^3$) 84, 63, 11, 23, 49, and 84. **B** Fourier shell correlations (FSCs) of separately refined half maps from the datasets from each SEM exposure condition. **C** Quantification of SEM-induced damage by B-factor analysis. 3 replicates were completed per each data point. *Caption continued on next page.*

Figure 5.6: *Caption continued from previous page:* Fits (dashed lines) used to determine an overall B-factor from the slope with >1600 particles to ensure the linear portion of the data were used (full opacity points). Error bars not displayed for clarity. A larger version of this figure with error bars can be found in the Appendix (Figure A.20).

To quantitatively assess the structural damage from each SEM exposure condition, an overall B-factor was calculated for each dataset by following the method of Rosenthal and Henderson [309]. This method eliminates dependence on the number of particles and allows for direct comparison between different sized datasets.

In Figure 5.6C, the squared inverse resolution of reconstructions from random particle subsets is plotted against the subset size on a logarithmic scale, a relationship that is theoretically linear [309]. By performing linear regression, B-factors were calculated for each condition. The non-irradiated control datasets (1 and 2) yielded B-factors of 123 and 139 $Å^2$ respectively, whereas the SEM-exposed conditions yielded higher B-factors, ranging from 156 - 345 $Å^2$. These data provide a quantitative demonstration that SEM exposure leads to a loss of high-resolution information.

To statistically validate the observed differences in damage, an Analysis of Covariance (ANCOVA) was performed to compare the B-factors across all six successfully refined datasets. The analysis revealed a highly significant difference in the gradient of all conditions ($F(5, 105) = 25.86$, $p < 0.001$), confirming that the SEM exposure strategy has a quantifiable impact on the final B-factor.

The calculated B-factor and standard error for each condition are presented in the bar chart in Figure 5.7A. To determine which specific conditions differed to one another, pairwise statistical tests were performed, with the results visualised as a grid in Figure 5.7B. Notably, both negative controls exhibited significantly lower B-factors than all SEM-irradiated samples (with the exception of negative control for grid 2 compared to the 5 kV 6.25 pA dataset, collected on grid 1). The 3 kV 6.25 pA condition resulted in the most damaged particles, with a B-factor

of 345 ± 42 Å^2, while the negative controls were the best quality samples with B-factors of 123 ± 8 and 139 ± 10 Å^2.

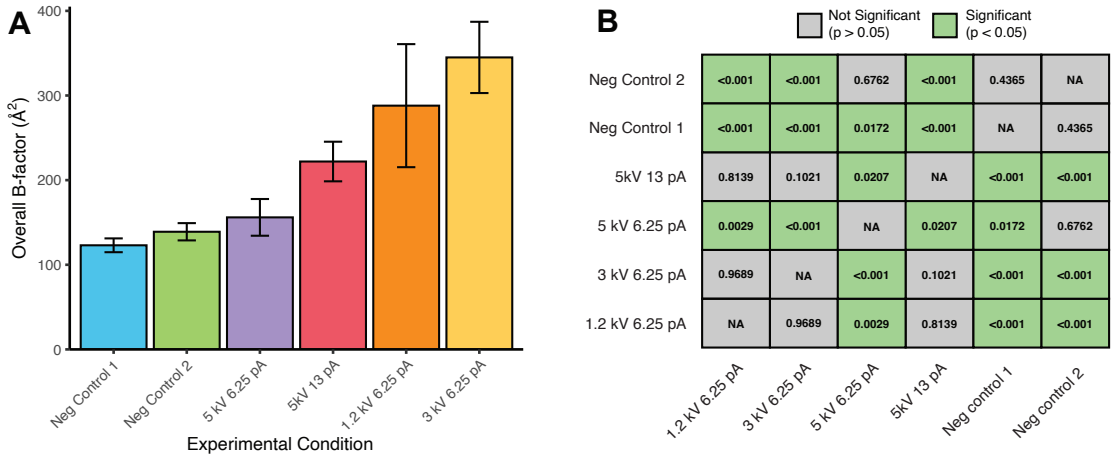


Figure 5.7: **B-factor analysis results and statistical tests**. **A** The B-factors as presented in A.20C, ordered from lowest (least damaged) to highest (most damaged). **B** results of the ANCOVA test, assessed at the 95% confidence level. Green squares indicate a statistically significant difference between the B-factors ($p < 0.05$).

As a complementary local measure of damage, the density of specific radiation-sensitive amino acid residues was also examined. It is well-established that amino acids with acidic side-chains – particularly Glutamic acid (Glu) and Aspartic acid (Asp) – are highly susceptible to decarboxylation upon electron or x-Ray irradiation, which results in a measurable loss of side-chain density in the reconstructed map [319–322]. To assess this effect for this dataset, a high-resolution model of apoferritin (PDB: 8CPV [311]) was fitted into each reconstructed map. As shown in Figure 5.8, visual inspection of the density at specific locations, such as Glu101 and Asp126, reveals a clear loss of side-chain electron density in the SEM-exposed datasets when compared to the non-irradiated controls 5.8.

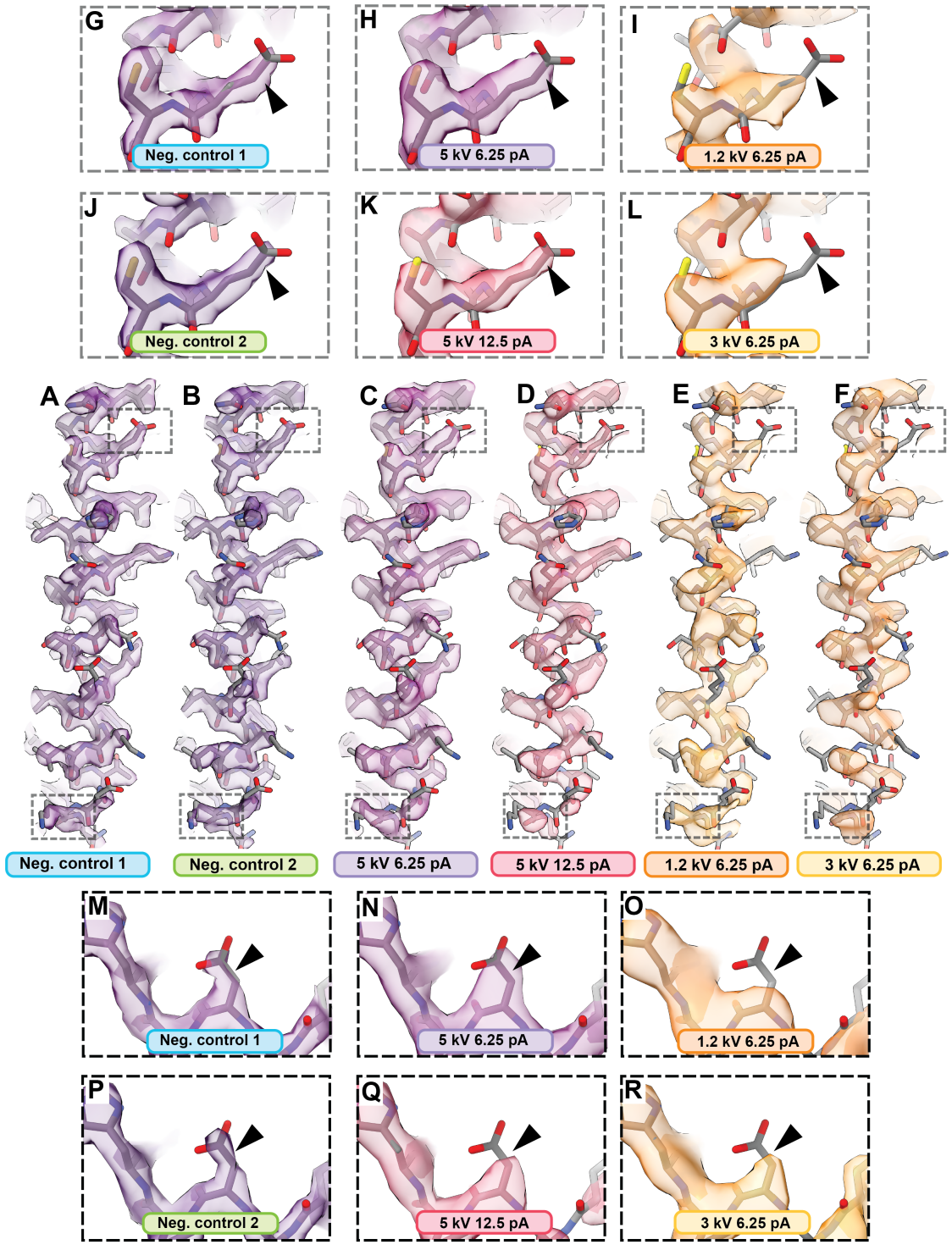


Figure 5.8: **Apoferritin model fit within the reconstructed maps showing radiation damage to acidic side chain residues**. Human heavy-chain apoferritin model (PDB 8CPV [311]) is shown fitted into an alpha helix (residues 94-126) of reconstructed maps (all displayed at the mean threshold + 4σ) for **A** negative control 1 (from grid 1), **B** negative control 2 (from grid 2), **C** 5 kV 6.25 pA, **D** 5 kV 12.5 pA, **E** 1.2 kV 6.25 pA, and **F** 3 kV 6.25 pA SEM irradiated datasets. The FSC-estimated resolution decreases from left to right. (*Figure caption continued on the next page*).

Figure 5.8: Dashed boxes on the top and bottom of each alpha helix are enlarged, displaying areas with a Glutamic acid residue, Glu126 (**G-L**), or an Aspartic acid residue, Asp101 (**M-R**), respectively. A clear loss of density around the side chain's terminal carboxylic acid group can be seen compared to the negative controls (black arrows).

To establish if a direct quantitative relationship between the energy deposited by the SEM and the resulting structural degradation exists, the overall B-factor (Figures 5.6C and 5.7 A) for each dataset was plotted against dose in MGy, calculated using Table 5.1. This plot of damage rate (gradient in units of $Å^2$ MGy^{-1}) shows an overall positive linear correlation between Dose and B-factor. This is consistent with observations from both X-ray/electron crystallography and single particle TEM data that show that structural disorder (and thus B-factor) increases proportionally to the applied dose [125, 322–324].

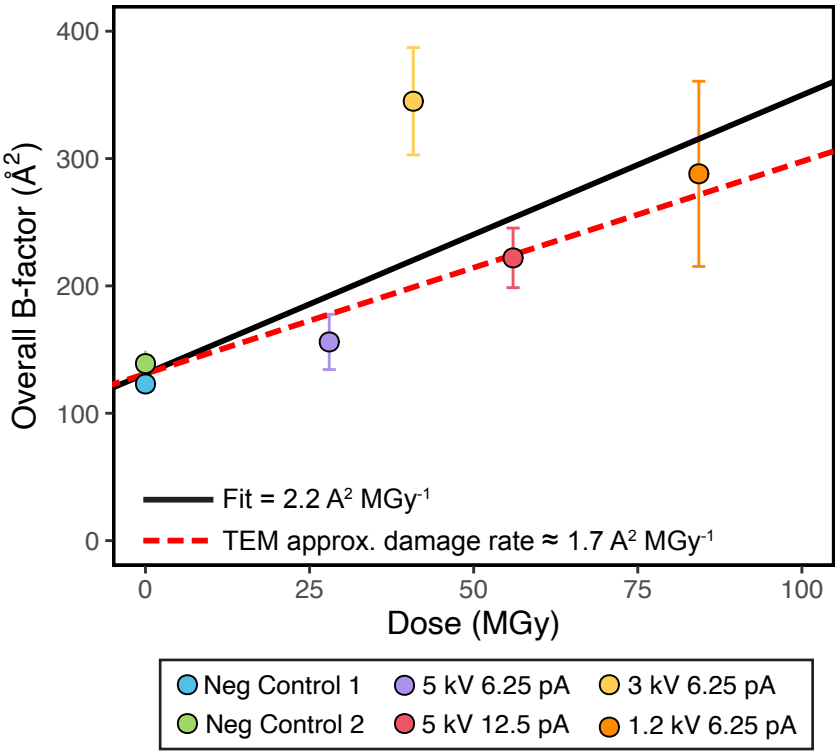


Figure 5.9: **Correlation between applied SEM dose and structural damage measured as B-factor.** The overall B-factor for each successfully refined dataset is plotted against the calculated absorbed dose from the initial SEM exposures at different conditions (using equations from 5.1). The data shows a linear trend fitted to all data (black solid line 2.2 Å^2 MGy^{-1}), and the approximate TEM damage rate, according to [79, 125] of ∼1.7 Å^2 MGy^{-1}. The intercept value is set as the mean of the negative control B-factors (131 Å^2).

Linear regression of the data yields an overall experimentally-determined damage rate (also called the coefficient of sensitivity, [325]) of 2.2 Å^2 MGy^{-1}. The 3 kV 6.25 pA condition seems to have a much greater B-factor than expected, and does not fit the overall trend of the rest of the data, which should be linear with increasing dose [157, 178].

Exclusion of the 3 kV dataset from the fit gives a value close to the expected damage rate of 1.7 Å^2 MGy^{-1} for cryogenic TEM data [79, 125, 157]. Additionally, measurements of damage in cryogenic X-ray crystallography of apoferritin suggest a damage rate of ≈ 1.4 Å^2 MGy^{-1} [324, 325].

To investigate this trend, the cumulative energy deposition from a scanning beam was simulated. By computationally overlapping the single probe energy profiles in Figure 5.2 J-L at 3.85 nm intervals, the accumulation of deposited energy can be visualised from successive beam positions. The resulting cumulative damage profiles for the 1.2, 3, and 5 kV beams are shown in Figure 5.10.

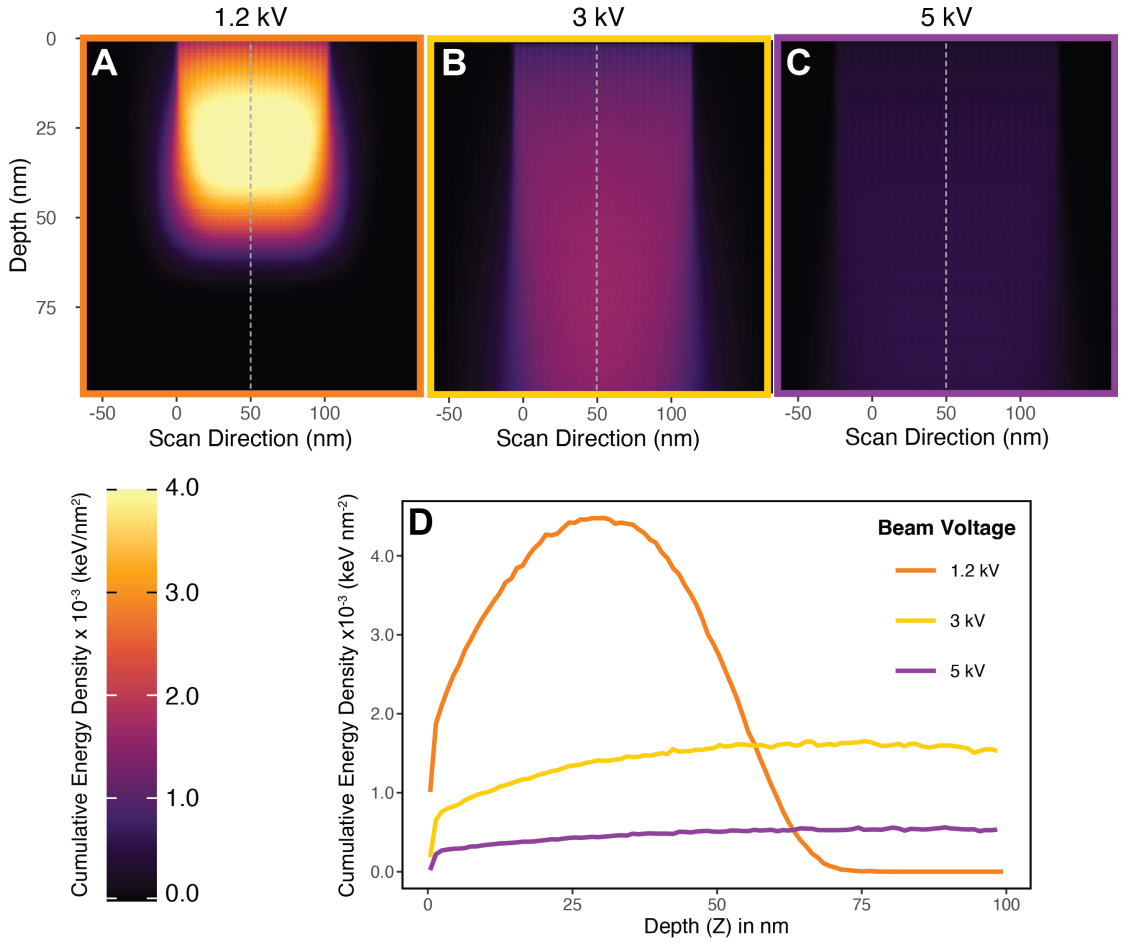


Figure 5.10: **Title**. Overlapped scan simulations are shown for **A** 1.2 kV, **B** 3 kV, and **C** 5 kV. The cumulative energy deposition is displayed, based on the addition of overlapping distributions from Figure 5.2J-L. The cumulative energy density from the middle of the scanned row (gray dashed line) as a function of depth is shown in **D**.

The vertical line profiles (Figure 5.10D) show that in 100 nm of ice, although the 1.2 kV overlaps do deposit the most energy, they only do so over 60 nm, whereas the 3 kV appears to deposit energy evenly over the whole thickness of the layer

of vitreous ice due to the overlap of adjacent beam positions. The 5 kV does not deposit as much energy as the 3 kV, although it does also deposit the energy evenly over the thickness (see appendix section A.5.1 for preliminary tomography data).

This analysis provides clear evidence of a damage rate for this SEM-based workflow, linking the calculated dose to a measurable loss of high-resolution information.

5.3.4 Exploratory Damage Mitigation Using Interleaved SEM Scanning

To further test the damage processes in the SEM and extend the research presented in Chapter 4 on alternative STEM scanning strategies, an interleaved scanning pattern was applied to the same apoferritin sample (as described in section 5.2.4). After careful consideration of the Monte Carlo simulated electron trajectories and energy deposition (section 5.3.1), 5 kV and 6.25 pA were selected as the SEM conditions, to ensure that high-resolution information was recoverable in both datasets.

The same overall workflow and data processing methodology was followed as for the data presented in section 5.3.3, with only one methodological change required for a valid comparison: both scans were performed using frame integrations (100 ns dwell $\times$ 100 frames) instead of line integrations. This is because a line integration is not possible to incorporate into an interleaved scan in a meaningful way, negating any beneficial effect of using an interleaved pattern. Therefore a raster-scanned frame integration (of 100 ns $\times$ 100 frame integrations) was compared to an interleaved frame integration (100 ns $\times$ 100 frame integrations).

As mentioned in section 5.2.4.2, a jump of $j = 10$ was used for the interleaved scan in this work. This corresponds to a 38.5 nm separation between consecutively scanned pixels, a distance sufficient to prevent overlap of the 90% contours of primary energy deposition volumes within 100 nm thick ice (see Figure 5.2L for the relevant energy deposition profile).

The same methods were used to assess the impact of SEM-irradiated damage as presented in the previous section (5.3.3) - namely the FSC-estimated resolution and B-factor plots (Figure 5.11), followed by site-specific damage at the acidic residues of a fitted atomic model (Figure 5.12).

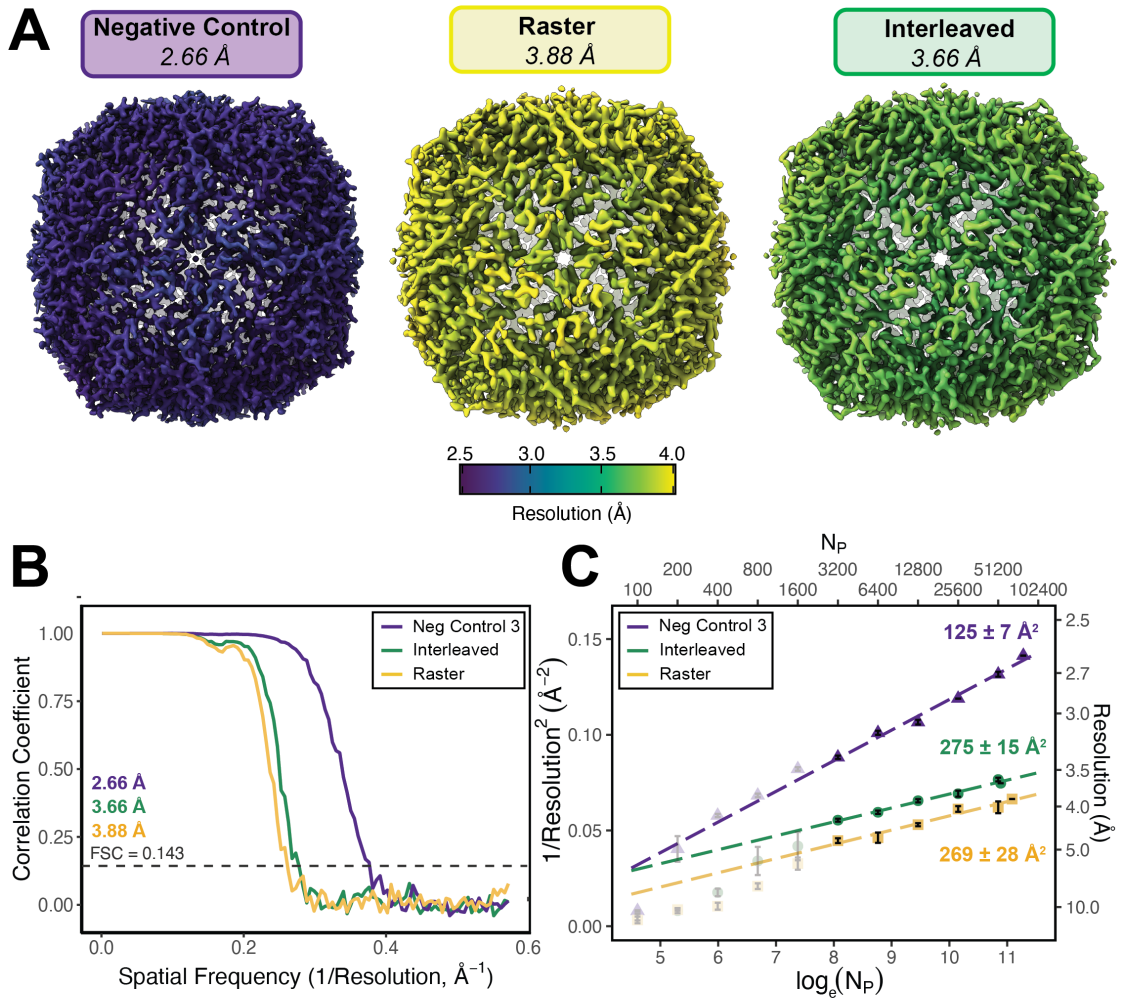


Figure 5.11: **Apoferritin reconstructions from raster and interleaved SEM-exposed grid squares**. **A** Refined cryo-EM maps of apoferritin (all displayed at the mean threshold + 4σ) from data acquired with different pre-exposure to either a raster, or interleaved scanning pattern in SEM, coloured by their local resolution on the scale shown. The scan pattern of SEM exposure (or negative control) and estimated resolutions are indicated in the label above each reconstruction. The numbers of particles used for each final model are (left to right, $\times 10^3$) 81, 71, and 57. **B** FSCs of separately refined half maps of the interleaved, raster, and negative control datasets. **C** Quantification of SEM-scan pattern-induced damage by B-factor analysis. Linear fits (dashed lines) are used to determine an overall B-factor from the slope. 3 replicates were completed per each data point, with standard error bars shown for each resolution point. Fits (dashed lines) used to determine an overall B-factor from the slope with >1600 particles to ensure the linear portion of the data were used.

As expected, the negative control dataset achieves a similarly high-resolution (2.66 Å)

to the negative control datasets in Figure 5.6. However, the 5 kV 6.25 pA irradiated in both raster and interleaved dropped to between 3.66 - 3.88 Å resolution. This is unexpected because the previous 5 kV 6.25 pA condition (Figure 5.6B) was resolved to 2.99 Å. This effect does not appear to be dependent on the particle number, as a similar number of particles were used across the data processing between all of these 5 kV 6.25 pA conditions (see Appendix Tables A.2 and A.3). This is confirmed by the different B-factors between these datasets of 156 ± 22 Å^2 for the line-integrated previous data and ∼270 Å^2 for the raster and interleaved frame-integrated data.

The results for the interleaved and raster SEM-scanned datasets may still be compared to each other. The B-factor comparison is shown in Figure 5.11C. The conventional raster scan yielded a B-factor of 269 ± 28 Å^2, whereas the interleaved scan produced a B-factor of 275 ± 15 Å^2, suggesting there is no difference in the efficiency of the particles between the raster and interleaved datasets. This is confirmed by the ANCOVA and Tukey test that showed the raster and interleaved B-factors are not statistically significantly different from each other ($p = 0.98$). This indicates that both SEM scanning strategies are statistically indistinguishable from each other using the B-factor as a measure of damage.

However, a consistent y-axis offset was observed between the two lines (Figure 5.11C), with the B-factor plot for the interleaved dataset positioned significantly higher than that of the raster scan across all particle numbers, as confirmed by the same statistical tests ($p = <0.001$). The magnitude of this difference is 0.012 ± 0.002 Å^{-2}.

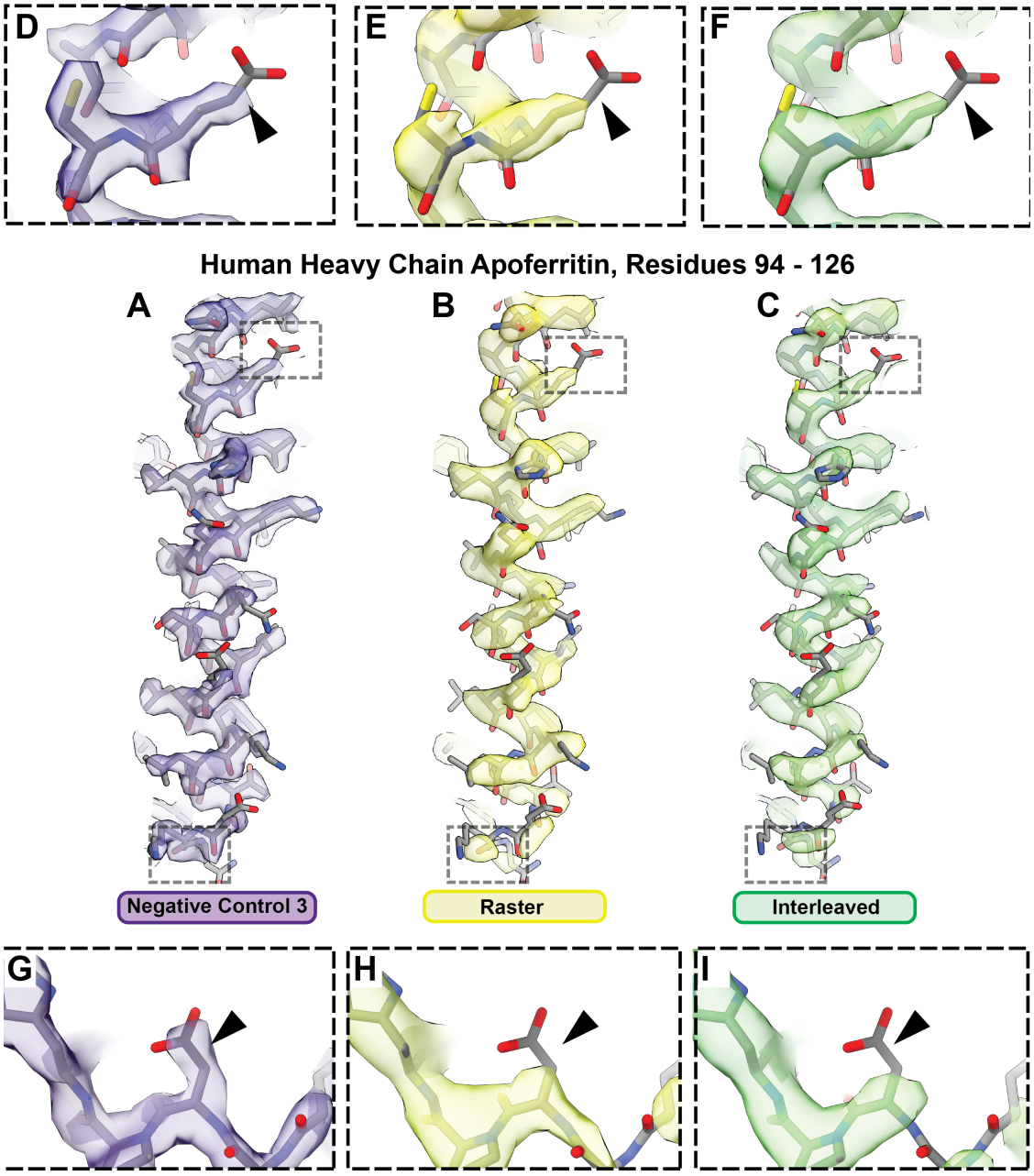


Figure 5.12: **Apoferritin model fit within the reconstructed maps showing radiation damage to acidic side chain residues**. Human heavy-chain apoferritin model (PDB 8CPV [311]) is shown fitted into an alpha helix (residues 94-126) of reconstructed maps (all displayed at the mean threshold + 4σ) for **A** negative control (no exposure to SEM), **B** raster scanning with 5 kV and 6.25 pA, and **C** interleaved scanning with 5 kV and 6.25 pA. Dashed boxes on the top and bottom of each alpha helix are enlarged above and below, displaying areas with a Glutamic acid residue, Glu101 (**D**-**F**), or an Aspartic acid reside, Asp126 (**G**-**I**), respectively. A clear loss of density around the side chain can be seen from both scanning methods compared to the negative control (black arrows).

The final maps (Figure 5.11A), their FSC-estimated resolutions (5.11B), and the B-factor plot (5.11C) all show a very minor increase in resolution using interleaved scanning, which was within the error of the B-factor plots (Figure 5.11). Furthermore, both the interleaved and raster data appear to show no difference in the reduced electron density around the acidic side chains of Asp126 and Glu101 (Figures 5.12E, F, H, and I), which is present in the negative control (Figures 5.12D and G), and are shown to be indicative of radiation sensitivity in the previous dataset (Figure 5.8).

5.4 Discussion

This work provides the first systematic and quantitative analysis of structural damage to proteins induced by low-voltage SEM imaging. Using single-particle analysis of apoferritin as a reporter for damage to protein samples, this work presents a clear, dose-dependent loss of high-resolution information resulting from SEM irradiation.

The B-factor analysis provides evidence that SEM exposure degrades sample quality long before any visual damage becomes apparent in the TEM or SEM micrographs. The B-factors for all irradiated datasets were significantly higher than for the non-irradiated controls. This confirms that even the extremely low-fluence imaging typically used for high-resolution SEM imaging imparts damage, which manifests as a reduction in the final achievable resolution of the protein reconstructions. This result highlights an often-overlooked variable in correlative workflows that could limit the potential of high-resolution cryo-ET.

For example, any of the lower voltage (1.2 and 3 kV) conditions, which used more than 6.25 pA (at 100 ns × 100 line integrations), resulted in severe damage to the particles. Thus, no 3D classes were produced with clear secondary structure and so these conditions were not data-processed to produce a high-resolution structure.

The calculated doses (Table 5.1) clearly suggest the lowest energy SEM beam to be the most damaging. In reality, the 3 kV 6.25 pA condition was the most damaged out of all the conditions that produced an alignment for a high-resolution structure. This finding is qualitatively supported by the initial 3D classifications of the particles at Bin4 in the data processing; the 3 kV acceleration voltage (column 2) appeared to be the worst preserved secondary structure of all of the particles (Figure A.19B and Appendix Figure A.19).

To speculate on the reason for this trend, it is important to consider the effective dose and its spatial profile within the finite thickness of the sample. The Monte Carlo simulations are key to this interpretation (see Figures 5.2 and 5.10). The 5 kV condition serves as the ideal baseline for evenly distributed damage. The electrons from this condition transmit through the entire sample, and its higher energy results in a relatively focused interaction volume, with even damage observed over the whole thickness of the vitreous ice. The damage is a direct consequence of inelastic scattering events from the primary beam. This is most similar to the TEM - as expected, the resulting B-factor aligns well with established damage rates from high-energy TEM studies (Figure 5.9).

Conversely, the 1.2 kV condition is the opposite of this. With penetration depth of only ~60 nm, the primary beam is shielded from the particles at the bottom of thicker ice. Some of the observed structural degradation may therefore not be caused by the primary beam, but by secondary effects, such as secondary electrons and the diffusion of highly reactive radicals generated in the irradiated ice layer above.

The 3 kV condition reveals an exceptionally damaging regime that could be explained by combining the worst aspects of the 1.2 kV and 5 kV incident beam. The beam is energetic enough to penetrate the full ice thickness and reach all of the particles, but has a high enough inelastic scattering cross-section to still deposit enough energy and produce a high yield of secondary electrons and radicals. This combination could create ideal conditions for generating a larger damaging effect within a thin sample.

Such an insight demonstrates that for correlative workflows, the choice of SEM voltage is not a simple trade-off but instead a complex decision whereby non-linear, catastrophic damage effects can emerge in specific energy windows and sample geometries. The next step for this work is to confirm the presence of a damage layer and validate Figure 5.10D by using cryo-ET to separate the depth effects hypothesised in this Chapter (see Appendix Figure A.21 for preliminary data).

The comparison between interleaved and raster scanning (at an identical dose and fluence) yielded no clear overall effect on B-factor. The B-factor plots for both datasets showed nearly identical slopes, resulting in the same calculated overall B-factor. This indicates that the rate of damage accumulation during subsequent TEM imaging was comparable between the two conditions.

Although the interleaved condition did not result in an improved B-factor compared to a conventional raster scan at the same dose, and fluence, the B-factor line did have a consistent increase in intercept (higher on y-axis). This indicates that, while the B-factor was the same, the interleaved scan may have preserved a higher intrinsic sample quality.

This phenomenon – parallel lines with identical slopes but different intercepts – has been theoretically modelled. For instance, Naydenova *et al.* demonstrated that a lower Efficiency of Orientation Distribution (E_{od}) can produce such an effect [326]. However, given the high octahedral symmetry of apoferritin, which largely negates the impact of preferred orientation, it is highly unlikely that a difference in E_{od} is the primary cause in this case.

A similar offset in B-factor plots, also attributed to differential charging effects, has recently been reported in studies using graphene-based supports (see [186], supplementary Figure 5). While this effect results in a consistent resolution advantage for the interleaved method, it is also important to note the diminishing

returns; the practical resolution difference between the two datasets becomes progressively smaller as more particles are added.

It must be acknowledged, however, that while this difference in intrinsic quality appears to be statistically significant, B-factor plots derived from experimental datasets can be subject to noise. Therefore, although these results suggest that interleaved scanning could offer some benefit, this interpretation is presented as a hypothesis warranting further investigation - rather than a definitive conclusion.

A more surprising effect was observed when comparing the two 5 kV, 6.25 pA raster scan datasets, which were identical apart from their integration method. The dataset acquired using line integration yielded a significantly better B-factor of $\sim$150 Å^2 compared to 203 Å^2 for the dataset acquired using frame integration. Each dataset's accompanying negative control reached $\sim$ 2.7 Å with comparable B-factors of 123 and 125 Å^2. This difference highlights the importance of the spatio-temporal distribution of the fluence.

One possible explanation is that the method of frame integration may lead to a more damaging, cumulative build-up of charge across the specimen, as reported in our previous work using a scan generator in SEM on biological samples to reduce charging (Figures 2B and 3B in [219]). This sustained charge may damage the high-resolution structure of protein molecules more effectively than the intense but localised charge from line integration - which could be allowed to dissipate.

5.4.1 Practical Considerations for Biologists: Workflow and Instrumentation

The choice of SEM imaging parameters is a critical, yet non-intuitive, variable for achieving preservation of high-resolution information in serial FIB-SEM workflows.

While the results from the thin, vitreous apoferritin sample suggest that a 1.2 kV SEM beam is highly damaging, the opposite is true in the context of a thick, bulk sample for serial milling workflows. For such workflows, using the lowest possible acceleration voltage (e.g., 1.2 kV) and beam current is likely the optimal strategy. The reason for this is that both the Monte Carlo simulations (Figure 5.2) and the calculated electron stopping distance (Table 5.1) predict that 1.2 kV electrons deposit their energy almost entirely within the top ∼60 nm of the specimen. This damaged volume falls completely within the sacrificial surface layer that is subsequently removed by the FIB beam, as the ion beam itself is known to damage vitrified biological material to a similar depth of ∼50-60 nm [17, 295, 327]. Therefore, the high dose delivered by the 1.2 kV beam becomes irrelevant to the final structure. Furthermore, the yield of secondary electrons (a consequence of the greater energy deposition) is greater at 1.2 kV than at higher acceleration voltages, giving optimal SNR in the SEM images.

However, many SEM columns are not optimised for high-resolution imaging at such low voltages, forcing many labs to operate at 3 kV or higher [147, 149, 328, 329]. This work reveals that operating at these intermediate energies can inadvertently maximise sample damage. At 3 kV, for example, the electron penetration depth extends significantly beyond the sacrificial FIB damage layer (∼330 nm at 3 kV, Table 5.1). Consequently, repeated SEM imaging during the serial milling process can accumulate a damaging dose in the region intended for downstream STA.

Past this intermediate voltage, at 5 kV, the incident electrons penetrate much deeper into the sample (∼800 nm, Table 5.1), depositing far less energy per unit volume within the near-surface region of interest. This potentially makes ∼5 kV a safer choice than ∼3 kV if a low voltage is unavailable. Ultimately, these findings should encourage biologists pursuing serial FIB-SEM to STA workflows to carefully consider their choice of SEM imaging voltage. A seemingly small change in parameters can have profound consequences for the preservation of high-resolution structural information.

For biologists using SEM, adopting dose as the primary metric for sample damage is strongly recommended. While fluence is much more commonly reported (if at all), dose more accurately represents the energy deposited into the specimen, providing a truer measure of potential structural degradation.

5.4.2 Limitations of the Methods Used

While this Chapter has successfully provided quantitative examples of damage to radiation sensitive biological material using SEM, several limitations should be acknowledged. It is important to note that these experiments were conducted using apoferritin, a highly stable and symmetric particle. It was chosen primarily because it is a standardised sample, commonly used to test resolution [7, 8, 157, 196, 311]. However, apoferritin may not fully represent the behaviour of more sensitive or non-symmetric proteins and complexes, particularly within the crowded environment of a cell. In this Chapter, apoferritin provided a reliable baseline for the fundamental damage processes involved, and allowed a much higher throughput than would have been achievable with a less symmetric protein.

A primary limitation of the Monte Carlo simulations is the use of pure vitreous ice as a proxy for a vitreous protein in buffer, or cell. A cell is significantly more heterogeneous, with a higher average density than – and different charging properties to – pure water, which may alter the spatial profile of the absorbed dose. Despite these differences, water was chosen as the simulation medium as it provides a well-researched baseline commonly used in many other cryo-EM calculations [26, 98, 176, 183]. Its properties serve as a reasonable first-order approximation for a hydrated biological sample, yielding foundational results that can be used as a reference for interpreting experimental data.

Finally, while a range of beam parameters was tested, this work represents a small subset of the possible conditions. The interplay between dose, dose rate, and the spatio-temporal distribution of the fluence/dose using different scanning

methods all warrant further investigation to build a complete model of SEM-induced damage to protein structure.

This Chapter has demonstrated that the conditions of SEM scanning in correlative workflows could be a source of damage, quantifiable long before it becomes visually apparent. It was shown that this damage is not a simple function of total fluence (as is most often reported in the literature), but is instead linked to the acceleration voltage – which dictates the 3D distribution of the dose – and the spatio-temporal scanning strategy. By understanding and controlling for these variables, the full potential of SEM-targeting for high-resolution *in-situ* structural biology can be realised.

6

Conclusions and Future Perspectives

Contents

6.1 Recapitulation and Summary of Findings 213
6.1.1 The Vision: An Integrated Workflow for *in-Situ* Structural Biology 213
6.1.2 Summary of the Investigation 214
6.2 A Revised Perspective: The Cumulative Damage Budget 214
6.3 Future Directions 216
6.3.1 Systematic Optimisation of Spatio-Temporal Dose Delivery 216
6.3.2 Standardisation of 'Low-Damage' Correlative SEM Protocols 217
6.4 Conclusion 217

6.1 Recapitulation and Summary of Findings

6.1.1 The Vision: An Integrated Workflow for *in-Situ* Structural Biology

A paramount challenge in modern structural biology remains the visualisation of specific macromolecules within their native, and functionally relevant, cellular milieu. To address this, this thesis proposed an ambitious, multi-stage workflow designed to bridge the scales from whole-cell targeting to near-atomic detail. The vision, as outlined in the introduction (Section 1.3), was as follows: an integrated pipeline built around a tripartite tag consisting of a targeting component for specificity, a fluorescent component for long-range guidance, and a small high-Z nanoparticle component as a precise, electron-dense marker for protein-level localisation.

Although this workflow was attempted (see Appendix section A.1.1 and Figures A.1 and A.2), the central premise of this strategy was to separate conflicting imaging requirements: an initial low-dose cryo-ET tilt series would capture pristine, high-resolution structural data, decoupled from a subsequent, high-dose STEM imaging step dedicated solely to the localisation of the heavy-element tag. This approach was conceived to maximise both structural preservation and localisation confidence. However, the transition of this workflow from a theoretical construct to a practical methodology hinged on a series of critical, unverified assumptions regarding heavy-element tag detectability and the consequences of the required electron dose. Therefore, this thesis was designed to systematically investigate these foundational aspects, thereby providing an analysis of the physical principles and practical limitations which govern such an approach.

6.1.2 Summary of the Investigation

Following this guiding principle, this thesis was structured as a logical progression from theory to practical application.

Following documentation of the relevant underlying principles in Chapter 2, the investigation began with Chapter 3, which established the theoretical foundation for tag-based localisation. Chapter 4 explored the practical consequences of electron fluence, using pure vitreous ice as a model system to test whether an alternative scanning method could mitigate damage. Finally, Chapter 5 expanded this investigation into the wider correlative workflow, seeking to quantify the role of SEM in causing radiation damage, using the high-resolution structure of apoferritin as a sensitive reporter.

6.2 A Revised Perspective: The Cumulative Damage Budget

Underpinning all future directions in the field of correlative workflows in cryo-ET is a more fundamental challenge: the incomplete understanding of the entire damage process in radiation-sensitive samples.

Whilst decades of research have elucidated many individual components of the damage cascade – such as the generation of secondary electrons [139, 169], beam-induced charging [188, 330], the production of radiolytic daughter fragments [162], and the cage effect [193] – a predictive model that accounts for the complex interplay between these mechanisms remains elusive.

The success of the interleaved pattern in reducing mass loss under certain conditions, as demonstrated in Chapter 4, points towards dynamic phenomena such as radical diffusion and local charge accumulation - but the precise physical basis for this

mitigation is not yet fully explained. This gap in the field's knowledge is not a minor detail; it represents the primary bottleneck which limits the achievable resolution of many workflows.

This fundamental complexity validates the empirical approach taken in this thesis and forces a re-evaluation of the initial workflow concept. The findings presented in this thesis, taken together, reveal that the entire cryogenic correlative process is governed by an overarching constraint: the cumulative damage budget.

The logical thread of this thesis follows this constraint. Chapter 3 began by establishing the theoretical mandate for a high-dose budget. The model confirmed that to overcome the low signal-to-noise ratio and confidently detect the smallest, most desirable AuNP tags (< 5 nm), a substantial electron fluence is unavoidable. This created the central conflict of the proposed workflow: the dose required for localisation was inherently at odds with the preservation of the biological specimen.

Chapter 4 then investigated the practical consequences of spending this budget. Using mass loss in pure vitreous ice as a metric, the work demonstrated that damage is not a simple function of total fluence or dose, but is critically dependent on the spatio-temporal distribution of the fluence. The key finding was that an interleaved scanning pattern, by providing a 'rest period' between the irradiation of adjacent pixels, could significantly reduce mass loss under long-dwell-time conditions. This provided the direct evidence that the damage budget for cryo-STEM is not fixed, but can be managed more efficiently through optimised fluence delivery.

Finally, Chapter 5 revealed that this budget begins to be consumed far earlier and more subtly than is commonly assumed. Using the high-resolution structure of apoferritin as a sensitive damage reporter, the work provided the first quantitative evidence that standard, low-voltage SEM imaging imparts a significant, dose-dependent loss of high-resolution information. These results broaden the scope of the problem from a single-instrument challenge to a workflow-wide constraint.

The findings also highlight a non-intuitive and nuanced nature for damage at intermediate SEM voltages (∼3 kV), where the combination of electron penetration depth and high inelastic scattering cross-section appeared to be exceptionally destructive in the thin samples tested.

This work therefore redefines the central problem. The challenge is not simply how to build a correlative workflow, but rather how to manage the structural integrity of a sample across every electron interaction, from the first low-magnification SEM search to the final high-dose TEM analysis.

6.3 Future Directions

The framework of a cumulative damage budget highlights a clear path for future research, focused on workflow optimisation.

6.3.1 Systematic Optimisation of Spatio-Temporal Dose Delivery

The proof-of-principle success of the interleaved scan in Chapter 4 warrants further investigation. A systematic study is needed to map the parameter space of scan patterns, pixel jump distances, and acquisition schema to minimise damage – not only for mass loss – but also for the preservation of protein structure, as measured in Chapter 5. Furthermore, the physical models proposed in Chapter 4 – which encompass radical diffusion and electrostatic effects – should be tested directly. One way to do so could be by conducting kinetic isotope effect experiments (D_2O, H_2O^{18}) to identify the mobile species and by attempting to directly visualise local charge fields using 4D-STEM techniques such as iDPC.

6.3.2 Standardisation of 'Low-Damage' Correlative SEM Protocols

The findings of Chapter 5 are important for the cryo-FIB-SEM community. The apoferritin B-factor analysis provides a robust method for establishing community-wide best practices to retain high-resolution structural integrity of proteins. A comprehensive study should be undertaken to define the optimal SEM imaging parameters (acceleration voltage, beam current, integration method) for different sample types (for example, thin layers vs. bulk samples for serial milling). This standardised approach would allow researchers to make informed decisions to minimise the cost of damage before a sample reaches the TEM.

6.4 Conclusion

In conclusion, whilst this thesis began with the goal of defining a specific workflow for *in-situ* structural biology, its most significant contribution is a foundational analysis that is applicable to all cryogenic correlative workflows where damage mitigation is a central issue. This thesis theoretically established the need for a high fluence, experimentally demonstrated a practical method for its mitigation, and quantitatively revealed a previously overlooked source of damage in the SEM. In doing so, this work emphasises the critical need to consider all sources of radiation in correlative experiments. It establishes the cumulative damage budget as an vital consideration for the development of the next generation of high-resolution discovery workflows for *in-situ* structural biology.

References

[1] J. C. Kendrew, G. Bodo, H. M. Dintzis, R. G. Parrish, and H. Wyckoff. "A Three Dimensional Model of the Myoglobin Molecule Obtained by X-Ray Analysis". *Nature* **181** (1958), pp. 622–666. DOI: 10.1038/181662a0.

[2] M. P. Williamson, T. F. Have, and K. Wüthrich. "Solution Conformation of Proteinase Inhibitor IIA from Bull Seminal Plasma by 1-H Nuclear Magnetic Resonance and Distance Geometry". *Journal of Molecular Bio-Energetics* **182** (1985), pp. 295–315. DOI: 10.1016/0022-2836(85)90347-x.

[3] R. Henderson, J. M. Baldwin, T. A. Ceskat, F. Zemlin, E. Beckmann, and K. H. Downing. "Model for the Structure of Bacteriorhodopsin Based on High-resolution Electron Cryo-microscopy". *Journal of Molecular Biology* **213** (1990), pp. 899–929. DOI: 10.1016/S0022-2836(05)80271-2.

[4] H. Berman, J. Westbrook, Z. Feng, G. Gilliland, T. Bhat, H. Weissig, I. Shindyalov, and P. Bourne. "The Protein Data Bank". *Nucleic Acids Research* **28** (2000), pp. 235–242. DOI: 10.1093/nar/28.1.235.

[5] J. Dubochet, F. Joachim, and R. Henderson. *Press Release: The Nobel Prize in Chemistry 2017 - "for developing cryo-electron microscopy for the high-resolution structure determination of biomolecules in solution"*. Tech. rep. Royal Swedish Academy of Sciences, 2017. DOI: 10.1142/9789814635660_0003.

[6] A. Wlodawer and Z. Dauter. "'Atomic resolution': A badly abused term in structural biology". *Acta Crystallographica Section D: Structural Biology* **73** (4) (2017), pp. 379–380. DOI: 10.1107/S205979831700225X.

[7] T. Nakane, A. Kotecha, A. Sente, G. McMullan, S. Masiulis, P. M. Brown, I. T. Grigoras, L. Malinauskaite, T. Malinauskas, J. Miehling, T. Uchański, L. Yu, D. Karia, E. V. Pechnikova, E. de Jong, J. Keizer, M. Bischoff, J. McCormack, P. Tiemeijer, S. W. Hardwick, D. Y. Chirgadze, G. Murshudov, A. R. Aricescu, and S. H. Scheres. "Single-particle cryo-EM at atomic resolution". *Nature* **587** (2020), pp. 152–156. DOI: 10.1038/s41586-020-2829-0.

[8] K. M. Yip, N. Fischer, E. Paknia, A. Chari, and H. Stark. "Atomic-resolution protein structure determination by cryo-EM". *Nature* **587** (7832) (2020), pp. 157–161. DOI: 10.1038/s41586-020-2833-4.

[9] S. Lövestam, F. A. Koh, B. van Knippenberg, A. Kotecha, A. G. Murzin, M. Goedert, and S. H. Scheres. "Assembly of recombinant tau into filaments identical to those of Alzheimer's disease and chronic traumatic encephalopathy". *eLife* **11** (2022), pp. 1–27. DOI: 10.7554/eLife.76494.

[10] M. Holm, S. K. Natchiar, E. J. Rundlet, A. G. Myasnikov, Z. L. Watson, R. B. Altman, H. Y. Wang, J. Taunton, and S. C. Blanchard. "mRNA decoding in human is kinetically and structurally distinct from bacteria". *Nature* **617** (2023), pp. 200–207. DOI: 10.1038/s41586-023-05908-w.

[11] W. Kühlbrandt. "The resolution revolution". *Science* **343** (2014), pp. 1443–1444. DOI: 10.1126/science.1251652.

[12] D. Homouz, M. Perham, A. Samiotakis, M. S. Cheung, and P. Wittung-Stafshede. "Crowded, cell-like environment induces shape changes in aspherical protein". *Proceedings of the National Academy of Sciences of the United States of America* **105** (2008), pp. 11754–11759. DOI: doi/10.1073/pnas.0803672105.

[13] J. Keller and R. Fernández-Busnadiego. "In situ studies of membrane biology by cryo-electron tomography". *Current Opinion in Cell Biology* **88** (2024). DOI: 10.1016/j.ceb.2024.102363.

[14] M. Kudryashev. "The big chill: Growth of in situ structural biology with cryo-electron tomography". *Quarterly Reviews of Biophysics Discovery* **5** (2024). DOI: 10.1017/qrd.2024.10.

[15] J. Jumper et al. "Highly accurate protein structure prediction with AlphaFold". *Nature* **596** (7873) (2021), pp. 583–589. DOI: 10.1038/s41586-021-03819-2. URL: http://dx.doi.org/10.1038/s41586-021-03819-2.

[16] M. Baek et al. *Accurate prediction of protein structures and interactions using a three-track neural network*. 2021. URL: https://predictioncenter.org/casp14/.

[17] C. Berger, M. Dumoux, T. Glen, N. B. Yee, J. M. Mitchels, Z. Patáková, M. C. Darrow, J. H. Naismith, and M. Grange. "Plasma FIB milling for the determination of structures in situ". *Nature Communications* **14** (2023), pp. 1–12. DOI: 10.1038/s41467-023-36372-9.

[18] Z. Hou, F. Nightingale, Y. Zhu, C. MacGregor-Chatwin, and P. Zhang. "Structure of native chromatin fibres revealed by Cryo-ET in situ". *Nature Communications* **14** (1) (2023), pp. 1–7. DOI: 10.1038/s41467-023-42072-1.

[19] J. Liu, E. K. McRae, M. Zhang, C. Geary, E. S. Andersen, and G. Ren. "Non-averaged single-molecule tertiary structures reveal RNA self-folding through individual-particle cryo-electron tomography". *Nature Communications* **15** (1) (2024), pp. 1–18. DOI: 10.1038/s41467-024-52914-1.

[20] L. Graham and J. M. Orenstein. "Processing tissue and cells for transmission electron microscopy in diagnostic pathology and research". *Nature Protocols* **2** (10) (2007), pp. 2439–2450. DOI: 10.1038/nprot.2007.304.

[21] R. F. Thompson, M. Walker, C. A. Siebert, S. P. Muench, and N. A. Ranson. "An introduction to sample preparation and imaging by cryo-electron microscopy for structural biology". *Methods* **100** (2016), pp. 3–15. DOI: 10.1016/j.ymeth.2016.02.017.

[22] D. Tegunov, L. Xue, C. Dienemann, P. Cramer, and J. Mahamid. "Multi-particle cryo-EM refinement with M visualizes ribosome-antibiotic complex at 3.5 Å in cells". *Nature Methods* **18** (2021), pp. 186–193. DOI: 10.1038/s41592-020-01054-7.

[23] H. Xing, R. Taniguchi, I. Khusainov, J. P. Kreysing, S. Welsch, B. Turoňová, and M. Beck. "Translation dynamics in human cells visualized at high resolution reveal cancer drug action". *Science* **381** (2023), pp. 70–75. DOI: 10.1126/science.adh1411.

[24] S. Klumpe, K. A. Senti, F. Beck, J. Sachweh, B. Hampoelz, P. Ronchi, V. Oorschot, M. Brandstetter, A. Yeroslaviz, J. A. Briggs, J. Brennecke, M. Beck, and J. M. Plitzko. "In-cell structure and snapshots of copia retrotransposons in intact tissue by cryo-ET". *Cell* **188** (8) (2025), pp. 2094–2110. DOI: 10.1016/j.cell.2025.02.003.

[25] L. Xue, C. M. Spahn, M. Schacherl, and J. Mahamid. "Structural insights into context-dependent inhibitory mechanisms of chloramphenicol in cells". *Nature Structural and Molecular Biology* **32** (2) (2025), pp. 257–267. DOI: 10.1038/s41594-024-01441-0.

[26] J. L. Dickerson, P. H. Lu, D. Hristov, R. E. Dunin-Borkowski, and C. J. Russo. "Imaging biological macromolecules in thick specimens: The role of inelastic scattering in cryo-EM". *Ultramicroscopy* **237** (2022), pp. 1–11. DOI: 10.1016/j.ultramic.2022.113510.

[27] T. Geiger, A. Wehner, C. Schaab, J. Cox, and M. Mann. "Comparative proteomic analysis of eleven common cell lines reveals ubiquitous but varying expression of most proteins". *Molecular and Cellular Proteomics* **11** (3) (2012), pp. 1–11. DOI: 10.1074/mcp.M111.014050.

[28] W. Baumeister. "Cryo-electron tomography: A long journey to the inner space of cells". *Cell* **185** (15) (2022), pp. 2649–2652. DOI: 10.1016/j.cell.2022.06.034.

[29] J. A. Pierson, J. E. Yang, and E. R. Wright. "Recent advances in correlative cryo-light and electron microscopy". *Current Opinion in Structural Biology* **89** (2024). DOI: 10.1016/j.sbi.2024.102934.

[30] G. H. Wu, P. G. Mitchell, J. G. Galaz-Montoya, C. W. Hecksel, E. M. Sontag, V. Gangadharan, J. Marshman, D. Mankus, M. E. Bisher, A. K. Lytton-Jean, J. Frydman, K. Czymmek, and W. Chiu. "Multi-scale 3D Cryo-Correlative Microscopy for Vitrified Cells". *Structure* **28** (11) (2020), pp. 1231–1237. DOI: 10.1016/j.str.2020.07.017.

[31] M. J. Rust, M. Bates, and X. Zhuang. "Sub-diffraction-limit imaging by stochastic optical reconstruction microscopy (STORM)". *Nature Methods* **3** (10) (2006), pp. 793–795. DOI: 10.1038/nmeth929.

[32] D. M. Owen, A. Magenau, D. J. Williamson, and K. Gaus. "Super-Resolution Imaging by Localization Microscopy". *Nanoimaging*. Ed. by A. A. Sousa, M. J. Kruhlak, and J. M. Walker. 1st ed. New York: Springer, 2013. Chap. 6, pp. 81–93. DOI: 10.1007/978-1-62703-137-0. URL: http://www.springer.com/series/7651.

[33] M. Lelek, M. T. Gyparaki, G. Beliu, F. Schueder, J. Griffié, S. Manley, R. Jungmann, M. Sauer, M. Lakadamyali, and C. Zimmer. "Single-molecule localization microscopy". *Nature Reviews Methods Primers* **1** (1) (2021). DOI: 10.1038/s43586-021-00038-x.

[34] G. Wolff, C. Hagen, K. Grünewald, and R. Kaufmann. "Towards correlative super-resolution fluorescence and electron cryo-microscopy". *Biology of the Cell* **108** (9) (2016), pp. 245–258. DOI: 10.1111/boc.201600008.

[35] P. D. Dahlberg and W. E. Moerner. "Cryogenic Super-Resolution Fluorescence and Electron Microscopy Correlated at the Nanoscale". *Annual Review of Physical Chemistry Downloaded from www.annualreviews.org. Guest* **25** (10) (2025), p. 10. DOI: 10.1146/annurev-physchem-090319. URL: https://doi.org/10.1146/annurev-physchem-090319-.

[36] B. Liu, Y. Xue, W. Zhao, Y. Chen, C. Fan, L. Gu, Y. Zhang, X. Zhang, L. Sun, X. Huang, W. Ding, F. Sun, W. Ji, and T. Xu. "Three-dimensional super-resolution protein localization correlated with vitrified cellular context". *Scientific Reports* **5** (2015), pp. 1–12. DOI: 10.1038/srep13017.

[37] M. W. Tuijtel, A. J. Koster, S. Jakobs, F. G. Faas, and T. H. Sharp. "Correlative cryo super-resolution light and electron microscopy on mammalian cells using fluorescent proteins". *Scientific Reports* **9** (1) (2019). DOI: 10.1038/s41598-018-37728-8.

[38] P. D. Dahlberg, S. Saurabh, A. M. Sartor, J. Wang, P. G. Mitchell, W. Chiu, L. Shapiro, and W. E. Moerner. "Cryogenic single-molecule fluorescence annotations for electron tomography reveal in situ organization of key proteins in Caulobacter". *Proceedings of the National Academy of Sciences of the United States of America* (2020). DOI: 10.1073/pnas.2001849117/.

[39] M. G. Last, L. M. Voortman, and T. H. Sharp. "Imaging intracellular components in situ using super-resolution cryo-correlative light and electron microscopy". *Methods in Cell Biology*. Vol. 187. Academic Press Inc., 2024, pp. 223–248. DOI: 10.1016/bs.mcb.2024.02.027.

[40] M. G. Last, M. W. Tuijtel, L. M. Voortman, and T. H. Sharp. "Selecting optimal support grids for super-resolution cryogenic correlated light and electron microscopy". *Scientific Reports* **13** (1) (2023), pp. 1–11. DOI: 10.1038/s41598-023-35590-x.

[41] S. Mojiri, J. M. Dobbs, N. Faul, T. P. Burg, J. Mahamid, and J. Ries. "Effects of base temperature, immersion medium, and EM grid material on devitrification thresholds in cryogenic optical super-resolution microscopy". *Journal of Structural Biology* (2025), pp. 1–10. DOI: 10.1101/2025.03.28.645948.

[42] S. Klein, M. Wachsmuth-Melm, S. L. Winter, A. Kolovou, and P. Chlanda. "Cryo-correlative light and electron microscopy workflow for cryo-focused ion beam milled adherent cells". *Methods in Cell Biology*. Vol. 162. Academic Press Inc., 2021, pp. 273–302. DOI: 10.1016/bs.mcb.2020.12.009.

[43] F. Yang, L. G. Moss, and G. N. Phillips. "The Molecular Structure of Green Fluorescent Protein". *Nature Biotechnology* **14** (1996). DOI: doi.org/10.1038/nbt1096-1246.

[44] E. Fatti, S. Khawaja, and K. Weis. "The dark side of fluorescent protein tagging-the impact of protein tags on biomolecular condensation". *Molecular biology of the cell* **36** (3) (2025), br10. DOI: 10.1091/mbc.E24-11-0521.

[45] J. B. Grimm and L. D. Lavis. "Caveat fluorophore: an insiders' guide to small-molecule fluorescent labels". *Nature Methods* **19** (2) (2022), pp. 149–158. DOI: 10.1038/s41592-021-01338-6.

[46] G. V. Los, L. P. Encell, M. G. McDougall, D. D. Hartzell, N. Karassina, C. Zimprich, M. G. Wood, R. Learish, R. F. Ohana, M. Urh, D. Simpson, J. Mendez, K. Zimmerman, P. Otto, G. Vidugiris, J. Zhu, A. Darzins, D. H. Klaubert, R. F. Bulleit, and K. V. Wood. "HaloTag: A novel protein labeling technology for cell imaging and protein analysis". *ACS Chemical Biology* **3** (6) (2008), pp. 373–382. DOI: 10.1021/cb800025k.

[47] B. Alberts, A. Johnson, J. Lewis, M. Raff, K. Roberts, and P. Walter. *Molecular Biology of the Cell*. 5th ed. New York: Garland Science, 2007. URL: https://www.ncbi.nlm.nih.gov/books/NBK26883/.

[48] M. Gruska, O. Medalia, W. Baumeister, and A. Leis. "Electron tomography of vitreous sections from cultured mammalian cells". *Journal of Structural Biology* **161** (3) (2008), pp. 384–392. DOI: 10.1016/j.jsb.2007.10.008.

[49] C. Berger, R. B. Ravelli, C. López-Iglesias, and P. J. Peters. "Endocytosed nanogold fiducials for improved in-situ cryo–electron tomography tilt-series alignment". *Journal of Structural Biology* **213** (1) (2021). DOI: 10.1016/j.jsb.2021.107698.

[50] D. N. Mastronarde and S. R. Held. "Automated tilt series alignment and tomographic reconstruction in IMOD". *Journal of Structural Biology* **197** (2) (2017), pp. 102–113. DOI: 10.1016/j.jsb.2016.07.011.

[51] S. Zheng, G. Wolff, G. Greenan, Z. Chen, F. G. Faas, M. Bárcena, A. J. Koster, Y. Cheng, and D. A. Agard. "AreTomo: An integrated software package for automated marker-free, motion-corrected cryo-electron tomographic alignment and reconstruction". *Journal of Structural Biology: X* **6** (2022). DOI: 10.1016/j.yjsbx.2022.100068.

[52] N. Joudeh and D. Linke. "Nanoparticle Classification, Physicochemical Properties, Characterization, and Applications: a Comprehensive Review for Biologists". *Journal of Nanobiotechnology* **20** (1) (2022). DOI: 10.1186/s12951-022-01477-8.

[53] N. Groysbeck, V. Hanss, M. Donzeau, J. M. Strub, S. Cianférani, D. Spehner, M. Bahri, O. Ersen, M. Eltsov, P. Schultz, and G. Zuber. "Bioactivated and PEG-Protected Circa 2 nm Gold Nanoparticles for in Cell Labelling and Cryo-Electron Microscopy". *Small Methods* **7** (6) (2023). DOI: 10.1002/smtd.202300098.

[54] C. E. Melia, J. R. Bolla, S. Katharios-Lanwermeyer, D. B. Mihaylov, P. C. Hoffmann, J. Huo, M. R. Wozny, L. M. Elfari, J. Böhning, A. N. Morgan, C. J. Hitchman, R. J. Owens, C. V. Robinson, G. A. O'toole, T. A. M. Bharat, S. William, and E. P. Greenberg. "Architecture of cell-cell junctions in situ reveals a mechanism for bacterial biofilm inhibition". *Proceedings of the National Academy of Sciences of the United States of America* **118** (31) (2021). DOI: 10.1073/pnas.2109940118/-/DCSupplemental.

[55] I. Dahan, S. Sorrentino, R. Boujemaa-Paterski, and O. Medalia. "Tiopronin-Protected Gold Nanoparticles as a Potential Marker for Cryo-EM and Tomography". *Structure* **26** (10) (2018), pp. 1408–1413. DOI: 10.1016/j.str.2018.06.009.

[56] Nanoprobes. *Product Information: 0.8 nm Undecagold Labeling Reagents*. 2025. URL: https://www.nanoprobes.com/products/Undecagold-Labeling-Reagents.html.

[57] J. A. Mindell and N. Grigorieff. "Accurate determination of local defocus and specimen tilt in electron microscopy". *Journal of Structural Biology* **142** (3) (2003), pp. 334–347. DOI: 10.1016/S1047-8477(03)00069-8.

[58] C. T. Beales and O. Medalia. "Gold nanomaterials and their potential use as cryo-electron tomography labels". *Journal of Structural Biology* **214** (3) (2022). DOI: 10.1016/j.jsb.2022.107880.

[59] M. Azubel, S. D. Carter, J. Weiszmann, J. Zhang, G. J. Jensen, Y. Li, and R. D. Kornberg. "FGF21 trafficking in intact human cellsrevealed by cryo-electron tomographywith gold nanoparticles". *eLife* (2019). DOI: 10.7554/eLife.43146.001. URL: https://elifesciences.org/articles/43146#abstract.

[60] K. Song, J. Awata, D. Tritschler, R. Bower, G. B. Witman, M. E. Porter, and D. Nicastro. "In situ localization of N and C termini of subunits of the flagellar nexin-dynein regulatory complex (N-DRC) using SNAP tag and cryo-electron tomography". *Journal of Biological Chemistry* **290** (9) (2015), pp. 5341–5353. DOI: 10.1074/jbc.M114.626556.

[61] L. N. Young, A. Sherrard, H. Zhou, F. Shaikh, J. Hutchings, M. Riggi, M. K. Rosen, A. J. Giraldez, and E. Villa. "ExoSloNano: Multi-Modal Nanogold Tags for identification of Macromolecules in Live Cells & Cryo-Electron Tomograms." *bioRxiv* (2024). DOI: 10.1101/2024.10.12.617288. URL: http://www.ncbi.nlm.nih.gov/pubmed/39416124%20http://www.pubmedcentral.nih.gov/articlerender.fcgi?artid=PMC11482945.

[62] C. Wang, I. Iacovache, and B. Zuber. "Genetically Encoded FerriTag as a Specific Label for Cryo-Electron Tomography". *bioRxiv* (2024). DOI: 10.1101/2024.09.10.612178. URL: http://biorxiv.org/lookup/doi/10.1101/2024.09.10.612178.

[63] I. Walev, S. Chakrit Bhakdi, F. Hofmann, N. Djonder, A. Valeva, K. Aktories, and S. Bhakdi. "Delivery of proteins into living cells by reversible membrane permeabilization with streptolysin-O". *Proceedings of the National Academy of Sciences of the United States of America* (2001). DOI: 10.1073pnas.051429498.

[64] J. D. Otvos, R. W. Olafson, and I. M. Armitage. "Structure of an Invertebrate Metallothionein from Scylla Serrata". *Journal of Biological Chemistry* **257** (5) (1982), pp. 2427–2431. URL: https://pubmed.ncbi.nlm.nih.gov/7061432/.

[65] K. B. Nielson, C. L. Atkin, and D. R. Winges. "Distinct Metal-binding Configurations in Metallothionein". *Journal of Biological Chemistry* **260** (9) (1985), pp. 5342–5350. DOI: doi.org/10.1016/S0021-9258(18)89027-5.

[66] C. P. Mercogliano and D. J. DeRosier. "Concatenated metallothionein as a clonable gold label for electron microscopy". *Journal of Structural Biology* **160** (1) (2007), pp. 70–82. DOI: 10.1016/j.jsb.2007.06.010.

[67] C. Bouchet-Marquis, M. Pagratis, R. Kirmse, and A. Hoenger. "Metallothionein as a clonable high-density marker for cryo-electron microscopy". *Journal of Structural Biology* **177** (1) (2012), pp. 119–127. DOI: 10.1016/j.jsb.2011.10.007.

[68] E. Diestra, J. Fontana, P. Guichard, S. Marco, and C. Risco. "Visualization of proteins in intact cells with a clonable tag for electron microscopy". *Journal of Structural Biology* **165** (3) (2009), pp. 157–168. DOI: 10.1016/j.jsb.2008.11.009.

[69] Z. Jiang, X. Jin, Y. Li, S. Liu, X. M. Liu, Y. Y. Wang, P. Zhao, X. Cai, Y. Liu, Y. Tang, X. Sun, Y. Liu, Y. Hu, M. Li, G. Cai, X. Qi, S. Chen, L. L. Du, and W. He. "Genetically encoded tags for direct synthesis of EM-visible gold nanoparticles in cells". *Nature Methods* **17** (9) (2020), pp. 937–946. DOI: 10.1038/s41592-020-0911-z.

[70] N. I. Clarke and S. J. Royle. "FerriTag is a new genetically-encoded inducible tag for correlative light-electron microscopy". *Nature Communications* **9** (1) (2018). DOI: 10.1038/s41467-018-04993-0.

[71] W. W. Sun, D. J. Michalak, K. A. Sochacki, P. Kunamaneni, M. A. Alfonzo-Méndez, A. M. Arnold, M. P. Strub, J. E. Hinshaw, and J. W. Taraska. "Cryo-electron tomography pipeline for plasma membranes". *Nature Communications* **16** (1) (2025). DOI: 10.1038/s41467-025-56045-z.

[72] P. W. Rothemund. "Folding DNA to create nanoscale shapes and patterns". *Nature* **440** (7082) (2006), pp. 297–302. DOI: 10.1038/nature04586.

[73] E. Silvester, B. Vollmer, V. Pražák, D. Vasishtan, E. A. Machala, C. Whittle, S. Black, J. Bath, A. J. Turberfield, K. Grünewald, and L. A. Baker. "DNA origami signposts for identifying proteins on cell membranes by electron cryotomography". *Cell* **184** (4) (2021), pp. 1110–1121. DOI: 10.1016/j.cell.2021.01.033.

[74] H. K. Fung, Y. Hayashi, V. T. Salo, A. Babenko, I. Zagoriy, A. Brunner, J. Ellenberg, C. W. Müller, S. Cuylen-Haering, and J. Mahamid. "Genetically encoded multimeric tags for subcellular protein localization in cryo-EM". *Nature Methods* **20** (12) (2023), pp. 1900–1908. DOI: 10.1038/s41592-023-02053-0.

[75] T. Bendory, A. Bartesaghi, and A. Singer. "Single-Particle Cryo-Electron Microscopy: Mathematical Theory, Computational Challenges, and Opportunities". *IEEE Signal Processing Magazine* **37** (2) (2020), pp. 58–76. DOI: 10.1109/MSP.2019.2957822.

[76] H. Li, H. Zhang, X. Wan, Z. Yang, C. Li, J. Li, R. Han, P. Zhu, and F. Zhang. "Noise-Transfer2Clean: Denoising cryo-EM images based on noise modeling and transfer". *Bioinformatics* **38** (7) (2022), pp. 2022–2029. DOI: 10.1093/bioinformatics/btac052.

[77] R. Henderson. "Image contrast in high-resolution electron microscopy of biological macromolecules: TMV in ice". *Ultramicroscopy* **46** (1992), pp. 1–18.

[78] G. McMullan, A. R. Faruqi, D. Clare, and R. Henderson. "Comparison of optimal performance at 300keV of three direct electron detectors for use in low dose electron microscopy". *Ultramicroscopy* **147** (2014), pp. 156–163. DOI: 10.1016/j.ultramic.2014.08.002.

[79] K. Naydenova, P. Jia, and C. J. Russo. "Cryo-EM with sub-1 Å specimen movement". *Science* **370** (2020). DOI: DOI:10.1126/science.abb7927.

[80] A. F. Brilot, J. Z. Chen, A. Cheng, J. Pan, S. C. Harrison, C. S. Potter, B. Carragher, R. Henderson, and N. Grigorieff. "Beam-induced motion of vitrified specimen on holey carbon film". *Journal of Structural Biology* **177** (3) (2012), pp. 630–637. DOI: 10.1016/j.jsb.2012.02.003.

[81] X. Li, P. Mooney, S. Zheng, C. R. Booth, M. B. Braunfeld, S. Gubbens, D. A. Agard, and Y. Cheng. "Electron counting and beam-induced motion correction enable near-atomic-resolution single-particle cryo-EM". *Nature Methods* **10** (6) (2013), pp. 584–590. DOI: 10.1038/nmeth.2472.

[82] X. Li, S. Q. Zheng, K. Egami, D. A. Agard, and Y. Cheng. "Influence of electron dose rate on electron counting images recorded with the K2 camera". *Journal of Structural Biology* **184** (2) (2013), pp. 251–260. DOI: 10.1016/j.jsb.2013.08.005.

[83] Y. Cheng, N. Grigorieff, P. A. Penczek, and T. Walz. "A primer to single-particle cryo-electron microscopy". *Cell* **161** (3) (2015), pp. 438–449. DOI: 10.1016/j.cell.2015.03.050.

[84] A. V. Crewe and J. Wall. "Visibility of Single Atoms". *Science* (1970), pp. 1338–1340. DOI: 10.1126/science.168.3937.1338.

[85] T. Walther, Y. Qiu, and A. G. Cullis. "Measuring the contrast in annular dark field STEM images as a function of camera length". *Journal of Physics: Conference Series*. Vol. 241. Institute of Physics Publishing, 2010. DOI: 10.1088/1742-6596/241/1/012068.

[86] T. Mullarkey, J. J. P. Peters, C. Downing, and L. Jones. "Using Your Beam Efficiently: Reducing Electron Dose in the STEM via Flyback Compensation". *Microscopy and Microanalysis* **28** (4) (2022), pp. 1428–1436. DOI: 10.1017/S1431927621013908.

[87] R. Brydson, P. Goodhew, G. Tatlock, L. M. Brown, A. Bleloch, Ramasse Q., P. Nellist, A. Craven, N. Hondow, M. D. Shannon, A. I. Kirkland, and S. J. Haigh. *Aberration-Corrected Analytical Transmission Electron Microscopy*. Ed. by R. Brydson. London: Wiley, 2011. DOI: 10.1002/9781119978848.

[88] S. J. Pennycook. "The impact of STEM aberration correction on materials science". *Ultramicroscopy* **180** (2017), pp. 22–33. DOI: 10.1016/j.ultramic.2017.03.020.

[89] A. V. Crewe and J. Walls. "A Scanning Microscope with 5 Å Resolution". *Journal of Molecular Biology* **48** (1970), pp. 375–393. DOI: 10.1016/0022-2836(70)90052-5.

[90] L. Gregori, J. F. Hainfeld, M. N. Simon, and D. Goldgaber. "Binding of Amyloid Protein to the 20S Proteasome". *Journal of Biological Chemistry* **272** (1997), pp. 58–62. DOI: 10.1074/jbc.272.1.58.

[91] A. A. Sousa, A. A. Azari, G. Zhang, and R. D. Leapman. "Dual-axis electron tomography of biological specimens: Extending the limits of specimen thickness with bright-field STEM imaging". *Journal of Structural Biology* **174** (1) (2011), pp. 107–114. DOI: 10.1016/j.jsb.2010.10.017.

[92] E. Kellenberger and W. Chiu. "Perspectives and Outlook for Electron Microscopy in Biology in General". *Ultramicroscopy* **10** (1982), pp. 165–178. DOI: 10.1016/0304-3991(82)90196-6.

[93] A. Engel. "Molecular Weight Determination by Scanning Transmission Electron Microscopy". *Ultramicroscopy* (3) (1978), pp. 273–281. DOI: 10.1016/S0304-3991(78)80037-0.

[94] S. G. Wolf, E. Shimoni, M. Elbaum, and L. Houben. "STEM Tomography in Biology". *Cellular Imaging: Electron Tomography and Related Techniques*. Ed. by E. Hanssen. 1st ed. Springer, 2018, pp. 33–60. DOI: 10.1007/978-3-319-68997-5.

[95] S. G. Wolf, L. Houben, and M. Elbaum. "Cryo-scanning transmission electron tomography of vitrified cells". *Nature Methods* **11** (2014), pp. 423–428. DOI: 10.1038/nmeth.2842.

[96] D. B. Williams and C. B. Carter. *Transmission Electron Microscopy: A Textbook for Materials Science*. 3rd. Springer, 2009, pp. 1–760. DOI: 10.1007/978-0-387-76501-3.

[97] I. Kawrakow. "Electron transport: Multiple and Plural Elastic Scattering". *Nuclear Instruments and Methods in Physics Research B* **108** (1996), pp. 23–34. DOI: 10.1016/0168-583X(95)01046-7.

[98] N. de Jonge. "Theory of the spatial resolution of (scanning) transmission electron microscopy in liquid water or ice layers". *Ultramicroscopy* **187** (2018), pp. 113–125. DOI: 10.1016/j.ultramic.2018.01.007.

[99] P. Kirchweger, D. Mullick, S. G. Wolf, and M. Elbaum. "Visualization of Organelles In Situ by Cryo-STEM Tomography". *Journal of Visualized Experiments* **2023** (2023), pp. 1–18. DOI: 10.3791/65052.

[100] P. Kirchweger, D. Mullick, P. P. Swain, S. G. Wolf, and M. Elbaum. "Correlating cryo-super resolution radial fluctuations and dual-axis cryo-scanning transmission electron tomography to bridge the light-electron resolution gap". *Journal of Structural Biology* **215** (3) (2023). DOI: 10.1016/j.jsb.2023.107982.

[101] K. Aoyama, H. Takazaki, M. Arie, H. Suemune, and S. Kawai. "Cryo-STEM tomography for cell biology using thick lamella". *Microscopy* (2025). DOI: 10.1093/jmicro/dfaf017.

[102] P. Rez. "Comparison of phase contrast transmission electron microscopy with optimized scanning transmission annular dark field imaging for protein imaging". *Ultramicroscopy* **96** (2003), pp. 117–124. DOI: 10.1016/S0304-3991(02)00436-9.

[103] S. G. Wolf, P. Rez, and M. Elbaum. "Phosphorus detection in vitrified bacteria by cryo-STEM annular dark-field analysis". *Journal of Microscopy* **260** (2015), pp. 227–233. DOI: 10.1111/jmi.12289.

[104] M. Ilett, M. S'Ari, H. Freeman, Z. Aslam, N. Koniuch, M. Afzali, J. Cattle, R. Hooley, T. Roncal-Herrero, S. M. Collins, N. Hondow, A. Brown, and R. Brydson. "Analysis of complex, beam-sensitive materials by transmission electron microscopy and associated techniques: TEM of Beam Sensitive Materials". *Philosophical Transactions of the Royal Society A: Mathematical, Physical and Engineering Sciences* **378** (2020). DOI: 10.1098/rsta.2019.0601.

[105] R. M. Glaeser. "Invited Review Article: Methods for imaging weak-phase objects in electron microscopy". *Review of Scientific Instruments* **84** (11) (2013). DOI: 10.1063/1.4830355.

[106] O. Pfeil-Gardiner, H. V. D. Rosa, D. Riedel, Y. S. Chen, D. Lörks, P. Kükelhan, M. Linck, H. Müller, F. Van Petegem, and B. J. Murphy. "Elemental mapping in single-particle reconstructions by reconstructed electron energy-loss analysis". *Nature Methods* **21** (12) (2024), pp. 2299–2306. DOI: 10.1038/s41592-024-02482-5.

[107] N. Elad, G. Bellapadrona, L. Houben, I. Sagi, and M. Elbaum. "Detection of isolated protein-bound metal ions by single-particle cryo-STEM". *Proceedings of the National Academy of Sciences of the United States of America* **114** (2017), pp. 11139–11144. DOI: 10.1073/pnas.1708609114.

[108] X. Pei, L. Zhou, C. Huang, M. Boyce, J. S. Kim, E. Liberti, Y. Hu, T. Sasaki, P. D. Nellist, P. Zhang, D. I. Stuart, A. I. Kirkland, and P. Wang. "Cryogenic electron ptychographic single particle analysis with wide bandwidth information transfer". *Nature Communications* **14** (2023). DOI: 10.1038/s41467-023-38268-0.

[109] X. Sang and J. M. LeBeau. "Revolving scanning transmission electron microscopy: Correcting sample drift distortion without prior knowledge". *Ultramicroscopy* **138** (2014), pp. 28–35. DOI: 10.1016/j.ultramic.2013.12.004.

[110] M. Mosse, J. J. P. Peters, M. Conroy, and L. Jones. "Moving with the Times: Predictive Drift Correction of Multi-frame STEM". *Microscopy and Microanalysis* **31** (Supplement_1) (2025). DOI: 10.1093/mam/ozaf048.934.

[111] M. C. Kang, J. Park, and C. W. Yang. "Registration-based method for correcting nonlinear drift and random jitter in STEM imaging and spectroscopic mapping". *Micron* **200** (2026). DOI: 10.1016/j.micron.2025.103926.

[112] N. H. Dekkers and H. de Lang. "Differential Phase Contrast in a STEM". *Optik* **41** (4) (1974), pp. 452–456. DOI: 10.1093/jmicro/dfac022.

[113] N. Shibata, S. D. Findlay, Y. Kohno, H. Sawada, Y. Kondo, and Y. Ikuhara. "Differential phase-contrast microscopy at atomic resolution". *Nature Physics* **8** (8) (2012), pp. 611–615. DOI: 10.1038/nphys2337.

[114] J. Bürger, T. Riedl, and J. K. Lindner. "Influence of lens aberrations, specimen thickness and tilt on differential phase contrast STEM images". *Ultramicroscopy* **219** (2020). DOI: 10.1016/j.ultramic.2020.113118.

[115] I. Lazić, E. G. Bosch, and S. Lazar. "Phase contrast STEM for thin samples: Integrated differential phase contrast". *Ultramicroscopy* **160** (2016), pp. 265–280. DOI: 10.1016/j.ultramic.2015.10.011.

[116] I. Lazić, M. Wirix, M. L. Leidl, F. de Haas, D. Mann, M. Beckers, E. V. Pechnikova, K. Müller-Caspary, R. Egoavil, E. G. Bosch, and C. Sachse. "Single-particle cryo-EM structures from iDPC–STEM at near-atomic resolution". *Nature Methods* **19** (2022), pp. 1126–1136. DOI: 10.1038/s41592-022-01586-0.

[117] X. Li, I. Lazić, X. Huang, M. Wirix, L. Wang, Y. Deng, T. Niu, D. Wu, L. Yu, and F. Sun. "Imaging biological samples by integrated differential phase contrast (iDPC) STEM technique". *Journal of Structural Biology* **214** (1) (2022). DOI: 10.1016/j.jsb.2022.107837.

[118] C. Ophus. "Four-Dimensional Scanning Transmission Electron Microscopy (4D-STEM): From Scanning Nanodiffraction to Ptychography and Beyond". *Microscopy and Microanalysis* **25** (3) (2019), pp. 563–582. DOI: 10.1017/S1431927619000497.

[119] G. Li, H. Zhang, and Y. Han. "4D-STEM Ptychography for Electron-Beam-Sensitive Materials". *ACS Central Science* **8** (12) (2022), pp. 1579–1588. DOI: 10.1021/acscentsci.2c01137.

[120] S. Seifer, P. Kirchweger, K. M. Edel, and M. Elbaum. "Optimizing Contrast in Automated 4D STEM Cryotomography". *Microscopy and Microanalysis* **30** (3) (2024), pp. 476–488. DOI: 10.1093/mam/ozae050.

[121] M. J. Humphry, B. Kraus, A. C. Hurst, A. M. Maiden, and J. M. Rodenburg. "Ptychographic electron microscopy using high-angle dark-field scattering for sub-nanometre resolution imaging". *Nature Communications* **3** (2012), pp. 1–7. DOI: 10.1038/ncomms1733.

[122] C. Huang, J. S. Kim, and A. I. Kirkland. "Cryo-Electron Ptychography: Applications and Potential in Biological Characterisation". *Current Opinion in Structural Biology* **83** (2023). DOI: 10.1016/j.sbi.2023.102730.

[123] Z. Chen, Y. Jiang, Y. T. Shao, M. E. Holtz, M. Odstrčil, M. Guizar-Sicairos, I. Hanke, S. Ganschow, D. G. Schlom, and D. A. Muller. "Electron ptychography achieves atomic-resolution limits set by lattice vibrations". *Science* **372** (6544) (2021), pp. 826–831. DOI: 10.1126/science.abg2533.

[124] C. Dwyer and D. M. Paganin. "Quantum and classical Fisher information in four-dimensional scanning transmission electron microscopy". *Physical Review B* **110** (1) (2024). DOI: 10.1103/PhysRevB.110.024110.

[125] A. Patwardhan, R. Henderson, and C. J. Russo. "Extending the reach of single-particle cryoEM". *Current Opinion in Structural Biology* **92** (2025). DOI: 10.1016/j.sbi.2025.103005.

[126] L. Zhou, J. Song, J. S. Kim, X. Pei, C. Huang, M. Boyce, L. Mendonça, D. Clare, A. Siebert, C. S. Allen, E. Liberti, D. Stuart, X. Pan, P. D. Nellist, P. Zhang, A. I. Kirkland, and P. Wang. "Low-dose phase retrieval of biological specimens using cryo-electron ptychography". *Nature Communications* **11** (2020). DOI: 10.1038/s41467-020-16391-6.

[127] B. Küçükoğlu, I. Mohammed, R. C. Guerrero-Ferreira, S. M. Ribet, G. Varnavides, M. L. Leidl, K. Lau, S. Nazarov, A. Myasnikov, M. Kube, J. Radecke, C. Sachse, K. Müller-Caspary, C. Ophus, and H. Stahlberg. "Low-dose cryo-electron ptychography of proteins at sub-nanometer resolution". *Nature Communications* **15** (1) (2024), p. 8062. DOI: 10.1038/s41467-024-52403-5. URL: https://www.nature.com/articles/s41467-024-52403-5.

[128] H. Yang, R. N. Rutte, L. Jones, M. Simson, R. Sagawa, H. Ryll, M. Huth, T. J. Pennycook, M. L. Green, H. Soltau, Y. Kondo, B. G. Davis, and P. D. Nellist. "Simultaneous atomic-resolution electron ptychography and Z-contrast imaging of light and heavy elements in complex nanostructures". *Nature Communications* **7** (2016). DOI: 10.1038/ncomms12532.

[129] J. S. Kim, C. Huang, E. Liberti, M. Gallagher-Jones, B. J. Caffrey, A. Pedrazo-Tardajos, M. Boyce, P. Wang, and A. I. Kirkland. "Strategies to Find Where's Waldo (Wally) in Biology using 4D STEM". *Microscopy and Microanalysis*. Vol. 30. 2024. Oxford University Press, 2024, p. 1819. DOI: 10.1093/mam/ozae044.900.

[130] Y. Yu, K. A. Spoth, M. Colletta, K. X. Nguyen, S. E. Zeltmann, X. S. Zhang, M. Paraan, M. Kopylov, C. Dubbeldam, D. Serwas, H. Siems, D. A. Muller, and L. F. Kourkoutis. "Dose-Efficient Cryo-Electron Microscopy for Thick Samples using Tilt-Corrected Scanning Transmission Electron Microscopy, Demonstrated on Cells and Single Particles". *bioRxiv* (2024), pp. 1–59. DOI: 10.1101/2024.04.22.590491. URL: http://biorxiv.org/lookup/doi/10.1101/2024.04.22.590491.

[131] Y. Yu, K. A. Spoth, M. Colletta, K. X. Nguyen, S. E. Zeltmann, X. S. Zhang, M. Paraan, M. Kopylov, C. Dubbeldam, D. Serwas, H. Siems, D. A. Muller, and L. F. Kourkoutis. "Dose-Efficient Cryo-Electron Microscopy for Thick Samples using Tilt-Corrected Scanning Transmission Electron Microscopy, Demonstrated on Cells and Single Particles". *bioRxiv* (2024), pp. 1–59. DOI: 10.1101/2024.04.22.590491. URL: http://biorxiv.org/lookup/doi/10.1101/2024.04.22.590491.

[132] G. Varnavides, S. M. Ribet, S. E. Zeltmann, Y. Yu, B. H. Savitzky, D. O. Byrne, F. I. Allen, V. P. Dravid, M. C. Scott, and C. Ophus. "Iterative Phase Retrieval Algorithms for Scanning Transmission Electron Microscopy". *Microscopy and Microanalysis* (2024), pp. 1–25. URL: http://arxiv.org/abs/2309.05250.

[133] B. Küçükoğlu, M. Kube, W.-L. Chung, G. Varnavides, S. M. Ribet, D. Stähli, J. Daraspe, J. Radecke, C. Ophus, and H. Stahlberg. "Phase Contrast 4D-STEM Tomography of Thick Biological Specimens". *Microscopy and Microanalysis* **31** (2025). DOI: 10.1093/mam/ozaf048.1126.

[134] Y. Yu, S. Zheng, E. A. Montabana, G. Greenan, N. Jean, S. M. Ribet, G. Varnavides, and C. Ophus. "Advancing Cryo-Electron Tomography with Tilt-corrected Bright-field STEM (tcBF-STEM)". *Microscopy and Microanalysis* **31** (2025). DOI: 10.1093/mam/ozaf048.1129.

[135] M. Marko, C. Hsieh, R. Schalek, J. Frank, and C. Mannella. "Focused-ion-beam thinning of frozen-hydrated biological specimens for cryo-electron microscopy". *Nature Methods* **4** (3) (2007), pp. 215–217. DOI: 10.1038/nmeth1014.

[136] A. Rigort, F. J. Bäuerlein, E. Villa, M. Eibauer, T. Laugks, W. Baumeister, and J. M. Plitzko. "Focused ion beam micromachining of eukaryotic cells for cryoelectron tomography". *Proceedings of the National Academy of Sciences of the United States of America* **109** (12) (2012), pp. 4449–4454. DOI: 10.1073/pnas.1201333109.

[137] C. Berger, N. Premaraj, R. B. Ravelli, K. Knoops, C. López-Iglesias, and P. J. Peters. "Cryo-electron tomography on focused ion beam lamellae transforms structural cell biology". *Nature Methods* **20** (4) (2023), pp. 499–511. DOI: 10.1038/s41592-023-01783-5.

[138] L. Reimer. *Scanning Electron Microscopy: Physics of Image Formation and Microanalysis*. Ed. by P. W. Hawkes. 2nd ed. Vol. 45. Berlin: Springer-Verlag, 1998. DOI: 10.1007/978-3-540-38967-5.

[139] R. F. Egerton, P. Li, and M. Malac. "Radiation damage in the TEM and SEM". *Micron*. Vol. 35. 2004, pp. 399–409. DOI: 10.1016/j.micron.2004.02.003.

[140] A. J. Noble and A. de Marco. "Cryo-focused ion beam for in situ structural biology: State of the art, challenges, and perspectives". *Current Opinion in Structural Biology* **87** (2024). DOI: 10.1016/j.sbi.2024.102864.

[141] S. Berkamp, D. Daviran, M. Smeets, A. Caignard, R. A. Jani, P. Sundermeyer, C. Jonker, S. Gerlach, B. Hoffmann, K. Lau, and C. Sachse. "Correlative Light and Electron Cryo-Microscopy Workflow Combining Micropatterning, Ice Shield, and an In-Chamber Fluorescence Light Microscope". *Bio-protocol* **13** (24) (2023). DOI: 10.21769/BioProtoc.4901.

[142] F. R. Wagner, R. Watanabe, R. Schampers, D. Singh, H. Persoon, M. Schaffer, P. Fruhstorfer, J. Plitzko, and E. Villa. "Preparing samples from whole cells using focused-ion-beam milling for cryo-electron tomography". *Nature Protocols* **15** (6) (2020), pp. 2041–2070. DOI: 10.1038/s41596-020-0320-x.

[143] L. M. Collinson, C. Bosch, A. Bullen, J. J. Burden, R. Carzaniga, C. Cheng, M. C. Darrow, G. Fletcher, E. Johnson, K. Narayan, C. J. Peddie, M. Winn, C. Wood, A. Patwardhan, G. J. Kleywegt, and P. Verkade. "Volume EM: a quiet revolution takes shape". *Nature Methods* **20** (6) (2023), pp. 777–782. DOI: 10.1038/s41592-023-01861-8.

[144] A. Schertel, N. Snaidero, H. M. Han, T. Ruhwedel, M. Laue, M. Grabenbauer, and W. Möbius. "Cryo FIB-SEM: Volume imaging of cellular ultrastructure in native frozen specimens". *Journal of Structural Biology* **184** (2) (2013), pp. 355–360. DOI: 10.1016/j.jsb.2013.09.024.

[145] N. Vidavsky, A. Akiva, I. Kaplan-Ashiri, K. Rechav, L. Addadi, S. Weiner, and A. Schertel. "Cryo-FIB-SEM serial milling and block face imaging: Large volume structural analysis of biological tissues preserved close to their native state". *Journal of Structural Biology* **196** (3) (2016), pp. 487–495. DOI: 10.1016/j.jsb.2016.09.016.

[146] L. Mendonça, A. Howe, J. B. Gilchrist, Y. Sheng, D. Sun, M. L. Knight, L. C. Zanetti-Domingues, B. Bateman, A. S. Krebs, L. Chen, J. Radecke, V. D. Li, T. Ni, I. Kounatidis, M. A. Koronfel, M. Szynkiewicz, M. Harkiolaki, M. L. Martin-Fernandez, W. James, and P. Zhang. "Correlative multi-scale cryo-imaging unveils SARS-CoV-2 assembly and egress". *Nature Communications* **12** (1) (2021). DOI: 10.1038/s41467-021-24887-y.

[147] S. Klumpe, H. K. Fung, S. K. Goetz, I. Zagoriy, B. Hampoelz, X. Zhang, P. S. Erdmann, J. Baumbach, C. W. Müller, M. Beck, J. M. Plitzko, and J. Mahamid. "A Modular Platform for Automated Cryo-FIB Workflows". *eLife* **10** (2021). DOI: 10.7554/eLife.70506.

[148] M. Dumoux, T. Glen, J. L. Smith, E. M. Ho, L. M. Perdigão, A. Pennington, S. Klumpe, N. B. Yee, D. Farmer, P. Y. A. Lai, W. Bowles, R. Kelley, J. M. Plitzko, L. Wu, M. Basham, D. K. Clare, C. A. Siebert, M. C. Darrow, J. H. Naismith, and M. Grange. "Cryo-Plasma FIB/SEM Volume Imaging of Biological Specimens". *eLife* **12** (2023), pp. 1–33. DOI: 10.7554/eLife.83623.

[149] D. Spehner, A. M. Steyer, L. Bertinetti, I. Orlov, L. Benoit, K. Pernet-Gallay, A. Schertel, and P. Schultz. "Cryo-FIB-SEM as a promising tool for localizing proteins in 3D". *Journal of Structural Biology* **211** (1) (2020). DOI: 10.1016/j.jsb.2020.107528.

[150] J. Kuba, J. Mitchels, M. Hovorka, P. Erdmann, L. Berka, R. Kirmse, J. König, J. De Bock, B. Goetze, and A. Rigort. "Advanced cryo-tomography workflow developments – correlative microscopy, milling automation and cryo-lift-out". *Journal of Microscopy* **281** (2) (2021), pp. 112–124. DOI: 10.1111/jmi.12939.

[151] R. M. Glaeser. "Commonsense and common nonsense opinions: PROSPECTS for further reducing beam damage in electron microscopy of radiation-sensitive specimens". *Ultramicroscopy* **271** (2025). DOI: 10.1016/j.ultramic.2025.114118.

[152] R. F. Egerton. "Mechanisms of radiation damage in beam-sensitive specimens, for TEM accelerating voltages between 10 and 300 kV". *Microscopy Research and Technique* **75** (2012), pp. 1550–1556. DOI: 10.1002/jemt.22099.

[153] R. F. Egerton. "Radiation damage to organic and inorganic specimens in the TEM". *Micron* **119** (2019), pp. 72–87. DOI: 10.1016/j.micron.2019.01.005.

[154] R. F. Egerton, R. McLeod, F. Wang, and M. Malac. "Basic questions related to electron-induced sputtering in the TEM". *Ultramicroscopy* **110** (8) (2010), pp. 991–997. DOI: 10.1016/j.ultramic.2009.11.003.

[155] C. J. Russo and R. F. Egerton. "Damage in electron cryomicroscopy: Lessons from biology for materials science". *MRS Bulletin* **44** (2019), pp. 935–941. DOI: 10.1557/mrs.2019.284.

[156] R. Egerton. "Radiation Damage and Nanofabrication in TEM and STEM". *Microscopy Today* **29** (2021), pp. 56–59. DOI: 10.1017/s1551929521000663.

[157] J. L. Dickerson, K. Naydenova, M. J. Peet, H. Wilson, B. Nandy, G. McMullan, R. Morrison, and Russo C. J. "Reducing the effects of radiation damage in cryo-EM using liquid helium temperatures". *Proceedings of the National Academy of Sciences of the United States of America* **122** (17) (2025), p. 2421538122. DOI: 10.1073/pnas.

[158] S. Uehara and H. Nikjoo. "Monte Carlo Simulation of Water Radiolysis for Low-energy Charged Particles". *J. Radiat. Res* **47** (1) (2006), pp. 69–81. URL: http://jrr.jstage.jst.go.jp.

[159] L. W. Hobbs. "Radiation Damage in Electron Microscopy of Inorganic Solids". *Ultramicroscopy* **3** (1979), pp. 381–386. DOI: 10.1016/S0304-3991(78)80058-8.

[160] R. F. Egerton. "Control of radiation damage in the TEM". *Ultramicroscopy* **127** (2013), pp. 100–108. DOI: 10.1016/j.ultramic.2012.07.006.

[161] Z. D. Draganić and I. G. Draganic. "Studies on the Formation of Primary Yields of Hydrogen Peroxide and Molecular Hydrogen in the Gamma-Ray Radiolysis of Neutral Aqueous Solutions". *The Journal of Physical Chemistry* **75** (26) (1971). URL: https://pubs.acs.org/sharingguidelines.

[162] P. Abellan, E. Gautron, and J. A. LaVerne. "Radiolysis of Thin Water Ice in Electron Microscopy". *Journal of Physical Chemistry C* **127** (2023), pp. 15336–15345. DOI: 10.1021/acs.jpcc.3c02936.

[163] N. Jiang. "Damage mechanisms in electron microscopy of insulating materials". *Journal of Physics D: Applied Physics* **46** (30) (2013). DOI: 10.1088/0022-3727/46/30/305502.

[164] R. M. Glaeser. "Limitations to Significant Information in Biological Electron Microscopy as a Result of Radiation Damages". *Journal of Ultrastructure Research* **36** (1971), pp. 466–482.

[165] R. M. Glaeser and K. H. Downing. "Specimen charging on thin films with one conducting layer: Discussion of physical principles". *Microscopy and Microanalysis* **10** (2004), pp. 790–796. DOI: 10.1017/S1431927604040668.

[166] N. Jiang. "Electron irradiation effects in transmission electron microscopy: Random displacements and collective migrations". *Micron* **171** (2023). DOI: 10.1016/j.micron.2023.103482.

[167] J. Brink, M. B. Sherman, J. Berriman, and W. Chiu. "Evaluation of charging on macromolecules in electron cryomicroscopy". *Ultramicroscopy* **72** (1998), pp. 41–52. URL: http://ncmi.bioch.bcm.tmc.edu/&brink/.

[168] L. Wang, D. Liu, F. Zhang, Z. Zhang, J. Cui, Z. Jia, Z. Yu, Y. Lv, and W. Liu. "Dynamics of the charging-induced imaging instability in transmission electron microscopy". *Nanoscale Advances* **3** (2021), pp. 3035–3040. DOI: 10.1039/d1na00140j.

[169] C. J. Russo and R. Henderson. "Charge accumulation in electron cryomicroscopy". *Ultramicroscopy* **187** (2018), pp. 43–49. DOI: 10.1016/j.ultramic.2018.01.009.

[170] C. J. Russo and R. Henderson. "Microscopic charge fluctuations cause minimal contrast loss in cryoEM". *Ultramicroscopy* **187** (2018), pp. 56–63. DOI: 10.1016/j.ultramic.2018.01.011.

[171] A. F. Brilot, J. Z. Chen, A. Cheng, J. Pan, S. C. Harrison, C. S. Potter, B. Carragher, R. Henderson, and N. Grigorieff. "Beam-induced motion of vitrified specimen on holey carbon film". *Journal of Structural Biology* **177** (2012), pp. 630–637. DOI: 10.1016/j.jsb.2012.02.003.

[172] R. E. Thorne. "Hypothesis for a mechanism of beam-induced motion in cryo-electron microscopy". *IUCrJ* **7** (2020), pp. 416–421. DOI: 10.1107/S2052252520002560.

[173] R. D. Leapman and S. Sun. "Cryo-electron energy loss spectroscopy: observations on vitrified hydrated specimens and radiation damage". *Ultramicroscopy* **59** (1995), pp. 71–79. DOI: 10.1016/0304-3991(95)00019-W.

[174] S. Yakovlev, M. Misra, S. Shi, and M. Libera. "Specimen thickness dependence of hydrogen evolution during cryo-transmission electron microscopy of hydrated soft materials". *Journal of Microscopy* **236** (3) (2009), pp. 174–179. DOI: 10.1111/j.1365-2818.2009.03215.x.

[175] R. M. Glaeser. "Retrospective: Radiation damage and its associated "Information Limitations"". *Journal of Structural Biology* **163** (3) (2008), pp. 271–276. DOI: 10.1016/j.jsb.2008.06.001.

[176] J. Z. Chen, C. Sachse, C. Xu, T. Mielke, C. M. Spahn, and N. Grigorieff. "A dose-rate effect in single-particle electron microscopy". *Journal of Structural Biology* **161** (1) (2008), pp. 92–100. DOI: 10.1016/j.jsb.2007.09.017.

[177] Y. Talmon, H. T. Davis, L. E. Scriven, and E. L. Thomas. "Mass loss and etching of frozen hydrated specimens". *Journal of Microscopy* **117** (3) (1979), pp. 321–332. DOI: 10.1111/j.1365-2818.1979.tb04689.x.

[178] M. Karuppasamy, F. Karimi Nejadasl, M. Vulovic, A. J. Koster, and R. B. Ravelli. "Radiation damage in single-particle cryo-electron microscopy: Effects of dose and dose rate". *Journal of Synchrotron Radiation* **18** (3) (2011), pp. 398–412. DOI: 10.1107/S090904951100820X.

[179] H.-G. Heide. "Observations on Ice Layers". *Ultramicroscopy* **14** (1984), pp. 271–278. DOI: 10.1016/0304-3991(84)90095-0.

[180] H.-G. Heide and E. Zeitler. "The Physical Behaviour of Solid Water at Low Temperatures and the Embedding of Electron Microscopical Specimens". *Ultramicroscopy* **16** (1985), pp. 151–160. DOI: 10.1016/0304-3991(85)90070-1.

[181] M. Stöger-Pollach. "Low voltage TEM: Influences on electron energy loss spectrometry experiments". *Micron* **41** (6) (2010), pp. 577–584. DOI: 10.1016/j.micron.2010.04.007.

[182] R. F. Egerton. "Dose measurement in the TEM and STEM". *Ultramicroscopy* **229** (2021). DOI: 10.1016/j.ultramic.2021.113363.

[183] M. J. Peet, R. Henderson, and C. J. Russo. "The energy dependence of contrast and damage in electron cryomicroscopy of biological molecules". *Ultramicroscopy* **203** (2019), pp. 125–131. DOI: 10.1016/j.ultramic.2019.02.007.

[184] G. I. McMullan, K. I. Naydenova, D. Mihaylov, K. I. Yamashita, M. J. Peet ID, H. I. Wilson, J. L. Dickerson ID, S. I. Chen, G. I. Cannone, Y. I. Lee, K. A. Hutchings ID, O. I. Gittins, M. A. Sobhy ID, T. I. Wells, M. M. El-Gomati ID, J. Dalby, M. I. Meffert, C. I. Schulze-Briese, R. I. Henderson, and C. J. Russo. "Structure determination by cryoEM at 100 keV". *Proceedings of the National Academy of Sciences of the United States of America* (2023). DOI: 10.1073/pnas.

[185] D. Zhu, H. Shi, C. Wu, and X. Zhang. "An electron counting algorithm improves imaging of proteins with low-acceleration-voltage cryo-electron microscope". *Communications Biology* **5** (1) (2022). DOI: 10.1038/s42003-022-03284-1.

[186] Y. Zhang, J. P. van Schayck, A. Pedrazo-Tardajos, N. Claes, W. E. Noteborn, P. H. Lu, H. Duimel, R. E. Dunin-Borkowski, S. Bals, P. J. Peters, and R. B. Ravelli. "Charging of Vitreous Samples in Cryogenic Electron Microscopy Mitigated by Graphene". *ACS Nano* **17** (16) (2023), pp. 15836–15846. DOI: 10.1021/acsnano.3c03722.

[187] J. Xu, X. Gao, L. Zheng, X. Jia, K. Xu, Y. Ma, X. Wei, N. Liu, H. Peng, and H. W. Wang. "Graphene sandwich–based biological specimen preparation for cryo-EM analysis". *Proceedings of the National Academy of Sciences of the United States of America* **121** (5) (2024). DOI: 10.1073/pnas.2309384121.

[188] K. Sader, M. Stopps, L. J. Calder, and P. B. Rosenthal. "Cryomicroscopy of radiation sensitive specimens on unmodified graphene sheets: Reduction of electron-optical effects of charging". *Journal of Structural Biology* **183** (3) (2013), pp. 531–536. DOI: 10.1016/j.jsb.2013.04.014.

[189] S. T. Skowron, S. L. Roberts, A. N. Khlobystov, and E. Besley. "The effects of encapsulation on damage to molecules by electron radiation". *Micron* **120** (2019), pp. 96–103. DOI: 10.1016/j.micron.2019.02.007.

[190] K. Naydenova, M. J. Peet, and C. J. Russo. "Multifunctional graphene supports for electron cryomicroscopy". *Proceedings of the National Academy of Sciences of the United States of America* **116** (24) (2019), pp. 11718–11724. DOI: 10.1073/pnas.1904766116.

[191] S. Khavnekar, V. Vrbovská, M. Zaoralová, R. Kelley, F. Beck, S. Klumpe, A. Kotecha, J. Plitzko, and P. S. Erdmann. "Optimizing Cryo-FIB Lamellas for sub-5Å in situ Structural Biology". *bioRxiv* (2022). DOI: 10.1101/2022.06.16.496417. URL: http://biorxiv.org/lookup/doi/10.1101/2022.06.16.496417.

[192] M. Schaffer, J. Mahamid, B. D. Engel, T. Laugks, W. Baumeister, and J. M. Plitzko. "Optimized cryo-focused ion beam sample preparation aimed at in situ structural studies of membrane proteins". *Journal of Structural Biology* **197** (2) (2017), pp. 73–82. DOI: 10.1016/j.jsb.2016.07.010.

[193] Y. Li, D. D. Kang, J. Y. Dai, and L. W. Wang. "The cage effect of electron beam irradiation damage in cryo-electron microscopy". *npj Computational Materials* **10** (2024). DOI: 10.1038/s41524-024-01299-2.

[194] W. Chiu, E. Knapek, T. W. Jeng, and I. Dietrich. "Electron Radiation Damage of a Thin Protein Crystal at 4 K". *Ultramicroscopy* **6** (1981), pp. 291–296. DOI: 10.1016/S0304-3991(81)80211-2.

[195] K. Naydenova, A. Kamegawa, M. J. Peet, R. Henderson, Y. Fujiyoshi, and C. J. Russo. "On the reduction in the effects of radiation damage to two-dimensional crystals of organic and biological molecules at liquid-helium temperature". *Ultramicroscopy* **237** (2022). DOI: 10.1016/j.ultramic.2022.113512.

[196] O. Pfeil-Gardiner, D. J. Mills, J. Vonck, and W. Kuehlbrandt. "A comparative study of single-particle cryo-EM with liquid-nitrogen and liquid-helium cooling". *IUCrJ* **6** (2019), pp. 1099–1105. DOI: 10.1107/S2052252519011503.

[197] E. R. Wright, C. V. Iancu, W. F. Tivol, and G. J. Jensen. "Observations on the behavior of vitreous ice at 82 and 12 K". *Journal of Structural Biology* **153** (3) (2006), pp. 241–252. DOI: 10.1016/j.jsb.2005.12.003.

[198] C. V. Iancu, E. R. Wright, J. B. Heymann, and G. J. Jensen. "A comparison of liquid nitrogen and liquid helium as cryogens for electron cryotomography". *Journal of Structural Biology* **153** (3) (2006), pp. 231–240. DOI: 10.1016/j.jsb.2005.12.004.

[199] C. J. Russo, J. L. Dickerson, and K. Naydenova. "Cryomicroscopy in situ: what is the smallest molecule that can be directly identified without labels in a cell?": *Faraday Discussions* **240** (2022), pp. 277–302. DOI: 10.1039/d2fd00076h.

[200] R. F. Egerton and I. Rauf. "Dose-rate dependence of electron-induced mass loss from organic specimens". *Ultramicroscopy* **80** (1999), pp. 247–254.

[201] E. J. Vandenbussche and D. J. Flannigan. "Reducing Radiation Damage in Soft Matter with Femtosecond-Timed Single-Electron Packets". *Nano Letters* **19** (2019), pp. 6687–6694. DOI: 10.1021/acs.nanolett.9b03074.

[202] E. J. Vandenbussche, C. P. Clark, R. J. Holmes, and D. J. Flannigan. "Mitigating Damage to Hybrid Perovskites Using Pulsed-Beam TEM". *ACS Omega* **5** (2020), pp. 31867–31871. DOI: 10.1021/acsomega.0c04711.

[203] H. Choe, E. Montgomery, I. Ponomarev, J. Lau, Y. Zhu, Y. Zhao, A. Liu, A. Kanareykin, and C. Jing. "Radiation damage study of organic molecules via laser-free ultrafast transmission electron microscopy". *Microscopy and Microanalysis* **27** (S1) (2021), pp. 3358–3359. DOI: 10.1017/s1431927621011545.

[204] R. Egerton, P. Rez, and Y. Zhu. "Dynamics of Beam Interaction and Damage within a Thin TEM Specimen". *Microscopy and Microanalysis*. Vol. 30. 2024. Oxford University Press, 2024, pp. 1449–1451. DOI: 10.1093/mam/ozae044.714.

[205] V. Kumar, J. Radecke, K. Chinmaya, I. Mohammed, R. C. Guerrero-Ferreira, D. Harder, D. Fotiadis, and H. Stahlberg. "Pulsed-electron illumination does not reduce beam damage for imaging biological macromolecules". *bioRxiv* (2025). DOI: 10.1101/2025.07.29.667395. URL: http://biorxiv.org/lookup/doi/10.1101/2025.07.29.667395.

[206] K. H. Downing. "Spot-Scan Imaging in Transmission Electron Microscopy". *Science* **251** (1991). DOI: 10.1126/science.1846047.

[207] P. Bullough and R. Henderson. "Use of Spot-Scan Procedure for Recording Low-Dose Micrographs of Beam-Sensitive Specimens". *Ultramicroscopy* **27** (1987), pp. 223–230. DOI: 10.1016/0304-3991(87)90147-1.

[208] M. Ilett, R. Brydson, A. Brown, and N. Hondow. "Cryo-analytical STEM of frozen, aqueous dispersions of nanoparticles". *Micron* **120** (2019), pp. 35–42. DOI: 10.1016/j.micron.2019.01.013.

[209] X. Sang, A. R. Lupini, R. R. Unocic, M. Chi, A. Y. Borisevich, S. V. Kalinin, E. Endeve, R. K. Archibald, and S. Jesse. "Dynamic scan control in STEM: spiral scans". *Advanced Structural and Chemical Imaging* **2** (1) (2016). DOI: 10.1186/s40679-016-0020-3.

[210] S. Seifer, L. Houben, and M. Elbaum. "Flexible STEM with Simultaneous Phase and Depth Contrast". *Microscopy and Microanalysis* **27** (2021), pp. 1476–1487. DOI: 10.1017/S1431927621012861.

[211] X. Li, O. Dyck, S. V. Kalinin, and S. Jesse. "Compressed sensing of Scanning Transmission Electron Microscopy (STEM) with nonrectangular scans". *Microscopy and Microanalysis* **24** (6) (2018), pp. 623–633. DOI: 10.1017/S143192761801543X.

[212] A. Velazco, A. Béché, D. Jannis, and J. Verbeeck. "Reducing electron beam damage through alternative STEM scanning strategies, Part I: Experimental findings". *Ultramicroscopy* **232** (2022). DOI: 10.1016/j.ultramic.2021.113398.

[213] D. Jannis, A. Velazco, A. Béché, and J. Verbeeck. "Reducing electron beam damage through alternative STEM scanning strategies, Part II: Attempt towards an empirical model describing the damage process". *Ultramicroscopy* **240** (2022). DOI: 10.1016/j.ultramic.2022.113568.

[214] R. F. Egerton. "Scattering delocalization and radiation damage in STEM-EELS". *Ultramicroscopy* **180** (2017), pp. 115–124. DOI: 10.1016/j.ultramic.2017.02.007.

[215] A. Zobelli, S. Y. Woo, A. Tararan, L. H. Tizei, N. Brun, X. Li, O. Stéphan, M. Kociak, and M. Tencé. "Spatial and spectral dynamics in STEM hyperspectral imaging using random scan patterns". *Ultramicroscopy* **212** (2020). DOI: 10.1016/j.ultramic.2019.112912.

[216] D. Nicholls, J. Wells, A. Stevens, Y. Zheng, J. Castagna, and N. D. Browning. "Sub-Sampled Imaging for STEM: Maximising Image Speed, Resolution and Precision Through Reconstruction Parameter Refinement". *Ultramicroscopy* **233** (2022). DOI: 10.1016/j.ultramic.2021.113451.

[217] A. Velazco, M. Nord, A. Béché, and J. Verbeeck. "Evaluation of different rectangular scan strategies for STEM imaging". *Ultramicroscopy* **215** (2020). DOI: 10.1016/j.ultramic.2020.113021.

[218] L. Donati, M. Nilchian, S. Trépout, C. Messaoudi, S. Marco, and M. Unser. "Compressed sensing for STEM tomography". *Ultramicroscopy* **179** (2017), pp. 47–56. DOI: 10.1016/j.ultramic.2017.04.003.

[219] A. Velazco, T. Glen, S. Klumpe, A. Pennington, J. Zhang, J. L. R. Smith, C. Glynn, W. Bowles, M. Kobylynska, R. A. Fleck, J. H. Naismith, J. S. Kim, M. C. Darrow, M. Grange, A. I. Kirkland, and M. Dumoux. "Reduction of SEM charging artefacts in native cryogenic biological samples". *Nature Communications* **16** (2025), p. 5204. DOI: 10.1038/s41467-025-60545-3. URL: https://www.nature.com/articles/s41467-025-60545-3.

[220] E. Abbe. *The Optical Aids of Microscopy*. Tech. rep. London: London International Exhibition, 1876. URL: https://digital.deutsches-museum.de/item/BV003455461/.

[221] J. J. Thompson. "Cathode Rays". *The Electrician* **39** (1897), pp. 104–109. URL: https://www.ub.edu/hcub/hfq/sites/default/files/thomson%2C%201897.pdf.

[222] L.-V. de Broglie. "On the Theory of Quanta (Recherches sur la théorie des quanta)". PhD thesis. Université de Paris, 1925. URL: https://fondationlouisdebroglie.org/LDB-oeuvres/De_Broglie_Kracklauer.pdf.

[223] M. Knoll and E. Ruska. "Beitrag zur geometrischen Elektronenoptik. II". *Annalen der Physik* **404** (1932), pp. 641–661. DOI: 10.1002/andp.19324040602.

[224] E. Ruska. "Nobel Lecture: The Development of the Electron Microscope and of Electron Microscopy". *Bioscience Reports* **7** (1987). DOI: 10.1007/BF01127674.

[225] L. Reimer and H. Kohl. *Transmission Electron Microscopy*. 5th ed. Springer, 2008. DOI: 10.1007/978-0-387-34758-5. URL: www.springeronline.com/series/624.

[226] S. J. Pennycook and P. D. Nellist. *Scanning Transmission Electron Microscopy Imaging and Analysis*. New York: Springer Science, 2011. DOI: 10.1007/978-1-4419-7200-2{_}2.

[227] A. Howie. "Image Contrast And Localized Signal Selection Techniques". *Journal of Microscopy* **117** (1979), pp. 11–23. DOI: 10.1111/j.1365-2818.1979.tb00228.x.

[228] R. H. Wade. "A brief look at imaging and contrast transfer". *Ultramicroscopy* **46** (1992), pp. 145–156. DOI: 10.1016/0304-3991(92)90011-8.

[229] CryoSPARC. *Contrast in Cryo-EM*. 2024. URL: https://guide.cryosparc.com/.

[230] A. Punjani, J. L. Rubinstein, D. J. Fleet, and M. A. Brubaker. "CryoSPARC: Algorithms for rapid unsupervised cryo-EM structure determination". *Nature Methods* **14** (3) (2017), pp. 290–296. DOI: 10.1038/nmeth.4169.

[231] L. Reimer. *Transmission Electron Microscopy: Physics of Image Formation and Microanalysis*. 4th ed. Berlin: Springer-Verlag, 2013. DOI: 10.1007/978-3-662-14824-2.

[232] H. Venugopal, J. Mobbs, C. Taveneau, D. R. Fox, Z. Vuckovic, S. Gulati, G. Knott, R. Grinter, D. Thal, S. Mick, C. Czarnik, and G. Ramm. "High-resolution cryo-EM using a common LaB 6 120-keV electron microscope equipped with a sub-200-keV direct electron detector". *Science Advances* **11** (2025), p. 438. URL: https://www.science.org.

[233] M. M. El-Gomati, T. Wells, X. Zha, R. Sykes, C. J. Russo, R. Henderson, and G. McMullan. "100 keV vacuum sealed field emission gun for high resolution electron microscopy". *Journal of Vacuum Science & Technology B, Nanotechnology and Microelectronics: Materials, Processing, Measurement, and Phenomena* **39** (6) (2021). DOI: 10.1116/6.0001275.

[234] F. Zemlin, E. Beckmann, and K. D. van der Mast. "A 200 kV Electron Microscope with Schottky Field Emitter and a Helium-Cooled Superconducting Objective Lens". *Ultramicroscopy* **63** (1996), pp. 227–8. DOI: 10.1016/0304-3991(96)00038-1.

[235] M. De Graef. "The transmission electron microscope". *Introduction to Conventional Transmission Electron Microscopy*. Cambridge University Press, 2003, pp. 136–234. DOI: 10.1017/CBO9780511615092.005. URL: https://www.cambridge.org/core/product/identifier/CBO9780511615092A027/type/book_part.

[236] C. Whittier and N. D. Bassim. "High-energy resolution monochromated STEM-EELS mapping across large areas". *Ultramicroscopy* **276** (2025). DOI: 10.1016/j.ultramic.2025.114202.

[237] Z. Zheng, C. S. Own, A. A. Wanner, R. A. Koene, E. W. Hammerschmith, W. M. Silversmith, N. Kemnitz, R. Lu, D. W. Tank, and H. S. Seung. "Fast imaging of millimeter-scale areas with beam deflection transmission electron microscopy". *Nature Communications* **15** (1) (2024). DOI: 10.1038/s41467-024-50846-4.

[238] T. E. Gage, H. Hou, and J. Wen. "Harnessing Nanosecond STEM Electron Pulses with an Electrostatic Beam Blanker for Angstrom Spatial Resolution in Time-Resolved Studies of Electrically Excited Dynamics". *Microscopy and Microanalysis*. Vol. 30. 2024. Oxford University Press, 2024, pp. 1465–1466. DOI: 10.1093/mam/ozae044.723.

[239] R. Egoavil, P. Potocek, E. Van Cappellen, M, Meledina, M. Wirix, and B. Freitag. "Advantages of an Electrostatic Beam Blanker in STEM". *Microscopy and Microanalysis*. Vol. 75. 11. 2025. DOI: 10.1093/mam/ozaf048.104.

[240] O. Scherzer. "The theoretical resolution limit of the electron microscope". *Journal of Applied Physics* **20** (1) (1949), pp. 20–29. DOI: 10.1063/1.1698233.

[241] M. Haider, H. Rose, S. Uhlemann, E. Schwan, B. Kabius, and K. Urban. "A spherical-aberration-corrected 200 kV transmission electron microscope". *Ultramicroscopy* **75** (1998), pp. 53–60.

[242] Y. E. Kwon, C. Han, S. C. Lee, J. M. Jeung, G. Lee, T. Y. Lee, and J. G. Kim. "Abnormal shadow contrast imaging for optimal objective lens condition in transmission electron microscope". *Journal of Analytical Science and Technology* **13** (1) (2022). DOI: 10.1186/s40543-022-00323-8.

[243] M. Weyland and D. A. Muller. "Tuning the convergence angle for optimum STEM performance". *arxiv* (2020). DOI: 10.48550/arXiv.2008.12870.

[244] N. Schnitzer, S. H. Sung, and R. Hovden. "Introduction to the Ronchigram and its Calculation with Ronchigram.com". *Microscopy Today* **27** (03) (2019), pp. 12–15. DOI: 10.1017/s1551929519000427.

[245] T. Mullarkey, M. Geever, J. J. Peters, I. Griffiths, P. D. Nellist, and L. Jones. "How Fast is Your Detector? The Effect of Temporal Response on Image Quality". *Microscopy and Microanalysis* **29** (4) (2023), pp. 1402–1408. DOI: 10.1093/micmic/ozad061.

[246] J. J. Peters, T. Mullarkey, E. Hedley, K. H. Müller, A. Porter, A. Mostaed, and L. Jones. "Electron counting detectors in scanning transmission electron microscopy via hardware signal processing". *Nature Communications* **14** (1) (2023). DOI: 10.1038/s41467-023-40875-w.

[247] P. L. Chiu, X. Li, Z. Li, B. Beckett, A. F. Brilot, N. Grigorieff, D. A. Agard, Y. Cheng, and T. Walz. "Evaluation of super-resolution performance of the K2 electron-counting camera using 2D crystals of aquaporin-0". *Journal of Structural Biology* **192** (2) (2015), pp. 163–173. DOI: 10.1016/j.jsb.2015.08.015.

[248] T. Grant and N. Grigorieff. "Measuring the optimal exposure for single particle cryo-EM using a 2.6Å reconstruction of rotavirus VP6". *eLife* (2015), pp. 1–19. DOI: 10.7554/eLife.06980.001.

[249] H. Demers, R. Ramachandra, D. Drouin, and N. De Jonge. "The probe profile and lateral resolution of scanning transmission electron microscopy of thick specimens". *Microscopy and Microanalysis* **18** (3) (2012), pp. 582–590. DOI: 10.1017/S1431927612000232.

[250] J. R. Michael and D. B. Williams. "A consistent definition of probe size and spatial resolution in the analytical electron microscope". *Journal of Microscopy* **147** (1987), pp. 289–303. DOI: 10.1111/j.1365-2818.1987.tb02840.x.

[251] J. W. S. Rayleigh. "XXXI. Investigations in optics, with special reference to the spectroscope". *The London, Edinburgh, and Dublin Philosophical Magazine and Journal of Science* **8** (1879), pp. 261–274. DOI: 10.1080/14786447908639684.

[252] E. Hecht. *Optics, Global Edition*. Global Edition. Vol. 5. Pearson Education, 2016, pp. 1–730. URL: http://www.ncbi.nlm.nih.gov/pubmed/5174663.

[253] G. B. Airy. "On the Diffraction of an Object-glass with Circular Aperture." *Transactions of the Cambridge Philosophical Society* **5** (1834), pp. 283–291. URL: https://archive.org/details/transactionsofca05camb/page/190/mode/2up.

[254] E. J. Kirkland. "On the optimum probe in aberration corrected ADF-STEM". *Ultramicroscopy* **111** (11) (2011), pp. 1523–1530. DOI: 10.1016/j.ultramic.2011.09.002.

[255] R. F. Egerton. *Physical Principles of Electron Microscopy*. 2nd ed. New York: Springer, 2005. DOI: 10.1007/978-3-319-39877-8.

[256] L. Fréchin, S. Holvec, O. von Loeffelholz, I. Hazemann, and B. P. Klaholz. "High-resolution cryo-EM performance comparison of two latest-generation cryo electron microscopes on the human ribosome". *Journal of Structural Biology* **215** (1) (2023). DOI: 10.1016/j.jsb.2022.107905.

[257] E. J. Kirkland. *Advanced Computing in Electron Microscopy*. Springer US, 2010, pp. 1–289. URL: https://doi.org/10.1007/978-1-4419-6533-2.

[258] M. Born and E. Wolf. *Principles Of Optics: Electromagnetic Theory of Propagation Interference and Diffraction of Light*. 6th. Pergamon, 1989, pp. 435–448. DOI: 10.1017/CBO9781139644181.

[259] A. Y. Borisevich, A. R. Lupini, and S. J. Pennycook. "Depth sectioning with the aberration-corrected scanning transmission electron microscope". *Proceedings of the National Academy of Sciences* **103** (2006), pp. 3044–3048. DOI: 10.1073/pnas.0507105103. URL: https://www.pnas.org.

[260] A. P. Pogany and P. S. Turner. "Reciprocity in electron diffraction and microscopy". *Acta Crystallographica Section A* **24** (1) (1968), pp. 103–109. DOI: 10.1107/S0567739468000136.

[261] Z. L. Wang. "Reciprocity in Electron Diffraction and Imaging". *Elastic and Inelastic Scattering in Electron Diffraction and Imaging*. Boston, MA: Springer, 1995. DOI: https://doi.org/10.1007/. URL: https://doi.org/10.1007/978-1-4899-1579-5_9.

[262] J. Liu and J. M. Cowley. "High-resolution scanning transmission electron microscopy". *Ultramicroscopy* **52** (1993), pp. 335–346. DOI: 10.1016/0304-3991(93)90044-X.

[263] S. Heydari and J. Liu. "High-throughput cryo-electron tomography enables multiscale visualization of the inner life of microbes". *Current Opinion in Structural Biology* **93** (2025). DOI: 10.1016/j.sbi.2025.103065.

[264] F. Eisenstein, H. Yanagisawa, H. Kashihara, M. Kikkawa, S. Tsukita, and R. Danev. "Parallel cryo electron tomography on in situ lamellae". *Nature Methods* **20** (1) (2023), pp. 131–138. DOI: 10.1038/s41592-022-01690-1.

[265] J. Biskupek, J. Leschner, P. Walther, and U. Kaiser. "Optimization of STEM tomography acquisition - A comparison of convergent beam and parallel beam STEM tomography". *Ultramicroscopy* **110** (9) (2010), pp. 1231–1237. DOI: 10.1016/j.ultramic.2010.05.008.

[266] S. G. Wolf and M. Elbaum. "CryoSTEM tomography in biology". *Methods in Cell Biology*. Ed. by T. Muller-Reichert and G. Pigino. Vol. 152. Elsevier Science Publishing Co Inc., 2019, pp. 197–215. DOI: 10.1016/bs.mcb.2019.04.001.

[267] T. Dahmen, J. P. Baudoin, A. R. Lupini, C. Kübel, P. Slusallek, and N. D. Jonge. "Combined scanning transmission electron microscopy tilt- and focal series". *Microscopy and Microanalysis* **20** (2014), pp. 548–560. DOI: 10.1017/S1431927614000075.

[268] T. Dahmen. "Tomographic Reconstruction of Combined Tilt- and Focal Series in Scanning Transmission Electron Microscopy". PhD thesis. Saarland University, 2015, pp. 1–121. URL: https://www.researchgate.net/publication/298070739.

[269] P. Gentsch, H. Gilde, and L. Reimer. "Measurement of the top bottom effect in scanning transmission electron microscopy of thick amorphous specimens". *Journal of Microscopy* **100** (1) (1974), pp. 81–92. DOI: 10.1111/j.1365-2818.1974.tb03915.x.

[270] J. K. Hyun, P. Ercius, and D. A. Muller. "Beam spreading and spatial resolution in thick organic specimens". *Ultramicroscopy* **109** (2008), pp. 1–7. DOI: 10.1016/j.ultramic.2008.07.003.

[271] G. J. I. "Quantitative X-ray analysis in the electron microscope". *Scanning Electron Microscopy* **1** (1977), pp. 315–324. URL: https://cir.nii.ac.jp/crid/1571980074588440064.bib?lang=en.

[272] S. J. B. Reed. "The Single-Scattering Model and Spatial Resolution in X-ray Analysis of Thin Foils". *Ultramicroscopy* **7** (1982), pp. 405–410. DOI: 10.1016/0304-3991(82)90263-7.

[273] D. C. Joy and C. S. Joy. "Scanning electron microscope imaging in liquids - Some data on electron interactions in water". *Journal of Microscopy* **221** (2) (2006), pp. 84–88. DOI: 10.1111/j.1365-2818.2006.01548.x.

[274] D. C. Joy and C. S. Joy. "Low Voltage Scanning Electron Microscopy". *Micron* **27** (4) (1996), pp. 247–263. DOI: 10.1016/0968-4328(96)00023-6.

[275] N. de Jonge, N. Poirier-Demers, H. Demers, D. B. Peckys, and D. Drouin. "Nanometer-resolution electron microscopy through micrometers-thick water layers". *Ultramicroscopy* **110** (9) (2010), pp. 1114–1119. DOI: 10.1016/j.ultramic.2010.04.001.

[276] P. Rez. "Scattering Cross Sections in Electron Microscopy and Analysis". *Microscopy and Microanalysis* **7** (4) (2001), pp. 356–362. DOI: 10.1007/s10005-001-0003-5.

[277] D. Rez, P. Rez, and I. Grant. "Dirac–Fock calculations of X-ray scattering factors and contributions to the mean inner potential for electron scattering". *Acta Crystallographica Section A* **50** (4) (1994), pp. 481–497. DOI: 10.1107/S0108767393013200.

[278] I. Lobato and D. V. Dyck. "An accurate parameterization for scattering factors, electron densities and electrostatic potentials for neutral atoms that obey all physical constraints". *Acta Crystallographica Section A: Foundations and Advances* **70** (2014) (2014), pp. 636–649. DOI: 10.1107/S205327331401643X.

[279] M. N. Yesibolati, S. Laganá, S. Kadkhodazadeh, E. K. Mikkelsen, H. Sun, T. Kasama, O. Hansen, N. J. Zaluzec, and K. Mølhave. "Electron inelastic mean free path in water". *Nanoscale* **12** (40) (2020), pp. 20649–20657. DOI: 10.1039/d0nr04352d.

[280] K. Yonekura, M. B. Braunfeld, S. Maki-Yonekura, and D. A. Agard. "Electron energy filtering significantly improves amplitude contrast of frozen-hydrated protein at 300 kV". *Journal of Structural Biology* **156** (3) (2006), pp. 524–536. DOI: 10.1016/j.jsb.2006.07.016.

[281] B. Feja and U. Aebi. "Determination of the inelastic mean free path of electrons in vitrified ice layers for on-line thickness measurements by zero-loss imaging". *Journal of Microscopy* **193** (1) (1999), pp. 15–19. DOI: 10.1046/j.1365-2818.1999.00436.x.

[282] R. Grimm, D. Typke, M. Bärmann, and W. Baumeister. "Determination of the Inelastic Mean Free Path in Ice by Examination of Tilted Vesicles and Automated Most Probably Loss Imaging". *Ultramicroscopy* **63** (1996), pp. 169–179. DOI: 10.1016/0304-3991(96)00035-6.

[283] K. T. Moore, J. M. Howe, D. R. Veblen, T. M. Murray, and E. A. Stach. "Analysis of electron intensity as a function of aperture size in energy-Filtered Transmission Electron Microscope imaging". *Ultramicroscopy* **80** (1999), pp. 221–236. DOI: 10.1016/S0304-3991(99)00115-1.

[284] H. G. Brown and E. Hanssen. "MeasureIce: accessible on-the-fly measurement of ice thickness in cryo-electron microscopy". *Communications Biology* **5** (1) (2022). DOI: 10.1038/s42003-022-03698-x.

[285] S. W. Smith. "Spectral Imaging Techniques". *The Scientist and Engineer's Guide to Digital Signal Processing*. 2nd ed. DSP, 1997. Chap. 25, pp. 423–450.

[286] M. T. Browne and J. F. L. Ward. "Detectors for STEM and the Measurement of their Detective Quantum Efficiency". *Ultramicroscopy* **7** (1982), pp. 249–262. DOI: 10.1016/0304-3991(82)90172-3.

[287] Y. L. Gao, S. Bi, Y. Wang, J. Li, T. Su, and X. Gao. "Co-ligand triphenylphosphine/alkynyl-stabilized undecagold nanocluster with a capped crown structure". *RSC Advances* **12** (18) (2022), pp. 11047–11051. DOI: 10.1039/d2ra01080a.

[288] A. A. Sheader, G. Vizcay-Barrena, R. A. Fleck, S. J. Flatters, and P. D. Nellist. "Subcellular localisation and identification of single atoms using quantitative scanning transmission electron microscopy". *Journal of Microscopy* **299** (1) (2025), pp. 36–48. DOI: 10.1111/jmi.13410.

[289] W. Faulk and G. M. Taylor. "An Immunocolloid Method for the Electron Microscope". *Immunochemistry* **8** (1971). DOI: 10.1016/0019-2791(71)90496-4.

[290] S. Homma-Takeda, H. Fujishiro, I. Tanaka, H. Yakumaru, K. Ayama, A. Uehara, M. Oikawa, S. Himeno, and H. Ishihara. "Single-cell imaging for studies of renal uranium transport and intracellular behavior". *Minerals* **11** (2) (2021), pp. 1–10. DOI: 10.3390/min11020191.

[291] J. W. Arblaster. "Osmium, the Densest Metal Known". *Platinum Metals Reviews* **4** (39) (1995), pp. 163–64. DOI: 10.1595/003214095X394164164.

[292] I. C. Smith, B. L. Carson, and T. L. Ferguson. "Osmium: An Appraisal of Environmental Exposure". *Environmental Health Perspectives* **8** (1974), pp. 201–213. DOI: 10.2307/3428200.

[293] A. Rose. "A Unified Approach to the Performance of Photographic Film, Television Pickup Tubes, and the Human Eye". *Journal of the Society of Motion Picture Engineers* **47** (4) (1946). DOI: 10.5594/J12772.

[294] A. E. Burgess. "Evaluation of detection model performance in power-law noise". *Society of Photo-Optical Instrumentation Engineers (SPIE)*. 2001, pp. 123–132. DOI: 10.1364/JOSAA.24.000B52.

[295] B. A. Lucas and N. Grigorieff. "Quantification of gallium cryo-FIB milling damage in biological lamella". *bioRxiv* (2023), pp. 526–705. DOI: 10.1101/2023.02.01.526705.

[296] D. Nicholls, J. Lee, H. Amari, A. J. Stevens, B. L. Mehdi, and N. D. Browning. "Minimising damage in high resolution scanning transmission electron microscope images of nanoscale structures and processes". *Nanoscale* **12** (41) (2020), pp. 21248–21254. DOI: 10.1039/d0nr04589f.

[297] H. S. Yoon, C. S. Kim, H. T. Lee, and S. H. Ahn. "Advanced scanning paths for focused ion beam milling". *Vacuum* **143** (2017), pp. 40–49. DOI: 10.1016/j.vacuum.2017.05.023.

[298] S. J. Pennycook. "Z-Contrast STEM For Materials Science". *Ultramicroscopy* **30** (1989), pp. 58–69. DOI: 10.1016/0304-3991(89)90173-3.

[299] V. Intaraprasonk, H. L. Xin, and D. A. Muller. "Analytic derivation of optimal imaging conditions for incoherent imaging in aberration-corrected electron microscopes". *Ultramicroscopy* **108** (2008), pp. 1454–1466. DOI: 10.1016/j.ultramic.2008.05.013.

[300] M. Warkentin, R. Badeau, J. Hopkins, and R. E. Thorne. "Dark progression reveals slow timescales for radiation damage between T = 180 and 240 K". *Acta Crystallographica Section D: Biological Crystallography* **67** (9) (2011), pp. 792–803. DOI: 10.1107/S0907444911027600.

[301] R Core Team. *R: A Language and Environment for Statistical Computing*. 2021. DOI: 10.21105/joss.00571.

[302] A. Moshtaghpour, A. Velazco-Torrejon, D. Nicholls, A. W. Robinson, A. I. Kirkland, and N. D. Browning. "Diffusion Distribution Model for Damage Mitigation in Scanning Transmission Electron Microscopy". *arXiv* (2024), pp. 1–46. URL: http://arxiv.org/abs/2406.02207.

[303] T. Susi, C. Hofer, G. Argentero, G. T. Leuthner, T. J. Pennycook, C. Mangler, J. C. Meyer, and J. Kotakoski. "Isotope analysis in the transmission electron microscope". *Nature Communications* **7** (2016). DOI: 10.1038/ncomms13040.

[304] M. Dumoux, J. L. Smith, T. Glen, M. Grange, M. C. Darrow, and J. H. Naismith. "A protocol for cryogenic volumetric imaging using serial plasma FIB/SEM". *Methods in Cell Biology*. Vol. 177. Academic Press Inc., 2023, pp. 327–358. DOI: 10.1016/bs.mcb.2023.01.015.

[305] D. Drouin, A. R. ´. E. Couture, D. Joly, X. Tastet, V. Aimez, and R. Gauvin. *CASINO V2.42-A Fast and Easy-to-use Modeling Tool for Scanning Electron Microscopy and Microanalysis Users*. Tech. rep. 2007, pp. 92–101. URL: www.gel.usherb.ca/casino..

[306] J. A. Ghormley and C. J. Hochanadel. "Amorphous Ice: Density and Reflectivity". *Science* **171** (1971), pp. 62–64. URL: https://www.science.org.

[307] J. Zivanov, T. Nakane, and S. H. Scheres. "A Bayesian approach to beam-induced motion correction in cryo-EM single-particle analysis". *IUCrJ* **6** (2019), pp. 5–17. DOI: 10.1107/S205225251801463X.

[308] A. Rohou and N. Grigorieff. "CTFFIND4: Fast and accurate defocus estimation from electron micrographs". *Journal of Structural Biology* **192** (2) (2015), pp. 216–221. DOI: 10.1016/j.jsb.2015.08.008.

[309] P. B. Rosenthal and R. Henderson. "Optimal determination of particle orientation, absolute hand, and contrast loss in single-particle electron cryomicroscopy". *Journal of Molecular Biology* **333** (4) (2003), pp. 721–745. DOI: 10.1016/j.jmb.2003.07.013.

[310] C. Berger, H. Watson, J. H. Naismith, M. Dumoux, and M. Grange. "Xenon plasma focused ion beam lamella fabrication on high-pressure frozen specimens for structural cell biology". *Nature Communications* **16** (1) (2025). DOI: 10.1038/s41467-025-57493-3.

[311] M. G. Last, W. E. Noteborn, L. M. Voortman, and T. H. Sharp. "Super-resolution fluorescence imaging of cryosamples does not limit achievable resolution in cryoEM". *Journal of Structural Biology* **215** (4) (2023). DOI: 10.1016/j.jsb.2023.108040.

[312] E. F. Pettersen, T. D. Goddard, C. C. Huang, G. S. Couch, D. M. Greenblatt, E. C. Meng, and T. E. Ferrin. "UCSF Chimera - A visualization system for exploratory research and analysis". *Journal of Computational Chemistry* **25** (13) (2004), pp. 1605–1612. DOI: 10.1002/jcc.20084.

[313] S. A. Fromm, T. A. Bharat, A. J. Jakobi, W. J. Hagen, and C. Sachse. "Seeing tobacco mosaic virus through direct electron detectors". *Journal of Structural Biology* **189** (2) (2015), pp. 87–97. DOI: 10.1016/j.jsb.2014.12.002.

[314] K. Kato, N. Miyazaki, T. Hamaguchi, Y. Nakajima, F. Akita, K. Yonekura, and J. R. Shen. "High-resolution cryo-EM structure of photosystem II reveals damage from high-dose electron beams". *Communications Biology* **4** (1) (2021). DOI: 10.1038/s42003-021-01919-3.

[315] R. Henderson. "C ryo-protection of protein crystals against radiation dam age in electron and X-ray diffraction". *Proceedings of the Royal Society London* **241** (1990), pp. 6–8. URL: https://royalsocietypublishing.org/.

[316] S. M. Seltzer, J. M. Fernández-Varea, P. Andreo, P. M. J. Bergstrom, D. T. Burns, I. Krajcar Bronić, C. K. Ross, and F. Salvat. *ICRU Key Data for Ionizing-Radiation Dosimetry: an update to ESTAR, PSTAR, and ASTAR Databases*. Oxford, 2016.

[317] W. J. Rice, A. Cheng, A. J. Noble, E. T. Eng, L. Y. Kim, B. Carragher, and C. S. Potter. "Routine determination of ice thickness for cryo-EM grids". *Journal of Structural Biology* **204** (1) (2018), pp. 38–44. DOI: 10.1016/j.jsb.2018.06.007.

[318] M. Wu and G. C. Lander. "How low can we go? Structure determination of small biological complexes using single-particle cryo-EM". *Current Opinion in Structural Biology* **64** (2020), pp. 9–16. DOI: 10.1016/j.sbi.2020.05.007.

[319] B. A. Barad, N. Echols, R. Y. R. Wang, Y. Cheng, F. Dimaio, P. D. Adams, and J. S. Fraser. "EMRinger: Side chain-directed model and map validation for 3D cryo-electron microscopy". *Nature Methods* **12** (10) (2015), pp. 943–946. DOI: 10.1038/nmeth.3541.

[320] E. Fioravanti, F. M. Vellieux, P. Amara, D. Madern, and M. Weik. "Specific radiation damage to acidic residues and its relation to their chemical and structural environment". *Journal of Synchrotron Radiation*. Vol. 14. 1. 2007, pp. 84–91. DOI: 10.1107/S0909049506038623.

[321] A. Bartesaghi, D. Matthies, S. Banerjee, A. Merk, and S. Subramaniam. "Structure of β-galactosidase at 3.2-Å resolution obtained by cryo-electron microscopy". *Proceedings of the National Academy of Sciences of the United States of America* **111** (32) (2014), pp. 11709–11714. DOI: 10.1073/pnas.1402809111.

[322] J. Hattne, D. Shi, C. Glynn, C. T. Zee, M. Gallagher-Jones, M. W. Martynowycz, J. A. Rodriguez, and T. Gonen. "Analysis of Global and Site-Specific Radiation Damage in Cryo-EM". *Structure* **26** (5) (2018), pp. 759–766. DOI: 10.1016/j.str.2018.03.021.

[323] R. J. Southworth-Davies, M. A. Medina, I. Carmichael, and E. F. Garman. "Observation of Decreased Radiation Damage at Higher Dose Rates in Room Temperature Protein Crystallography". *Structure* **15** (12) (2007), pp. 1531–1541. DOI: 10.1016/j.str.2007.10.013.

[324] M. Warkentin, J. B. Hopkins, J. B. Haber, G. Blaha, and R. E. Thorne. "Temperature-dependent radiation sensitivity and order of 70S ribosome crystals". *Acta Crystallographica Section D: Biological Crystallography* **70** (11) (2014), pp. 2890–2896. DOI: 10.1107/S1399004714017672.

[325] J. Kmetko, N. S. Husseini, M. Naides, Y. Kalinin, and R. E. Thorne. "Quantifying X-ray radiation damage in protein crystals at cryogenic temperatures". *Acta Crystallographica Section D: Biological Crystallography* **62** (9) (2006), pp. 1030–1038. DOI: 10.1107/S0907444906023869.

[326] K. Naydenova and C. J. Russo. "Measuring the effects of particle orientation to improve the efficiency of electron cryomicroscopy". *Nature Communications* **8** (1) (2017). DOI: 10.1038/s41467-017-00782-3.

[327] M. W. Tuijtel, S. Cruz-León, J. P. Kreysing, S. Welsch, G. Hummer, M. Beck, and B. Turoňová. "Thinner is not always better: Optimizing cryo-lamellae for subtomogram averaging". *Science Advances* (10) (2024). DOI: 10.1126/sciadv.adk6285. URL: https://www.science.org.

[328] H. T. D. Nguyen, G. Perone, N. Klena, R. Vazzana, F. Kaluthantrige Don, M. Silva, S. Sorrentino, P. Swuec, F. Leroux, N. Kalebic, F. Coscia, and P. S. Erdmann. "Serialized on-grid lift-in sectioning for tomography (SOLIST) enables a biopsy at the nanoscale". *Nature Methods* **21** (9) (2024), pp. 1693–1701. DOI: 10.1038/s41592-024-02384-6.

[329] M. F. Hayles and D. A. de Winter. "An introduction to cryo-FIB-SEM cross-sectioning of frozen, hydrated Life Science samples". *Journal of Microscopy* **281** (2) (2021), pp. 138–156. DOI: 10.1111/jmi.12951.

[330] M. T. Schreiber, A. Maigné, M. Beleggia, S. Shibata, and M. Wolf. "Temporal dynamics of charge buildup in cryo-electron microscopy". *Journal of Structural Biology: X* **7** (2023). DOI: 10.1016/j.yjsbx.2022.100081.

[331] Thermo Fisher Scientific. *Application Note: Fringe-Free Imaging (FFI) and Aberration-Free Image Shift (AFIS)*. 2021.

Appendices

A

Appendix

Please note that upon submission, the thesis was limited to a maximum file size that prevented the appendices from being included within the thesis document. As a result, the links between the thesis and appendices will not function as intended.

A.1 Appendix for Chapter 1: Introduction

A.1.1 STEM-TEM Correlation Attempts

This appendix details the preliminary investigation into establishing a correlative cryo-STEM and cryo-ET workflow for localising specific proteins within cellular lamellae (presented in Chapters1 and 3). The strategy was based on using AuNPs as high-contrast fiducial markers that would be visible in both imaging modalities. While this approach was theoretically sound, it encountered significant technical challenges in both sample preparation and particle targeting, which are documented here. The findings from these attempts informed the decision to pivot to the alternative strategies detailed in the main body of this thesis. Much of this work was completed in collaboration with Dr. Siva Ramadurai (SR). Specifically, SR trained the author in cell culture techniques and protein-tag conjugation, and performed tag internalisation protocols and confocal fluorescence microscopy before vitrification.

A.1.1.1 Methods

Preparation of Gold Nanoparticles BSA-coupled 6 nm gold nanoparticles in 15 mM NaN_3 (Aurion) were washed and resuspended in PBS (Gibco) using a 5 kDa concentrator (Sartorius). The concentration of Au-BSA was estimated using a spectrophotometer at 520 nm using an extinction coefficient of 1×10^7 M^{-1} cm^{-1} to be 4×10^{12} nanoparticles ml^{-1}.

Cellular Culture HeLa cells were grown in DMEM with non-essential amino acids supplemented with 10% (v/v) foetal bovine serum (Gibco) and 1% (v/v) penicillin/streptomycin (Gibco). Cells were maintained at 37°C and 5% CO2 at >80% humidity. Cells were then trypsinised and counted. $\sim 1 \times 10^5$ cells ml^{-1} of medium were seeded onto gold UltrAuFoil 200 Au mesh R2/2 grids (Quantifoil Micro Tools). 30 minutes prior to freezing, the old media was removed and the cells were washed twice with PBS (Gibco). After 400 µl of fresh media was added, 100 µl of the 6 nm Au-BSA-AF568 beads was pipetted over the grids.

Sample Preparation 10 minutes before freezing, the media was removed and the cells were washed with fresh media with 10% glycerol (v/v) (Sigma Aldrich) as cryoprotectant. Grids were plunge-frozen in nitrogen-cooled liquid ethane using a Vitrobot mkIV (ThermoFisher Scientific) with offset to favour back-blotting using a blot time of 8 seconds and blot force of 10 at 70% humidity. Grids were then clipped into Autogrids (ThermoFisher Scientific) and stored in liquid nitrogen.

pFIB Milling The clipped grids were loaded into an autoloader cassette for the Arctis pFIB-SEM (ThermoFisher Scientific). The SEM was used to screen the grids and identify suitable sites for lamella preparation using the MAPS software (40 identified in total). Grids were then coated with a layer of sputtered platinum metal from a platinum target with the Argon pFIB beam at 12.0 kV and 70 nA (microsputtering). A layer of organo-platinum was then added using the gas injection system (GIS, 60 sec) and one more layer of microsputter was added to this, as previously described. The AutoTEM cryo software was then used to fabricate lamellae using Argon. Three rough milling steps were used to remove material above and below the intended lamella position at 15 nA, 4.0 nA, and 1.0 nA. These lamellae were then polished using 100 pA and 30 pA down to the target thickness (∼200 nm), giving 33 usable lamellae.

TEM Grids were then loaded into a Titan Krios 4 (ThermoFisher Scientific) equipped with a Falcon 4i camera and a Selectris energy filter at 10 eV. Tomo 5 (Thermofisher scientific) was used to collect 33 dose-symmetric tilt series at a nominal magnification of 81,000 x, corresponding to a pixel size 1.57 Å px^{-1} and a field of view of ∼640 nm at 300 kV and -5 µm defocus. Images were recorded in electron counting mode from 60°C to -60°C in 3°C increments (corrected for the milling angle), with a total fluence of 120 $e^{-}Å^{-2}$ split over 41 images. Images were taken using the data acquisition settings of a gold cross-grating (Agar Scientific, 2160 lines mm^{-1}). All TEM was completed before switching to STEM mode.

STEM The Titan Krios was switched first to microprobe and then to nanoprobe STEM mode and aligned using the gold cross-grating. The alignment for nanoprobe was completed at 4.00 mRad convergence angle, using a 20 µm aperture and the 3CL lens system to fine-tune the convergence angle. This convergence angle gave

an approximate depth of focus of 246 nm. The fluorescent screen current was 3 pA. The nominal magnification for data collection was 135 k×, resulting in a 735 nm field of view, similar to the TEM data acquisition. The estimated probe size was 3.13 Å, and the pixel size was 3.5 Å px^{-1}. During the data acquisition, the dwell time was refined to 10 µs in a 2048 × 2048 scan size (frame time = 41.9 sec) resulting in a total fluence of 15.3 $e^{-}Å^{-2}$. The bright field detector was used to manually focus on the lamella. The nominal camera length was 275 mm.

Reconstruction and Data Analysis The TEM tilt series were imported to Warp (v1.0.9) [22] for gain and motion correction, fractionation of the .eer files into groups of 10 (0.29 $e^{-}Å^{-2}$ $group^{-1}$), fitting the CTF, and creating stacks for alignment. The stacks were aligned and reconstructed using AreTomo 1.2.5 [51] and tomograms were viewed and flipped using IMOD 4.11 [50].

A.1.1.2 Results

Initial TEM and STEM imaging of the prepared lamellae revealed numerous electron-dense clusters, which were initially hypothesised to be the target AuNPs (Figure A.1A, B). However, analysis of the reconstructed tomograms provided confirmation: the clusters were localised exclusively to the top and bottom surfaces of the lamellae (Figure A.1C, E), with none observed within the biological material itself (Figure A.1D).

This surface localisation strongly indicates that the clusters were not internalised AuNPs. Instead, they are likely artefacts from the FIB preparation process, such as redeposited platinum from the GIS coating or sputtered gold from the grid bars, or gold grid (Figure A.1F, G). This redeposition is a known challenge in cryo-FIB milling, and these results highlight the difficulty in distinguishing such artefacts from genuine AuNP tags.

A subsequent attempt to use smaller 3 nm anti-ACE2-GFP nanobody-conjugated AuNPs also faced significant hurdles. Despite screening 36 lamellae, only one instance of internalised nanoparticles was observed (Figure A.2). This extremely low uptake rate, combined with the persistent challenge of GIS redeposition, made reliable target identification impractical. Given these compounding difficulties in the sample preparation and particle internalisation stages, the decision was made to deprioritise this correlative STEM-TEM approach in favour of the more direct damage-mitigation strategies presented in Chapters 4 and 5 in this thesis.

[H]

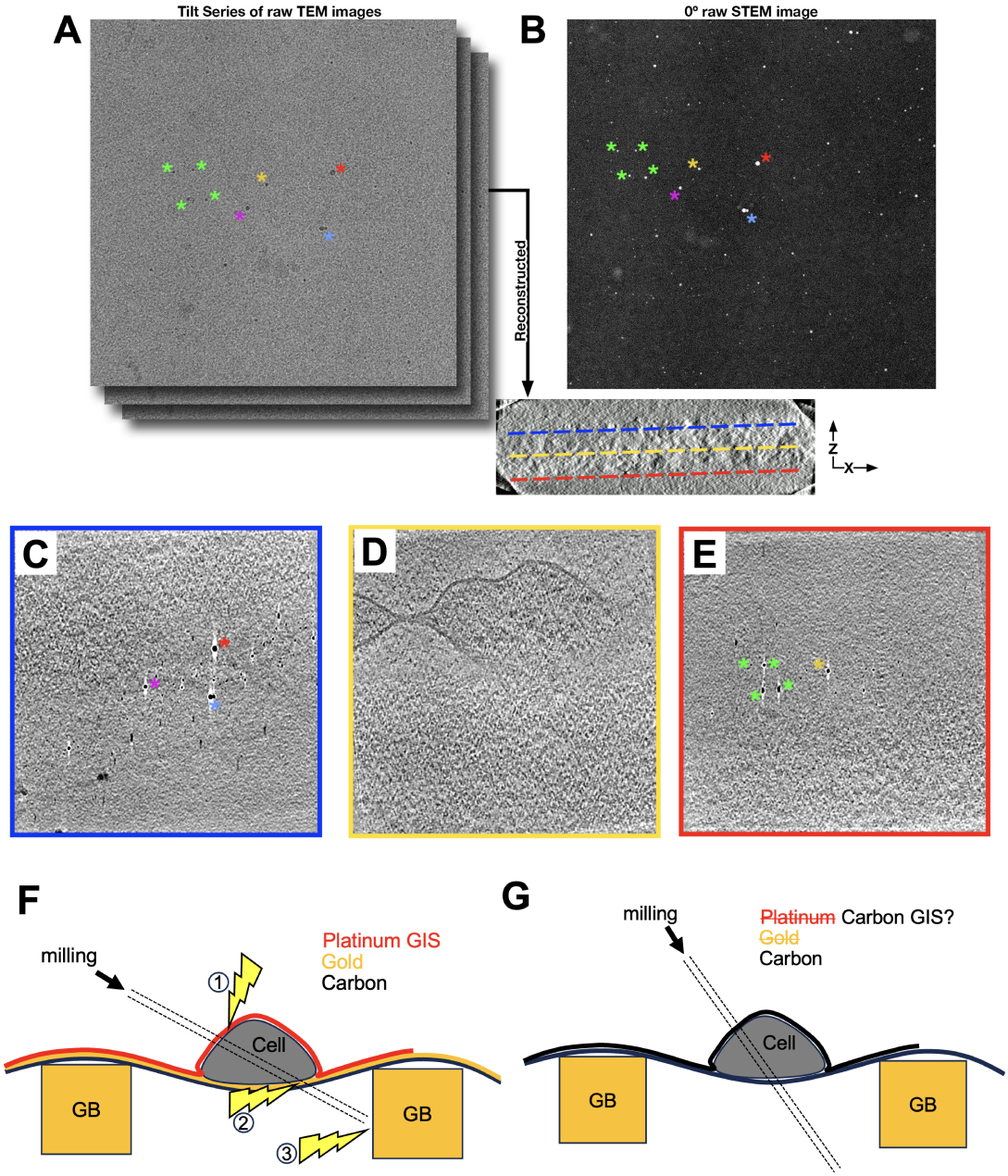


Figure A.1: **Correlation of cryo-ET and cryo-STEM A** Raw TEM and **B** STEM image at 0° tilt. Asterisks (*) mark electron-dense nanoparticles/putative redeposited GIS clusters in all images. As indicated by the xz slice shown (with blue, yellow, and red dashed lines), the clusters are found only on the top and bottom surfaces **C** and **E**, while **D** contains the biologically relevant membranes and proteins but no nanoparticles. **F** shows all of the potential sources of redeposited GIS during the sample preparation stages in the FIB (indicated by the yellow lightning symbols), and **G** shows how they might be mitigated. Return to Introduction.

[H]

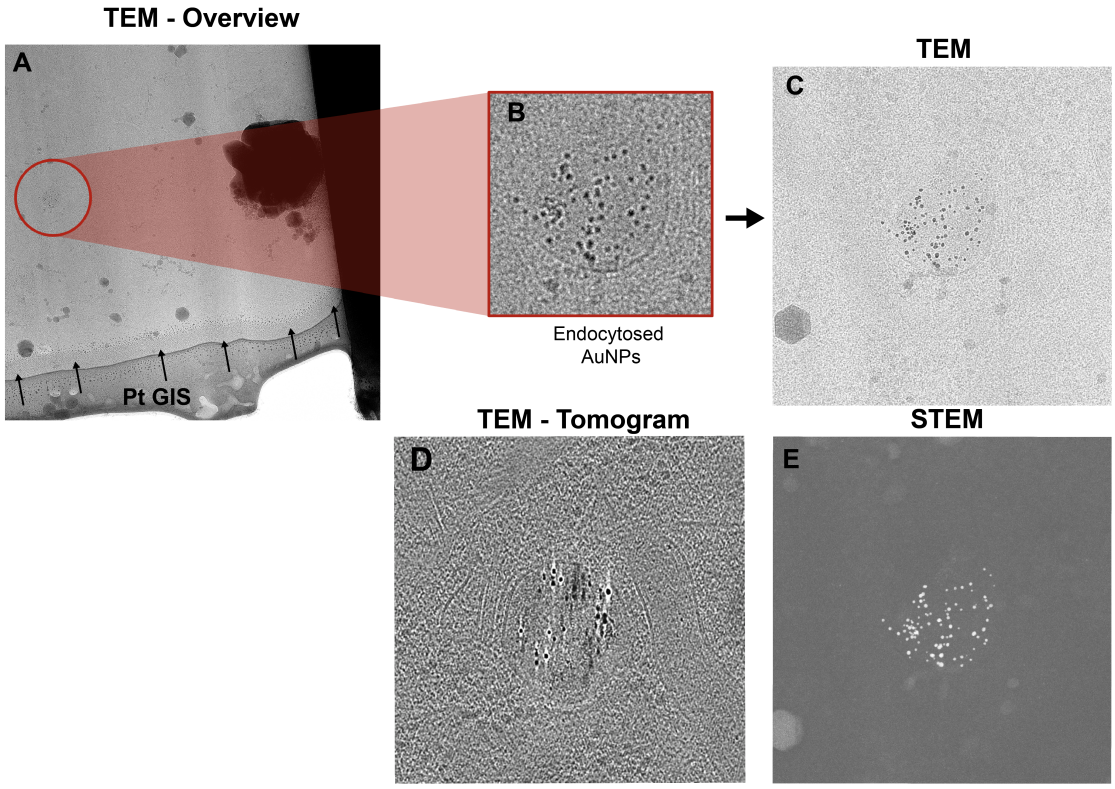


Figure A.2: **Correlation of cryo-ET and cryo-STEM A** TEM overview image of the lamella, showing a region highlighted and magnified in **B**. **C** shows the TEM image at 0° tilt, with the corresponding slice from the bin-8 reconstructed tomogram in **D**. The STEM-HAADF image was acquired after all tomography steps and is located on the same feature, with an expected absence of membranes and other cellular features due to the high-angle of collection. Return to Introduction.

A.2 Appendix for Chapter 2: Background

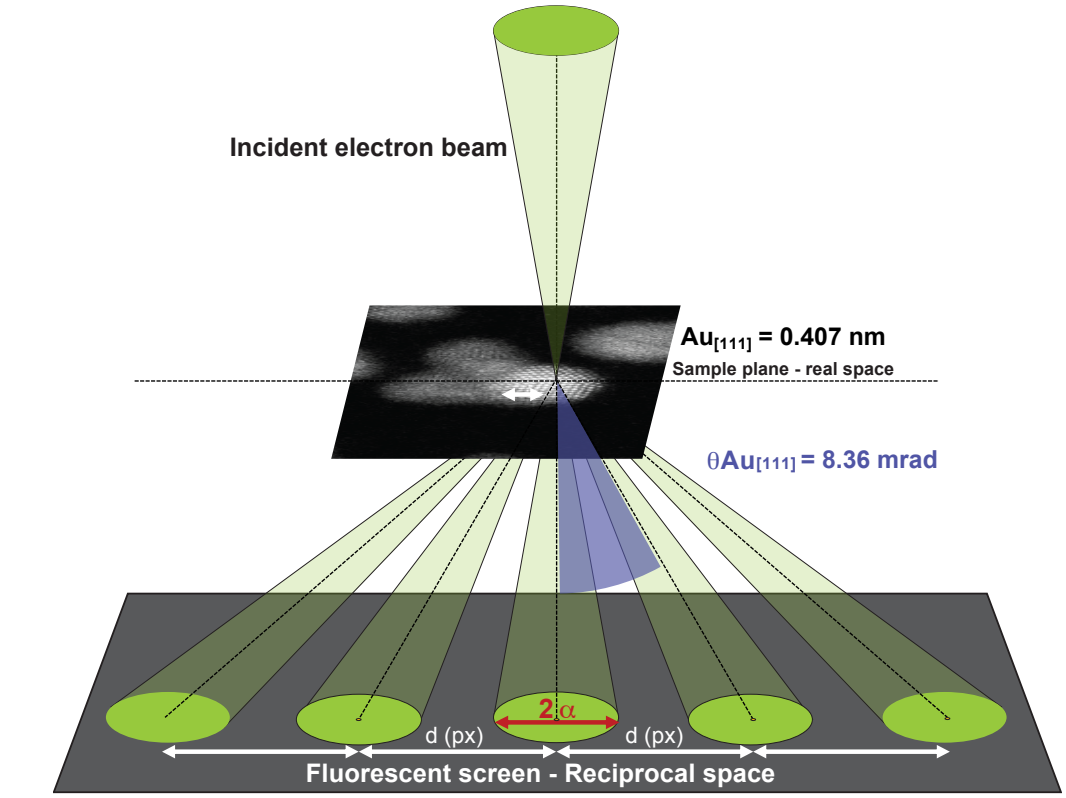
A.2.1 Calibration of Titan Krios G4 Collection angles

The precise inner and outer collection angles of the STEM detectors are critical parameters for the quantitative scattering models developed in Chapter 3. On the Titan Krios G4, the use of the Aberration-Free Image System (AFIS) and Fringe-Free-Imaging (FFI) alters the standard specimen height, shifting it down in the column by around 70 µm (toward the detector) [331]. This change invalidates the default angular calibrations, necessitating a calibration for all STEM images acquired using the Titan Krios.

The calibration was performed using a gold cross-grating specimen. A region oriented

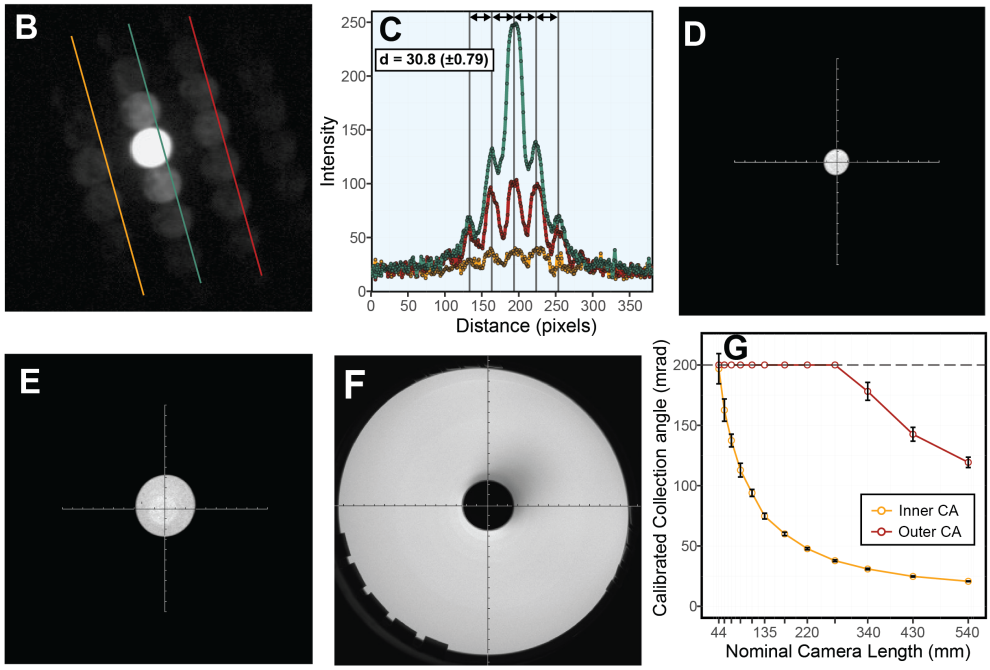
to the [111] zone axis was located. A Convergent Beam Electron Diffraction (CBED) pattern was recorded. The known lattice spacing of gold in this orientation produces a diffraction pattern with a predictable spacing in the diffraction plane, as shown in Figure A.3a . The distance between the central beam and the n-order diffracted spots was used to establish a calibrated scale for the diffraction pattern in units of mrad/pixel (Figures A.3b B and C).

Using this scale, the convergence semi-angle (α) was determined by measuring the radius of the bright central disk. The inner collection angles of the Annular Dark-Field (ADF) detectors were then measured from the inner edge of their corresponding shadows on an expanded beam (removing the C2 aperture). To measure the outer collection angles, the microscope was switched from diffraction mode to image the detector plane in STEM mode itself. The outer edges of the detectors were identified on this image, and their angles were calculated as a ratio, using the previously established calibration for the inner collection angle. Measurements were all conducted using the same gain and offset of the fluorescent screen. Measurements were taken in the x and y directions (Figures A.3b D, E, and F), yielding error bars on the final measurements (Figures A.3b G). The measurements were seen to be approximately 20% greater than the nominal software values.



[H]

(a)



(b)

Figure A.3: **CBED calibration procedure for ThermoFisher Scientific Titan Krios G4**. **A** region of [111] gold was located in STEM imaging mode. *Caption continued on the next page*

[t]

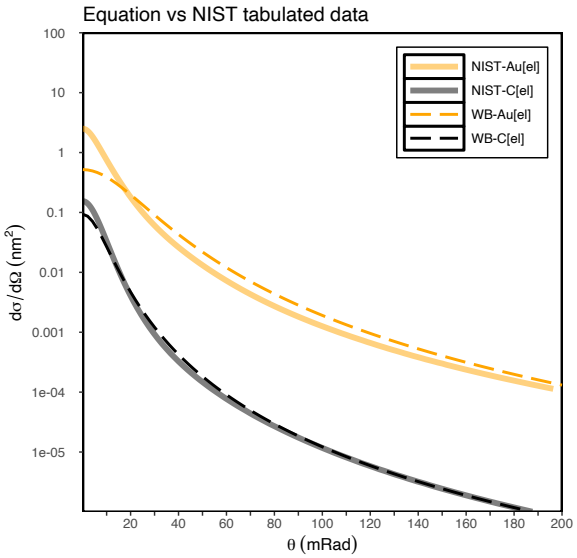
Figure A.3: *Continued caption:* The beam was then blanked and the fluorescent screen inserted. A [111] oriented region of a polycrystalline gold standard was located in STEM imaging mode. The [111] orientation was confirmed by identifying the crystal axis that produced the smallest diffraction spot spacing. **B** the CBED pattern produced on the fluorescent screen when imaging the [111] oriented region of the gold cross grating in one direction. Coloured lines indicate the line profiles taken and plotted in **C**, with a demonstrated spacing in pixels to achieve a calibration of 0.45 ± 0.01 mrad/pixel. **D** and **E** show images of the inner collection angle shadow of the HAADF detector, measured in x and y. **F**, the image of the detector plane in STEM out of diffraction mode, displaying the inner and outer edges of the detector. **G** graphical representation of the inner and outer collection angles as a function of the nominal camera length given in the software. Link back to Chapter 2.

(A) A [111] oriented region of a polycrystalline gold standard was located in STEM imaging mode. The [111] orientation was confirmed by identifying the crystal axis that produced the smallest diffraction spot spacing. (B) The Convergent Beam Electron Diffraction (CBED) pattern recorded from the [111] region. (C) Line profiles taken from the CBED pattern (indicated by coloured lines in B) were used to calibrate the effective pixel size, yielding a value of 0.45 ± 0.01 mrad/pixel. (D, E) Images of the shadow cast by the inner collection ring of the HAADF detector, measured in orthogonal directions. (F) An image of the detector plane recorded outside of diffraction mode, clearly showing the inner and outer edges of the detector rings. (G) A plot of the calibrated inner and outer HAADF collection angles as a function of the nominal camera length selected in the microscope software.

Table A.1: Calibrations for the Titan Krios G4 STEM detector collection angles. Columns are for the nominal software camera lengths, the applied diffraction lens % for the calibrated values, the calibration conversion value between the fluorescent screen and the diffraction plane (in mrad/px), the measured diameter of the inner collection angle, the calculated diameter of the outer collection angle (assuming 5.76 × inner CA), and the nominal inner and outer collection angles. Link back to Chapter 2.

Cam. Len. (mm)	Diff. Lens (%)	Diameter (px)	mrad/px	Calibrated Values		Nominal Software Values	
				Inner θ (mrad)	Outer θ (mrad)	Inner θ (mrad)	Outer θ (mrad)
44	NA	8.83 (±0.39)	1.98	196.9 (±12.5)	345.54 (±15.1)	131	200
55	NA	10.74 (±0.40)	1.63	162.6 (±9.2)	345.5 (±15.1)	105	200
69	44.812	12.60 (±0.28)	1.39	137.4 (±5.3)	345.5 (±15.1)	85	200
87	43.726	15.34 (±0.51)	1.14	112.9 (±5.7)	345.5 (±15.1)	68	200
110	42.496	18.59 (±0.20)	0.94	94.0 (±2.9)	345.5 (±15.1)	54	200
135	19.695	23.38 (±0.24)	0.75	74.7 (±2.4)	345.5 (±15.1)	43	200
175	21.640	29.38 (±0.13)	0.60	60.0 (±1.4)	345.5 (±15.1)	34	200
220	23.352	36.56 (±0.03)	0.48	47.7 (±0.9)	274.9 (±10.8)	27	163
275	24.214	45.78 (±0.02)	0.38	37.78 (±0.8)	217.6 (±8.8)	21	130
340	34.644	56.50 (±0.10)	0.31	30.9 (±0.7)	178.1 (±7.4)	17	104
430	35.407	69.09 (±0.07)	0.25	24.8 (±0.5)	142.6 (±5.8)	14	84
540	34.589	87.51 (±0.57)	0.20	20.7 (±0.3)	119.3 (±4.3)	11	66

A.3 Appendix for Chapter 3: Theoretical Considerations for STEM Nanoparticle Localisation



[H]

Figure A.4: **Elastic scattering differential cross section functions**. Plotted from equations 3.5 - 3.10 against The National Institute of Standards and Technology (NIST) tabulated data, showing a reasonable agreement. Tabulated data not used as different atomic Z values are needed for water/buffer/cell compared to purely atomic Z in tabulated data. Link back to Chapter 3.

[H]

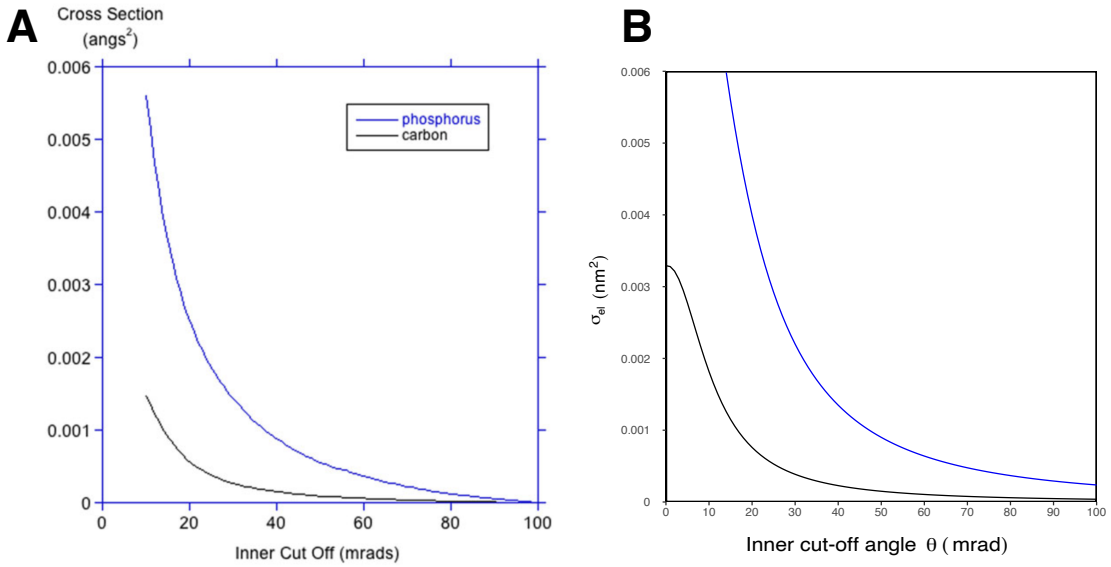


Figure A.5: Graph showing comparable results from Figure 1 in [103] (**A**), of the integrated elastic cross section of phosphorous and carbon as a function of the inner collection angle to equations 3.5-**??** (**B**) presented in this work. Link back to Chapter 3 discussion.

A.3.0.1 Mean Thickness

The concept of mean projected thickness for a spherical particle is derived by considering a cylinder of equivalent volume and radius. Given that the volume of a sphere is $\frac{4}{3}\pi r^3$ and the volume of a cylinder is $\pi r^2 h$, equating these volumes establishes that the uniform height (h) of the cylinder must be $\frac{4}{3}r = \frac{2}{3}d$. This height is analogous to the mean projected thickness of the sphere over its circular cross-section.

[H]

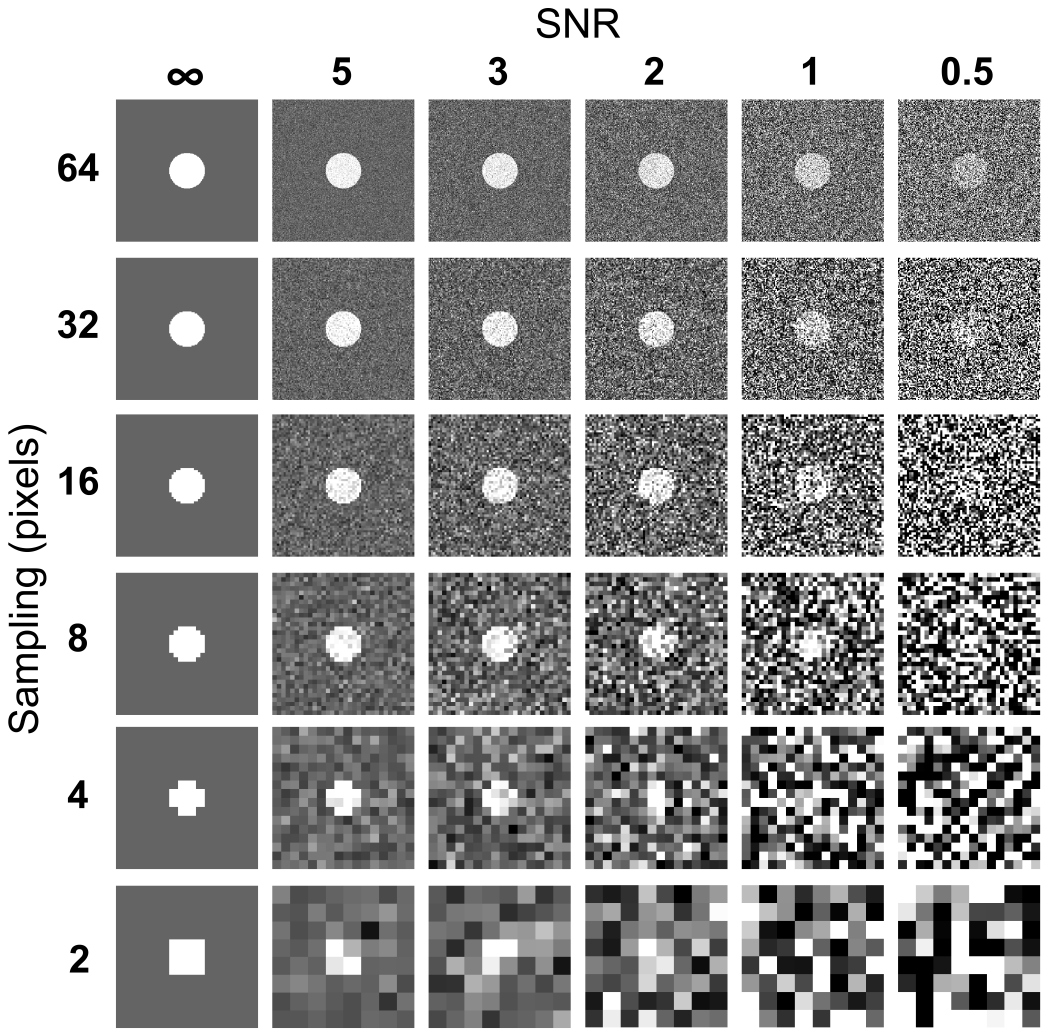


Figure A.6: SNR and Sampling. Monte Carlo simulations completed for a fixed ratio of total image dimension to nanoparticle diameter, as the sampling decreased down the figure. SNR decreases from left to right. For instance, when the diameter of the nanoparticle measures 64 pixels, it remains discernible even at a SNR of 0.5. Conversely, when the diameter is reduced to 4 pixels with an SNR of 2, the presence of the nanoparticle becomes considerably more ambiguous. Link back to Chapter 3 discussion.

[H]

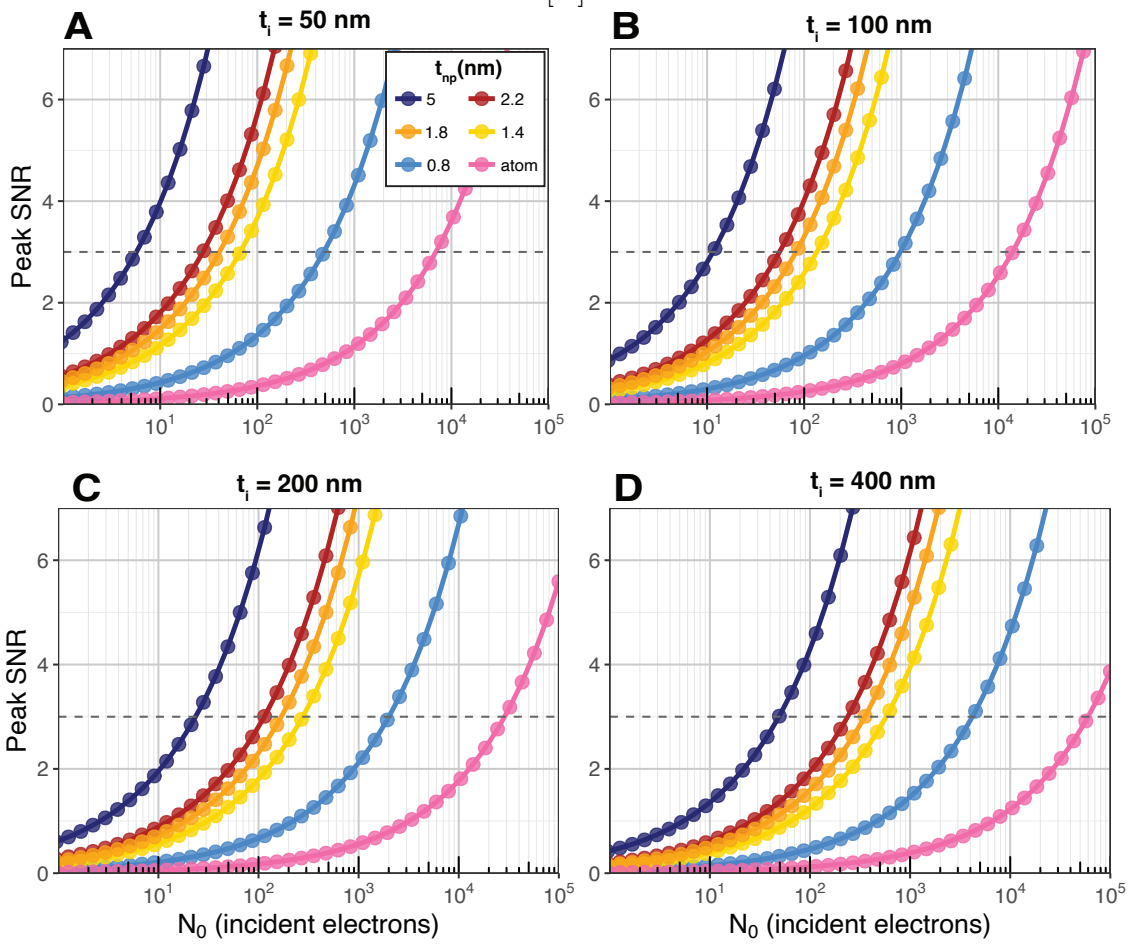


Figure A.7: **Plots of the peak SNR against number of incident electrons for available gold nanoparticles.** Similar to Figure 3.11A in the main text, the plots are **A** at 50, **B** at 100, **C** at 200 nm, and **D** at 400 nm thickness of vitreous ice. The dashed horizontal line indicates the rose criterion, at an SNR of 3. Link Back to Figure 3.8

[H]

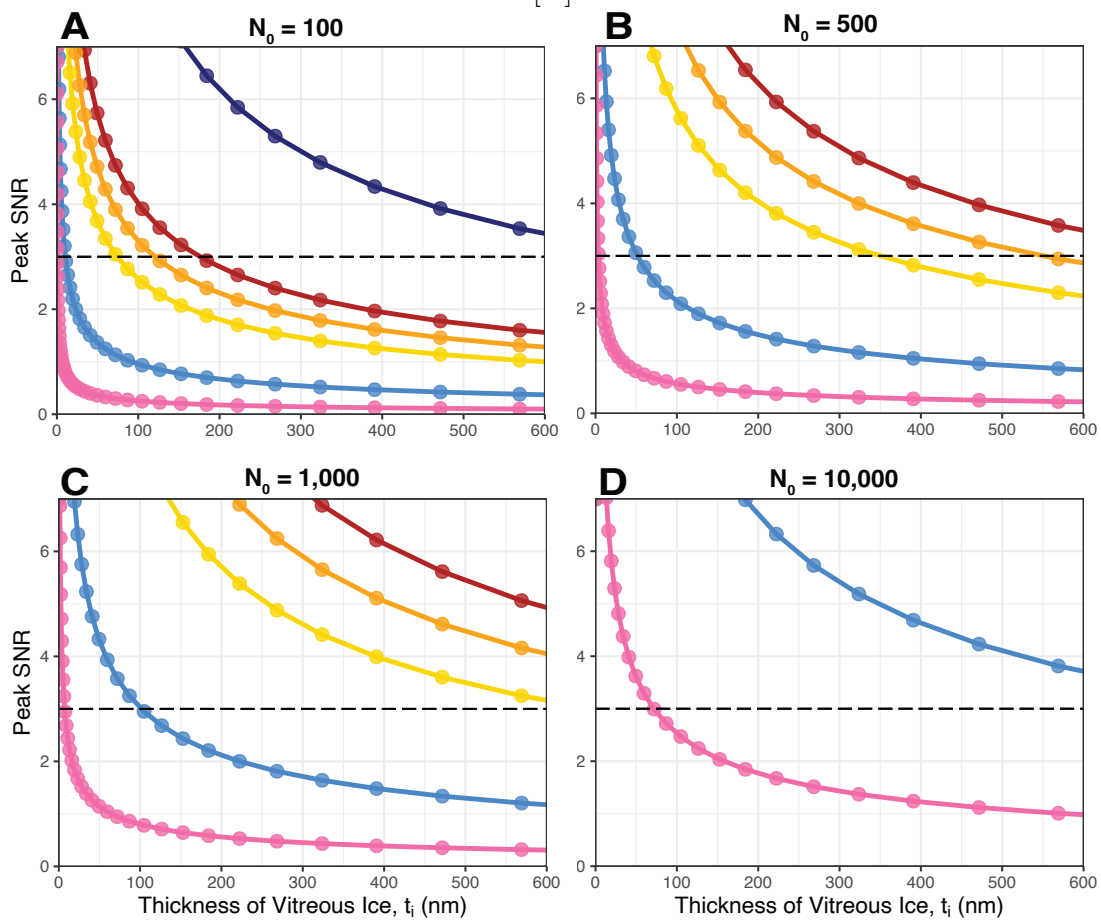


Figure A.8: **Plots of the peak SNR against thickness of vitreous ice for available gold nanoparticles.** Similar to Figure 3.11B in the main text, the plots are **A** at 100, **B** at 500, **C** at 1000, and **D** at 10,000 incident electrons. The dashed horizontal line indicates the rose criterion, at an SNR of 3. Link Back to Figure 3.8

A.4 Appendix for Chapter 4: STEM Damage

Calculation of the Probe Response

For a series of images acquired at different pixel dwell times (ranging from 2 µs to 200 µs), multiple data points were extracted from the flyback region. The measurement process for a single data point involved identifying a distinct feature within the distorted, mirrored region (equated to a time, t) and its corresponding, undistorted position in the stable part of the scan (equated to a distance, d). t was calculated from the horizontal width of the distorted region and the known pixel dwell time for that acquisition.

The collected time-distance (t, d) data pairs were fitted to an exponential function model:

$$d(t) = A \times (1 - e^{-t/\tau}) \tag{A.1}$$

A non-linear least squares fit to the data yielded the characteristic parameters of the scanning system. The asymptote, A, was found to be 175.6 nm, consistent with the total width of the scan. The time constant, τ, for the flyback was determined to be 96.2 µs. This represents the time taken for the probe to move to $1 - 1/e = 63\%$ of the distance during a flyback period.

The application of this model to the interleaved scanning routine reveals two distinct effects on beam positioning. First, the start of each new scan line is influenced by the probe settling from the large (∼174 nm) flyback movement, a process governed by the 96.2 µs time constant. This can result in positional inaccuracies over the first several pixels of the line. However, once this initial settling is complete, the model can be used to determine the transit time for subsequent, small inter-pixel skips.

For a typical 1.02 nm gap between interleaved pixels, the calculated skip time is approximately 0.55 µs. This confirms that after the initial flyback recovery, the time spent on off-target irradiation during steady-state inter-pixel movement is negligible compared to the pixel dwell time.

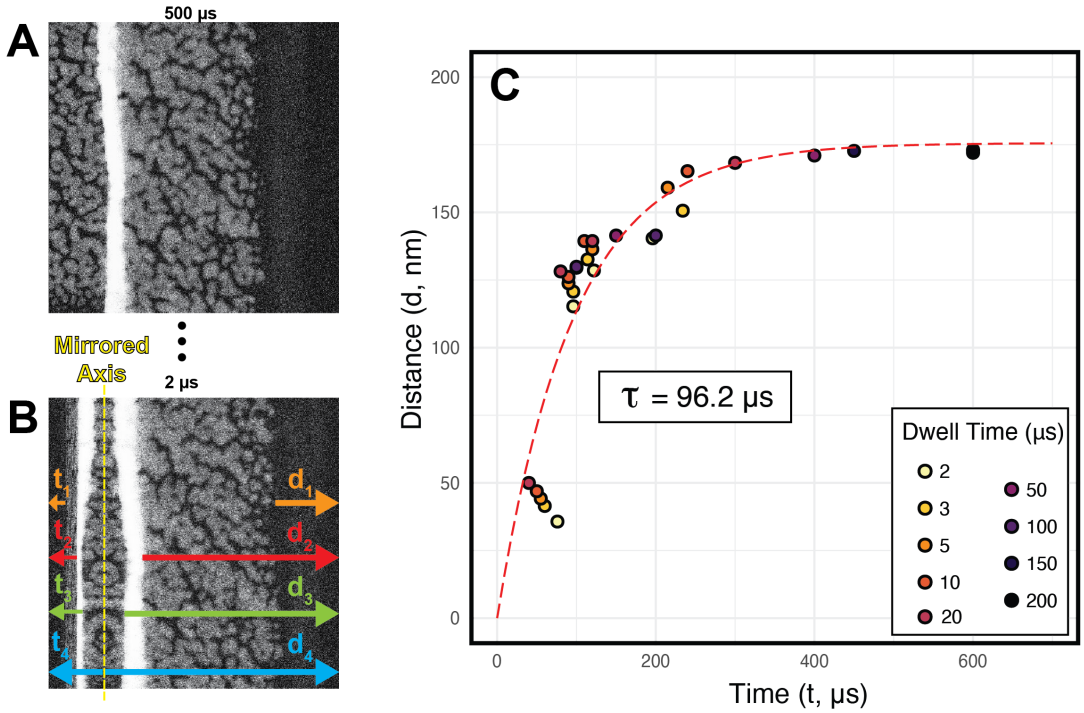
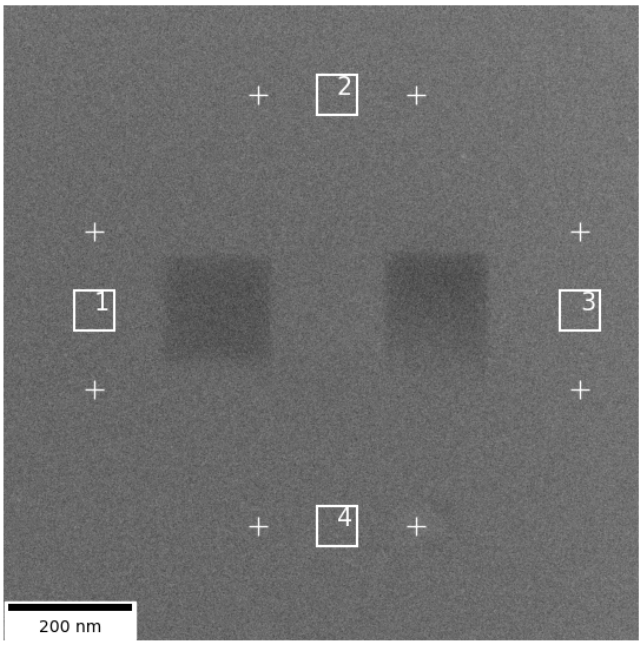


Figure A.9: **Analysis of the probe response.** Figure X: Characterisation of the probe flyback response. **A** A reference STEM image of the sample acquired with a long pixel dwell time (500 µs), showing the undistorted lattice structure. **B** The same region imaged with a short dwell time (2 µs), revealing a significant flyback artefact on the left. This distortion creates a 'mirrored axis' (yellow vertical dashed line) that enables direct measurement of the probe's positional error (d) over time (t). The coloured arrows display how corresponding features on either side of this axis are used to extract multiple (t, d) data pairs from a single image. A full series of images at intermediate dwell times (3, 5, 10, 20, 50, 100, 150, and 200 µs) were acquired and measured as described. **C** A plot of all (t, d) data points collected from the entire series. The data is fitted with a first-order exponential response model (equation A.1, red dashed line), yielding a system time constant of 96.2 µs. Link back to main text.

Applying this model to the interleaved scanning routine, the calculated time for the probe to travel the 1.02 nm gap between pixels is approximately 0.55 µs. This exceptionally short transit time confirms that off-target irradiation during inter-pixel movement along an interleaved scanned line is negligible compared to a typical pixel dwell time.



[H]

Figure A.10: **Analysis of the thickness variation on the overview acquisitions.** A preliminary evaluation of the thickness variation was carried out over the field of view of overview images acquired after the experiments. A variation in thickness was estimated by comparing the integrated intensity inside each of the white squares 1, 2, 3, and 4. A relative standard deviation, with respect to the mean, of 4.9% was estimated in this case. Link back to main text.

[H]

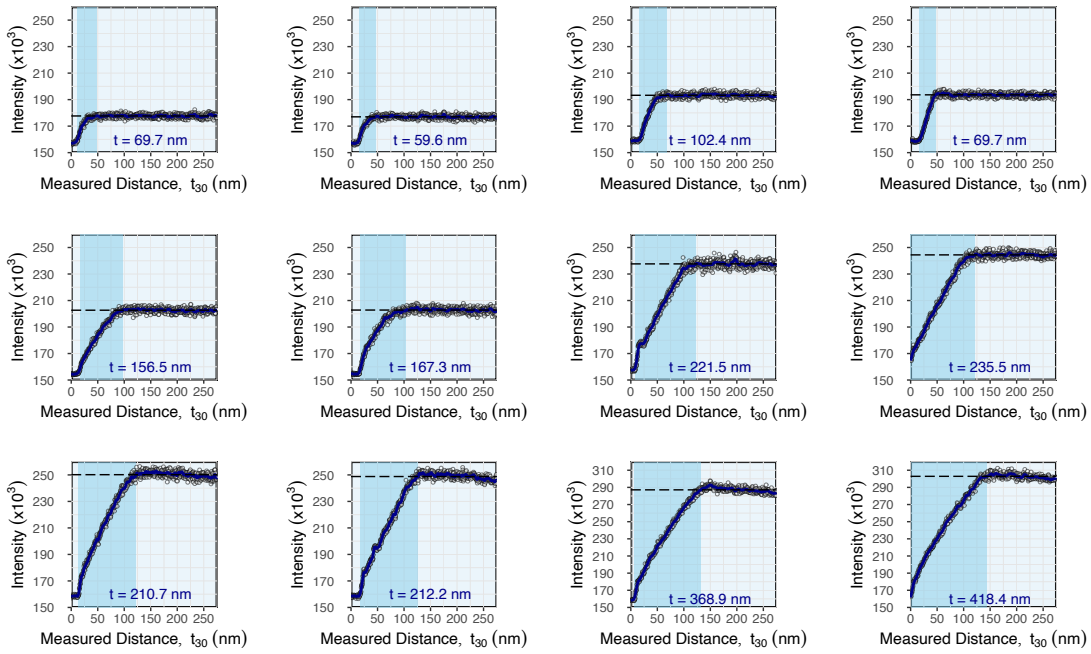


Figure A.11: **Projected thickness measurements for all data to construct calibration curve.** Measured distances are the projected face of the void of vitreous ice. Calculated thicknesses, displayed in blue range from 60 to 420 nm, encompassing the entire data range. Link back to main text.

Calculation of the Time Spent Irradiating Outside the Experimentally Scanned Trench Areas

The distance between each sequentially scanned trench within one column is dependent on the magnification and pattern used in Figures 4.12 and 4.13.

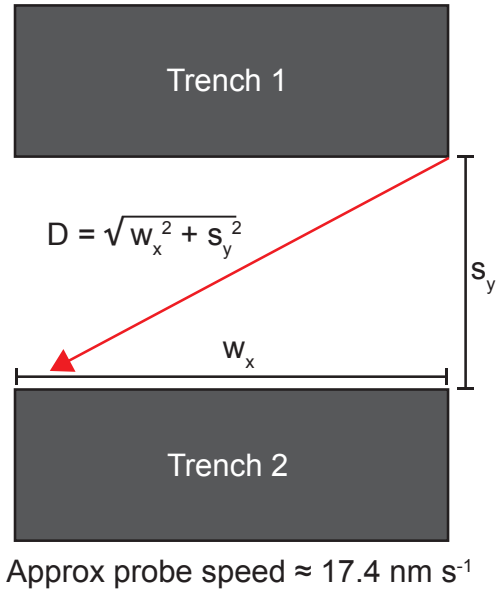
At a maximum, this is the lowest magnification and largest distance covered (between the end of one trench and the beginning of the next trench in Figure 4.12B at 200 k× nominal magnification, 2.74 Å pixel^{-1}).

At a minimum, this is the highest magnification and smallest distance covered (between the end of one trench and the beginning of the next trench in Figure 4.13B at 400 k× nominal magnification, 1.67 Å pixel^{-1}).

The minimum and maximum distances travelled between the end of one trench to the start of the next in a single column is then:

$$D = \sqrt{w_x^2 + s_y^2}$$

where w_x is the width in x-direction of the trench, s_y is the spacing between trenches in the y-direction.



[H]

Figure A.12: **Probe inter-Trench distance diagram**

The maximum is therefore $w_x = 140$ nm and $s_y = 140$ nm, giving $D = 198$ nm, and the minimum is $w_x = 43$ nm and $s_y = 16$ nm, giving $D = 45$ nm.

Although the maximum distance (198 nm) is larger than the scan width previously used to calculate the flyback times (174 nm), as an approximation, the same time constant as calculated in the Appendix section A.4 is used ($\tau = 96.2$ µs). For this case, 3τ remains ≈ 290 µs, and for the minimum distance, the irradiated time is ≈ 28 µs.

A.4.1 Further Examples of Trench Scanning Experiments

[H]

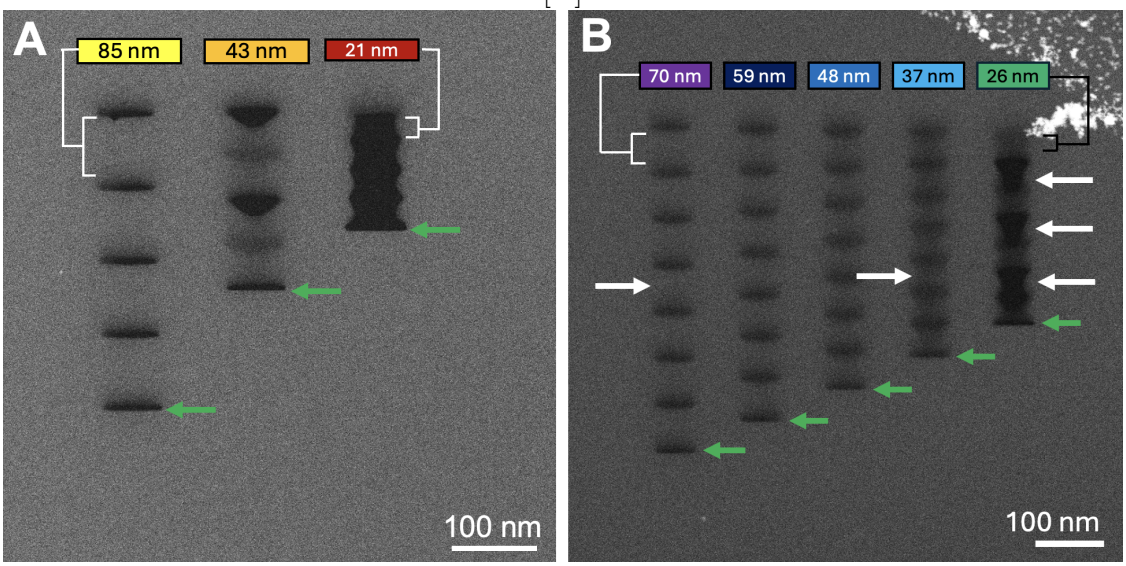


Figure A.13: **Further trench experiments**. Green arrows indicate the abrupt end to each column's final trench as discussed in the main text, while white arrows show regions of notable absence or presence of mass loss between scanned regions. **A** Overview image (taken at 300 k×) of the completed experiment at 400 k× (1.67 Å pixel^{-1}), and using the same pattern as used in Figures 4.12 and 4.2.3A. **B** Overview image (taken at 200 k×) of the completed experiment at 250 k× (2.74 Å pixel^{-1}), and using the same pattern as in Figures 4.13 and 4.2.3B. Vertical spacings are indicated with corresponding colour above each column. Particularly notable is the recurrence of the patterned and triangular shaped mass loss during scanning (in the 43 nm column in **A**, and of the 26 nm column in **B**). (Return to Trench Figure 4.12).

A.4.2 Further Explanations of the Raster and Interleaved Scanning

[H]

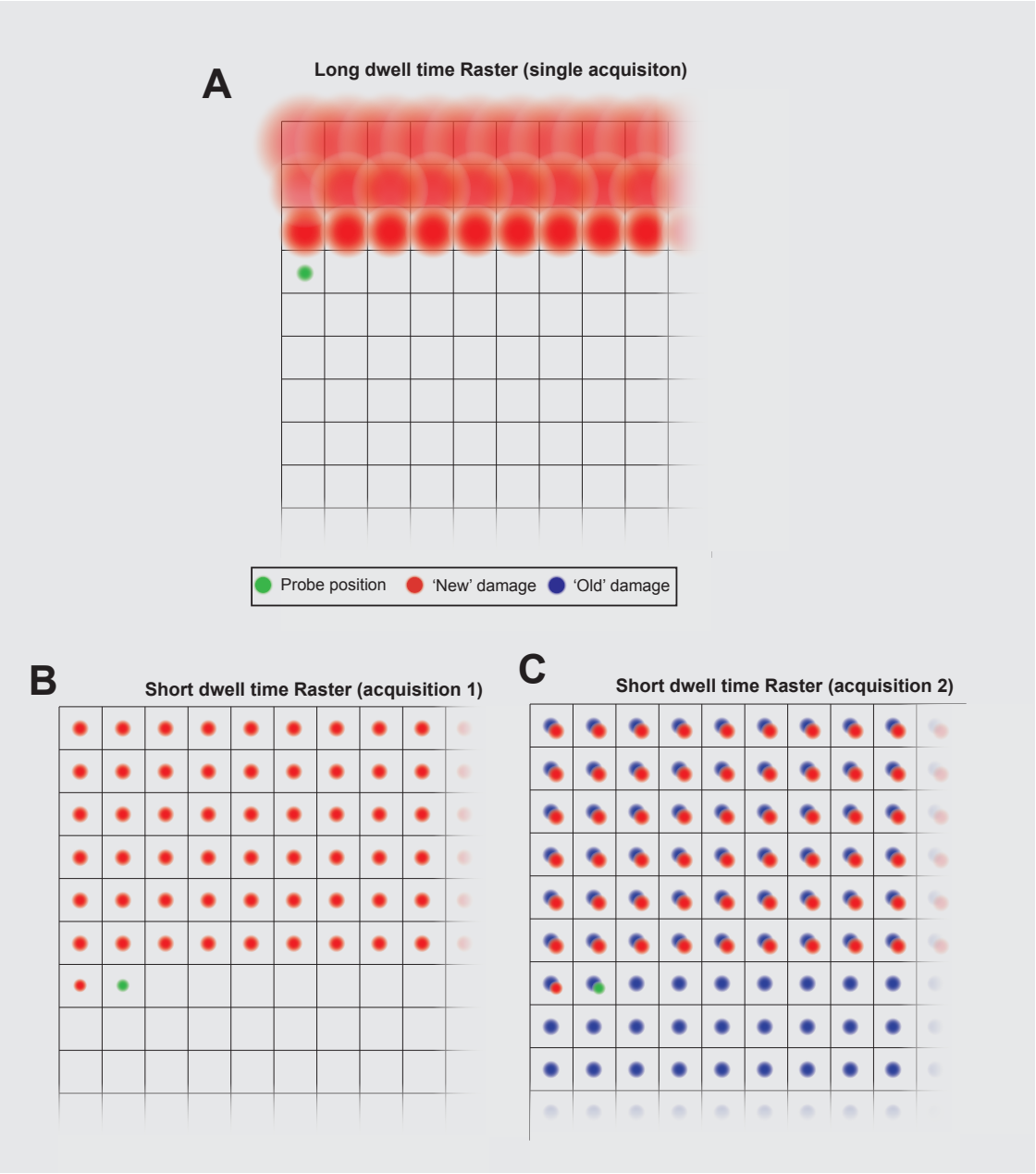


Figure A.14: **Raster Scanning Explanation Schematics**. **A** The Raster scanning with a long dwell time. The probe irradiates sequential pixels slowly enough that in the slow scan direction (y), there is considerable overlap between each outwardly expanding region of newly created damage. In other words, the probe is scanning on already freshly damaged area. **B** The Raster scanning with a short dwell time, in the first acquisition and **C**, in the second acquisition. The probe irradiates sequential pixels fast enough to 'outrun' the expanding circular regions of newly created damage in the slow-scan (y) direction. *(Figure caption continued on the following page).*

Figure A.14: *(continued figure caption)*: All pixels must be visited in this acquisition, meaning the probe is relatively slow to return back to the first position for the second acquisition. By this time, the damage has become 'old' damage, and so the probe re-scans the same areas again once the damage mediators have sufficiently dissipated.(Return to Chapter 4)

[H]

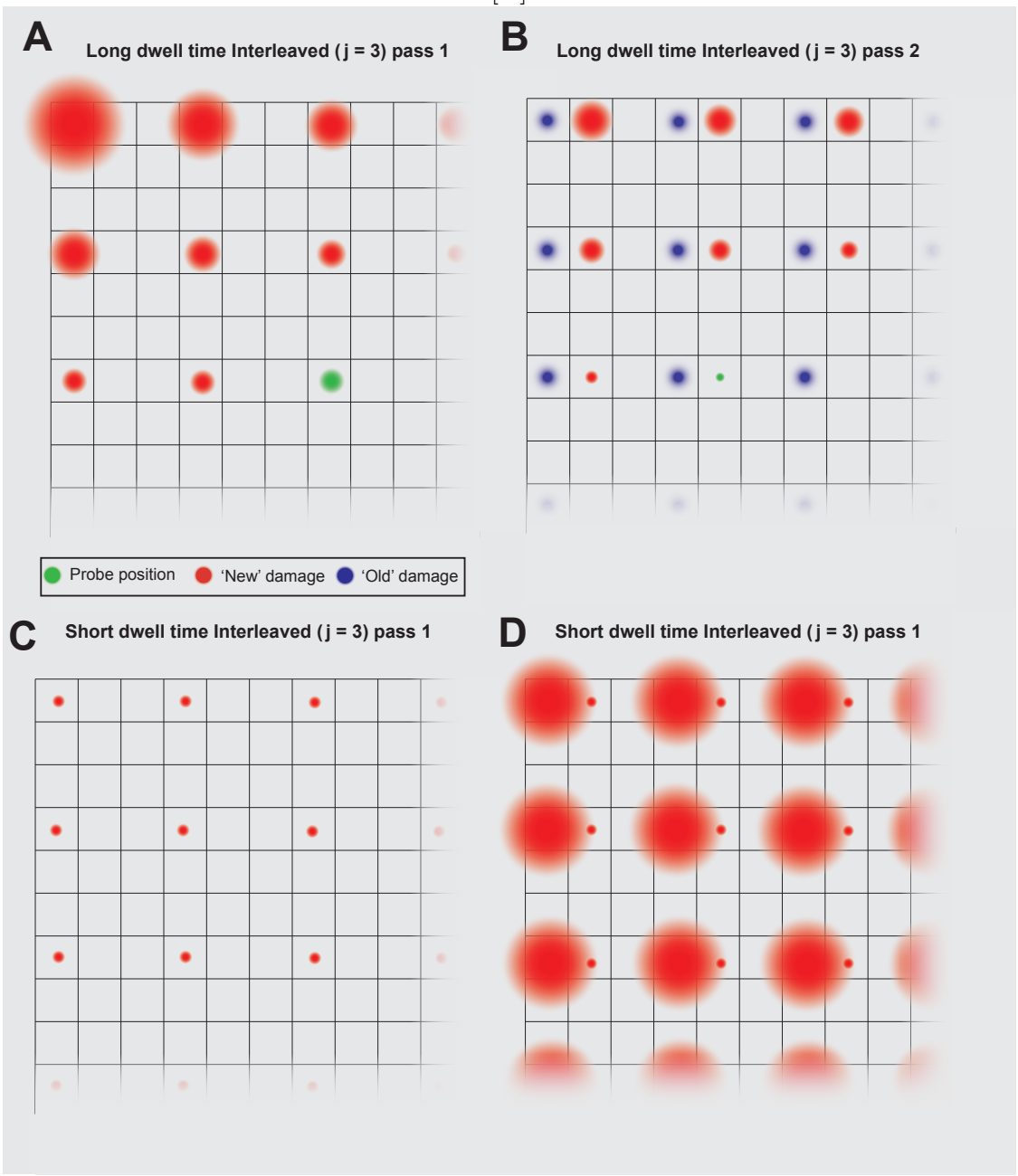


Figure A.15: **Interleaved Scanning Explanation Schematics A** The first pass of the interleaved scanning with a long dwell time allows sufficient space between sequentially-scanned positions for the products of damage to diffuse away from the irradiated areas. **B** Once the second pass of scanning occurs using an interleaved scan, sufficient time has passed to allow *(Figure caption continued on the following page).*

Figure A.15: *(continued figure caption)*: the products from the previously irradiated positions (blue) to diffuse or quench so that scanning o an adjacent pixel is no longer a runaway effect as with raster. **C** The first pass with a fast interleaved scan may complete the entire frame fast enugh that while no overlap of scanned regions occurs during this pass, the probe returns to the next adjacent pixel quickly enough that it does not allow enough time for the products from the previously irradiated positions to diffuse or quench (red larger circles). This is a possible explanation for the counter-intuitive but highly consistent mass loss results obtained from interleaved and raster scanning at the different dwell time acquisition schemes tested. (Return to Chapter 4)

A.5 Appendix for Chapter 5: SEM Damage

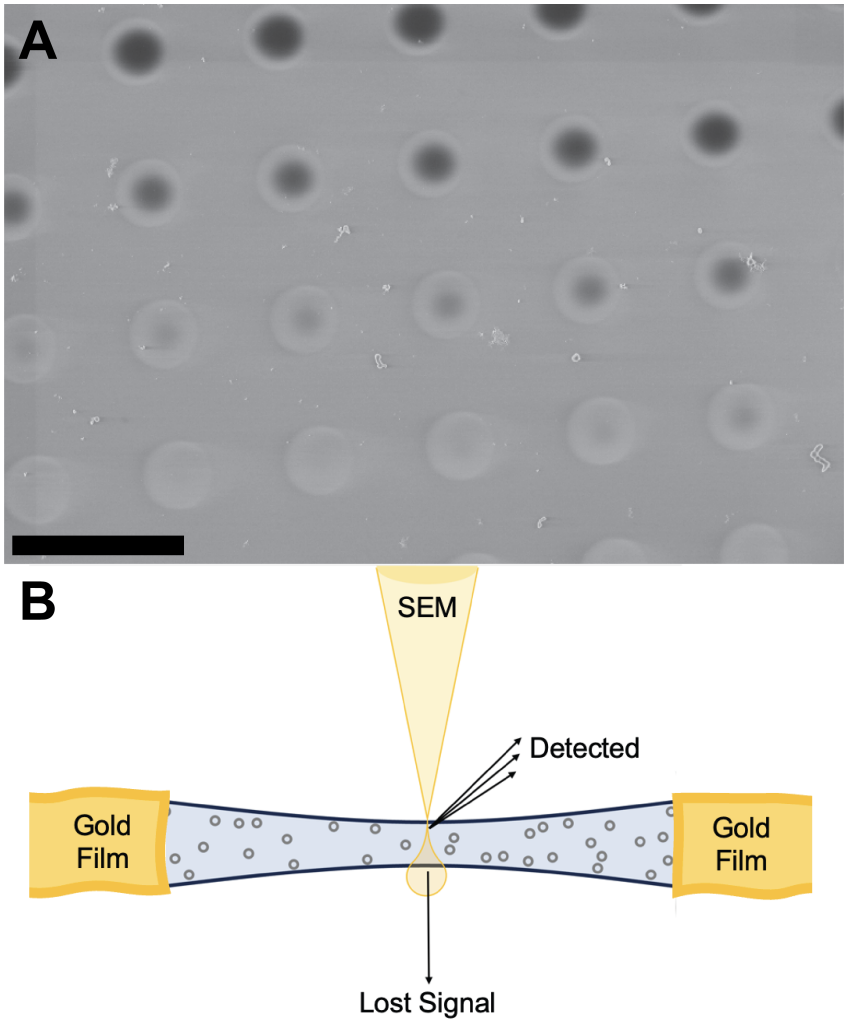


Figure A.16: **Thickness gradient across SPA type sample of apoferritin from Chapter 5. A** It is hypothesised that the darker regions in the centre of the holes towards the top of the frame are due to the escape of some secondary electrons from the bottom surface of the thin sample, as demonstrated in schematic in **B**. This effect was useful for locating regions of the grid that were likely suitable for TEM imaging downstream. Scale bar 5 µm. (Return to Chapter 5)

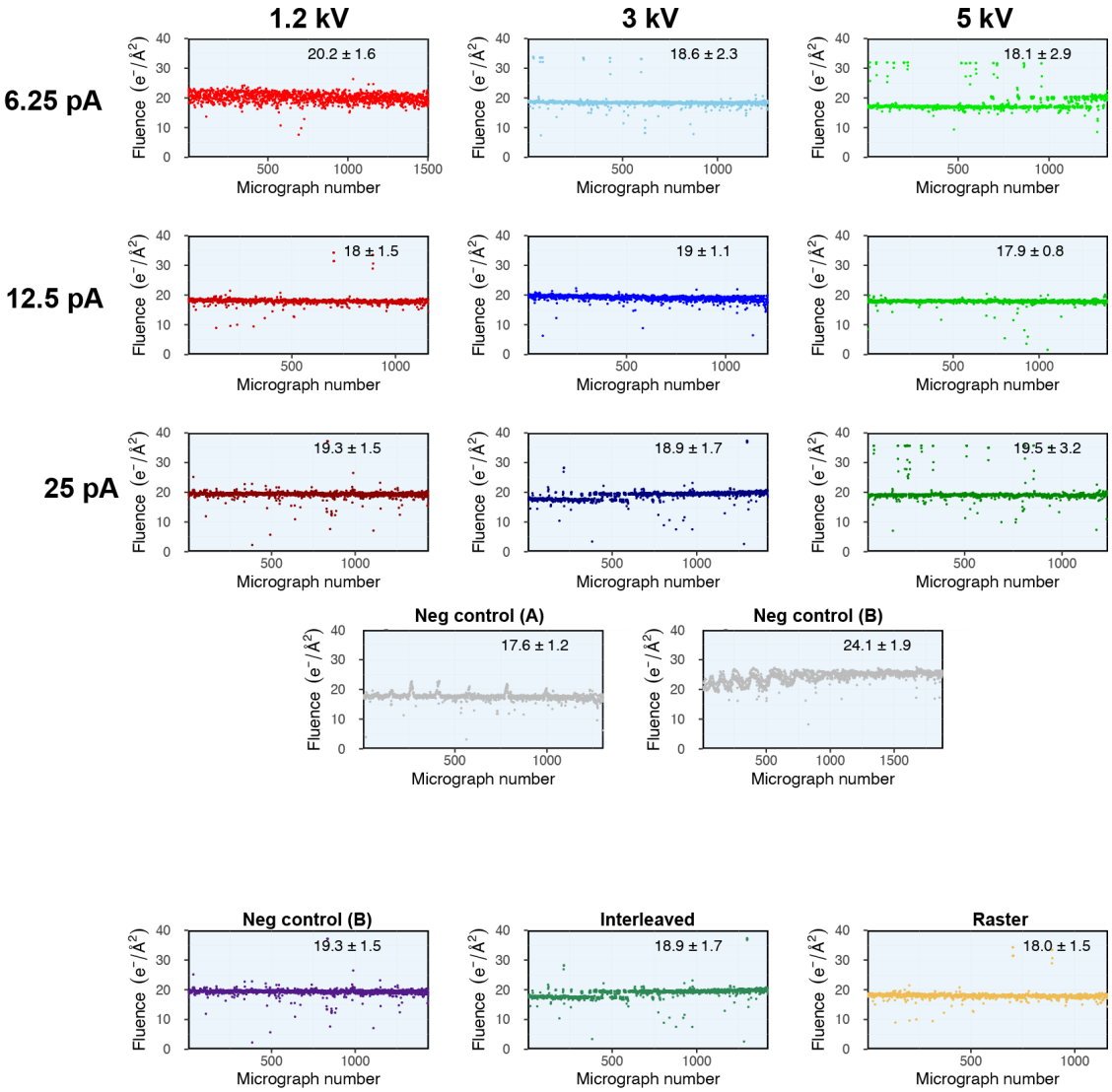


Figure A.17: **'Dose on Camera' as output by ThermoFisher Titan Krios EPU data**. Used as a relative proxy for ice thickness, the 'dose' (fluence) on the Falcon 4i is plotted for each micrograph and every condition (separate gridsquares). Overall there is general agreement between the values, at a mean of 19.0 ± 1.5 $e^{-}Å^{-2}$. (Return to Chapter 5)

Table A.2: Data processing summary for the 5 kV, 1.2 kV, and 3 kV datasets presented in Chapter 5. Numbers in the job titles (e.g. 001) refer to the job numbers in 5.1. Percentages of the particles kept from the last classification job are displayed in brackets. Red bold numbers indicate jobs that were unable to be aligned and were therefore discontinued. (Return to Chapter 5)

		Import (001-009)	Autopick (062-070)		Class 2D (Bin4) (087-094)	Class 3D (Bin4) C1 (145-156)	Refine3D (Bin4) C1 (230-239)	Class 3D (Bin2) C1 (285-293)	Refine3D (Bin2) Oct (458-475)	Class 3D (Bin1) C1 (488-494)	Refine3D (Bin1) Oct (549-568)
Order acq. TEM (Grid)	Condition	Micro-graphs	Particles $\times 10^3$	Particles per img	Particles $\times 10^3$ (%)	Particles $\times 10^3$ (%)	Resolution (Å)	Particles $\times 10^3$ (%)	Resolution (Å)	Particles $\times 10^3$ (%)	Resolution (Å)
9 (1)	Neg Cont (1)	1,308	556	425	183 (33%)	148 (81%)	6.06	135 (91%)	3.03	84 (62%)	2.65
12 (2)	Neg Cont (2)	1,884	819	434	388 (47%)	168 (43%)	6.06	148 (88%)	3.03	84 (57%)	2.73
11 (2)	1.2 kV 6.25 pA	1,958	844	431	429 (51%)	120 (28%)	6.25	42 (35%)	4.12	11 (26%)	4.04
3 (1)	1.2 kV 12.5pA	1,160	485	418	182 (38%)	47 (26%)	**9.24**	-	-	-	-
1 (1)	1.2 kV 25 pA	1,440	585	406	230 (39%)	62 (27%)	**9.24**	-	-	-	-
6 (1)	3 kV 6.25pA	1,324	560	423	187 (33%)	80 (42%)	6.47	40 (50%)	4.73	23 (58%)	4.22
7 (1)	3 kV 12.5 pA	1,400	589	420	222 (38%)	79 (36%)	**8.09**	-	-	-	-
4 (1)	3 kV 25pA	1,236	509	412	153 (30%)	46 (30%)	**10.74**	-	-	-	-
8 (1)	5 kV 6.25 pA	1,286	539	425	199 (37%)	127 (64%)	6.06	107 (83%)	3.13	63 (59%)	2.99
5 (1)	5 kV 12.5pA	1,216	510	419	174 (34%)	122 (70%)	6.06	88 (71%)	3.66	49 (56%)	3.47
2 (1)	5 kV 25 pA	1,424	575	404	237 (41%)	71 (30%)	**8.44**	-	-	-	-
TOTAL		15,636	6,571	420	4,584	1,070	-	560	-	560	-

Table A.3: Data processing summary for the negative control, raster, and interleaved datasets presented in Chapter 5 (Return to Chapter 5)

		Import (001-003)	Autopick (064-066)		Class 2D (Bin4) (081-083)	Class 3D (Bin4) C1 (093-096)	Refine3D (Bin4) C1 (104-119)	Class 3D (Bin2) C1 (123-125)	Refine3D (Bin2) Oct (183-191)	Class 3D (Bin1) C1 (195-197)	Refine3D (Bin1) Oct (253-264)
Order (grid)	Condition	Micro-graphs	Particles $\times 10^3$	Particles per img	Particles $\times 10^3$ (%)	Particles $\times 10^3$ (%)	Resolution (Å)	Particles $\times 10^3$ (%)	Resolution (Å)	Particles $\times 10^3$ (%)	Resolution (Å)
13 (2)	Neg Control (2)	1988	528	264	362 (68%)	252 (70%)	6.06	238 (94%)	3.03	81 (34%)	2.65
14 (2)	Raster (5kv, 6.25 pA)	1644	413	251	288 (68%)	203 (70%)	6.06	120 (60%)	4.12	71 (60%)	3.88
15 (2)	Interleaved (5kv, 6.25 pA)	1636	408	249	273 (68%)	204 (74%)	6.06	163 (80%)	3.66	57 (35%)	3.66

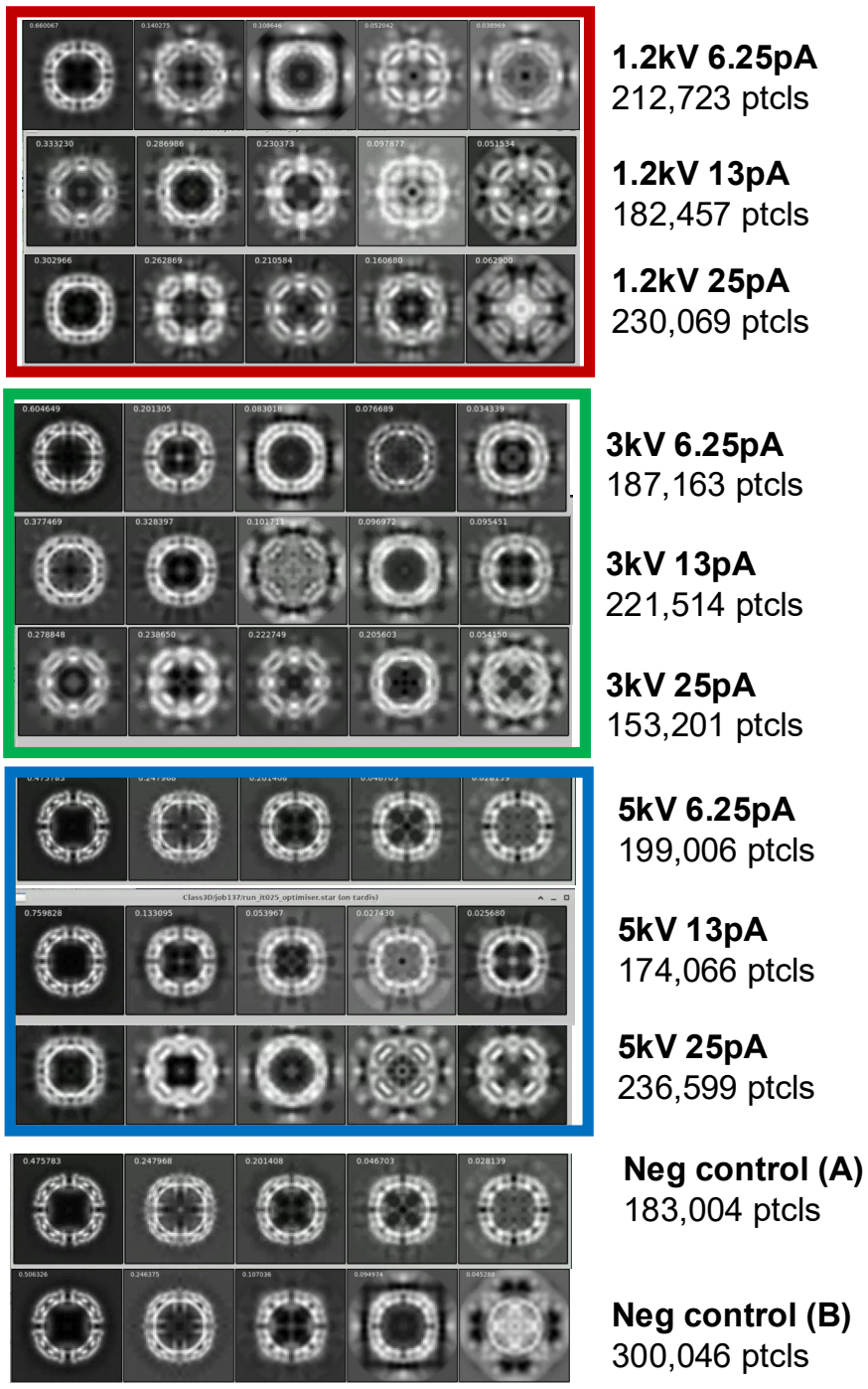


Figure A.18: **Octahedral (O) symmetry 3D classification results**. Central slices of each 3D model produced are shown, at 3.03 Å pixel^{-1} (Bin4), after using 25 iterations to sort particles. The conditions used in the SEM (1.2 kV, 3 kV, and 5 kV in red, green, and blue boxes, respectively, with increasing currents) are displayed along with the total number of particles to the right of each group of 5 classes. (Return to Chapter 5)

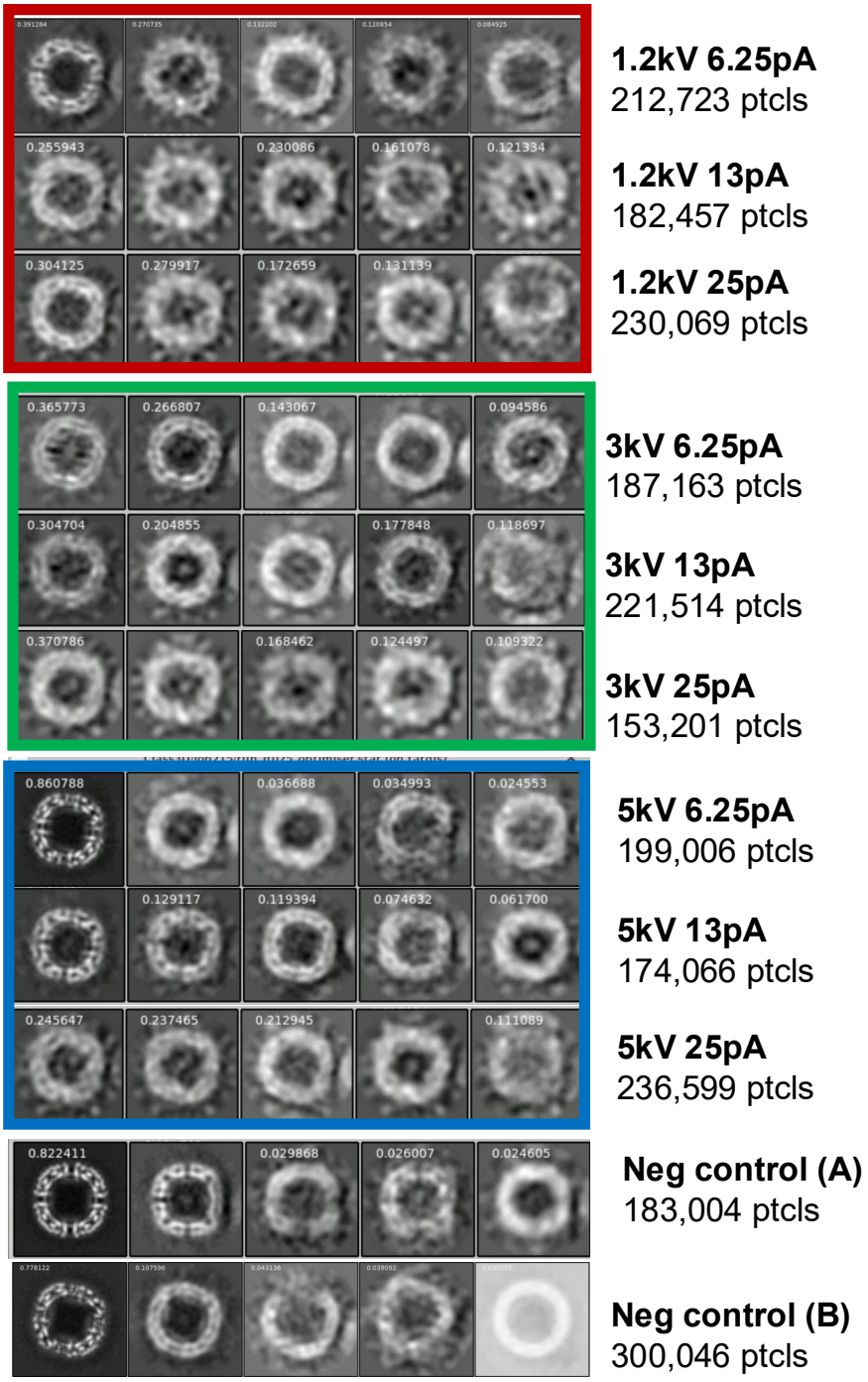


Figure A.19: **No symmetry (C1) 3D classification results**. Central slices of each 3D model produced are shown, at 3.03 Å pixel^{-1} (Bin4), after using 50 iterations to sort particles. The conditions used in the SEM (1.2 kV, 3 kV, and 5 kV in red, green, and blue boxes, respectively, with increasing currents) are displayed along with the total number of particles to the right of each group of 5 classes.

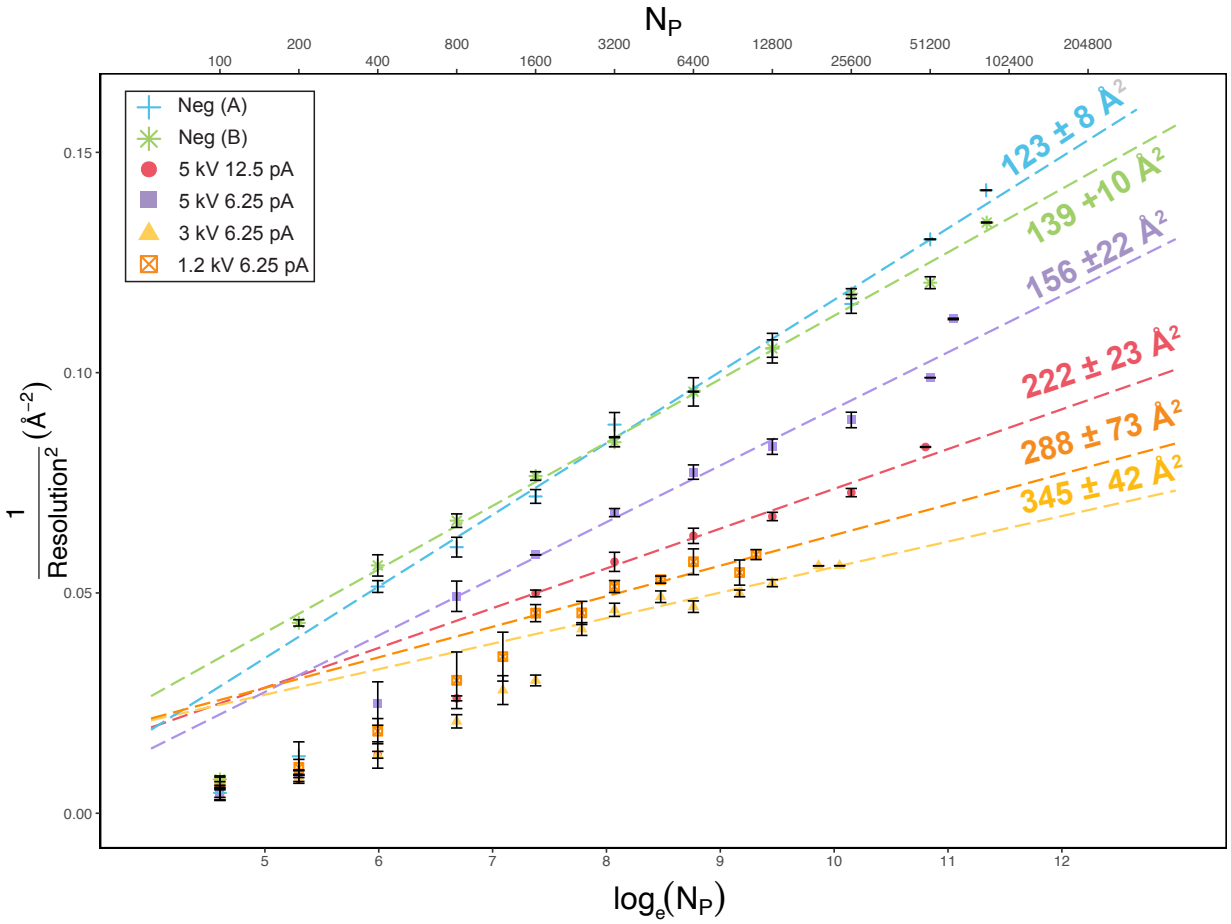


Figure A.20: **Larger plot of Figure 5.6C, with displayed error bars**. Error bars calculated from standard error of 3 measurements of resolution at FSC = 0.143 for each point. Lines fitted from 1600 particles to ensure the linear portion of the data were used.

A.5.1 Preliminary Tomography Dataset

Briefly, the same grid was used for the interleaved and raster dataset collection, and the 1.2 kV 6.25 pA was used to collect cryo-ET data. 195 tomograms were taken in total, 65 for each condition (1.2 kV 6.25 pA, 5 kV 6.25 pA, and negative control), at a reduced pixel size of 1.57 Å pixel^{-1} compared to the SPA data presented in Chapter 5. The exact methods for the tomography data collection are as described in Section A.1.1.1

These data have not yet been fully processed in STA, however a method was established to annotate boundaries in order to calculate distance from the top surface of the vitreous ice for subsequent analysis, as shown in Figure A.21 below:

[H]

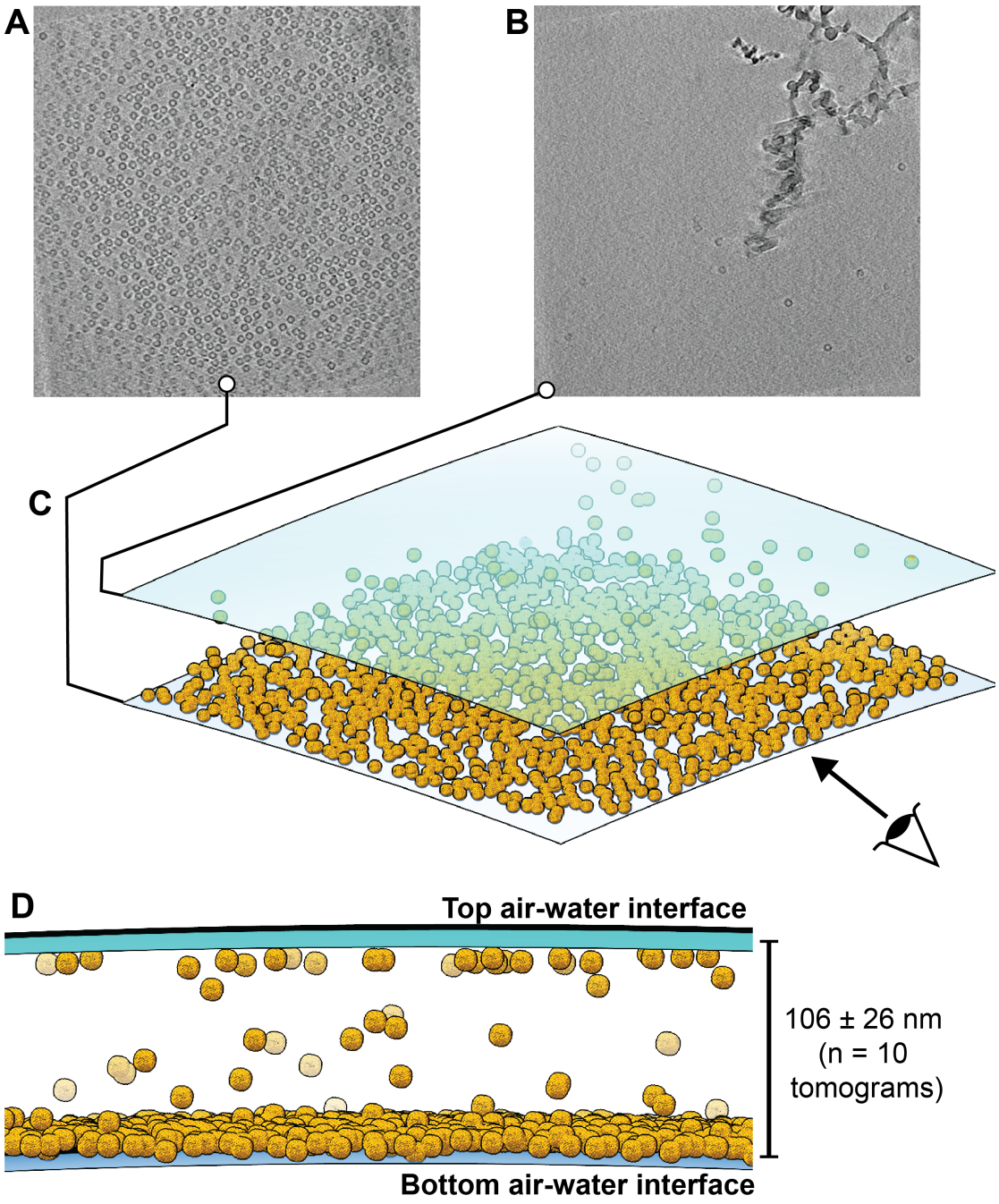


Figure A.21: **Preliminary Tomography Data A** Tomogram slices from Aretomo-reconstructed tomograms displaying Apoferritin thoughout the volume on two surfaces. **B**, **C**, **D** show a side-on view of the annotated boundaries, with the top and bottom air water interfaces labelled, displaying the mean ± 1 SD of thicknesses observed over 10 tomograms. (Return to Chapter 5)

Although these tomography data are preliminary, they do offer some insight into the thickness of the grid, and verify that the 100 nm estimate of sample thickness

for the simulations (Figures 5.2 and 5.10) are approximately correct.